Exploring Cancer Metabolism through Isotopic Tracing and Metabolic Flux Analysis

by

Wentao Dong

B.S. Chemical Engineering, University of Wisconsin – Madison (2014)

B.S. Chemistry, University of Wisconsin – Madison (2014)

M.S. Chemical Engineering Practice, Massachusetts Institute of Technology (2017)

Submitted to the Department of Chemical Engineering

in partial fulfillment of the requirements for the degree of

Doctor of Philosophy in Chemical Engineering

at the

MASSACHUSETTS INSTITUTE OF TECHNOLOGY

July 2020

Author……

Department of Chemical Engineering

July 21, 2020

Certified by……

Gregory Stephanopoulos
Willard Henry Dow Professor in Biotechnology and Chemical Engineering

Thesis Supervisor

Accepted by……

Patrick S. Doyle
Robert T. Haslam (1911) Professor of Chemical Engineering

Chairman, Committee for Graduate Students

Exploring Cancer Metabolism through Isotopic Tracing and Metabolic Flux Analysis

By

Wentao Dong

Submitted to the Department of Chemical Engineering

On July 21, 2020, in partial fulfillment of the

requirements for the degree of

Doctor of Philosophy in Chemical Engineering

Abstract

Cancer is the second leading cause of death following heart diseases in the U.S. During the past two decades, cancer metabolism has emerged as an indispensable part of contemporary cancer research. Various types of metabolic alterations in cancer cells have been documented, prompting extensive investigation of the link between reprogrammed cell signaling pathways and rewired cellular metabolism. In addition, drug targeting of rewired metabolic pathways has been demonstrated to be a promising cancer treatment strategy. Despite this progress, a fundamental question remains unanswered: whether there is a difference in the metabolism of cancerous, fast growing cells and normal proliferative cells. This deficiency has hindered our understanding of cancer metabolism and the efforts to develop effective cancer therapies targeting metabolism with reduced side effects.

In this thesis, we used ^{13}C-isotope tracing and metabolic flux analysis (MFA) to study cancer metabolism and identify metabolic pathways differentially activated in cancer cells. To support efforts to design effective therapeutic therapies, we sought to distinguish metabolic behavior in cancer versus normal cells growing at the same speed, and obtain a systematic

understanding of cancer metabolism. To this end, we dissected bioreaction networks in human mammary epithelial cells (HMECs) that have been genetically modified to exhibit different levels of tumorigenicity. We discovered distinct substrate utilization pattern in the tricarboxylic acid (TCA) cycle and *de novo* lipogenesis. Specifically, we found that glucose was catabolized in the TCA cycle up to the formation of citrate, which was then used primarily for lipogenesis. The majority of the TCA cycle flux, however, was maintained by glutamine anaplerosis. ^{13}C-MFA further revealed that some metabolic reactions were more activated in tumorigenic HMECs. By introducing a new quantity termed metabolic flux intensity, defined as pathway flux divided by the specific growth rate, we identified three most enhanced reactions – oxidative pentose phosphate pathway (oxPPP), malate dehydrogenase (MDH) and isocitrate dehydrogenase (IDH) in the most tumorigenic HMEC. Targeting of these three pathways with small molecule inhibitors selectively reduced growth in the cancerous HMEC line. In addition, our study provides direct evidence that metabolism may be dually controlled by proliferation and oncogenotypes.

Thesis Supervisor: Gregory Stephanopoulos

Title: Willard Henry Dow Professor in Biotechnology and Chemical Engineering

Acknowledgements

Graduate school has been such an amazing experience. Cambridge was where I spent the second longest period of time so far after my hometown. There are many people that I would like to acknowledge for their companionship and support during my time at MIT.

First of all, I would like to thank my thesis advisor, Professor Gregory Stephanopoulos, for his valuable guidance on my research and immense support for my career development. As a chemical engineer, I have always had a keen interest in chemistry and molecular analysis of biological phenomena. I was excited to learn that our research interests matched perfectly during my first meeting with Professor Stephanopoulos. I knew immediately that I would like to join his research group. Professor Stephanopoulos has always been supportive of any ideas that I come up with and fostered my research independence. When things were not working, he was encouraging and patient, often asking insightful questions that prompted me to think deeper about the projects. Throughout my PhD, Professor Stephanopoulos has supported me in many ways toward my career development. One thing I appreciate the most is his responsiveness to my requests for help ranging from seeking advice and scheduling meetings to asking for recommendation letters. I can definitely feel that he truly cares about my academic and professional growth within and beyond graduate school.

My thesis committee, Professors Othon Iliopoulos, Joanne Kelleher, Hadley Sikes and Matt Vander Heiden, has been an incredibly valuable resource throughout my PhD training. Their collective input and feedback not only provided immense guidance on my thesis, but also promoted my intellectual growth to become a better scientist and engineer. In particular, I would like to acknowledge Matt for welcoming me into his research group and allowing me to access his lab and research instruments. Matt has also been extremely supportive of my professional development, especially during my postdoc applications. In addition to my thesis projects, I also worked on type II diabetic metabolism under the mentorship of Professor Brice Emanuelli, who has been instrumental in guiding me through an unfamiliar yet fascinating project.

I am eternally grateful for Mark Keibler, who has been a fantastic mentor during the early stage of my PhD training. We also become close friends outside of lab. I remember when I first joined the lab, Mark was the one who introduced me to the group members and taught me how to

perform metabolic assays. We collaborated extensively on several projects, during which I learned tremendous amount of knowledge and research skills. We have been keeping in touch with each other after his graduation, and luckily, he still lived in town. We have been chatting everything including sciences, politics and career options. It is safe to say that Mark is one of the nicest people I have ever met in my life so far.

In addition to Mark, I am also thankful to our lab's mammalian cell metabolism subgroup. Sun Jin Moon, a younger generation of our subgroup, has been collaborating with me a lot near the end of my PhD. It has been a wonderful experience from which I learned several non-metabolic research techniques from him. Although Marie Isidor only visited MIT for a semester, our collaboration was fruitful and she has taught me several critical skills for experimental designs. Zhe Zhang, Woo Suk Ahn and Bobby Basu have been very supportive of my work and provided many insightful suggestions along the way. At the beginning of my PhD, Mark and I worked closely with several UROPS, Aasavari Phanse, Orlando Arevalo and Jennifer Lee, who worked diligently and contributed to a series of projects related to the HMEC study.

I would also like to thank other current and past members of the Stephanopoulos Lab: Nian Liu, Junyoung Park, Jingbo Li, Vincent Zu, Yongshuo Ma, Brian Pereira, Ben Woolston, Alkis Chatzivasileiou, Boon Uranukul, Bob Van Hove, David Emerson, Peng Xu, Haoran Zhang, Kang Zhou, Wen Wang, Zbigniew Lazar, Kangjian Qiao, Zhengshan Luo, Felix Lam, Jack Hammond, Costas Katsimpouras, George Daletos, Jingyang Xu, Irum Perveen, Zhengjun Li, Valerie Ward, Devin Currie, Jason King, Ahsan Islam, Steven Edgar, Tom Wasylenko, Andy Silverman, Michael Reiter, Ying Wang, Claude Hoeltgen, Amit Kumar, Niju Narayanan, Yuting Zheng, Peter Enyeart, Rosangela dos Santos and Nicholas Pasinella. Particularly, Nian is one of my best friends in graduate school. We had a lot of fun talking about research, video games and many more. Jun was always happy in the lab, cheering everyone up and spreading happiness. Jingbo, Vincent and Yongshuo organized the best festival celebrations, during which I had great food and so much fun. I enjoyed lunching out and chatting with Brian, Ben, Zhengshan, Alkis, Boon, Bob, David, Peng, Haoran, Jack, Kang, Wen, Zibi, Kangjian, Haoran, Costas, George, Valerie, Devin and Jason during group events. Toward the end of my PhD, Jun, Ben, Kang, Haoran and Peng also gave me great advice for postdoc hunting. Rosangela and Nicholas have been extremely helpful in a variety of ways, and their dedication to the lab's administration has

made my daily life much easier. Rosangela is also one of the kindest persons I have ever met. I wish her all the best for a happy retirement in Florida.

Over the years, I have collaborated with many brilliant scientists from MIT and Harvard: Jon Coloff, Patricia Cho, Marlies Rossmann, Cheuk Him Man, Zhaoqi Li, Evan Lien, Dan Schmidt, Keene Abbott, Nick Matheson, Allison Lau, Alex Muir and Brooke Bevis. Specifically, Jon and Patricia helped me with the western blotting experiments for one of my thesis projects. Marlies and Cheuk shared their fascinating projects from which I learned sciences outside of my thesis. Zhaoqi, Evan, Dan, Keene, Nick, Allison, Alex and Brooke from Matt's lab helped me with several assays and provided valuable comments and recommendations for my thesis work.

Graduate school is rewarding not only because of the research experiences. I also enjoyed being a graduate teaching assistant. I would like to thank the instructors of the courses, Professors Yuriy Román, Heather Kulik and Paul Barton for having me as their TA. In addition, I am also grateful to my fellow TAs: Tedrick Thomas Salim Lew, John Mikhail, Patrick Asinger and Andrew Biedermann. In addition to teaching, I also joined with my colleagues and worked at FDA and Corning for practice school (an internship program unique to MIT ChemE). I enjoyed collaborating on several interesting projects with Eric Xu, Gang Wang, Kai-Jher Tan, John Swalec, Shuting Feng, Connor Coley, Patricia Meyer and Emily Patt. We also had great time sightseeing and hiking together during weekends in the DC and Upstate New York areas. In addition, I am grateful to our station directors Bob Fisher and Claude Lupis, who provided helpful guidance to our projects. Outside of lab, I had great fun with many friends, who have always been cheerful and supportive. I want to acknowledge a few in particular: Albert Liu, Jim Chu, Mark Goldman, Joey Gu, Moo Sun Hong, Yiming Mo, Max Liu and Yinying Ren.

Throughout my PhD, I have received countless valuable academic and career advice from my former mentors, Xiaojun Lian and Xiaoping Bao, who are currently professors at Penn State and Purdue University, respectively. I would also like to acknowledge the continuous support from my academic advisors in college, Professors Sean Palecek and Manos Mavrikakis, who have constantly encouraged my research progress over the years. In addition, I am eternally thankful for my middle school (9th grade) chemistry teacher, Ms. Yu Li, who sparkled my interest in chemistry that propelled my research career through and beyond graduate school.

Last but not least, everything would not be possible without my family: my mother Bufang Lei, father Liang Dong and wife Shiyun Tian. Although we were usually far away from each other, their love and support have always been tremendously helpful in every way imaginable. I cannot express my gratitude enough for all the sacrifices they have made and motivations they have provided throughout my journey in graduate school.

Contents

1. Introduction.....34

1.1 Cancer metabolism 37

1.2 ^{13}C-isotope tracing and metabolic flux analysis.....38

1.3 Thesis motivation..... 40

1.4 Thesis overview 42

1.5 References.....44

2. Metabolic pathways differentially activated in cancer cells.....53

2.1 Abstract..... 54

2.2 Introduction.....54

2.3 The Warburg effect..... 58

2.4 Metabolic alterations along glycolysis..... 59

2.5 Reductive metabolism of glutamine.....66

2.6 Isocitrate dehydrogenase mutations.....71

2.7 Serine and glycine metabolism..... 72

2.8 Acetate metabolism and alternative sources of acetyl-CoA..... 76

2.9 Oncogene-specific metabolic rewiring.....78

2.10 Concluding remarks.....82

2.11 References.....86

3. Dissecting Mammalian Cell Metabolism through ^{13}C- and ^{2}H-Isotope Tracing: Interpretations at the Molecular and Systems Levels.....102

3.1 Abstract.....104

3.2 Introduction.....104

3.3 Glucose-Driven TCA Cycle Probed by U-$^{13}C_6$-Glucose.....106

3.4 Glutamine-Driven TCA Cycle Probed by U-$^{13}C_5$-, 1-^{13}C-, and 5-^{13}C-Glutamine.....120

3.5 Acetate-Driven TCA Cycle Probed by 1,2-$^{13}C_2$-Acetate and 1-^{13}C-/1,6-$^{13}C_2$-Glucose.....135

3.6 Pentose Phosphate Pathway (PPP) Probed by 1,2-$^{13}C_2$-, 2-^{13}C- and 3-^{13}C-Glucose.....141

3.7 ^{2}H-Isotopic tracers.....150

3.8 ^{13}C-metabolic flux analysis.....158

3.9 Discussion and conclusions.....164

3.10 Nomenclature.....169

3.11 References.....181

4. Oncogenic metabolic rewiring independent of proliferative control in human mammary epithelial cells.....190

4.1 Abstract.....192

4.2 Introduction.....193

4.3 Construction of HMECs with differing levels of tumorigenicity.....194

4.4 Quantification of extracellular fluxes suggests dual control of metabolism by proliferation and oncogenotypes.....200

4.5 C-isotopic labeling reveals distinct substrate utilization patterns in the TCA cycle and *de novo* lipogenesis.....205

4.6 Quantification of intracellular metabolism via ^{13}C-metabolic flux analysis (^{13}C-MFA) corroborates proliferative control of metabolism.....214

4.7 Normalizing fluxes against growth by introducing metabolic flux intensity (MFI).....225

4.8 Assessing the therapeutic potential of targeting oxPPP, MDH and IDH.....228

4.9 Discussion and conclusions.....231

4.10 Experimental procedures.....236

4.11 References.....247

5. Conclusions and future work.....256

5.1 Summary and concluding remarks …….....258

5.2 Future directions …….....262

5.3 References …….....266

List of Figures

2.1 A global overview of the metabolic network critical in cancer cells.....59

2.2 The PKM2-mediated glycolytic pathway..... 61

2.3 The GAPDH-mediated reversal of glycolytic flux..... 63

2.4 The isotopic labeling pattern generated by 1,2-$^{13}C_2$-glucose.....65

2.5 The isotopic labeling pattern generated by U-$^{13}C_5$- glutamine..... 69

2.6 Serine and glycine metabolism..... 75

2.7 Upstream of the RTK pathway.....78

2.8 Downstream of the RTK pathway..... 79

2.9 Ras and the MAP kinase pathway..... 80

2.10 Detailed summary of rewired metabolic pathways in cancer cells.....85

3.1a Chemical structures of TCA cycle metabolites and carbon transition maps highlighting the positional information through reactions.....108

3.1b Labeling results of TCA cycle intermediates after the first round of cycling.....109

3.1c Labeling results of TCA cycle intermediates after the second round of cycling by 1,2-$^{13}C_2$-oxaloacetate.....109

3.1d Labeling results of TCA cycle intermediates after the second round of cycling by 3,4-$^{13}C_2$-oxaloacetate.....110

3.1e Labeling results of TCA cycle intermediates after the third round of cycling by 1,2,3-$^{13}C_3$-oxaloacetate.....110

3.1f Labeling results of TCA cycle intermediates after the third round of cycling by 2,3,4-$^{13}C_3$-oxaloacetate.....111

3.1g Labeling results of TCA cycle intermediates after the third round of cycling by 1,2,4-$^{13}C_3$-oxaloacetate.....111

3.1h Labeling results of TCA cycle intermediates after the third round of cycling by 1,3,4-$^{13}C_3$-oxaloacetate.....112

3.2a Chemical structures and carbon transition maps highlighting the positional information through the PC reaction.....114

3.2b Labeling results of TCA cycle intermediates within the first round of cycling with both PDH and PC reactions, assuming the PC flux cannot reverse the entire TCA cycle but dominates the labeling patterns along the reversible reactions within the cycle.....114

3.2c Labeling results of TCA cycle intermediates within the first round of cycling with both PDH and PC reactions, assuming the PC flux totally reverses and dominates the entire TCA cycle.....115

3.2d Chemical structures and carbon transition maps highlighting the positional information through the ME reaction.....115

3.2e Labeling results of TCA cycle intermediates within the first round of cycling with both PDH and ME reactions.....116

3.2f Chemical structures and carbon transition maps highlighting the positional information through the PEPCK reaction.....116

3.2g Labeling results of TCA cycle intermediates within the first round of cycling with both PDH and PEPCK reactions.....117

3.3a Labeling patterns of TCA cycle intermediates after the first round of PDH cycling.....118

3.3b Alterations of labeling patterns by PC, ME/PEPCK and the reversible scrambling reactions among oxaloacetate, malate, fumarate and succinate during the first round of cycling.....118

3.3c Labeling patterns of TCA cycle intermediates after the second round of PDH cycling, based on available isotopomers of oxaloacetate and pyruvate from the previous round.....119

3.4a Labeling patterns of TCA cycle intermediates by U-$^{13}C_5$-glutamine through glutamine anaplerosis.....123

3.4b Labeling patterns of TCA cycle intermediates within the first round of oxidative cycling in the presence of both PDH and glutamine anaplerosis.....124

3.4c Labeling patterns of TCA cycle intermediates through reductive glutamine metabolism.....124

3.4d Alterations of labeling patterns by PC, ME/PEPCK and the reversible scrambling reactions among oxaloacetate, malate, fumarate and succinate during the first round of cycling.....125

3.4e Labeling patterns of TCA cycle intermediates after the second round of oxidative cycling, based on available isotopomers of α-ketoglutarate from the previous round.....126

3.4f Labeling patterns of TCA cycle intermediates after the third round of oxidative cycling, based on available isotopomers of α-ketoglutarate from the previous round.....126

3.5 Labeling patterns of TCA cycle intermediates by U-$^{13}C_5$-glutamine dominated by pyruvate dehydrogenase (PDH) that supplies unlabeled acetyl-CoA (AcCoA).....128

3.6 Additional labeling patterns of TCA cycle intermediates by U-$^{13}C_5$-glutamine dominated by pyruvate dehydrogenase (PDH) that supplies unlabeled acetyl-CoA (AcCoA).....129

3.7a Labeling patterns of TCA cycle intermediates by 1-(carboxyl)-^{13}C- and 5-(amine)-^{13}C-glutamine through glutamine anaplerosis.....131

3.7b Labeling results of TCA cycle intermediates by 1-(carboxyl)-^{13}C-glutamine through reductive glutamine metabolism.....132

3.7c Labeling results of TCA cycle intermediates by 5-(amine)-^{13}C-glutamine within the first round of oxidative cycling in the presence of both PDH and glutamine anaplerosis.....132

3.7d The presence of PC and ME/PEPCK reactions does not change the labeling patterns of TCA cycle intermediates by 5-(amine)-^{13}C-glutamine.....133

3.7e Labeling results of TCA cycle intermediates by 5-(amine)-^{13}C-glutamine through reductive glutamine metabolism.....134

3.8a Labeling patterns of TCA cycle intermediates by 1,2-$^{13}C_2$-acetate and 1-^{13}C-/1,6-$^{13}C_2$-glucose.....136

3.8b Labeling results of TCA cycle intermediates by 1-^{13}C-/1,6-$^{13}C_2$-glucose within the first round of PDH cycling.....137

3.8c Alterations of labeling patterns by PC, ME/PEPCK and the reversible scrambling reactions among oxaloacetate, malate, fumarate and succinate during the first round of cycling.....137

3.8d Labeling results of TCA cycle intermediates after the second round of PDH cycling, based on available isotopomers of oxaloacetate and pyruvate from the previous round.....138

3.8e Alterations of labeling patterns by PC, ME/PEPCK and the reversible scrambling reactions among oxaloacetate, malate, fumarate and succinate during the second round of cycling.....139

3.8f Labeling results of TCA cycle intermediates after the third round of PDH cycling, based on available isotopomers of oxaloacetate and pyruvate from the previous round.....139

3.9a The pentose phosphate pathway (PPP) and glycolysis probed by 1,2-$^{13}C_2$-, 2-^{13}C- and 3-^{13}C-glucose.....143

3.9b Labeling patterns of PPP intermediates by 1,2-$^{13}C_2$-glucose, assuming no backward cycling of ^{13}C-labeled F6P.....144

3.9c Chemical structures and carbon transition maps highlighting the positional information through glycolysis.....145

3.9d Labeling patterns of glycolytic intermediates by 1,2-$^{13}C_2$-glucose.....146

3.9e Labeling patterns of PPP intermediates by 2-^{13}C-glucose, assuming no backward cycling of ^{13}C-labeled F6P.....147

3.9f Labeling patterns of PPP intermediates by 3-^{13}C-glucose, assuming no backward cycling of ^{13}C-labeled F6P.....148

3.9g Labeling patterns of glycolytic intermediates by 2-^{13}C-glucose.....149

3.9h Labeling patterns of glycolytic intermediates by 3-^{13}C-glucose.....149

3.10a Deuterium isotopic tracers for assessing pathway activities of NAD(P)H generation as well as fatty acid and amino acid synthesis.....152

3.10b 1-^{2}H-glucose and 3-^{2}H-glucose are used to label NADPH in the oxPPP and the upper part of glycolysis.....153

3.10c 4-^{2}H-glucose is used to label NADH.....154

3.10d 2,3,3-$^{2}H_3$-serine, 3-3-$^{2}H_2$-serine and 2-2-$^{2}H_2$–glycine are used to label NADPH in cytosol and mitochondria.....155

3.10e 2,2,3,3-$^{2}H_4$-dimethyl succinate is incorporated into the TCA cycle, allowing hydride transfer of the second carbon of malate to NADPH via the ME reaction.....156

3.10f Deuterium oxide ($^{2}H_2O$) is used to examine relative pathway magnitudes of *de novo* fatty acid and amino acid syntheses.....157

3.11a Demonstration of ^{13}C-metabolic flux analysis (^{13}C-MFA) for resolving complex metabolic patterns in the TCA cycle with multiple anaplerotic reactions.....161

3.11b Mass isotopomer distributions (MIDs) of TCA cycle intermediates in three different cases.....162

3.11c Metabolic fluxes of major TCA cycle and anaplerotic reactions in three different cases.....162

3.11d Labeling strength of TCA cycle intermediates in three different cases.....163

3.12 Labeling patterns of TCA cycle intermediates by U-$^{13}C_5$-glutamine dominated by pyruvate dehydrogenase (PDH) that supplies unlabeled acetyl-CoA (AcCoA).....172

3.13 First round labeling patterns of TCA cycle intermediates by 3-^{13}C-glucose.....174

4.1a Successful integration of p53DD in HMEC-p53DD-KRas was validated by the p53 antibody with β-actin as the loading control.....196

4.1a Successful integration of p53DD in HMEC-p53DD-KRas was validated by the p53 antibody with β-actin as the loading control.....196

4.1b Elevated expression of EGFR in HMEC-EGFR was validated by the EGFR antibody with β-actin as the loading control.....196

4.1c Successful integration of SV40ER in HMEC-SV40ER-KRas was validated by the SV40ER-Larte T antibody with β-actin as the loading control.....196

4.1d Elevated expression of Ras in HMEC-KRas, HMEC-p53DD-KRas and HMEC-SV40ER-KRas were validated by the enhanced phosphorylation states of the downstream target ERK1/2 probed by the phospho-ERK1/2 antibody.....196

4.1e Overexpression of defined oncogenes and dominant negative mutant forms of tumor suppressors in HMECs increased tumorigenicity.....197

4.1f Proliferation of the normal HMECs in response to different EGF concentrations.....199

4.1g Specific growth rate of the normal HMECs as a function of EGF concentration.....199

4.1h Growth factor independence observed in genetically modified HMECs with increasing levels of tumorigenicity, which was further corroborated by several other criteria.....200

4.2a Extracellular fluxes of glucose, lactate, glutamine and glutamate for HMECs at +/- EGF conditions.....202

4.2b Lactate yields from glucose, glutamate yields from glutamine and net glutamine uptake rates for HMECs at +/- EGF conditions.....202

4.2c Extracellular fluxes of +/- EGF HMECs plotted against specific growth rates. Error bars.....203

4.2d Lactate yields from glucose, glutamate yields from glutamine and net glutamine uptake rates against specific growth rates for both +/- EGF conditions.....203

4.2e Extracellular fluxes of only the +EGF HMECs plotted against specific growth rates.....204

4.2f Lactate yields from glucose, glutamate yields from glutamine and net glutamine uptake rates against specific growth rates for only the +EGF condition.....204

4.2g Compared to HMECs growth at both +/-EGF conditions, the +EGF subgroup exhibited similar growth rates.....205

4.2h Compared to HMECs growth at both +/-EGF conditions, the proliferative control of metabolism, as measured by the R2 values, was decreased in the +EGF subgroup.....205

4.3a U-$^{13}C_6$-glucose labeling pattern suggests weak incorporations of glucose-derived carbons into the TCA cycle except for citrate, the majority of which stays at M+2.....206

4.3b Labeling profiles of TCA cycling intermediates by 1,2-$^{13}C_2$-glucose confirmed that glucose is not the primary anaplerotic substrate, and that citrate is the only TCA cycle metabolite moderately labeled by glucose tracers.....207

4.3c U-$^{13}C_5$-glutamine labeling pattern suggests much stronger incorporations of glutamine-derived carbons into the TCA cycle.....208

4.3d U-$^{13}C_5$-glutamine labeling pattern suggests weak incorporations of glutamine-derived carbons into *de novo* fatty acid synthesis.....210

4.3e U-$^{13}C_6$-glucose labeling pattern suggests stronger incorporations of glucose-derived carbons into *de novo* fatty acid synthesis.....211

4.3f Isotopomer spectral analysis (ISA) confirmed that glucose dominated lipogenesis over glutamine.....212

4.3g Schematic overview of isotopomer spectral analysis (ISA).....212

4.3h ^{13}C-isotopic labeling analysis revealed a distinct substrate utilization pattern within the TCA cycle and *de novo* lipogenesis in contrast to the canonical view.....213

4.4a Essential components and steps for ^{13}C-metabolic flux analysis (^{13}C-MFA).....215

4.4b Metabolic pathways are color coded to indicate different parts of the metabolism.....216

4.4c ^{13}C-MFA generated consistent results with the labeling data regarding the partition of fluxes between glycolysis and oxPPP and the anaplerotic contributions from glucose and glutamine.....218

4.4d ^{13}C-isotopic labeling analysis suggests that the strength of PPP.....219

4.4e Consistent with ^{13}C-isotopic labeling analysis, ^{13}C-MFA also indicates that the absolute metabolic flux of PPP.....219

4.4f ^{13}C-MFA suggested that both intracellular and extracellular metabolism may be dually controlled by proliferation and oncogenotypes.....222

4.4g ^{13}C-MFA suggests that the pyruvate dehydrogenase (PDH) pathway is the main route of acetyl-CoA anaplerosis rather than the pyruvate carboxylase (PC) pathway.....223

4.4h TCA contribution from glucose and glutamine.....224

4.4i Lipogenic contribution from glucose and glutamine.....224

4.4j CO_2 contribution from glucose and glutamine.....224

4.4k Fates of glucose to lactate, lipids and CO_2.....224

4.4l Fates of glutamine to glutamate, lactate, lipids and CO_2.....224

4.5a Two modes through which oncogenotypes and proliferation affect metabolism, as well as the rationale and mathematical definition of the new quantity – metabolic flux intensity (MFI).....225

4.5b Quantitative ^{13}C-MFI analysis validated that oncogenotypes directly impact metabolism independent of proliferative control.....227

4.6a ^{13}C-MFI analysis identified oxPPP as the most enhanced reaction in HMEC-hTERT-LT-HRas.....228

4.6b ^{13}C-MFI analysis identified MDH and IDH as one of the most enhanced reactions in HMEC-hTERT-LT-HRas.....229

4.6c Drug targeting results for oxPPP, MDH and IDH.....230

4.6d Drug targeting of ATP-citrate lyase (ACLY), which showed invariant MFI across tumorigenicity, yielded no selective toxicity.....230

4.7a Metabolic fluxes of the malic enzyme (left) and the oxPPP (right) reactions.....233

4.7b Consistent with the metabolic flux results, the flux intensities of the malic enzymes stayed constant across different levels of tumorigenicity, suggesting strong proliferative control.....233

4.7c Normalized MFA results for all HMECs at +EGF condition. Darker orange color indicates higher levels of tumorigenicity.....235

5.1 Truncated TCA cycle: glutamine-fueled TCA oxidation and glucose-supported lipogenesis.....261

5.2 Metabolic flux intensity analysis suggested dual control of metabolism by proliferation and oncogenotypes.....261

5.3 Metabolic flux intensity analysis (top) identified oxPPP, MDH and IDH to be the most upregulated pathways in the tumorigenic HMECs (hTERT-LT-HRas).....262

List of Tables

3.1 Labeling patterns of oxaloacetate by U-$^{13}C_6$-glucose at each round of the TCA cycle with PDH as the only contributing reaction.....113

3.2 Labeling patterns of oxaloacetate at each round by U-13C5-glutamine dominated by PDH that supplies unlabeled AcCoA.....127

3.3 Applications of selected ^{13}C-isotopic tracers.....167

3.4 Applications of selected ^{2}H -isotopic tracers.....168

3.5 Biochemical reactions and carbon atom transitions used in ^{13}C-MFA.....176

3.6 ^{13}C-MFA results for Case I. Unit of fluxes and 95% confidence intervals is arbitrary (AU).....178

3.7 ^{13}C-MFA results for Case II. Unit of fluxes and 95% confidence intervals is arbitrary (AU).....179

3.8 ^{13}C-MFA results for Case IIII. Unit of fluxes and 95% confidence intervals is arbitrary (AU).....180

4.1 Biochemical reactions and carbon atom transitions used in ^{13}C-MFA.....245

Introduction

Chapter 1

Introduction

Adapted from

Dong, W.; Keibler, M. A.; Stephanopoulos, G. Review of Metabolic Pathways Activated in Cancer Cells as Determined through Isotopic Labeling and Network Analysis. Metab. Eng. 2017, 43, 113−124.

Dong, W., Moon, S. J., Kelleher, J. K., & Stephanopoulos, G. Dissecting mammalian cell metabolism through 13C- and 2H-isotope tracing: Interpretations at the molecular and systems levels. ACS Ind. Eng. Chem. Res., 2019, 59(6), 2593-2610.

Dong, W., Keibler, M. A., Moon, S. J., Cho, P., Liu, N., Berrios, C. J., Kelleher, J. K., Sikes, H. D., Iliopoulos, O., Coloff, J. L., Vander Heiden, M. G., & Stephanopoulos, G. Oncogenic metabolic rewiring independent of proliferative control in human mammary epithelial cells. Pending Submission.

1.1 Cancer metabolism

Genetically, cancer is characterized by gain of functions of oncogenes and loss of functions of tumor suppressor genes[1]. As dictated by such genetic modifications, cancer cells usually exhibit uncontrolled proliferation, meaning cell growth is independent of external stimulation or suppression. In order to fuel the continuous reproduction of cancer cells, a stable supply of anabolic building blocks, reducing equivalents and energy carriers is required[2–4].

Cancer cells have evolved to acquire rewired enzymatic mechanisms to extract building blocks and energy from substrates. One of the major features of this reprogrammed cellular metabolism was first observed by Otto Warburg in early 20th century. The fact that cancer cells preferentially convert pyruvate to lactate from glucose even under aerobic conditions has been persistently perplexing to biologists[5]. Warburg referred to his observation as aerobic glycolysis, describing the inputs and outputs of the "black box" while leaving the underlying cellular mechanisms unresolved. Limited by the techniques available at the time, only hypotheses could be made. Warburg suspected that impaired mitochondrial function might be responsible for inducing aerobic glycolysis. Yet even at this time of writing, the Warburg effect is still not fully understood. Further, it was not until the beginning of the 21st century – and the use of isotopic tracers for the fine dissection of central carbon metabolic pathways, the development of molecular biology and recombinant DNA technology, and the maturation of systems-level approaches to study biology – that researchers began to explore the full ramifications of metabolic rewiring.

In contrast to Warburg's analysis in which he treated glycolysis as an isolated system, modern researchers are able to dissect the pathway into different segments controlled by various

glycolytic enzymes. Studies on many of these enzymes have generated a plethora of significant findings in the effort to elucidate the conundrum of the Warburg effect and topics beyond[6,7]. In addition, focus has shifted beyond glucose to also include the extensive profiling of extracellular fluxes of different nutrients, amino acids such as glutamine, serine and glycine, as well as other unconventional substrates like acetate[8–13]. Finally, research on various aspects in cancer metabolism suggests the coordination of multiple metabolic rewiring phenomena. For instance, the cross-talk between glycolysis, serine metabolism, and the tricarboxylic acid cycle (TCA) anaplerosis suggest that the complexity of metabolic reprogramming extends beyond single pathways and is a multidimensional phenomenon[6,9].

1.2 ^{13}C-isotope tracing and metabolic flux analysis

The complex and dynamic nature of metabolic networks thus presents special challenges in the study of metabolism. Although metabolic activities can be inferred in some cases from metabolite concentrations, this is not true in general. Metabolite concentrations alone are insufficient to quantify fluxes and cannot distinguish the contributions of different substrates to metabolite pools. In addition, as a single metabolite is usually involved in multiple reactions, the concentration itself provides no information about the activities of those pathways. More importantly, changes of metabolite pool sizes do not necessarily correlate with fluxes. For instance, increased metabolite concentrations can result from enhanced fluxes of production pathways or reduced fluxes of consumption pathways. Similarly, a steady metabolite concentration does not necessarily imply unchanged fluxes as the latter can fluctuate significantly but in equal amounts, resulting in unchanged metabolite abundance.

In order to solve these problems, isotopic tracers are used to track the flows of multiple substrates in metabolic networks, and generate distinct labeling patterns indicative of different metabolic routes. Unique substrate utilization patterns have been discovered through the use of tracers. For example, ^{13}C-labeled acetate was employed to validate the ability of brain astrocytes to metabolize acetate into acetyl-CoA (AcCoA)[14]. Similarly, ^{13}C-labeling experiments showed that lactate, commonly deemed as a metabolic waste product, can be converted back to pyruvate and sustain brain energetics[15]. Additionally, activities of different metabolic pathways can be compared by analyzing labeling patterns generated by isotopic tracers. For instance, 1,2-$^{13}C_2$-glucose is used to assess the fluxes of the pentose phosphate pathway (PPP) against glycolysis[16]. The relative contributions of the oxidative tricarboxylic acid (TCA) cycle and the reductive carboxylation pathway can be estimated by U-$^{13}C_5$-glutamine[17].

Despite the fact that tracers are capable of generating substrate- and pathway-specific information, the convoluted labeling patterns are difficult to decipher. It is particularly challenging to interpret isotopic labeling results within complex networks that involve cyclic and compartmentalized reactions, both of which are frequently encountered in the study of mammalian cell metabolism. In order to correctly understand labeling patterns and obtain metabolic insights, we need to first analyze tracer data at the molecular level. Unique metabolite labeling profiles are rendered by atomic transitions of isotopes governed by reaction schemes of metabolic pathways. Therefore, stepwise tracking of isotopes through reaction networks is used to interpret labeling data. Furthermore, to extract additional useful information from the data, metabolic fluxes can be estimated via a systems approach – metabolic flux analysis (MFA). The term metabolic flux refers to reaction rate per cell, normalizing the rates by metrics such as cell

numbers[18] or protein content[19]. MFA estimates metabolic fluxes based on a reaction model comprising all pathways that may affect metabolite concentrations at steady state.

One of the most widely used flux analysis methods is ^{13}C-MFA[20,21], which relies on ^{13}C-labeling data to resolve flux distributions. ^{13}C-MFA works under the pseudo-steady state assumption, which implies that all metabolic fluxes within the system are constant, and that the mass isotopomer distributions (MIDs) of intracellular metabolites do not change over time. The analysis then needs a metabolic model, which consists of reactions with specified directionality and reversibility. Extracellular flux measurements are also required, as these values determine the absolute scales of all fluxes. Flux distributions are determined through the incorporation of isotopic labeling results into the system. ^{13}C-MFA is essentially a flux fitting methodology whereby initial fluxes are guessed and readjusted such as to best fit metabolite labeling measurements. Upon convergence, metabolic fluxes are estimated and reported with uncertainties based on sensitivities to measurement error[22].

1.3 Thesis motivation

Through the use of ^{13}C-isotope tracing and metabolic flux analysis, our knowledge of cancer metabolism has now extended beyond the Warburg effect[23–28]. Over the past decades, various types of metabolic alterations in cancer cells have been documented[8,18,28–30], prompting extensive investigation of the link between reprogrammed cell signaling pathways and rewired cellular metabolism[31–35]. In addition, drug targeting of rewired metabolism has been demonstrated to be a promising cancer treatment strategy[36–38]. Despite this progress, a fundamental question remains unanswered: whether there is a difference in the metabolism of cancerous, fast growing cells and normal proliferative cells. This deficiency has hindered our understanding of cancer metabolism

and the efforts to develop effective cancer therapies targeting metabolism with reduced side effects.

This question has not been directly addressed before. It has been speculated that rewired metabolic behavior associated with cancer may be a simple manifestation of reprogrammed cellular energetics required to accommodate faster deregulated cell growth[1,39,40]. For example, the Warburg effect is observed in both tumor and highly proliferative normal cells[1,2,41]. Several types of proliferating immune cells and stem cells rely on the glycolytic phenotype, a metabolic hallmark of cancer, to maintain their respective functionality and lineage[42–46]. Furthermore, both cancer and normal proliferating cells may selectively express the M2 isoform of pyruvate kinase, which is capable of promoting anabolism and cellular growth[3,7]. Reductive carboxylation of glutamine has been reported in both proliferating endothelial cells[47] and several types of cancer cells[10,48], suggesting that rewired glutamine metabolism is not unique to cancer.

However, the notion that metabolic behavior in cancer and normal proliferative cells is equivalent is still questionable. For example, comparison between normal proliferative and tumorigenic liver cells revealed that the latter exhibited upregulated glutaminase and transaminase activities[38]. In addition, copy number amplification of phosphoglycerate dehydrogenase was reported in melanoma relative to normal tissue counterparts[49,50]. Moreover, increased expression of proline oxidase has been observed in pancreatic ductal adenocarcinoma compared to normal pancreatic cells[51]. Although these findings suggest that cancer metabolism may not be simply regarded as rewired proliferative energetics, the evidence is still inconclusive: the proliferation rate of cancer cells in these studies was different than that of the normal cells. Therefore, the metabolic alteration due to proliferation introduces a confounding factor in the

observed metabolic shifts. This challenge limits our ability to conclusively determine whether metabolism of cancer cells is truly different than that of proliferating cells.

In order to address this question, we developed a panel of cell lines from the same genetic background yet exhibiting different levels of tumorigenicity due to different combinations of oncogenic manipulations. Through the use of ^{13}C-MFA and the introduction of a new quantity referred to as metabolic flux intensity (MFI), we decoupled proliferative control of metabolism and removed cellular growth as factor affecting metabolic rewiring. In addition, ^{13}C-isotopic labeling analysis and MFA also revealed a distinct metabolic pattern within the tricarboxylic acid (TCA) cycle and lipogenesis. Our results suggest that metabolism is directly controlled by both oncogenotypes and proliferation. The proliferation-independent metabolic shifts identified in our work support the effort to design cancer therapies that target specific metabolic pathways related with tumors only and not affecting cellular growth.

1.4 Thesis overview

The overarching objective of this thesis is to study whether metabolism of cancer cells is different than that of normal proliferating cells. To provide background and methodology necessary to explain my work, this thesis is divided into 5 chapters:

We will first review metabolic pathways differentially activated in cancer cells in **Chapter 2**. The list of such pathways consists of the Warburg effect, rewired glycolysis, reductive metabolism of glutamine, enhanced non-oxidative pentose phosphate pathway, acetate metabolism, serine and glycine metabolism, isocitrate dehydrogenase-mediated metabolic reprograming and oncogene-specific metabolic shifts.

Chapter 3 then introduces ^{13}C-isotope labeling and metabolic flux analysis, which serve as powerful tools to investigate mammalian cell metabolism at the molecular and systems level. We discuss and interpret labeling patterns from multiple ^{13}C tracers: U-$^{13}C_6$-glucose, U-$^{13}C_5$-glutamine, 1-^{13}C-glutamine, 5-^{13}C-glutamine**,** 2-$^{13}C_2$-acetate and 1-^{13}C-glucose, 1,6-$^{13}C_2$-glucose, 1,2-$^{13}C_2$-glucose, 2-^{13}C-glucose and 3-^{13}C-glucose. Multiple ^{2}H tracers are also extensively reviewed. Metabolic flux analysis is then explained and illustrated by a case study.

Chapter 4 describes the development of a panel of cell lines used to differentiate cancer and proliferative metabolism. We then report extracellular fluxes and intracellular ^{13}C-labeling results, from which a distinct substrate utilization pattern is uncovered throughout the cells. Next, ^{13}C-metabolic flux analysis is employed to quantitatively resolve the entire metabolic network. By introducing metabolic flux intensity, we directly investigate oncogenic metabolic rewiring independent of proliferative control. In addition, three metabolic reactions are identified to be most enhanced in the cancer cell line relative to the normal counterpart. This chapter closes by reporting the promising drug targeting results of these three metabolic pathways.

Chapter 5 concludes the thesis and discusses future directions to continue this thesis work.

1.5 References

(1) Hanahan, D.; Weinberg, R. A. Hallmarks of Cancer: The next Generation. *Cell*. 2011, pp 646–674.

(2) Vander Heiden, M. G.; Cantley, L. C.; Thompson, C. B.; Mammalian, P.; Exhibit, C.; Metabolism, A. Understanding the Warburg Effect : Cell Proliferation. *Science (80-.).* **2009**, *324* (5), 1029–1034.

(3) Vander Heiden, M. G.; Lunt, S. Y.; Dayton, T. L.; Fiske, B. P.; Israelsen, W. J.; Mattaini, K. R.; Vokes, N. I.; Stephanopoulos, G.; Cantley, L. C.; Metallo, C. M.; Locasale, J. W. Metabolic Pathway Alterations That Support Cell Proliferation. *Cold Spring Harb. Symp. Quant. Biol.* **2011**, *76*, 325–334.

(4) Locasale, J. W. Serine, Glycine and One-Carbon Units: Cancer Metabolism in Full Circle. *Nat. Rev. Cancer* **2013**, *13* (8), 572–583.

(5) Warburg, O. Injuring of Respiration the Origin of Cancer Cells. *Science (80-.).* **1956**, *123* (3191), 309–314.

(6) Vander Heiden, M. G.; Locasale, J. W.; Swanson, K. D.; Sharfi, H.; Rabinowitz, J. D.; Asara, J. M.; Cantley, L. C. Evidence for an Alternative Glycolytic. *Science (80-.).* **2010**, *329* (5998), 1492–1499.

(7) Christofk, H. R.; Vander Heiden, M. G.; Harris, M. H.; Ramanathan, A.; Gerszten, R. E.; Wei, R.; Fleming, M. D.; Schreiber, S. L.; Cantley, L. C. The M2 Splice Isoform of Pyruvate Kinase Is Important for Cancer Metabolism and Tumour Growth. *Nature* **2008**, *452* (7184), 230–233.

(8) Pacold, M. E.; Brimacombe, K. R.; Chan, S. H.; Rohde, J. M.; Lewis, C. A.; Swier, L. J. Y. M.; Possemato, R.; Chen, W. W.; Sullivan, L. B.; Fiske, B. P.; Cho, S.; Freinkman, E.; Birsoy, K.; Abu-Remaileh, M.; Shaul, Y. D.; Liu, C. M.; Zhou, M.; Koh, M. J.; Chung, H.; et al. A PHGDH Inhibitor Reveals Coordination of Serine Synthesis and One-Carbon Unit Fate. *Nat. Chem. Biol.* **2016**, *12* (4).

(9) Possemato, R.; Marks, K. M.; Shaul, Y. D.; Pacold, M. E.; Kim, D.; Birsoy, K.; Sethumadhavan, S.; Woo, H.-K.; Jang, H. G.; Jha, A. K.; Chen, W. W.; Barrett, F. G.; Stransky, N.; Tsun, Z.-Y.; Cowley, G. S.; Barretina, J.; Kalaany, N. Y.; Hsu, P. P.; Ottina, K.; et al. Functional Genomics Reveal That the Serine Synthesis Pathway Is Essential in Breast Cancer. *Nature* **2011**, *476* (7360), 346–350.

(10) Metallo, C. M.; Gameiro, P. A.; Bell, E. L.; Mattaini, K. R.; Yang, J.; Hiller, K.; Jewell, C. M.; Johnson, Z. R.; Irvine, D. J.; Guarente, L.; Kelleher, J. K.; Heiden, M. G. Vander; Iliopoulos, O.; Stephanopoulos, G. Reductive Glutamine Metabolism by IDH1 Mediates Lipogenesis under Hypoxia. TL - 481. *Nature* **2011**, *481 VN*- (7381), 380–384.

(11) Schug, Z. T.; Peck, B.; Jones, D. T.; Zhang, Q.; Grosskurth, S.; Alam, I. S.; Goodwin, L. M.; Smethurst, E.; Mason, S.; Blyth, K.; McGarry, L.; James, D.; Shanks, E.; Kalna, G.; Saunders, R. E.; Jiang, M.; Howell, M.; Lassailly, F.; Thin, M. Z.; et al. Acetyl-CoA Synthetase 2 Promotes Acetate Utilization and Maintains Cancer Cell Growth under Metabolic Stress. *Cancer Cell* **2015**, *27* (1), 57–71.

(12) Mashimo, T.; Pichumani, K.; Vemireddy, V.; Hatanpaa, K. J.; Singh, D. K.; Sirasanagandla, S.; Nannepaga, S.; Piccirillo, S. G.; Kovacs, Z.; Foong, C.; Huang, Z.; Barnett, S.; Mickey, B. E.; Deberardinis, R. J.; Tu, B. P.; Maher, E. A.; Bachoo, R. M.

Acetate Is a Bioenergetic Substrate for Human Glioblastoma and Brain Metastases. *Cell* **2014**, *159* (7), 1603–1614.

(13) Comerford, S. A.; Huang, Z.; Du, X.; Wang, Y.; Cai, L.; Witkiewicz, A. K.; Walters, H.; Tantawy, M. N.; Fu, A.; Manning, H. C.; Horton, J. D.; Hammer, R. E.; Mcknight, S. L.; Tu, B. P. Acetate Dependence of Tumors. *Cell* **2014**, *159* (7), 1591–1602.

(14) Deelchand, D. K.; Nelson, C.; Shestov, A. A.; Uğurbil, K.; Henry, P. G. Simultaneous Measurement of Neuronal and Glial Metabolism in Rat Brain in Vivo Using Co-Infusion of [1,6-13C2]Glucose and [1,2-13C2]Acetate. *J. Magn. Reson.* **2009**, *196* (2), 157–163.

(15) De Feyter, H. M.; Mason, G. F.; Shulman, G. I.; Rothman, D. L.; Petersen, K. F. Increased Brain Lactate Concentrations without Increased Lactate Oxidation during Hypoglycemia in Type 1 Diabetic Individuals. *Diabetes* **2013**, *62* (9), 3075–3080.

(16) Brekke, E. M. F.; Walls, A. B.; Schousboe, A.; Waagepetersen, H. S.; Sonnewald, U. Quantitative Importance of the Pentose Phosphate Pathway Determined by Incorporation of 13 C from 2-13 C-and 3-13 Cglucose into TCA Cycle Intermediates and Neurotransmitter Amino Acids in Functionally Intact Neurons. *J. Cereb. Blood Flow Metab.* **2012**, *32* (9), 1788–1799.

(17) Dong, W.; Keibler, M. A.; Stephanopoulos, G. Review of Metabolic Pathways Activated in Cancer Cells as Determined through Isotopic Labeling and Network Analysis. *Metab. Eng.* **2017**, *43*, 113–124.

(18) Metallo, C. M.; Gameiro, P. A.; Bell, E. L.; Mattaini, K. R.; Yang, J.; Hiller, K.; Jewell, C. M.; Johnson, Z. R.; Irvine, D. J.; Guarente, L.; Kelleher, J. K.; Vander Heiden, M. G.; Iliopoulos, O.; Stephanopoulos, G. Reductive Glutamine Metabolism by IDH1 Mediates

Lipogenesis under Hypoxia. *Nature* **2012**, *481* (7381), 380–384.

(19) Srivastava, S.; Chan, C. Application of Metabolic Flux Analysis to Identify the Mechanisms of Free Fatty Acid Toxicity to Human Hepatoma Cell Line. *Biotechnol Bioeng.* **2008**, *99* (2), 399–410.

(20) Antoniewicz, M. R. A Guide to 13C Metabolic Flux Analysis for the Cancer Biologist. *Exp. Mol. Med.* **2018**, *50* (4), 19.

(21) Long, C. P.; Antoniewicz, M. R. High-Resolution 13C Metabolic Flux Analysis. *Nat. Protoc.* **2019**, *14* (10), 2856–2877.

(22) Buescher, J. M.; Antoniewicz, M. R.; Boros, L. G.; Burgess, S. C.; Brunengraber, H.; Clish, C. B.; DeBerardinis, R. J.; Feron, O.; Frezza, C.; Ghesquiere, B.; Gottlieb, E.; Hiller, K.; Jones, R. G.; Kamphorst, J. J.; Kibbey, R. G.; Kimmelman, A. C.; Locasale, J. W.; Lunt, S. Y.; Maddocks, O. D. K.; et al. A Roadmap for Interpreting 13C Metabolite Labeling Patterns from Cells. *Curr. Opin. Biotechnol.* **2015**, *34*, 189–201.

(23) DeBerardinis, R. J.; Mancuso, A.; Daikhin, E.; Nissim, I.; Yudkoff, M.; Wehrli, S.; Thompson, C. B. Beyond Aerobic Glycolysis: Transformed Cells Can Engage in Glutamine Metabolism That Exceeds the Requirement for Protein and Nucleotide Synthesis. *Proc. Natl. Acad. Sci. U. S. A.* **2007**, *104* (49), 19345–19350.

(24) Hsu, P. P.; Sabatini, D. M. Cancer Cell Metabolism: Warburg and Beyond. *Cell* **2008**, *134* (5), 703–707.

(25) Liberti, M. V.; Locasale, J. W. The Warburg Effect: How Does It Benefit Cancer Cells? *Trends Biochem. Sci.* **2016**, *41* (3), 211–218.

(26) Bensinger, S. J.; Christofk, H. R. New Aspects of the Warburg Effect in Cancer Cell Biology. *Seminars in Cell and Developmental Biology*. 2012.

(27) Koppenol, W. H.; Bounds, P. L.; Dang, C. V. Otto Warburg's Contributions to Current Concepts of Cancer Metabolism. *Nature Reviews Cancer*. 2011.

(28) Tran, T. Q.; Hanse, E. A.; Habowski, A. N.; Li, H.; Ishak Gabra, M. B.; Yang, Y.; Lowman, X. H.; Ooi, A. M.; Liao, S. Y.; Edwards, R. A.; Waterman, M. L.; Kong, M. α-Ketoglutarate Attenuates Wnt Signaling and Drives Differentiation in Colorectal Cancer. *Nat. Cancer* **2020**.

(29) Diaz-Moralli, S.; Aguilar, E.; Marin, S.; Coy, J. F.; Dewerchin, M.; Antoniewicz, M. R.; Meca-Cortés, O.; Notebaert, L.; Ghesquière, B.; Eelen, G.; Thomson, T. M.; Carmeliet, P.; Cascante, M. A Key Role for Transketolase-like 1 in Tumor Metabolic Reprogramming. *Oncotarget* **2016**, *7* (32).

(30) Ahn, W. S.; Dong, W.; Zhang, Z.; Cantor, J. R.; Sabatini, D. M.; Iliopoulos, O.; Stephanopoulos, G. Glyceraldehyde 3-Phosphate Dehydrogenase Modulates Nonoxidative Pentose Phosphate Pathway to Provide Anabolic Precursors in Hypoxic Tumor Cells. *AIChE J.* **2018**, *64* (12), 4289–4296.

(31) Gaglio, D.; Metallo, C. M.; Gameiro, P. A.; Hiller, K.; Danna, L. S.; Balestrieri, C.; Alberghina, L.; Stephanopoulos, G.; Chiaradonna, F. Oncogenic K-Ras Decouples Glucose and Glutamine Metabolism to Support Cancer Cell Growth. *Mol. Syst. Biol.* **2011**, *7*, 523.

(32) Son, J.; Lyssiotis, C. a; Ying, H.; Wang, X.; Hua, S.; Ligorio, M.; Perera, R. M.; Ferrone, C. R.; Mullarky, E.; Shyh-Chang, N.; Kang, Y.; Fleming, J. B.; Bardeesy, N.; Asara, J.

M.; Haigis, M. C.; DePinho, R. a; Cantley, L. C.; Kimmelman, A. C. Glutamine Supports Pancreatic Cancer Growth through a KRAS-Regulated Metabolic Pathway. *Nature* **2013**, *496* (7443), 101–105.

(33) Dang, C. V; Kim, J.; Gao, P.; Yustein, J. The Interplay between MYC and HIF in Cancer. *Nat. Rev. Cancer* **2008**, *8* (1), 51–56.

(34) Liu, W.; Le, a.; Hancock, C.; Lane, a. N.; Dang, C. V.; Fan, T. W.-M.; Phang, J. M. Reprogramming of Proline and Glutamine Metabolism Contributes to the Proliferative and Metabolic Responses Regulated by Oncogenic Transcription Factor C-MYC. *Proc. Natl. Acad. Sci.* **2012**, *109* (23), 8983–8988.

(35) Polyak, K.; Xia, Y.; Zweier, J. L.; Kinzler, K. W.; Vogelstein, B. A Model for P53-Induced Apoptosis. *Nature* **1997**.

(36) Vander Heiden, M. G. Targeting Cancer Metabolism: A Therapeutic Window Opens. *Nat. Rev. Drug Discov.* **2011**, *10* (9), 671–684.

(37) Ngoi, N. Y. L.; Eu, J. Q.; Hirpara, J.; Wang, L.; Lim, J. S. J.; Lee, S. C.; Lim, Y. C.; Pervaiz, S.; Goh, B. C.; Wong, A. L. A. Targeting Cell Metabolism as Cancer Therapy. *Antioxidants and Redox Signaling*. 2020.

(38) Méndez-lucas, A.; Lin, W.; Driscoll, P. C.; Legrave, N.; Novellasdemunt, L.; Xie, C.; Charles, M.; Wilson, Z.; Jones, N. P.; Rayport, S.; Rodríguez-justo, M.; Li, V.; Macrae, J. I.; Hay, N.; Chen, X.; Yuneva, M. Identifying Strategies to Target the Metabolic Flexibility of Tumours. *Nat. Metab.* **2020**, *2* (April), 335–350.

(39) Ward, P. S.; Thompson, C. B. Metabolic Reprogramming: A Cancer Hallmark Even

Warburg Did Not Anticipate. *Cancer Cell*. 2012.

(40) Schulze, A.; Harris, A. L. How Cancer Metabolism Is Tuned for Proliferation and Vulnerable to Disruption. *Nature* **2012**, *491* (7424), 364–373.

(41) Vander Heiden, M. G.; DeBerardinis, R. J. Understanding the Intersections between Metabolism and Cancer Biology. *Cell*. 2017.

(42) Ananieva, E. Targeting Amino Acid Metabolism in Cancer Growth and Anti-Tumor Immune Response. *World J. Biol. Chem.* **2015**.

(43) Chen, Z.; Liu, M.; Li, L.; Chen, L. Involvement of the Warburg Effect in Non-Tumor Diseases Processes. *J. Cell. Physiol.* **2017**.

(44) Vacanti, N. M.; Metallo, C. M. Exploring Metabolic Pathways That Contribute to the Stem Cell Phenotype. *Biochimica et Biophysica Acta - General Subjects*. 2013.

(45) Folmes, C. D. L.; Dzeja, P. P.; Nelson, T. J.; Terzic, A. Metabolic Plasticity in Stem Cell Homeostasis and Differentiation. *Cell Stem Cell* **2012**, *11* (5), 596–606.

(46) Agathocleous, M.; Harris, W. A. Metabolism in Physiological Cell Proliferation and Differentiation. *Trends in Cell Biology*. 2013.

(47) Kim, B.; Li, J.; Jang, C.; Arany, Z. Glutamine Fuels Proliferation but Not Migration of Endothelial Cells. *EMBO J.* **2017**.

(48) Mullen, A. R.; Wheaton, W. W.; Jin, E. S.; Chen, P.-H.; Sullivan, L. B.; Cheng, T.; Yang, Y.; Linehan, W. M.; Chandel, N. S.; DeBerardinis, R. J. Reductive Carboxylation Supports Growth in Tumour Cells with Defective Mitochondria. *Nature* **2012**, *481* (7381), 385–388.

(49) Beroukhim, R.; Mermel, C. H.; Porter, D.; Wei, G.; Raychaudhuri, S.; Donovan, J.; Barretina, J.; Boehm, J. S.; Dobson, J.; Urashima, M.; McHenry, K. T.; Pinchback, R. M.; Ligon, A. H.; Cho, Y. J.; Haery, L.; Greulich, H.; Reich, M.; Winckler, W.; Lawrence, M. S.; et al. The Landscape of Somatic Copy-Number Alteration across Human Cancers. *Nature* **2010**.

(50) Locasale, J. W.; Grassian, A. R.; Melman, T.; Lyssiotis, C. A.; Mattaini, K. R.; Bass, A. J.; Heffron, G.; Metallo, C. M.; Muranen, T.; Sharfi, H.; Sasaki, A. T.; Anastasiou, D.; Mullarky, E.; Vokes, N. I.; Sasaki, M.; Beroukhim, R.; Stephanopoulos, G.; Ligon, A. H.; Meyerson, M.; et al. Phosphoglycerate Dehydrogenase Diverts Glycolytic Flux and Contributes to Oncogenesis. *Nat. Genet.* **2011**, *43* (9), 869–874.

(51) Olivares, O.; Mayers, J. R.; Gouirand, V.; Torrence, M. E.; Gicquel, T.; Borge, L.; Lac, S.; Roques, J.; Lavaut, M. N.; Berthezène, P.; Rubis, M.; Secq, V.; Garcia, S.; Moutardier, V.; Lombardo, D.; Iovanna, J. L.; Tomasini, R.; Guillaumond, F.; Vander Heiden, M. G.; et al. Collagen-Derived Proline Promotes Pancreatic Ductal Adenocarcinoma Cell Survival under Nutrient Limited Conditions. *Nat. Commun.* **2017**.

Metabolic pathways differentially activated in cancer cells

Chapter 2

Metabolic pathways differentially activated in cancer cells

Adapted from

Dong, W.; Keibler, M. A.; Stephanopoulos, G. Review of Metabolic Pathways Activated in Cancer Cells as Determined through Isotopic Labeling and Network Analysis. Metab. Eng. 2017, 43, 113−124.

Conceptualization, W. Dong and M.A. Keibler; Writing, W. Dong; Revision, W. Dong and M.A. Keibler; Supervision, G. Stephanopoulos.

This work is published on Metabolic Engineering, 2017.

2.1 Abstract

Cancer metabolism has emerged as an indispensable part of contemporary cancer research. During the past two decades, the use of stable isotopic tracers and network analysis have unveiled a number of metabolic pathways activated in cancer cells. Here, we review such pathways along with the particular tracers and labeling observations that led to the discovery of their rewiring in cancer cells. The list of such pathways comprises the reductive metabolism of glutamine, altered glycolysis, serine and glycine metabolism, mutant isocitrate dehydrogenase (IDH) induced reprogramming and the onset of acetate metabolism. Additionally, we demonstrate the critical role of isotopic labeling and network analysis in identifying these pathways. The alterations described in this review do not constitute a complete list, and future research using these powerful tools is likely to discover other cancer-related pathways and new metabolic targets for cancer therapy.

2.2 Introduction

According to American Cancer Society, cancer is the second leading cause of death following heart disease in 2020[1]. Although the death rates of cancer have decreased by 23% since 1991, the mortality of certain types of cancer kept increasing over the past few decades[2].

Cancer cells are characterized by their ability to proliferate in an uncontrolled manner and to invade parts of healthy organs via metastasis. Since cancer cells have greater potential to compete with the healthy counterparts for limited nutrients and resources, this advantage often leads to the death of healthy tissues and eventually the entire human body. The current understanding of cancer is largely based on their mutated genomes, which often involve gain of

functions of oncogenes and loss of functions of tumor suppressors[3]. Under normal circumstances, multiple genomic modifications are required to transform normal cells to become fully cancerous[4]. Due to the autonomous cellular growth independent of environmental stimulations, cancer cells exhibit robust proliferative capability. In addition, the surveillance mechanisms kept by normal cells are often breached or escaped during tumorigenesis. Even if apoptosis and the immune system function normally, the fact that most cancer cells can divide indefinitely[5] creates additional challenges to eliminate these erratic populations. Some cancer cells are not constrained by nutrient transport since they can stimulate the formation of blood vessels near their colonies and the so-called sustained angiogenesis keeps them alive under harsh physiological conditions. Finally, malignant cells are able to escape from one colony and move to other regions where nutrients and growth space are more desirable. The resulting metastasis is responsible for 90% of deaths caused by cancer[6].

Cancer can be induced via various external factors, many of which promote gain of functions of oncogenes. Alcohol and smoking are the two major chemical inducers of cancer. Alcohol is listed as a Group 1 carcinogen by International Agency for Research on Caner (IARC)[7]. Tobacco is the leading cause of lung cancer, contributing to 85% of the overall death records for lung cancer[8]. Viral infection is another major contributor to cancer. Many types of viruses can integrate their oncogene segments into human cells, while others harboring non-oncogenic components also promote tumorigenesis. These viruses are referred to as oncoviruses. Examples include Epstein Barr Virus (EBV)[9], Kaposi's sarcoma associated herpesvirus (KSHV)[10] and Hepatitis B Virus (HBV)[11]. In addition, other internal and external cue such as ultraviolet radiation[12] and obesity[13] may also lead to cancer.

During the past decades of cancer research, a plethora of cancer treatments have been developed. Traditionally, cancer treatment relied almost exclusively on surgery to remove chunks of tumors from human body[14]. Unfortunately, due to frequent, the survival rate after the surgery was often low. It was not until the late 20th century that other therapies began to emerge. Chemotherapy is one of the major treatments nowadays. One example is Capecitabine, which upon conversion to cytotoxic 5-fluorouracil (5-FU), is used to treat liver cancer[15]. Another type of anti-cancer drug is taxol, a microtubule stabilizer that inhibits depolymerization events triggering chromosome segregation, thus hindering cancer cell proliferation. Taxol also promotes phosphorylation of B-cell lymphoma 2 (Bcl-2) and eventually trigger cell apoptosis.[16] In addition to chemotherapy, radiation is also used to selectively kill cancer cells based on spatial localization. Other common cancer treatments include hormonal therapy, adjuvant therapy and immunotherapy[14]. Among these treatments, targeted cancer therapy has many advantages. Through specific targeting of cancer cells, potential side-effects on normal healthy cells are significantly reduced. Researchers have designed drug molecules aimed for specific mutated kinases along the oncogenic signaling pathway. For example, imatinib mesylate (Gleevec) targets Abelson murine leukemia viral oncogene (Abl). Kit and Platelet-derived growth factor receptor (PDFGR) inhibitors have also been approved for clinical trial[17].

As biological events are intrinsically dictated by gene regulations, cancer cells exhibit a unique set of metabolic behaviors due to gain of functions of oncogenes and loss of functions of tumor suppressors. Recent studies have revealed a plethora of metabolic shifts regarding the Warburg effect and topics beyond[18,19]. In addition, profiling of different extracellular nutrients have identified metabolic fates of a diverse group of substrates such as glutamine, serine, glycine, as well as other unconventional metabolites like acetate[20–25]. Moreover, recent work also

suggests potential coordination of multiple metabolic rewiring phenomena. For instance, the glycolysis, serine/glycine metabolism and the TCA cycle may be tightly connected, manifesting a multidimensional phenomenon[18,21].

Of great significance in the exploration of complex rewired energetics in cancer is isotopic labeling and network analysis. To quantitatively characterize the metabolic phenotype of mammalian cells, ^{13}C isotopic labeling and metabolic flux analysis (MFA) are widely used[26–28]. MFA is based on a comprehensive stoichiometric model of all biochemical reactions within a specific set of metabolic network. To decipher the internal structure of this network within a cell, the crosstalk between the cell and its environment has to be quantified. Cells exchange nutrients and other biochemical species with the environment. The influxes of nutrients and the effluxes of waste species or natural products are referred to as extracellular fluxes. Extracellular fluxes can be measured experimentally in a fairly straightforward manner. The intracellular fluxes can be estimated under a pseudo-steady-state assumption that the concentrations of all intracellular metabolites of interest remain unchanged during the course of analysis. The mass balance of each metabolite within the cell in conjunction with the quantified extracellular fluxes leads to a system of equations that can be solved to resolve the distribution of intracellular fluxes within cells. As one of the most widely used tools to fully specify a metabolic system, stable isotope labeling is an essential technique to couple extracellular flux measurements and for fluxes within a metabolic network. When cells are cultured with isotopically labeled nutrients, the intracellular metabolites acquire specific labeling patterns through biochemical reactions that convert the labeled substrates into these intermediates. The reaction mechanisms dictate the transfer of labeled atoms into intracellular species, rendering a unique labeling profile for each metabolite.

2.3 The Warburg effect

Among all metabolic rewiring phenomena, the Warburg effect is the most commonly observed in cancer cells. The reasoning of the appearance of the Warburg effect is still being actively researched. Yet some hypotheses consistent with the traits and special needs of cancer cells have been proposed. One possible explanation is that the cost of synthesizing the TCA cycle enzymes may exceed the corresponding marginal gain of ATP through respiration, so that cells can extract more free energy when metabolizing substrates solely through glycolysis[29]. Also, despite their active contribution to angiogenesis, cancer cells are subject to variations of oxygen supply under physiological conditions. In this case, aerobic glycolysis confers cancer cells with an internal resistance to such fluctuations since it functions invariantly under both hypoxic and normoxic conditions[30]. It is also possible that, besides decoupling glycolysis from the physiological oxygen level, aerobic glycolysis may also assist cancer cells to escape from apoptosis. One argument in support of this hypothesis is that decreased TCA flux and corresponding electron transport chain activity lead to attenuated depolarization of the mitochondrial membrane potential, inhibiting the release of the apoptosis effector cytochrome c[31]. Without mitochondrial release of cytochrome c, the apoptosome cannot be assembled and apoptosis is repressed[32]. Metabolically, it has been proposed that elevated glucose consumption induced by the Warburg effect could promote anabolic reactions in serine biosynthesis, pentose phosphate pathway (PPP), *de novo* lipogenesis, one-carbon metabolism[33], etc. In addition, the Warburg effect is believed to be capable of modulating cell signaling in favor of tumorigenesis through reactive oxygen species (ROS), histone acetylation and deacetylation[33]. Finally, others have proposed that lactate, the product of aerobic glycolysis may be responsible for resistance to chemotherapies[34]. Increased lactate in the

microenvironment can upregulate several transporters and enzymes that are critical for toxin clearance in cancer cells[30].

With the rapid progress of recent research, more metabolic rewiring phenomena have been observed, and the diversity and sophistication of cancer metabolism research have exceeded the centrality of the Warburg effect. An overview of our current understanding of the metabolic network critical in cancer metabolism, as described in this manuscript, is illustrated in Figure 2.1.

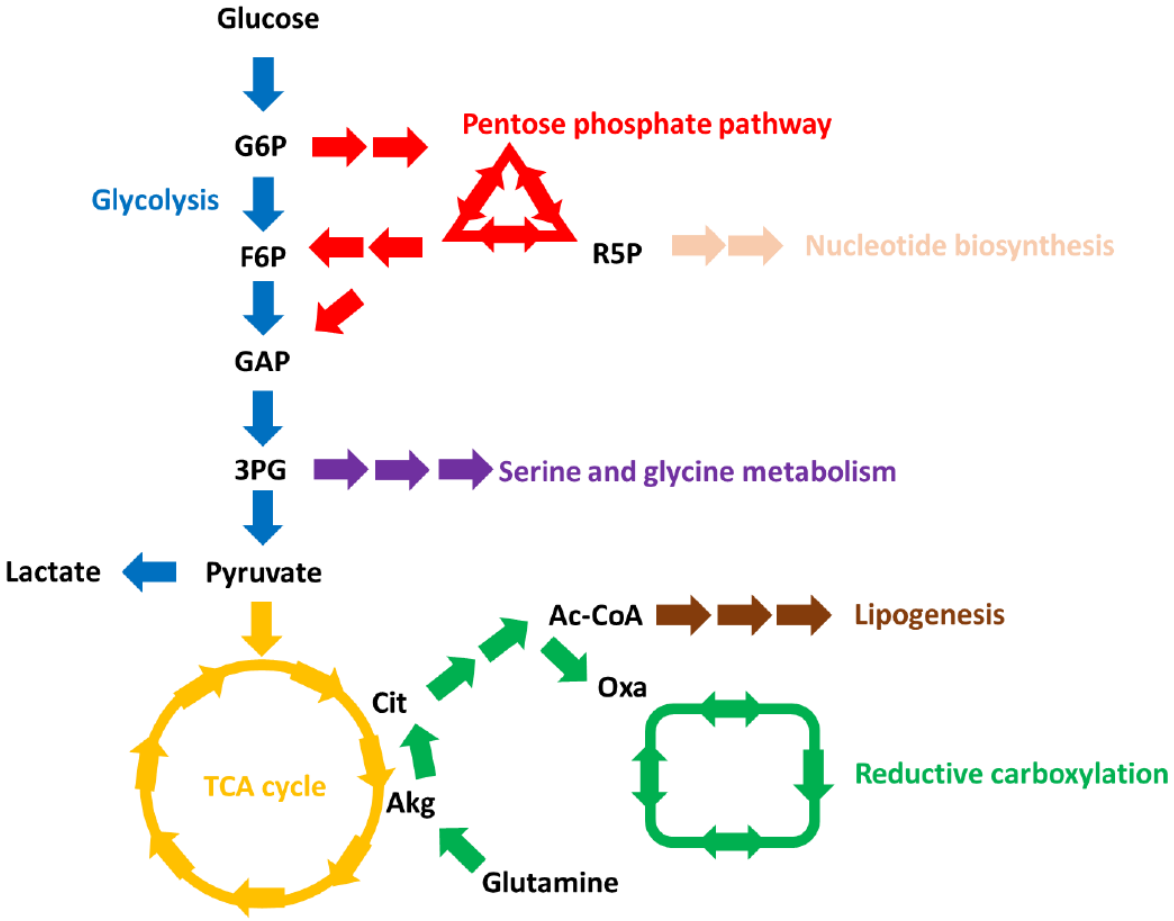

Figure 2.1. A global overview of the metabolic network critical in cancer cells.

Glucose is the most highly consumed carbon substrate, and its entry initiates glycolysis, which contains several anabolic arms. The pentose phosphate pathway (PPP) directs glucose-derived glucose-6-phosphate (G6P) toward oxidative PPP where NADPH is generated. From ribulose-5-

phosphate (Ru5P), the non-oxidative PPP continues, supplying building blocks for nucleotide biosynthesis and reversibly exchanging metabolites with glycolysis via fructose-6-phosphate (F6P) and glyceraldehyde-3-phosphate (GAP). Serine and glycine metabolism branches from 3-phosphoglycerate (3PG) and connects central carbon metabolism with one-carbon metabolism. The end product pyruvate can be converted to lactate or can enter the TCA cycle in the form of acetyl-CoA, which can also be derived from acetate under certain conditions. Glutamine is metabolized to glutamate and then α-ketoglutarate, which can enter the TCA cycle for replenishing anaplerosis or be reductively metabolized via a carboxylation reaction to fuel de novo lipogenesis. Various pathways are altered to sustain the uncontrolled proliferation exhibited by cancer cells.

G6P, glucose-6-phosphate; F6P, fructose-6-phosphate; GAP, glyceraldehyde-3-phosphate; 3PG, 3-phosphoglycerate; R5P, ribose-5-phosphate; Akg, α-ketoglutarate; Cit, citrate; Ac-CoA, acetyl-CoA; Oxa, oxaloacetate.

2.4 Metabolic alterations along glycolysis

High expression of the M2 isoform of pyruvate kinase (PKM2) has been observed in cancerous and healthy proliferative cells. This preferential selective expression of PKM2 is also believed to be essential for the Warburg effect[19]. PKM2 exhibits reduced catalytic activity compared to PKM1, but surprisingly, the elevation of glycolytic flux is associated with this "weaker" isoform. Contrary to the conventional view of a one-directional linear glycolytic pathway, it has been hypothesized that there is an alternative glycolytic step in which the generation of ATP may be decoupled from pyruvate kinase (PK) activity. In this model, phosphoenolpyruvate (PEP) transfers its phosphate group to the enzyme phosphoglycerate mutase 1 (PGAM1), generating pyruvate independent of PK[18]. Because phosphorylation of PGAM1 is required for its activation, this process may further promote the production of PEP, constituting a positive

feedback loop which further increases overall glycolytic flux[35]. In addition, this feedback loop may also increase the ratio of 3-phosphoglycerate (3PG) to 2-phosphoglycerate (2PG), which promotes serine biosynthesis pathway that branches at 3PG[36,37]. A schematic of this alternative glycolytic pathway is illustrated in Figure 2.2.

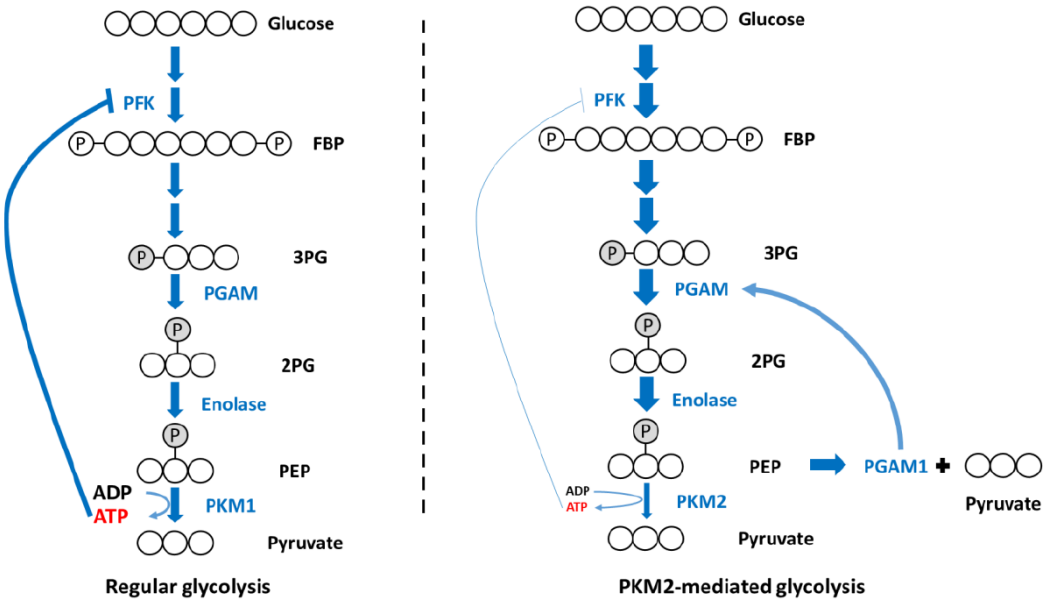

Figure 2.2. The PKM2-mediated glycolytic pathway.

The M2 isoform of pyruvate kinase (PKM2), which is preferentially expressed by cancer cells, has been hypothesized to promote an alternative catalytic activity that does not produce ATP, in contrast to PKM1. This potential mechanism would likely contribute to continual activation of phosphofructokinase (PFK), which is inhibited by ATP. Consequently, glycolytic flux may be enhanced. This alternative mechanism involves transfer of the phosphate group from phosphoenolpyruvate (PEP) to phosphoglycerate mutase 1 (PGAM1), which activates it. This positive feedback mechanism may drive the enhanced production of 2-phosphoglycerate (2PG), PEP and eventually enhance the overall PGAM1 activity. Through this mechanism, the generation of pyruvate may become partially decoupled from ATP production, which could enable a high rate of glycolysis.

Activation and inhibition of enzyme activity are denoted by arrows and blunt arrows, respectively. The relative strengths of metabolic pathways and activation/inhibition effects are shown by the thickness of the arrows.

Additionally, the M2 isoform of PK is inhibited by tyrosine-phosphorylated proteins such as epidermal growth factor receptor (EGFR) and platelet-derived growth factor receptor (PDGFR). This inhibition is hypothesized to increase the accumulation of PEP and 3PG[18,19,38]. This bottleneck may then subsequently lead to elevated anabolic metabolism through *de novo* serine synthesis. The alternative pathway may be preferential for sustaining a high rate of glycolysis since ATP allosterically inhibits phosphofructokinase (PFK) at a high ATP/AMP ratio[18].

Similar to the PKM2-mediated glycolytic pathway in the context of serine biosynthesis, cancer cells must also coordinate their metabolic network to generate nucleotide precursors in support of fast proliferation. To this end, it has been demonstrated that some tumor cells are able to upregulate glucose uptake and enhance non-oxidative PPP due to the presence of KRAS oncogene[39].In fact, it has also been proposed that cancer cells could promote the synthesis of ribose 5-phosphate (R5P) through non-oxidative PPP[40]. The enhanced reverse flux along glycolysis is mediated by the aldolase and transaldolase reactions.

It was observed that the magnitude of oxidative PPP flux (relative to glycolytic flux) is reduced under hypoxia. On the other hand, as an alternative pathway to supply cancer cells with nucleotide biosynthetic precursors, the non-oxidative PPP increases to produce more R5P. Mechanistically, the enzyme glyceraldehyde 3-phosphate dehydrogenase (GAPDH) plays a critical role in this metabolic shift. Hypoxia-mediated reduction of the NAD^+/NADH ratio results in a decrease in GAPDH activity. In contrast, the expression of the other lower glycolytic

enzymes is elevated upon stabilization of hypoxia-inducible factors. As a result, GAPDH creates a bottleneck at the lower glycolytic pathway, enabling accumulation of high concentrations of upper glycolytic metabolites, which in turn increase the reversible non-oxidative PPP reactions toward nucleotide biosynthesis via mass action. This is shown in Figure 2.3 [40].

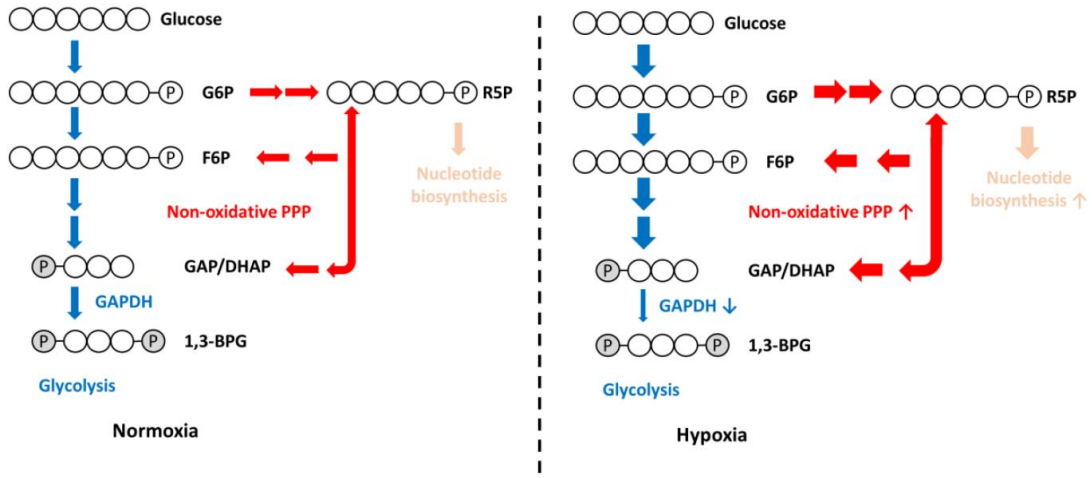

Figure 2.3. The GAPDH-mediated reversal of glycolytic flux.

Under hypoxic condition, GAPDH activity is inhibited while the expression of other upper glycolytic enzymes is elevated. Due to the accumulation of high concentrations of upper glycolytic metabolites and the reversibility of the non-oxidative PPP, more ribose-5-phosphate (R5P) is synthesized to promote nucleotide biosynthesis.

G6P, glucose-6-phosphate, F6P, fructose-6-phosphate; GAP, glyceraldehyde-3-phosphate; DHAP, dihydroxyacetone phosphate; 1,3-BPG, 1,3-bisphosphoglycerate. The relative strengths of metabolic pathways and activation/inhibition effects are shown by the thickness of the arrows.

The figure is adapted from Ahn et al[40].

In fact, GAPDH plays a critical role in balancing nucleotide biosynthesis via PPP and energy production via the TCA cycle; as such, modulation of GAPDH activity alters the viability of cancer cells. This is supported by a recent report that the uptake of dehydroascorbate (DHA), the oxidized form of vitamin C, is able to inhibit GAPDH and lead to energy crisis in colorectal cancer (CRC) cells containing mutations in KRAS and BRAF. The CRC cells similarly exhibited high rates of glycolysis and the non-oxidative PPP. The "bottleneck" role of GAPDH was shown to be vital in this trade-off between ATP generation and nucleotide biosynthesis. The inhibition caused by DHA increased oxidative PPP flux at the expense of the pyruvate entry into TCA cycle, depriving cancer cells of robust energy support as evidenced by an elevated AMP/ATP ratio[41].

To quantitatively derive the aforementioned conclusions, the isotopic labeling tracer 1,2-$^{13}C_2$-glucose was employed. Entry of this tracer into the oxidative PPP results in a loss of the carbon in the 1-position as $^{13}CO_2$, which contributes triose phosphates that contain one fewer ^{13}C label than those that bypass the PPP via upper glycolytic reactions. Through comparison of the M2/M1 isotopomer ratio of these metabolites, the relative magnitude of glycolysis (Figure 2.4a) and oxidative PPP (Figure 2.4b) can be estimated. Similarly, the oxidative PPP also yields one fewer ^{13}C labeled carbon in the ribose products than the non-oxidative PPP following nucleotide biosynthesis, so the M1/M2 ratio of the RNA-derived ribose can be used to compare the relative contributions of the oxidative and non-oxidative PPPs[40].

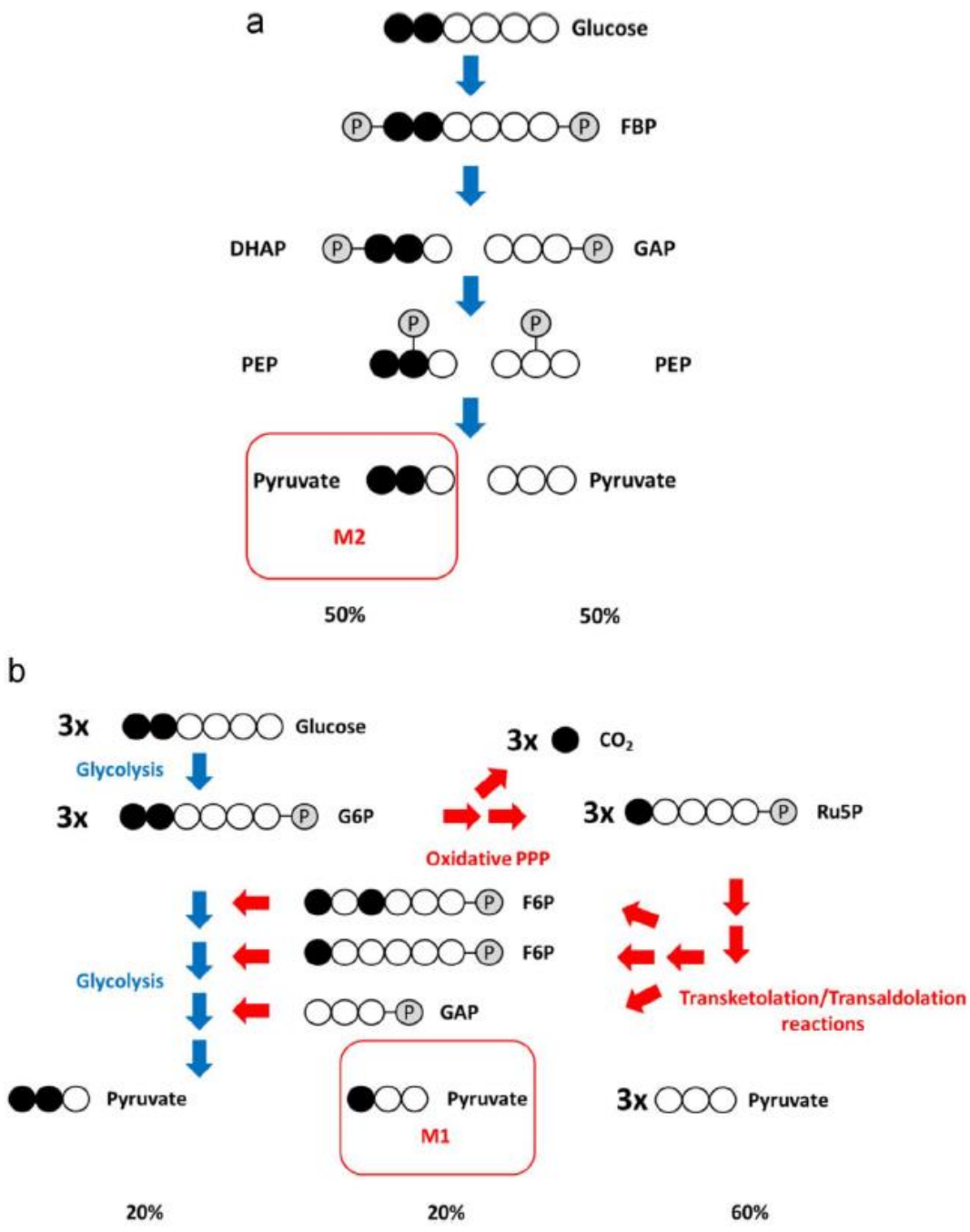

Figure 2.4. The isotopic labeling pattern generated by 1,2-$^{13}C_2$-glucose.

(**a**) Following exclusive use of the glycolytic pathway, the M2-labeled pattern retains until fructose-1,6-bisphosphate (FBP). The aldolase-catalyzed cleavage reaction produces M2-labeled dihydroxyacetone (DHAP) and unlabeled glyceraldehyde-3-phosphate (GAP). The labeling

pattern is eventually inherited by pyruvate, yielding an equimolar mixture of M2-labeled and unlabeled pyruvate.

(**b**) This labeling pattern can be best explained by analyzing three molecules of 1,2-$^{13}C_2$-glucose going through the oxidative PPP. The first step in glycolysis transforms all 1,2-$^{13}C_2$-glucose into M2-labeled glucose-6-phosphate (G6P). The oxidative PPP releases one molecule of heavy labeled carbon dioxide per molecule of 1,2-$^{13}C_2$ G6P. The resulting three molecules of M1-labeled ribulose-5-phosphate (Ru5P) have equal chances of going through three distinct biochemical reactions. The transketolation and transaldolation reactions lead to one molecule of M2-labeled fructose-6-phosphate (F6P), one molecule of M1-labeled F6P, and one molecule of unlabeled glyceraldehyde-3-phosphate (GAP). These metabolite intermediates are then diverted back to the glycolytic pathway. One molecule of M2-labeled G6P generates equimolar mixture of M2-labeled and unlabeled pyruvate. Similarly, one molecule of M1-labeled G6P generates an equimolar mixture of M1-labeled and unlabeled pyruvate. The unlabeled GAP molecule yields one molecule of unlabeled pyruvate. Therefore, theoretically, if all 1,2-$^{13}C_2$-glucose goes through the oxidative PPP exclusively, there would be 20% of M2-labeled pyruvate, 20% of M1-labeled pyruvate and 60% of unlabeled pyruvate.

2.5 Reductive metabolism of glutamine

The Warburg effect is associated with significant inefficiency of substrate utilization, as predominant conversion to lactate results in a smaller fraction of glucose-derived carbon skeletons used for anabolism or high-yield ATP production via respiration. Considering the fact that cancer cells require a robust supply of energy and anabolic precursors, alternative pathways must be activated to compensate for the reduced supply from aerobic glycolysis. Reductive metabolism of glutamine is one of the metabolic reprogramming switches used to achieve this objective.

Glutamine has a special significance in central carbon metabolism since it is the second most consumed carbon source following glucose in some cells and the most abundant amino acid in serum[42]. Previously, it was discovered that a reductive metabolic pathway from glutamine exists in adipocytes and is responsible for a substantial *de novo* fatty acid synthesis[43]. It was further demonstrated that this reductive pathway was active in numerous cancer cell lines[22]. Extracellular glutamine can be internalized through cytoplasmic glutamine transporters. Following the conversion of glutamine to glutamate via glutaminase, glutamate can be transformed to α-ketoglutarate via transamination reactions. The key step then takes place as α-ketoglutarate is carboxylated into isocitrate with the condensation of one molecule of carbon dioxide. This reaction is catalyzed by isocitrate dehydrogenases (IDHs) and is $NADP^+$ dependent[22,44,45]. Further research demonstrates that this behavior is associated with elevation of the α-ketoglutarate to citrate ratio[46,47]. The citrate molecules produced through this mechanism can be cleaved in the cytosol into oxaloacetate and acetyl-CoA in the presence of the enzyme ATP citrate lyase. Acetyl-CoA is then ready to be recruited for fatty acid synthesis. It is worth mentioning that, however, some labeling experiments on fatty acid from glutamine tracers suggest exchange flux rather than net reductive metabolism of glutamine[48]. Still, cancer and proliferating cells are capable of switching their carbon source from glucose to glutamine for lipogenesis especially under hypoxic conditions. As the amount of building blocks for fatty acids decreases from the upstream glycolytic pathway, cells use an alternative substrate to replenish the need for biosynthesis, exhibiting a unique way of metabolic rewiring. Although many of these findings are based on tissue culture experiments, which usually artificially increases the concentration of glutamine, we anticipate that the physiological relevance of this phenomenon still holds, as suggested by comparable results obtained through *in vivo* labeling experiments[47].

Indeed, glutamine consumption rate is persistently high in some cancer cell lines[49,50], and the so-called glutamine addiction reflects the anabolic significance of the aforementioned reductive metabolism.

Isotopic labeling and network analysis contributed to this work, as both 1-^{13}C- and U-$^{13}C_5$- glutamine provided quantitative information about the magnitude of reductive carboxylation[51]. In the case of 1-^{13}C-glutamine, the only heavily labeled carbon corresponds to the carboxyl group, which is lost as CO_2 during the oxidative decarboxylation reaction in the TCA cycle. Only through the reductive pathway is the ^{13}C labeled carbon retained in the intracellular pools of citrate, oxaloacetate, malate, fumarate and aspartate. Alternatively, similar information can be inferred from the uniformly labeled tracer U-$^{13}C_5$- glutamine. All the ^{13}C labeled carbon atoms are retained through the reductive pathway after the condensation of unlabeled carbon dioxide at the carboxylation step (Figure 2.5a). However, through oxidative reactions along the TCA cycle, the ^{13}C labeled carbon atoms are successively lost as carbon dioxide, leading to reduced labeling patterns for all TCA metabolites (Figure 2.5b and 2.5c)[22]. On a relative basis, the ratio of oxidative TCA flux to reductive carboxylation flux can be compared by evaluating the M4/M5 ratio of citrate under the condition of strong glutamine influx. In addition, the combination of the labeling results from 5-^{13}C- and U-$^{13}C_5$- glutamine enables estimation of the fraction of lipids generated through the carboxylation mechanism. The acetyl-CoA molecules generated by these two glutamine tracers yield different labeling patterns during *de novo* lipogenesis. U-$^{13}C_5$-glutamine produces fully labeled acetyl-CoA whereas only one carbon atom per molecule of acetyl-CoA is labeled following the addition of 5-^{13}C-glutamine[22]. These differential labeling results form the basis for quantification of the reductive flux from glutamine.

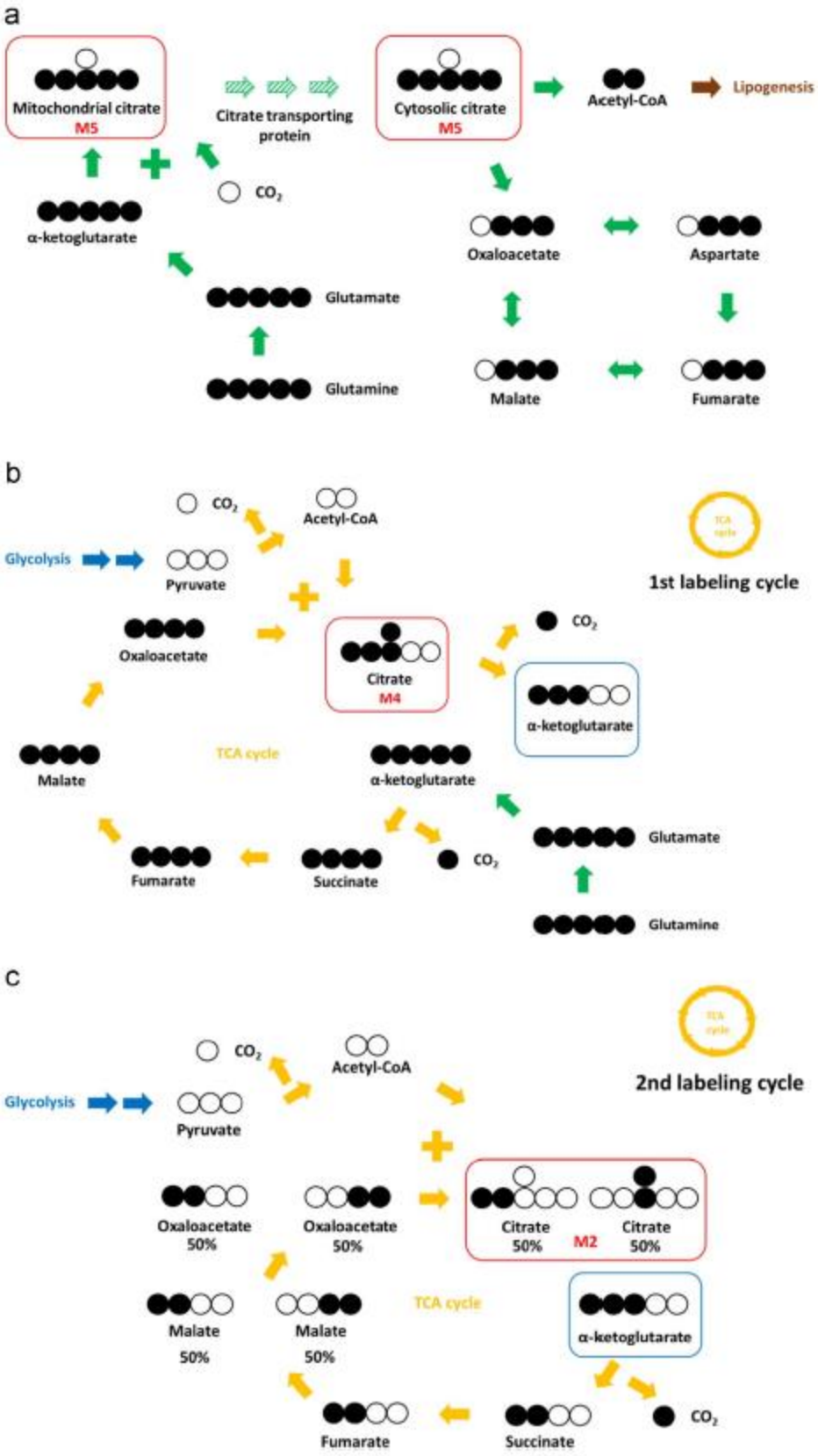
a
Mitochondrial citrate
M5
Citrate transporting protein
Cytosolic citrate
M5
Acetyl-CoA
Lipogenesis
CO2
α-ketoglutarate
Oxaloacetate
Aspartate
Glutamate
Glutamine
Malate
Fumarate
b
CO2
Acetyl-CoA
Glycolysis
Pyruvate
1st labeling cycle
Oxaloacetate
Citrate
M4
CO2
α-ketoglutarate
Malate
TCA cycle
α-ketoglutarate
Glutamate
Fumarate
Succinate
CO2
Glutamine
c
2nd labeling cycle
CO2
Acetyl-CoA
Glycolysis
Pyruvate
Oxaloacetate
50%
Oxaloacetate
50%
Citrate
50%
M2
Citrate
50%
Malate
50%
Malate
50%
TCA cycle
α-ketoglutarate
Fumarate
Succinate
CO2

Figure 2.5. The isotopic labeling pattern generated by U-$^{13}C_5$- glutamine.

(a) The isotopically labeled U-$^{13}C_5$- glutamine is converted to glutamate via glutaminase. Transamination or deamination reactions then take place to transform glutamate to α-ketoglutarate. M5-labeled citrate is formed in the mitochondria and cytosol through reductive carboxylation by isocitrate dehydrogenases (IDHs). This citrate is cleaved into oxaloacetate and acetyl-CoA, and this heavy labeled acetyl-CoA is employed for *de novo* lipogenesis. The reaction network in cytosol further generates M3-labeled oxaloacetate, aspartate, malate and fumarate.

The figure is adapted from Metallo et al[52].

(**b**) In the first cycle of oxidative metabolism of U-$^{13}C_5$- glutamine, the uniform labeling pattern no longer holds at citrate, which is generated by consolidating unlabeled acetyl-CoA with M4 labeled oxaloacetate. The beginning of the second cycle primes at M3-labeled α-ketoglutarate (in the blue box) after the release of a heavy labeled carbon dioxide. When there is a strong influx of glutamine, the labeling pattern of the first cycle dominates.

(**c**) Starting from the M3 labeled α-ketoglutarate (in the blue box), the release of another heavy labeled carbon dioxide further reduces the labeling pattern to generate M2-labeled succinate and fumarate. Due to the molecular asymmetry of malate and oxaloacetate, two different forms of M2-labeled compounds are generated in equimolar ratio. After the consolidation of unlabeled acetyl-CoA and M2-labeled oxaloacetate, M2-labeled citrate is generated. The labeling pattern of the second cycle is less important when there is a strong glutamine influx.

2.6 Isocitrate dehydrogenase (IDH) mutations

IDHs are normally responsible for the interconversion between isocitrate and α-ketoglutarate. There are three isoforms of IDH enzymes. Mutations in cytosolic isocitrate dehydrogenase (IDH1) and mitochondrial isocitrate dehydrogenase (IDH2) are observed in glioblastomas and leukemias[53–55]. The mutations are usually heterozygous with only one allele of normal IDH exchanged for its oncogenic version.

Since these IDH enzymes participate in cellular functions in the form of heterodimers, earlier analyses have focused on the dominant negative effect of these heterozygous mutations on the metabolic balance between isocitrate and α-ketoglutarate[56,57]. However, recent studies revealed another critical metabolic alteration due to IDH mutations: The intracellular level of 2-hydroxyglutarate increases upon expression of R132 or R172 mutants of IDH1 and IDH2, respectively[57,58]. The oxidative direction of IDH enzymes is concomitant with NADPH production. Consistent with this mechanism, both IDH1 and IDH2 mutants result in significant reduction of the rate of NADPH formation in the presence of isocitrate. Interestingly, the consumption rate of NADPH increased when the starting substrate was exchanged to α-ketoglutarate which can be reductively transformed to 2-hydroxyglutarate via mutated IDH enzymes. Since the production of 2-hydroxyglutarate is correlated with brain and blood tumor cells harboring IDH mutations, it is proposed that 2-hydroxyglutarate functions as a oncometabolite[57]. It is also believed that accumulation of 2-hydroxyglutarate can elevate the level of intracellular ROS[59,60]. Cellular redox homeostasis is further disrupted since the formation of ROS can aggravate the effect of reduced NADPH production due to decreased flux from isocitrate to α-ketoglutarate. In addition, 2-hydroxyglutarate is able to impede histone methylation, which plays an essential role in the temporal regulation of gene expression[61]. The

delay of cell differentiation resulting from the accumulation of 2-hydroxyglutarate enables fast proliferation of undifferentiated progenitor cells, which promotes tumorigenesis of gliomas and leukemias[57].

So far, the metabolic rewiring due to IDH mutations is unique in the sense that it creates an accumulation of a single metabolite 2-hydroxyglutarate, which triggers cascades of events stimulating tumorigenesis. However, IDH mutations also lead to redistribution of substrates into different metabolic pathways, exhibiting another level of metabolic reprogramming. As discussed previously, the reductive carboxylation from α-ketoglutarate to isocitrate is catalyzed by IDH1[22]. IDH1 mutations have been demonstrated to hinder the reductive metabolism in glutamine, leading to reduced proliferation under hypoxia and electron transport chain inhibition [62]. Furthermore, the isotopic labeling experiment using U-$^{13}C_5$- glutamine shows a reduction of the M5/M4 ratio for citrate in cells treated with IDH2 siRNAs, supporting the possibility that IDH2 may be essential for mitochondrial reductive carboxylation[57]. These data collectively show that IDH mutations can also inhibit proliferation through suppression of reductive carboxylation reactions under certain contexts.

2.7 Serine and glycine metabolism

One of the major categories of chemotherapeutic drugs is antifolates, which target one-carbon metabolism, a complex metabolic network involving folate and methionine cycles[63]. Serine and glycine metabolism links one-carbon and central carbon metabolism, which has led to its emergence as a significant topic of study. In addition to being imported from the extracellular environment, serine can also be synthesized *de novo* in a linear pathway (Figure 2.6). The

glycolytic intermediate 3PG can be transformed to 3-phosphohydroxypyruvate (P-pyruvate) via the enzyme phosphoglycerate dehydrogenase (PHGDH) in conjunction with NAD^{+}[64]. P-pyruvate is converted to phosphoserine via the transamination reaction catalyzed by phosphoserine aminotransferase. The enzyme phosphoserine phosphatase removes the phosphate group and yields serine[20].

The conversion between serine and glycine is reversibly catalyzed by serine hydroxymethyl transferases (SHMTs). Glycine is produced along with cytosolic 5,10-methylenetetrahydrofolate (5,10-CH_2-THF) from serine, supplying methyl groups for DNA methylation and nucleotide biosynthesis[65]. In addition, glycine is an essential precursor for glutathione, an important antioxidant protecting cellular machinery from ROS[66].

Copy number amplification of the PHGDH gene has been observed in breast cancers and melanomas[67]. The tumorigenicity of PHGDH also brings attention since it is likely to promote metastasis in mouse models[68]. PHGDH suppression does not affect intracellular serine levels, but it decreases the levels of α-ketoglutarate, presumably since the serine biosynthetic pathway produces equimolar amounts of serine and α-ketoglutarate via P-pyruvate transamination. In cells with high PHGDH expression, about half of the anaplerotic flux from glutamine has been attributed to the serine synthesis pathway[21]. Through a series of metabolic and transcriptional studies, researchers have demonstrated that the regulation of PHGDH and other key enzymes in the serine biosynthetic pathway is achieved by the transcription factor nuclear factor erythroid-2-related factor 2 (NRF) in non-small cell lung cancer[69].

In addition to likely facilitating TCA anaplerosis, serine and glycine synthesis also regulates nucleotide biosynthesis via critical modulations on one-carbon metabolism. Cytoplasmic 5,10-CH_2-THF can be combined with glycine to form serine by the catalysis of

cytosolic serine hydroxymethyl transferase (SHMT1)[70,71]. However, 5,10-CH_2-THF is also essential for nucleotide biosynthesis. In addition to synthesizing serine intracellularly, the serine pathway is also responsible for inhibiting SHMT1 activity in order to push one-carbon metabolites toward the direction of nucleotide synthesis. These hypotheses may help explain the observation that nucleotide synthesis from glucose-derived and extracellular serine is attenuated under PHGDH inhibition[20]. Furthermore, metabolic reprogramming also takes place inside mitochondria. The mitochondrial serine hydroxymethyl transferase (SHMT2) is believed to be responsible for the defense mechanism against hypoxic stress. Another mitochondrial enzyme ALDH1L2 which generates NADPH at the expense of consuming one-carbon metabolites could protect cells against oxidative stress. The upregulation of these enzymes imparts cancer cells with enhanced antioxidant defense[72].

Isotopic labeling plays an important role in this analysis. The amount of glucose-derived serine and glycine can be quantified through examining their M3 and M2 labeling fractions, respectively, in cells treated with U-$^{13}C_6$-glucose[20]. By following the biochemical pathways that produce dTMP and AMP, rates of nucleotide biosynthesis can also be determined. In addition, the striking discovery that the serine synthesis pathway inhibits one-carbon metabolism is also corroborated by isotopic labeling experiments. In the presence of exogenous uniformly labeled serine, the labeling fractions of AMP and dTMP decrease in their M1-4 and M1 pools, respectively[20].

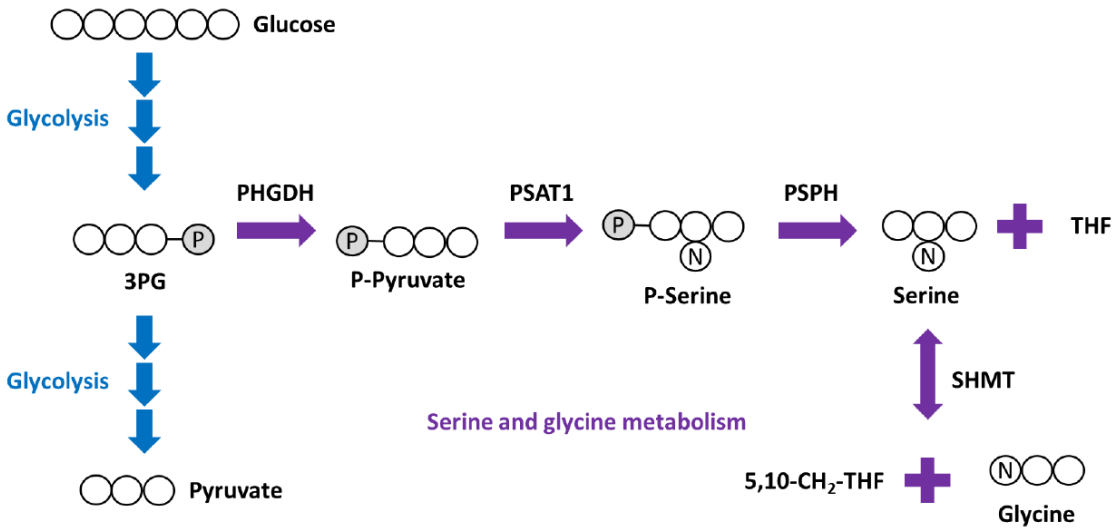

Figure 2.6. Serine and glycine metabolism.

The *de novo* serine biosynthesis pathway branches from glycolysis at 3-phosphoglycerate (3PG). The enzyme phosphoglycerate dehydrogenase (PHGDH) oxidizes 3PG to phosphohydroxypyruvate (P-pyruvate) in the presence of cofactor NAD^+. P-pyruvate is then converted to phosphoserine (P-ser) by phosphoserine aminotransferase 1 (PSAT1). Serine is eventually synthesized after the last step of dephosphorylation by phosphoserine phosphatase (PSPH). Glycine metabolism is linked to serine metabolism through serine hydroxymethyltransferase (SHMT). This reversible reaction is critical in bridging glycolytic substrates with compounds in one-carbon metabolism.

The figure is adapted from Possemato et al.[21] and Pacold et al.[20]

2.8 Acetate metabolism and alternative sources of acetyl-CoA

Mammalian cell metabolism has been primarily focused on glucose and glutamine, presumably due to their high rates of consumption[73]. Recently, various research work has shown that some unconventional metabolites could be utilized as carbon sources in certain types of cancer cells. For instance, alanine could replenish the TCA cycle in pancreatic stellate cells in the context of pancreatic ductal adenocarcinoma[74]. In addition, the tumor cells harboring non-small cell lung cancer is believed to be capable of consuming lactate as nutrient to fuel cell metabolism [75]. In the realm of microbial cell metabolism, acetate has been demonstrated to be a robust substrate for normal cell growth and lipid production[76–78]. Recently, it was discovered that acetate is able to substitute, at least partially, for the roles of glucose and glutamine to fuel cancer cell metabolism under hypoxia, particularly for *de novo* lipogenesis[23].

Under normoxic conditions, the majority of cellular acetyl-CoA is derived from glucose or glutamine. In contrast, the total contribution from glucose and glutamine to acetyl-CoA decreases significantly under hypoxia[79], whereas acetate at physiological levels may contribute up to 20%-50% of the acetyl-CoA pool[80]. In another independent parallel experiment, the isotopic labeling analysis in tumors from patients with brain cancer showed that more than half of the acetyl-CoA pool is made from sources other than glucose[81]. The anaplerotic flux of acetyl-CoA synthesis from glutamine has been shown to be minimal in mouse brain tumors[24]. The key enzyme that appears to control this metabolic rewiring is acetyl-CoA synthetase 2 (ACSS2)[23,25]. Although physiological levels of acetate exhibit great variability (50-600 μM), the acetate concentration in the blood stream could reach millimolar level in chronic alcoholics[73,82,83]. From another perspective, *in vivo* recycling and the circulation system may function in a way to recapture acetate released from protein deacetylation[84], suggesting the physiological significance

of acetate metabolism. We expect tissues where such recapturing events are active to exhibit even more dysregulated acetate metabolism, which may potentially be validated through additional *in vivo* labeling work.

Acetate may also serve as a critical metabolite interconnecting glycolysis, the pentose phosphate pathway and *de novo* lipogenesis. Recent work suggests that the enzyme transketolase-like 1 (TKTL1) may resemble its bacterial counterpart phosphoketolase[85,86] in terms of its capability of cleaving xylulose-5-phosphate into GAP and acetate[87]. GAP is diverted back to glycolysis while acetate can be utilized to replenish acetyl-CoA for lipid synthesis. Thus, in addition to being supplied through reductive glutamine metabolism and exogenous acetate, acetyl-CoA may be produced from TKTL1-mediated cleavage in cancer cells. Collectively, these sources may represent alternative means of replenishing acetyl-CoA for *de novo* lipogenesis despite reduced production due to the Warburg effect.

The above results again are derived from various types of isotopic labeling experiments. For the general study of acetate metabolism, the percentage labeling of acetyl-CoA from U-$^{13}C_6$-glucose or U-$^{13}C_5$- glutamine was shown to dominate over other sources under normoxia. The percentage labeling of acetyl-CoA from labeled amino acids were also shown to constitute a minor portion under normoxia. However, the contributions from glucose and glutamine were demonstrated to decrease significantly under hypoxia. With these quantitative results, the authors concluded that acetate is the dominant source of labeling for acetyl-CoA under hypoxic conditions[24,80]. In addition, the TKTL1 activity was suggested through a 1,2-$^{13}C_2$-glucose labeling experiment in which the labeling pattern of lactate was altered following genetic knockdown in a manner consistent with the presence of the cleavage reaction catalyzed by TKTL1[87].

2.9 Oncogene-specific metabolic rewiring

Decades of modern cancer research have identified many genes that promote tumorigenesis. With contemporary knowledge of cell biology, the mechanisms surrounding protein regulation have been further elucidated. Recent efforts to consolidate our understanding on cellular functions of oncogenes and various metabolic alterations have shed light on links between metabolism and the genetic origins of cancer.

One of the most extensively studied oncogenes is KRAS. It is involved in the mitogen-activated protein (MAP) kinase pathway, functioning as a messenger to deliver proliferative signals to downstream targets[88]. Upon stimulation from upstream receptor tyrosine kinases (RTKs), the RAS-GDP complex is switched to its activated RAS-GTP form, which subsequently can activate downstream MAP kinases and promote cellular growth[89]. The mutant KRAS oncogene encodes the RAS protein which stays at its activated GTP-bound form, thus constitutively transducing growth signals and conferring cells with uncontrolled proliferation[90]. In addition to KRas, epidermal growth factor receptor (EGFR) and phosphatidylinositol 3-kinase (PI3K) are both involved to some extent in the RTK pathway, the upstream of which is shown in Figure 2.7.

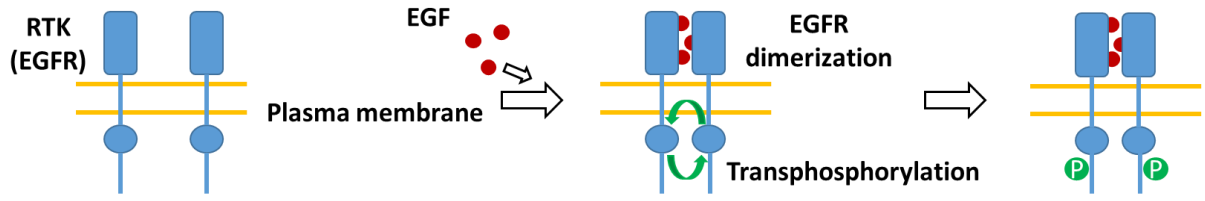

Figure 2.7. Upstream of the RTK pathway.

As a receptor tyrosine kinase, EGF receptor (EGFR) is normally present on plasma membranes and remain distant from each other. EGFRs dimerize with each other in the presence of extracellular EGFs. The intracellular portions of the dimerized EGFRs then trans-phosphorylate each other at multiple phosphorylated tyrosine sites. Next, the downstream of the RTK pathway or the mitogen-activated protein (MAP) kinase pathway can be activated. Additionally, PI3-kinase participates in the downstream of the RTK pathway upon trans-phosphorylation of EGFRs, which is shown in Figure 2.8.

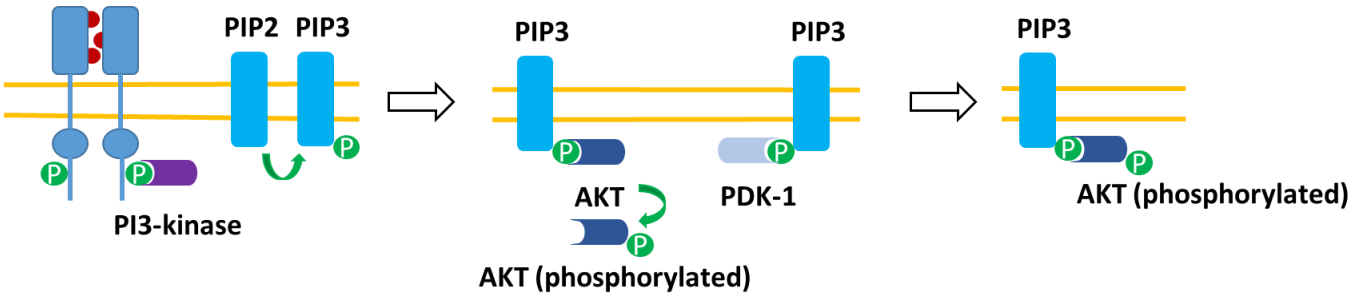

Figure 2.8. Downstream of the RTK pathway.

The phosphorylated tyrosine residues at the intracellular domain of the EGFRs arerecognized and bound by PI3-kinase via its Src Homolog 2 (SH2) domain. Due to this binding event, PI3-kinase is then recruited within close proximity to the plasma membrane, enabling it to phosphorylate phosphatidylinostitol 4,5-bisphosphate (PIP2) and transform PIP2 into phosphatidylinostitol 3,4,5-bisphosphate (PIP3). The activated PIP3 can then recruit two different kinases near the plasma membrane – protein kinase B (PKB/AKT) and phosphoinositide-dependent kinase 1 (PDK-1). The binding event is achieved via the Pleckstrin homology (PH) domains on these kinases. PDK-1 can then phosphorylate AKT, which activates the mammalian target of rapamycin (mTOR) and subsequently promotes cell growth.

Meanwhile, AKT also activates glycogen synthase kinase 3-β (GSK3B)m which can then elevate c-Myc expressions[91] and stimulate cell proliferation.

In addition to the continuing activation of RTK pathway, Ras and the corresponding MAP kinase pathway are also turned on, which is shown in Figure 2.9.

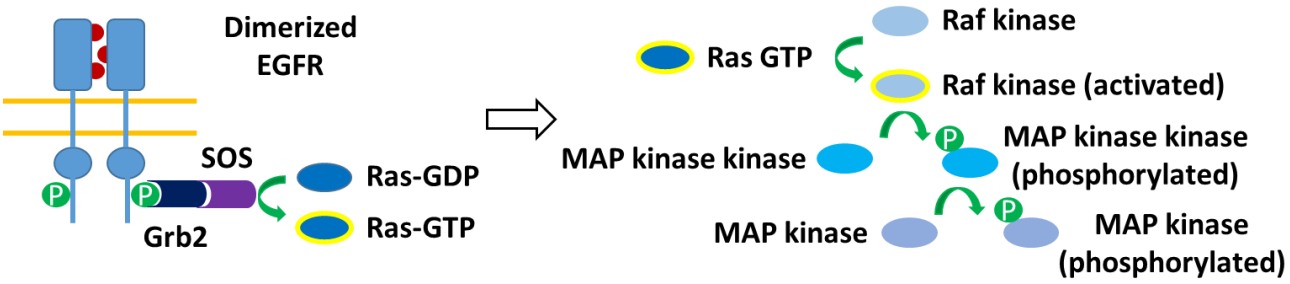

Figure 2.9. Ras and the MAP kinase pathway.

Similar to the downstream RTK pathway, growth factor receptor-bound protein 2 (Grb2) binds to phosphorylated tyrosine residues via its SH2 domain. Grb2 also has a Src Homolog 3 (SH3) domain which binds to another protein referred to as son of sevenless (SOS). The activated SOS acts as a guanine nucleotide exchange factor (GEF) which facilitates the transformation of Ras-GDP to Ras-GTP. When Ras-GTP is formed, it activates rapidly accelerated fibrosarcoma (Raf) kinase. The activated Raf kinase then phosphorylates MAP kinase kinase, which then phosphorylates MAP kinase. The resulting activated MAP kinase upregulates the transcription factor c-Finkel-Biskis-Jinkins murine osteogenic sarcoma (c-Fos), which induces expressions of proteins used to progress through cell cycle.

By reviewing the roles of EGFR, KRas and PI3K in the RTK and MAP kinase pathways, it is clear that each constitutively active mutation of these genes in addition to simple overexpression of c-Myc can result in elevated cell growth. For instance, the constitutively active

KRas mutant results in a non-hydrolysable form of KRas-GTP, which keeps Raf kinase activated at all time. The constitutively activated Raf kinase then keeps phosphorylating MAP kinase kinase and subsequently MAP kinase. As a result, the MAP kinase stays hyperactive and promotes cell cycle through c-Fos transcription.

Metabolically, KRAS promotes glucose consumption as well as glutamine utilization[92,93] to sustain deregulated doubling of cellular contents, Although the oxidative TCA cycle flux is reduced upon mutant KRAS induction, the glycolytic flux together with various anabolic fluxes extracting nitrogen from glutamine are elevated. It has been proposed that upon KRAS transformation, cells adapt themselves to rely on glucose for energy support and glutamine for the supply of anabolic building blocks[92]. Further research has elucidated the primary metabolic route of glutamine-derived glutamate in KRAS-reprogrammed pancreatic ductal adenocarcinoma cells. Instead of converting glutamate to α-ketoglutarate via deamination through glutamate dehydrogenase, the KRAS mutation has been shown to favor the transamination reaction through which aspartate is produced. Mitochondrial aspartate may be then transported into the cytosol after which NADPH is generated through subsequent reactions. This altered metabolism is believed to be beneficial to maintain the redox status conducive for deregulated proliferation [93]. Concomitantly, anabolism can be further reinforced through increased flux along the non-oxidative PPP to generate precursors for nucleotide biosynthesis in pancreatic ductal adenocarcinoma cells[39].

In addition to KRAS and EGFR, the oncogene c-Myc also promotes deregulated proliferation. As an example of the intricacy of cell signaling pathways, the KRAS-mediated MAP kinase pathway also stabilizes c-Myc protein and thus further enhances growth signals[94]. Metabolically, c-Myc has been demonstrated to also support aerobic glycolysis[95]. Outside of the

centrality of the Warburg effect, researchers have shown that c-Myc also plays a critical role in altered glutamine metabolism in cancer cells. As a transcription factor, c-Myc inhibits the expression of microRNAs which downregulate mitochondrial glutaminase responsible for converting glutamine to glutamate[96]. As mentioned previously, glutaminase catalyzes this crucial catabolic reaction, which fuels cancer cells with anaplerotic flux from glutamine. As the Warburg effect directs a significant portion of glucose toward lactate, anaplerosis from glutamine may hold immense significance in maintaining an ample supply of energy, anabolic building blocks and reducing equivalents. Furthermore, c-Myc is also capable of replenishing glutamine through epigenetic modulations of *de novo* glutamine synthesis in many cell lines. DNA demethylation can be triggered by c-Myc to upregulate the expression of glutamine synthetase to facilitate the production of glutamine from glutamate and ammonia[97]. Moreover, c-Myc is believed to be able to suppress proline synthesis, which potentially functions as a tumor suppressing pathway, strengthening the role of c-Myc as a potent oncogene[98,99].

2.10 Concluding remarks

We reviewed recently elucidated metabolic pathways in cancer cells, as determined by stable isotopic labeling and network analysis. The detailed metabolic network illustrating this is shown in Figure 2.10. The compendium of our knowledge of cancer metabolism has passed its infancy, owing to our improved ability to resolve metabolic activity at the molecular and enzymatic level, the diversity of substrates and the coordination of different metabolic pathways. Research on the effect of enzymatic activities[18,20,45,62], mass action kinetics[46] and cofactor ratios on biochemical reaction systems[40] has strengthened our fundamental understanding of this field. Studies on the

use of unconventional substrates may have brought us closer to approximating the physiological environment that nurtures cancer cells. The interconnection of pathways imparts us with a global systematic view of cancer metabolism. The recent progress made in this field also contributes to the joint effort to find the causalities and connections between signaling pathways and metabolic behaviors. Taken together, such advancement will hopefully direct us toward the discovery of innovative therapeutic targets for cancer treatment.

The pathways described above do not provide an absolutely exhaustive picture of metabolic rewiring in cancer cells, and it is likely that additional pathways that we have not yet identified are activated during tumorigenesis. In this effort, we believe that isotopic labeling using stable ^{13}C-, ^{2}H-, ^{18}O-, ^{15}N- and ^{35}S-based tracers will facilitate the discovery and investigation of these metabolic alterations.

One area largely underdeveloped in this field is the study of metabolic reprogramming inside cellular compartments such as mitochondria. The main reason for this is the limited capability to dissect metabolic pathways with the current techniques. We expect this to be a promising area as new methods are being developed to probe the intricacy of sub-cellular metabolic activities. One excellent example is the ^{2}H-isotopic labeling work performed to resolve the NADPH metabolism in different cellular compartments[100]. Other alternative approaches such as organelle isolation and coupled database analysis also demonstrate great potential to investigate compartmentalized metabolism[101].

In addition, recent research on amino acid metabolism has increasingly demonstrated an important role of substrates other than glucose and glutamine. Quantification of the composition of cells argues that amino acids contributed to the majority of the cell mass in proliferating mammalian cells. Although the consumption rates of glucose and glutamine are usually the

highest, it is amino acids that eventually provide most of the anabolic building blocks for fast growing cells[102]. Aside from the significance of glutamine, serine and glycine metabolism, it was discovered that the amino acid aspartate also plays a vital role in proliferating cells. Aspartate production requires the supply of electron acceptors to be fully functional. Electron acceptors can be provided by compounds such as pyruvate or α-ketobutyrate to rescue growth when the electron transport chain is compromised. The work demonstrates the dependence of proliferation on aspartate synthesis and its connection with electron transport chain[103,104].

Another emerging area is *in vivo* labeling analysis. While most previous work has been conducted in cultured cells, researchers have begun to investigate metabolic behaviors subject to different physiological conditions. Studies on lung cancer have demonstrated that the tumor microenvironment exerts discernible effects on the metabolic phenotypes of cells, especially with respect to glutamine metabolism[105]. In addition, the heterogeneity in tumor tissues has been shown to confer cells with altered substrate utilization preference, such as the onset of lactate metabolism, in non-small cell lung cancer[75].

The value of the research we reviewed stems not only from the overarching objective to elucidate basic cancer biochemistry, but also the profound implications for cancer therapy. Novel pharmaceutical targets are being identified concomitant with the theoretical development in cancer metabolism. This was recently reviewed in an article highlighting the clinical effort to implement IDH inhibitors in cancer treatment[106]. We believe that the combination of glucose and glutamine targeting, potentially in conjunction with restricting the supply of other substrates, may be able to enhance the effectiveness of the overall chemotherapy.

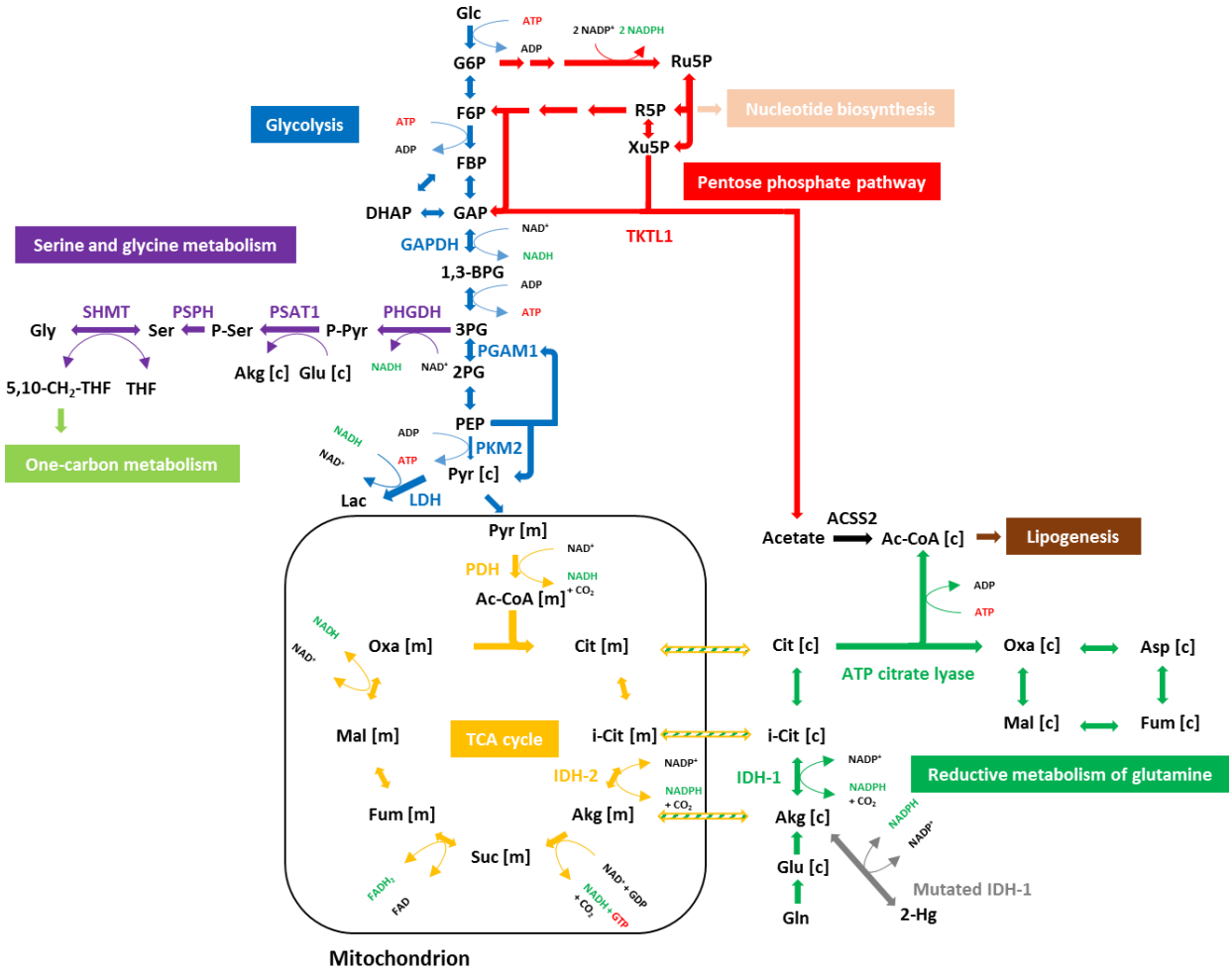

Figure 2.10. Detailed summary of rewired metabolic pathways in cancer cells. Metabolic reprogramming along glycolysis, reductive carboxylation of glutamine, serine and glycine metabolism, IDH mutations and TKTL1-mediated acetate metabolism are shown in a detailed depiction.

2.11 References

(1) Society, A. C. *Cancer Facts & Figures 2020*; 2020.

(2) Data, M. Cancer Statistics, 2016. **2016**, *66* (1), 7–30.

(3) Hanahan, D. The Hallmarks of Cancer. *Cell*. 2000, pp 57–70.

(4) Hahn, W. C.; Counter, C. M.; Lundberg, a S.; Beijersbergen, R. L.; Brooks, M. W.; Weinberg, R. a. Creation of Human Tumour Cells with Defined Genetic Elements. *Nature* **1999**, *400* (6743), 464–468.

(5) Wyllie, A. H.; Kerr, J. F. R.; Currie, A. R. Cell Death: The Significance of Apoptosis. *Int. Rev. Cytol.* **1980**, *68*, 251–306.

(6) Sporn, M. B. *The War on Cancer*; 1996; Vol. 347.

(7) Cogliano, V. J.; Baan, R.; Straif, K.; Grosse, Y.; Lauby-Secretan, B.; Ghissassi, F. El; Bouvard, V.; Benbrahim-Tallaa, L.; Guha, N.; Freeman, C.; Galichet, L.; Wild, C. P. Preventable Exposures Associated with Human Cancers. *Journal of the National Cancer Institute*. 2010, pp 1827–1839.

(8) Hoffmann, D.; Hecht, S. Nicotine-Derived N-Nitrosamines and Tobacco-Related Cancer: Current Status and Future Directions. *Cancer Res.* **1985**, *45* (March), 935–944.

(9) Morris, J. D. H.; Eddleston, A. L. W. F.; Crook, T. Viral Infection and Cancer. *The Lancet*. 1995, pp 754–758.

(10) McLaughlin-Drubin, M. E.; Munger, K. Viruses Associated with Human Cancer. *Biochim. Biophys. Acta* **2008**, *1782* (3), 127–150.

(11) Pagano, J. S.; Blaser, M.; Buendia, M. A.; Damania, B.; Khalili, K.; Raab-Traub, N.; Roizman, B. Infectious Agents and Cancer: Criteria for a Causal Relation. *Seminars in Cancer Biology*. 2004, pp 453–471.

(12) Yarosh, D.; Alas, L. G.; Yee, V.; Oberyszyn, A.; Kibitel, J. T.; Mitchell, D.; Rosenstein, R.; Spinowitz, A.; Citron, M. Pyrimidine Dimer Removal Enhanced by DNA Repair Liposomes Reduces the Incidence of UV Skin Cancer in Mice. *Cancer Res.* **1992**, *52* (15), 4227–4231.

(13) Calle, E. E.; Kaaks, R. Overweight, Obesity and Cancer: Epidemiological Evidence and Proposed Mechanisms. *Nat. Rev. Cancer* **2004**, *4* (8), 579–591.

(14) Sudhakar, a. History of Cancer, Ancient and Modern Treatment Methods Akulapalli. *J Cancer Sci Ther.* **2010**, *1* (2), 1–4.

(15) Miwa, M.; Ura, M.; Nishida, M.; Sawada, N.; Ishikawa, T.; Mori, K.; Shimma, N.; Umeda, I.; Ishitsuka, H. Design of a Novel Oral Fluoropyrimidine Carbamate, Capecitabine, Which Generates 5 Fluorouracil Selectively in Tumours by Enzymes Concentrated in Human Liver and Cancer Tissue. *Eur. J. Cancer* **1998**, *34* (8), 1274–1281.

(16) Haldar, S.; Chintapalli, J.; Croce, C. M. Taxol Induces Bcl-2 Phosphorylation and Death of Prostate Cancer Cells. *Cancer Res.* **1996**, *56* (6), 1253–1255.

(17) Sawyers, C. Targeted Cancer Therapy. *Nature* **2004**, *432* (7015), 294–297.

(18) Vander Heiden, M. G.; Locasale, J. W.; Swanson, K. D.; Sharfi, H.; Rabinowitz, J. D.; Asara, J. M.; Cantley, L. C. Evidence for an Alternative Glycolytic. *Science (80-.).* **2010**,

329 (5998), 1492–1499.

(19) Christofk, H. R.; Vander Heiden, M. G.; Harris, M. H.; Ramanathan, A.; Gerszten, R. E.; Wei, R.; Fleming, M. D.; Schreiber, S. L.; Cantley, L. C. The M2 Splice Isoform of Pyruvate Kinase Is Important for Cancer Metabolism and Tumour Growth. *Nature* **2008**, *452* (7184), 230–233.

(20) Pacold, M. E.; Brimacombe, K. R.; Chan, S. H.; Rohde, J. M.; Lewis, C. A.; Swier, L. J. Y. M.; Possemato, R.; Chen, W. W.; Sullivan, L. B.; Fiske, B. P.; Cho, S.; Freinkman, E.; Birsoy, K.; Abu-Remaileh, M.; Shaul, Y. D.; Liu, C. M.; Zhou, M.; Koh, M. J.; Chung, H.; et al. A PHGDH Inhibitor Reveals Coordination of Serine Synthesis and One-Carbon Unit Fate. *Nat. Chem. Biol.* **2016**, *12* (4).

(21) Possemato, R.; Marks, K. M.; Shaul, Y. D.; Pacold, M. E.; Kim, D.; Birsoy, K.; Sethumadhavan, S.; Woo, H.-K.; Jang, H. G.; Jha, A. K.; Chen, W. W.; Barrett, F. G.; Stransky, N.; Tsun, Z.-Y.; Cowley, G. S.; Barretina, J.; Kalaany, N. Y.; Hsu, P. P.; Ottina, K.; et al. Functional Genomics Reveal That the Serine Synthesis Pathway Is Essential in Breast Cancer. *Nature* **2011**, *476* (7360), 346–350.

(22) Metallo, C. M.; Gameiro, P. A.; Bell, E. L.; Mattaini, K. R.; Yang, J.; Hiller, K.; Jewell, C. M.; Johnson, Z. R.; Irvine, D. J.; Guarente, L.; Kelleher, J. K.; Heiden, M. G. Vander; Iliopoulos, O.; Stephanopoulos, G. Reductive Glutamine Metabolism by IDH1 Mediates Lipogenesis under Hypoxia. TL - 481. *Nature* **2011**, *481 VN*- (7381), 380–384.

(23) Schug, Z. T.; Peck, B.; Jones, D. T.; Zhang, Q.; Grosskurth, S.; Alam, I. S.; Goodwin, L. M.; Smethurst, E.; Mason, S.; Blyth, K.; McGarry, L.; James, D.; Shanks, E.; Kalna, G.; Saunders, R. E.; Jiang, M.; Howell, M.; Lassailly, F.; Thin, M. Z.; et al. Acetyl-CoA

Synthetase 2 Promotes Acetate Utilization and Maintains Cancer Cell Growth under Metabolic Stress. *Cancer Cell* **2015**, *27* (1), 57–71.

(24) Mashimo, T.; Pichumani, K.; Vemireddy, V.; Hatanpaa, K. J.; Singh, D. K.; Sirasanagandla, S.; Nannepaga, S.; Piccirillo, S. G.; Kovacs, Z.; Foong, C.; Huang, Z.; Barnett, S.; Mickey, B. E.; Deberardinis, R. J.; Tu, B. P.; Maher, E. A.; Bachoo, R. M. Acetate Is a Bioenergetic Substrate for Human Glioblastoma and Brain Metastases. *Cell* **2014**, *159* (7), 1603–1614.

(25) Comerford, S. A.; Huang, Z.; Du, X.; Wang, Y.; Cai, L.; Witkiewicz, A. K.; Walters, H.; Tantawy, M. N.; Fu, A.; Manning, H. C.; Horton, J. D.; Hammer, R. E.; Mcknight, S. L.; Tu, B. P. Acetate Dependence of Tumors. *Cell* **2014**, *159* (7), 1591–1602.

(26) Sauer, U. Metabolic Networks in Motion: 13C-Based Flux Analysis. *Mol. Syst. Biol.* **2006**, *2*, 62.

(27) Hiller, K.; Metallo, C. M. Profiling Metabolic Networks to Study Cancer Metabolism. *Curr. Opin. Biotechnol.* **2013**, *24* (1), 60–68.

(28) Weindl, D.; Wegner, A.; Hiller, K. MIA: Non-Targeted Mass Isotopolome Analysis. *Bioinformatics* **2016**, *32* (18), 2875–2876.

(29) Basan, M.; Hui, S.; Okano, H.; Zhang, Z.; Shen, Y.; Williamson, J. R.; Hwa, T. Overflow Metabolism in Escherichia Coli Results from Efficient Proteome Allocation. *Nature* **2015**, *528* (7580), 99–104.

(30) Hsu, P. P.; Sabatini, D. M. Cancer Cell Metabolism: Warburg and Beyond. *Cell* **2008**, *134* (5), 703–707.

(31) Bonnet, S.; Archer, S. L.; Allalunis-Turner, J.; Haromy, A.; Beaulieu, C.; Thompson, R.; Lee, C. T.; Lopaschuk, G. D.; Puttagunta, L.; Bonnet, S.; Harry, G.; Hashimoto, K.; Porter, C. J.; Andrade, M. A.; Thebaud, B.; Michelakis, E. D. A Mitochondria-K+ Channel Axis Is Suppressed in Cancer and Its Normalization Promotes Apoptosis and Inhibits Cancer Growth. *Cancer Cell* **2007**, *11* (1), 37–51.

(32) Riedl, S. J.; Salvesen, G. S. The Apoptosome: Signalling Platform of Cell Death. *Nat. Rev. Mol. Cell Biol.* **2007**, *8* (5), 405–413.

(33) Liberti, M. V.; Locasale, J. W. The Warburg Effect: How Does It Benefit Cancer Cells? *Trends Biochem. Sci.* **2016**, *41* (3), 211–218.

(34) Fang, J.; Quinones, Q. J.; Holman, T. L.; Morowitz, M. J.; Wang, Q.; Zhao, H.; Sivo, F.; Maris, J. M.; Wahl, M. L. The H+-Linked Monocarboxylate Transporter (MCT1/SLC16A1): A Potential Therapeutic Target for High-Risk Neuroblastoma. *Mol. Pharmacol.* **2006**, *70* (6), 2108–2115.

(35) Fothergill-Gilmore, L. A.; Watson, H. C. Phosphoglycerate Mutases. *Biochem. Soc. Trans.* **1990**, *18* (2), 190–193.

(36) de Koning, T. J.; Snell, K.; Duran, M.; Berger, R.; Poll-The, B.-T.; Surtees, R. L-Serine in Disease and Development. *Biochem. J.* **2003**, *371* (Pt 3), 653–661.

(37) Vander Heiden, M. G.; Lunt, S. Y.; Dayton, T. L.; Fiske, B. P.; Israelsen, W. J.; Mattaini, K. R.; Vokes, N. I.; Stephanopoulos, G.; Cantley, L. C.; Metallo, C. M.; Locasale, J. W. Metabolic Pathway Alterations That Support Cell Proliferation. *Cold Spring Harb. Symp. Quant. Biol.* **2011**, *76*, 325–334.

(38) Hitosugi, T.; Kang, S.; Vander Heiden, M. G.; Chung, T.; Elf, S.; Lythgoe, K.; Dong, S.; Lonial, S.; Wang, X.; Chen, G. Z.; Xie, J.; Gu, T.-L.; Polakiewicz, R. D.; Roesel, J. L.; Boggon, T. J.; Khuri, F. R.; Gilliland, D. G.; Cantley, L. C.; Kaufman, J.; et al. Tyrosine Phosphorylation Inhibits PKM2 to Promote the Warburg Effect and Tumor Growth. *Growth (Lakeland)* **2010**, *2* (97), 1–16.

(39) Ying, H.; Kimmelman, A. C.; Lyssiotis, C. A.; Hua, S.; Chu, G. C.; Fletcher-Sananikone, E.; Locasale, J. W.; Son, J.; Zhang, H.; Coloff, J. L.; Yan, H.; Wang, W.; Chen, S.; Viale, A.; Zheng, H.; Paik, J. H.; Lim, C.; Guimaraes, A. R.; Martin, E. S.; et al. Oncogenic Kras Maintains Pancreatic Tumors through Regulation of Anabolic Glucose Metabolism. *Cell* **2012**, *149* (3), 656–670.

(40) Ahn, W. S.; Dong, W.; Zhang, Z.; Cantor, J. R.; Sabatini, D. M.; Iliopoulos, O.; Stephanopoulos, G. Glyceraldehyde 3-Phosphate Dehydrogenase Modulates Nonoxidative Pentose Phosphate Pathway to Provide Anabolic Precursors in Hypoxic Tumor Cells. *AIChE J.* **2018**, *64* (12), 4289–4296.

(41) Yun, J.; Mullarky, E.; Lu, C.; Bosch, K. N.; Kavalier, A.; Rivera, K.; Roper, J.; Chio, I. I. C.; Giannopoulou, E. G.; Rago, C.; Muley, A.; Asara, J. M.; Paik, J.; Elemento, O.; Chen, Z.; Pappin, D. J.; Dow, L. E.; Papadopoulos, N.; Gross, S. S.; et al. Vitamin C Selectively Kills KRAS and BRAF Mutant Colorectal Cancer Cells by Targeting GAPDH. *Science (80-.).* **2015**, *350* (6266), 1391–1396.

(42) Smith, R. J. Glutamine Metabolism and Its Physiologic Importance. *J. Parenter. Enterral Nutr.* **1990**, *14* (4), 40–44.

(43) Yoo, H.; Antoniewicz, M. R.; Stephanopoulos, G.; Kelleher, J. K. Quantifying Reductive

Carboxylation Flux of Glutamine to Lipid in a Brown Adipocyte Cell Line. *J. Biol. Chem.* **2008**, *283* (30), 20621–20627.

(44) Wise, D. R.; Ward, P. S.; Shay, J. E. S.; Cross, J. R.; Gruber, J. J.; Sachdeva, U. M.; Platt, J. M.; DeMatteo, R. G.; Simon, M. C.; Thompson, C. B. Hypoxia Promotes Isocitrate Dehydrogenase-Dependent Carboxylation of α-Ketoglutarate to Citrate to Support Cell Growth and Viability. *Proc. Natl. Acad. Sci. U. S. A.* **2011**, *108* (49), 19611–19616.

(45) Mullen, A. R.; Wheaton, W. W.; Jin, E. S.; Chen, P.-H.; Sullivan, L. B.; Cheng, T.; Yang, Y.; Linehan, W. M.; Chandel, N. S.; DeBerardinis, R. J. Reductive Carboxylation Supports Growth in Tumour Cells with Defective Mitochondria. *Nature* **2012**, *481* (7381), 385–388.

(46) Fendt, S.-M.; Bell, E. L.; Keibler, M. A.; Olenchock, B. A.; Mayers, J. R.; Wasylenko, T. M.; Vokes, N. I.; Guarente, L.; Vander Heiden, M. G.; Stephanopoulos, G. Reductive Glutamine Metabolism Is a Function of the α-Ketoglutarate to Citrate Ratio in Cells. *Nat. Commun.* **2013**, *4*, 2236.

(47) Gameiro, P. A.; Yang, J.; Metelo, A. M.; P??rez-Carro, R.; Baker, R.; Wang, Z.; Arreola, A.; Rathmell, W. K.; Olumi, A.; L??pez-Larrubia, P.; Stephanopoulos, G.; Iliopoulos, O. In Vivo HIF-Mediated Reductive Carboxylation Is Regulated by Citrate Levels and Sensitizes VHL-Deficient Cells to Glutamine Deprivation. *Cell Metab.* **2013**, *17* (3), 372–385.

(48) Fan, J.; Kamphorst, J. J.; Rabinowitz, J. D.; Shlomi, T. Fatty Acid Labeling from Glutamine in Hypoxia Can Be Explained by Isotope Exchange without Net Reductive Isocitrate Dehydrogenase (IDH) Flux. *J. Biol. Chem.* **2013**, *288* (43), 31363–31369.

(49) Wise, D. R.; Thompson, C. B. Glutamine Addiction: A New Therapeutic Target in Cancer. *Trends Biochem Sci* . **2011**, *35* (8), 427–433.

(50) Hensley, C. T.; Wasti, A. T.; Deberardinis, R. J. Review Series Glutamine and Cancer : Cell Biology , Physiology , and Clinical Opportunities. *J. Clin. Invest.* **2013**, *123* (9), 3678–3684.

(51) Zhang, J.; Ahn, W. S.; Gameiro, P. A.; Keibler, M. A.; Zhang, Z.; Stephanopoulos, G. 13C Isotope-Assisted Methods for Quantifying Glutamine Metabolism in Cancer Cells. *Methods Enzymol.* **2014**, *542*, 369–389.

(52) Metallo, C. M.; Gameiro, P. A.; Bell, E. L.; Mattaini, K. R.; Yang, J.; Hiller, K.; Jewell, C. M.; Johnson, Z. R.; Irvine, D. J.; Guarente, L.; Kelleher, J. K.; Vander Heiden, M. G.; Iliopoulos, O.; Stephanopoulos, G. Reductive Glutamine Metabolism by IDH1 Mediates Lipogenesis under Hypoxia. *Nature* **2012**, *481* (7381), 380–384.

(53) Mi, R. K.; Min, S. K.; Ji, E. O.; Yoo, R. K.; Sang, Y. S.; Seong, I. S.; Ji, Y. L.; Nam, J. Y.; Sug, H. L. Mutational Analysis of IDH1 Codon 132 in Glioblastomas and Other Common Cancers. *Int. J. Cancer* **2009**, *125* (2), 353–355.

(54) Cohen, A. L.; Holmen, S. L.; Colman, H. IDH1 and IDH2 Mutations in Gliomas. *Curr. Neurol. Neurosci. Rep.* **2013**, *13* (5), 345.

(55) Mardis, E. E. R. E.; Ding, L.; Dooling, D. J.; Larson, D. E.; McLellan, M. D.; Chen, K.; Koboldt, D. C.; Fulton, R. S.; Delehaunty, K. D.; McGrath, S. D.; Fulton, L. a; Locke, D. P.; Magrini, V. J.; Abbott, R. M.; Vickery, T. L.; Reed, J. S.; Robinson, J. S.; Wylie, T.; Smith, S. M.; et al. Recurring Mutations Found by Sequencing an Acute Myeloid Leukemia Genome. *N. Engl. J. Med.* **2009**, *361* (11), 1058–1066.

(56) Zhao, S.; Lin, Y.; Xu, W.; Jiang, W.; Zha, Z.; Wang, P.; Yu, W.; Li, Z.; Gong, L.; Peng, Y.; Ding, J.; Lei, Q.; Guan, K.-L.; Xiong, Y. Glioma-Derived Mutations in IDH1 Dominantly Inhibit IDH1 Catalytic Activity and Induce HIF-1 . *Science (80-.).* **2009**, *324* (5924), 261–265.

(57) Ward, P. S.; Patel, J.; Wise, D. R.; Abdel-Wahab, O.; Bennett, B. D.; Coller, H. A.; Cross, J. R.; Fantin, V. R.; Hedvat, C. V.; Perl, A. E.; Rabinowitz, J. D.; Carroll, M.; Su, S. M.; Sharp, K. A.; Levine, R. L.; Thompson, C. B. The Common Feature of Leukemia-Associated IDH1 and IDH2 Mutations Is a Neomorphic Enzyme Activity Converting α-Ketoglutarate to 2-Hydroxyglutarate. *Cancer Cell* **2010**, *17* (3), 225–234.

(58) Dang, L.; White, D. W.; Gross, S.; Bennett, B. D.; Bittinger, M. A.; Driggers, E. M.; Fantin, V. R.; Jang, H. G.; Jin, S.; Keenan, M. C.; Marks, K. M.; Prins, R. M.; Ward, P. S.; Yen, K. E.; Liau, L. M.; Rabinowitz, J. D.; Cantley, L. C.; Thompson, C. B.; Vander Heiden, M. G.; et al. Cancer-Associated IDH1 Mutations Produce 2-Hydroxyglutarate. *Nature* **2009**, *462* (7274), 739–744.

(59) Latini, A.; Scussiato, K.; Rosa, R. B.; Llesuy, S.; Belló-Klein, A.; Dutra-Filho, C. S.; Wajner, M. D-2-Hydroxyglutaric Acid Induces Oxidative Stress in Cerebral Cortex of Young Rats. *Eur. J. Neurosci.* **2003**, *17* (10), 2017–2022.

(60) Kölker, S.; Pawlak, V.; Ahlemeyer, B.; Okun, J. G.; Hörster, F.; Mayatepek, E.; Krieglstein, J.; Hoffmann, G. F.; Köhr, G. NMDA Receptor Activation and Respiratory Chain Complex V Inhibition Contribute to Neurodegeneration in D-2-Hydroxyglutaric Aciduria. *Eur. J. Neurosci.* **2002**, *16* (1), 21–28.

(61) Lu, C.; Ward, P. S.; Kapoor, G. S.; Rohle, D.; Turcan, S.; Abdel-Wahab, O.; Edwards, C.

R.; Khanin, R.; Figueroa, M. E.; Melnick, A.; Wellen, K. E.; Oĝrourke, D. M.; Berger, S. L.; Chan, T. A.; Levine, R. L.; Mellinghoff, I. K.; Thompson, C. B. IDH Mutation Impairs Histone Demethylation and Results in a Block to Cell Differentiation. *Nature* **2012**.

(62) Grassian, A. R.; Parker, S. J.; Davidson, S. M.; Divakaruni, A. S.; Green, C. R.; Zhang, X.; Slocum, K. L.; Pu, M.; Lin, F.; Vickers, C.; Joud-Caldwell, C.; Chung, F.; Yin, H.; Handly, E. D.; Straub, C.; Growney, J. D.; Vander Heiden, M. G.; Murphy, A. N.; Pagliarini, R.; et al. IDH1 Mutations Alter Citric Acid Cycle Metabolism and Increase Dependence on Oxidative Mitochondrial Metabolism. *Cancer Res.* **2014**, *74* (12), 3317–3331.

(63) Farber, S.; Diamond, L. K.; Mercer, R. D.; Sylvester, R. F. J.; Wolff, J. A. Temporary Remissions in Acute Leukemia in Children Produced by Folic Acid Antagonist, 4-Aminopteroyl-Glutamic Acid (Aminopterin). *N. Engl. J. Med.* **1948**, *238* (23), 787–793.

(64) Deberardinis, R. J. Serine Metabolism: Some Tumors Take the Road Less Traveled. *Cell Metab.* **2011**, *14* (3), 285–286.

(65) Amelio, I.; Cutruzzolá, F.; Antonov, A.; Agostini, M.; Melino, G. Serine and Glycine Metabolism in Cancer. *Trends Biochem. Sci.* **2014**, *39* (4), 191–198.

(66) Ruiz-Ramírez, A.; Ortiz-Balderas, E.; Cardozo-Saldaña, G.; Diaz-Diaz, E.; El-Hafidi, M. Glycine Restores Glutathione and Protects against Oxidative Stress in Vascular Tissue from Sucrose-Fed Rats. *Clin. Sci. (Lond).* **2014**, *126* (1), 19–29.

(67) Locasale, J. W.; Grassian, A. R.; Melman, T.; Lyssiotis, C. A.; Mattaini, K. R.; Bass, A. J.; Heffron, G.; Metallo, C. M.; Muranen, T.; Sharfi, H.; Sasaki, A. T.; Anastasiou, D.; Mullarky, E.; Vokes, N. I.; Sasaki, M.; Beroukhim, R.; Stephanopoulos, G.; Ligon, A. H.;

Meyerson, M.; et al. Phosphoglycerate Dehydrogenase Diverts Glycolytic Flux and Contributes to Oncogenesis. *Nat. Genet.* **2011**, *43* (9), 869–874.

(68) Pollari, S.; Kakonen, S. M.; Edgren, H.; Wolf, M.; Kohonen, P.; Sara, H.; Guise, T.; Nees, M.; Kallioniemi, O. Enhanced Serine Production by Bone Metastatic Breast Cancer Cells Stimulates Osteoclastogenesis. *Breast Cancer Res. Treat.* **2011**, *125* (2), 421–430.

(69) DeNicola, G. M.; Chen, P.-H.; Mullarky, E.; Sudderth, J. A.; Hu, Z.; Wu, D.; Tang, H.; Xie, Y.; Asara, J. M.; Huffman, K. E.; Wistuba, I. I.; Minna, J. D.; DeBerardinis, R. J.; Cantley, L. C. NRF2 Regulates Serine Biosynthesis in Non–Small Cell Lung Cancer. *Nat. Genet.* **2015**, *47* (12), 1475–1481.

(70) Renwick, S. B.; Snell, K.; Baumann, U. The Crystal Structure of Human Cytosolic Serine Hydroxymethyltransferase: A Target for Cancer Chemotherapy. *Structure* **1998**, *6* (9), 1105–1116.

(71) Garrow, T. A.; Brenner, A. A.; Michael Whitehead, V.; Chen, X. N.; Duncan, R. G.; Korenberg, J. R.; Shane, B. Cloning of Human CDNAs Encoding Mitochondrial and Cytosolic Serine Hydroxymethyltransferases and Chromosomal Localization. *J. Biol. Chem.* **1993**, *268* (16), 11910–11916.

(72) Ducker, G. S.; Rabinowitz, J. D. One-Carbon Metabolism in Health and Disease. *Cell Metab.* **2016**, No. 2016, 1–16.

(73) Hosios, A. M.; Vander Heiden, M. G. Acetate Metabolism in Cancer Cells. *Cancer Metab.* **2014**, *2* (1), 27.

(74) Sousa, C. M.; Biancur, D. E.; Wang, X.; Halbrook, C. J.; Sherman, M. H.; Zhang, L.;

Kremer, D.; Hwang, R. F.; Witkiewicz, A. K.; Ying, H.; Asara, J. M.; Evans, R. M.; Cantley, L. C.; Lyssiotis, C. A.; Kimmelman, A. C. Pancreatic Stellate Cells Support Tumour Metabolism through Autophagic Alanine Secretion. *Nat. Publ. Gr.* **2016**, *536* (7617), 479–483.

(75) Hensley, C. T.; Faubert, B.; Yuan, Q.; Lev-Cohain, N.; Jin, E.; Kim, J.; Jiang, L.; Ko, B.; Skelton, R.; Loudat, L.; Wodzak, M.; Klimko, C.; McMillan, E.; Butt, Y.; Ni, M.; Oliver, D.; Torrealba, J.; Malloy, C. R.; Kernstine, K.; et al. Metabolic Heterogeneity in Human Lung Tumors. *Cell* **2016**, *164* (4), 681–694.

(76) Smith, M. R.; Mah, R. A. Acetate as Sole Carbon and Energy Source for Growth of Methanosarcina Strain 227. *Appl. Environ. Microbiol.* **1980**, *39* (5), 993–999.

(77) Barbosa, M. J.; Rocha, J. M. S.; Tramper, J.; Wijffels, R. H. Acetate as a Carbon Source for Hydrogen Production by Photosynthetic Bacteria. *J. Biotechnol.* **2001**, *85* (1), 25–33.

(78) Liu, N.; Qiao, K.; Stephanopoulos, G. 13C Metabolic Flux Analysis of Acetate Conversion to Lipids by Yarrowia Lipolytica. *Metab. Eng.* **2016**, *38*.

(79) Kamphorst, J. J.; Cross, J. R.; Fan, J.; de Stanchina, E.; Mathew, R.; White, E. P.; Thompson, C. B.; Rabinowitz, J. D. Hypoxic and Ras-Transformed Cells Support Growth by Scavenging Unsaturated Fatty Acids from Lysophospholipids. *Proc Natl Acad Sci U S A* **2013**, *110* (22), 8882–8887.

(80) Kamphorst, J. J.; Chung, M. K.; Fan, J.; Rabinowitz, J. D. Quantitative Analysis of Acetyl-CoA Production in Hypoxic Cancer Cells Reveals Substantial Contribution from Acetate. *Cancer Metab.* **2014**, *2*, 23.

(81) Maher, E. A.; Marin-Valencia, I.; Bachoo, R. M.; Mashimo, T.; Raisanen, J.; Hatanpaa, K. J.; Jindal, A.; Jeffrey, F. M.; Choi, C.; Madden, C.; Mathews, D.; Pascual, J. M.; Mickey, B. E.; Malloy, C. R.; DeBerardinis, R. J. Metabolism of [U-13 C]Glucose in Human Brain Tumors in Vivo. *NMR Biomed.* **2012**, *25* (11), 1234–1244.

(82) Nuutinen, H.; Lindros, K.; Hekali, P.; Salaspuro, M. Elevated Blood Acetate as Indicator of Fast Ethanol Elimination in Chronic Alcoholics. *Alcohol* **1985**, *2* (4), 623–626.

(83) Korri, U.; Nuutinen, H.; Salaspuro, M. Increased Blood Acetate: A New Laboratory Marker of Alcoholism and Heavy Drinking. *Alcohol. Clin. Exp. Res.* **1985**, *9* (5), 468–471.

(84) Lyssiotis, C. A.; Cantley, L. C. Acetate Fuels the Cancer Engine. *Cell* **2014**, *159* (7), 1492–1494.

(85) Heath, E. C.; Hurwitz, J.; Horecker, B. L.; Ginsburg, A. Pentose Fermentation by Lactobacillus Plantarum. I. The Cleavage of Xylulose 5-Phosphate by Phosphoketolase. *J. Biol. Chem.* **1958**, *231* (2), 1009–1029.

(86) Schramm, M.; Klybas, V.; Racker, E. Phosphorolytic Cleavage of Fructose-6-Phosphate by Fructose-6-Phosphate Phosphoketolase from Acetobacter Xylinum. *J. Biol. Chem.* **1958**, *233* (6), 1283–1288.

(87) Diaz-Moralli, S.; Aguilar, E.; Marin, S.; Coy, J. F.; Dewerchin, M.; Antoniewicz, M. R.; Meca-Cortés, O.; Notebaert, L.; Ghesquière, B.; Eelen, G.; Thomson, T. M.; Carmeliet, P.; Cascante, M. A Key Role for Transketolase-like 1 in Tumor Metabolic Reprogramming. *Oncotarget* **2016**, *7* (32).

(88) Dhillon, A. S.; Hagan, S.; Rath, O.; Kolch, W. MAP Kinase Signalling Pathways in Cancer. *Oncogene* **2007**, *26* (22), 3279–3290.

(89) Pearson, G.; Robinson, F.; Beers Gibson, T.; Xu, B. E.; Karandikar, M.; Berman, K.; Cobb, M. H. Mitogen-Activated Protein (MAP) Kinase Pathways: Regulation and Physiological Functions. *Endocr. Rev.* **2001**, *22* (2), 153–183.

(90) Bos, J. L. Ras Oncogenes in Human Cancer : A Review Ras Oncogenes in Human Cancer. *Cancer Res.* **1989**, *49* (17), 4682–4689.

(91) Tsai, W. Bin; Aiba, I.; Long, Y.; Lin, H. K.; Feun, L.; Savaraj, N.; Kuo, M. T. Activation of Ras/PI3K/ERK Pathway Induces c-Myc Stabilization to Upregulate Argininosuccinate Synthetase, Leading to Arginine Deiminase Resistance in Melanoma Cells. *Cancer Res.* **2012**, *72* (10), 2622–2633.

(92) Gaglio, D.; Metallo, C. M.; Gameiro, P. A.; Hiller, K.; Danna, L. S.; Balestrieri, C.; Alberghina, L.; Stephanopoulos, G.; Chiaradonna, F. Oncogenic K-Ras Decouples Glucose and Glutamine Metabolism to Support Cancer Cell Growth. *Mol. Syst. Biol.* **2011**, *7*, 523.

(93) Son, J.; Lyssiotis, C. a; Ying, H.; Wang, X.; Hua, S.; Ligorio, M.; Perera, R. M.; Ferrone, C. R.; Mullarky, E.; Shyh-Chang, N.; Kang, Y.; Fleming, J. B.; Bardeesy, N.; Asara, J. M.; Haigis, M. C.; DePinho, R. a; Cantley, L. C.; Kimmelman, A. C. Glutamine Supports Pancreatic Cancer Growth through a KRAS-Regulated Metabolic Pathway. *Nature* **2013**, *496* (7443), 101–105.

(94) Sears, R.; Nuckolls, F.; Haura, E.; Taya, Y.; Tamai, K.; Nevins, J. R. Multiple Ras-Dependent Phosphorylation Pathways Regulate Myc Protein Stability. *Genes Dev.* **2000**,

14 (19), 2501–2514.

(95) Dang, C. V; Kim, J.; Gao, P.; Yustein, J. The Interplay between MYC and HIF in Cancer. *Nat. Rev. Cancer* **2008**, *8* (1), 51–56.

(96) Gao, P.; Tchernyshyov, I.; Chang, T.-C.; Lee, Y.-S.; Kita, K.; Ochi, T.; Zeller, K. I.; De Marzo, A. M.; Van Eyk, J. E.; Mendell, J. T.; Dang, C. V. C-Myc Suppression of MiR-23a/b Enhances Mitochondrial Glutaminase Expression and Glutamine Metabolism. *Nature* **2009**, *458* (7239), 762–765.

(97) Bott, A. J.; Peng, I. C.; Fan, Y.; Faubert, B.; Zhao, L.; Li, J.; Neidler, S.; Sun, Y.; Jaber, N.; Krokowski, D.; Lu, W.; Pan, J. A.; Powers, S.; Rabinowitz, J.; Hatzoglou, M.; Murphy, D. J.; Jones, R.; Wu, S.; Girnun, G.; et al. Oncogenic Myc Induces Expression of Glutamine Synthetase through Promoter Demethylation. *Cell Metab.* **2015**, *22* (6), 1068–1077.

(98) Liu, W.; Le, a.; Hancock, C.; Lane, a. N.; Dang, C. V.; Fan, T. W.-M.; Phang, J. M. Reprogramming of Proline and Glutamine Metabolism Contributes to the Proliferative and Metabolic Responses Regulated by Oncogenic Transcription Factor C-MYC. *Proc. Natl. Acad. Sci.* **2012**, *109* (23), 8983–8988.

(99) Polyak, K.; Xia, Y.; Zweier, J. L.; Kinzler, K. W.; Vogelstein, B. A Model for P53-Induced Apoptosis. *Nature* **1997**, *389* (6648), 300–305.

(100) Lewis, C. A.; Parker, S. J.; Fiske, B. P.; McCloskey, D.; Gui, D. Y.; Green, C. R.; Vokes, N. I.; Feist, A. M.; Vander Heiden, M. G.; Metallo, C. M. Tracing Compartmentalized NADPH Metabolism in the Cytosol and Mitochondria of Mammalian Cells. *Mol. Cell* **2014**, *55* (2), 253–263.

(101) Chen, W. W.; Freinkman, E.; Wang, T.; Birsoy, K.; Sabatini, D. M. Absolute Quantification of Matrix Metabolites Reveals the Dynamics of Mitochondrial Metabolism. *Cell* **2016**, *166* (5), 1324-1337.e11.

(102) Hosios, A. M.; Hecht, V. C.; Danai, L. V.; Johnson, M. O.; Rathmell, J. C.; Steinhauser, M. L.; Manalis, S. R.; Vander Heiden, M. G. Amino Acids Rather than Glucose Account for the Majority of Cell Mass in Proliferating Mammalian Cells. *Dev. Cell* **2016**, *36* (5), 540–549.

(103) Sullivan, L. B.; Gui, D. Y.; Hosios, A. M.; Bush, L. N.; Freinkman, E.; Vander Heiden, M. G. Supporting Aspartate Biosynthesis Is an Essential Function of Respiration in Proliferating Cells. *Cell* **2015**, *162* (3), 552–563.

(104) Birsoy, K.; Wang, T.; Chen, W. W.; Freinkman, E.; Abu-Remaileh, M.; Sabatini, D. M. An Essential Role of the Mitochondrial Electron Transport Chain in Cell Proliferation Is to Enable Aspartate Synthesis. *Cell* **2015**, *162* (3), 540–551.

(105) Davidson, S. M.; Papagiannakopoulos, T.; Olenchock, B. A.; Heyman, J. E.; Keibler, M. A.; Luengo, A.; Bauer, M. R.; Jha, A. K.; O'Brien, J. P.; Pierce, K. A.; Gui, D. Y.; Sullivan, L. B.; Wasylenko, T. M.; Subbaraj, L.; Chin, C. R.; Stephanopolous, G.; Mott, B. T.; Jacks, T.; Clish, C. B.; et al. Environment Impacts the Metabolic Dependencies of Ras-Driven Non-Small Cell Lung Cancer. *Cell Metab.* **2016**, *23* (3), 517–528.

(106) Garber, K. Cancer Anabolic Metabolism Inhibitors Move into Clinic. *Nat. Biotechnol.* **2016**, *34* (8), 794–795.

Dissecting Mammalian Cell Metabolism through ^{13}C- and ^{2}H-Isotope Tracing: Interpretations at the Molecular and Systems Levels

Chapter 3

Dissecting Mammalian Cell Metabolism through ^{13}C- and ^{2}H-Isotope Tracing: Interpretations at the Molecular and Systems Levels

Adapted from

Dong, W., Moon, S. J., Kelleher, J. K., & Stephanopoulos, G. Dissecting mammalian cell metabolism through 13C- and 2H-isotope tracing: Interpretations at the molecular and systems levels. ACS Ind. Eng. Chem. Res., 2019, 59(6), 2593-2610.

Conceptualization, W. Dong; Writing – ^{13}C isotopic tracers, W. Dong; Writing – ^{2}H isotopic tracers, S.J. Moon; Writing – ^{13}C-MFA, W. Dong; Software, W. Dong; Supervision, J.K. Kelleher and G. Stephanopoulos.

This work is published on ACS Industrial and Engineering Chemistry Research, 2019.

3.1 Abstract

Isotopic tracers have been widely used to probe specific pathways within metabolic networks. Tracers are metabolized through various metabolic routes, generating differential labeling patterns. Correct interpretations of the labeling data require understanding of atomic transitions of isotopes along biochemical reactions. Here, we review common ^{13}C- and ^{2}H-isotopic tracers used to investigate mammalian cell metabolism. Labeling patterns obtained from those tracers are presented and explained through stepwise tracking in the tricarboxylic acid (TCA) cycle, glycolysis, pentose phosphate pathway (PPP) and anaplerotic reactions. Metabolic insights regarding relative pathway activities and substrate utilization patterns are obtained by analyzing distinct enrichment profiles of metabolites. Finally, we introduce and demonstrate the use of ^{13}C-metabolic flux analysis (^{13}C-MFA) for deciphering complex metabolic networks at the systems level.

3.2 Introduction

Cellular metabolism consists of thousands of biochemical reactions. It is important to understand metabolism because it plays a vital role in cancer[1–3], type-2 diabetes[4–6], developmental biology[7–9], immunology[10–12] and other areas of biology[13,14]. However, the complex and dynamic nature of metabolic networks presents special challenges in the study of metabolism. As discussed in the overall introduction of this thesis, isotopic tracers and metabolic flux analysis play a significant role in deciphering the convoluted nature of biochemical networks. Although certain conclusions can be drawn by analyzing the labeling data alone, step-wise molecular tracking of the isotope transfer is necessary to interpret non-linear metabolic pathways. For those reaction networks that

exceed the capability of step-wise isotope tracking, metabolic flux analysis (MFA) provides a more reliable approach to quantitively dissect the system. As briefly described in Chapter 2.2, MFA relies on the pseudo-steady-state approximation that assumes constant levels of metabolite intermediates and isotopic labeling percentages over time. Under this condition, the metabolic fluxes stay invariant and can then be resolved by constrained optimizations. In short, MFA consolidates labeling data and extracellular flux measurements to estimate intracellular fluxes. The essential steps and detailed explanations of MFA are discussed in Chapter 4.6.

In this paper, we review common ^{13}C-and ^{2}H-isotopic tracers used to study mammalian cell metabolism, with a particular focus on interpreting isotopic labeling patterns. The transfer of isotopes along reaction pathways is depicted in detail through stepwise analysis. Chemical formulas are provided alongside the reactions for unambiguous representations of labeling profiles. Particularly for the TCA cycle, we systematically analyze labeling patterns generated by U-$^{13}C_6$-, 1-^{13}C-, 1,6-$^{13}C_2$-glucose, U-$^{13}C_5$-, 1-^{13}C-, 5-^{13}C-glutamine and 1,2-$^{13}C_2$-acetate. Moreover, several anaplerotic reactions are included in the analysis to account for their prevalence in mammalian cell metabolism. In addition, the complex series of reactions in the PPP and glycolysis are thoroughly dissected by 1,2-$^{13}C_2$-, 2-^{13}C- and 3-^{13}C-glucose, and the resulting labeling patterns are explained by simultaneous tracking of multiple tracer molecules. As for systems-level interpretations of labeling data, we present a brief case study using ^{13}C-MFA and demonstrate the capability of this approach to generate metabolic insights that are otherwise difficult to obtain through regular isotopic labeling analysis.

3.3 Glucose-driven TCA cycle probed by U-$^{13}C_6$-glucose

U-$^{13}C_6$-glucose is one of the most commonly used isotopic tracers to investigate the TCA cycle[24–26]. Due to the cyclic nature of this pathway as well as the presence of multiple anaplerotic reactions, the labeling results are usually complex and a stepwise analysis is recommended to deconvolute the patterns. To analyze the series of cyclic reactions in a systematic manner, we artificially break the cycles into multiple rounds, each separated at the step of citrate synthase (CS).

A simplified view of the TCA cycle metabolism involves the pyruvate dehydrogenase (PDH) reaction as the only inward flux to the cycle (Figure 3.1a). In this reaction scheme, cells cultured in U-$^{13}C_6$-glucose generate metabolites carrying two ^{13}C atoms (M+2) following one round of the TCA cycle (Figure 3.1b). It is worth noting that the positional labeling patterns of ^{13}C atoms are scrambled in succinate, fumarate, malate and oxaloacetate. Since succinate and fumarate are molecularly symmetrical, the scrambling effects are shown only for malate and oxaloacetate (Figure 3.1b). The second round of the TCA cycle produces all four ^{13}C-isotopomers of M+3 oxaloacetate (Figure 3.1c-d). Next, two of the M+3 oxaloacetate isotopomers generate fully labeled M+4 species (Figure 3.1e-f). The remaining two produce M+3 oxaloacetate again, keeping the labeling state of oxaloacetate at M+3 by the end of the third round (Figure 3.1g-h). The complete labeling patterns of oxaloacetate beyond three rounds of TCA cycling are summarized in Table 3.1.

In addition to PDH, there are three additional anaplerotic reactions that complicate isotopic labeling patterns in the TCA cycle. The pyruvate carboxylase (PC) reaction extends the end of a pyruvate molecule by a carboxyl group. This step retains all ^{13}C atoms during pyruvate

entry into the TCA cycle, and generates M+3 oxaloacetate, malate, fumarate and succinate after the first round of TCA cycling (Figure 3.2a-b). Depending on the actual directionality of the reactions catalyzed by α-ketoglutarate dehydrogenase (OGDC) and isocitrate dehydrogenase (IDH), which have been historically deemed as irreversible steps, M+3 α-ketoglutarate and citrate can also be produced (Figure 3.2b-c). Conversely, the malic enzyme (ME) reaction is effectively the reverse of the PC reaction, generating pyruvate from malate through a decarboxylation step (Figure 3.2d). In a simplified scenario where only PDH and ME reactions are contributing to the TCA cycle, M+1 and M+2 pyruvate isotopomers are produced by the ME reaction after the first round of cycling (Figure 3.2e). Additionally, phosphoenolpyruvate carboxykinase (PEPCK) also catalyzes the decarboxylation reaction which transforms oxaloacetate to phosphoenolpyruvate (PEP) (Figure 3.2f). Through glycolysis, PEP is metabolized to pyruvate, conserving the ^{13}C-labeling pattern. Therefore, the PEPCK reaction is equivalent to the ME reaction in terms of altering labeling patterns in the TCA cycle (Figure 3.2g). For subsequent analysis involving multiple anaplerotic reactions, the PEPCK reaction is treated indistinguishably from the ME reaction.

When PC, ME and PEPCK reactions are all present in addition to the PDH reaction, the labeling patterns of TCA cycle intermediates by U-$^{13}C_6$-glucose become intricate. In order to analyze each round systematically, we treat those anaplerotic reactions as if they proceeded in a stepwise fashion. For each round, the PDH reaction is allowed to progress first (Figure 3.3a), followed by the reversible scrambling reactions among oxaloacetate, malate, fumarate and succinate. Lastly, the PC and ME/PEPCK reactions conclude the round that stops before going through the PDH reaction again (Figure 3.3b). The second round then proceeds based on the available isotopomers of oxaloacetate and pyruvate generated in the previous cycle (Figure 3.3c).

Compared to the simplified view of the TCA cycle with PDH as the only contributing reaction (Figure 3.1), a more complex metabolic network with PDH, PC and ME/PEPCK reactions is able to produce additional forms of isotopomers at each round (Figure 3.3d). At the end of the second round, all possible isotopomers of succinate, fumarate, oxaloacetate and AcCoA are generated (Figure 3.3c). Thus, at the beginning of the third round, all forms of citrate isotopomers can be produced. As citrate contains the most carbon atoms among all TCA cycle intermediates, all isotopomeric forms of TCA cycle metabolites can be derived within three rounds of TCA cycling, in the presence of PDH, PC and ME/PEPCK reactions.

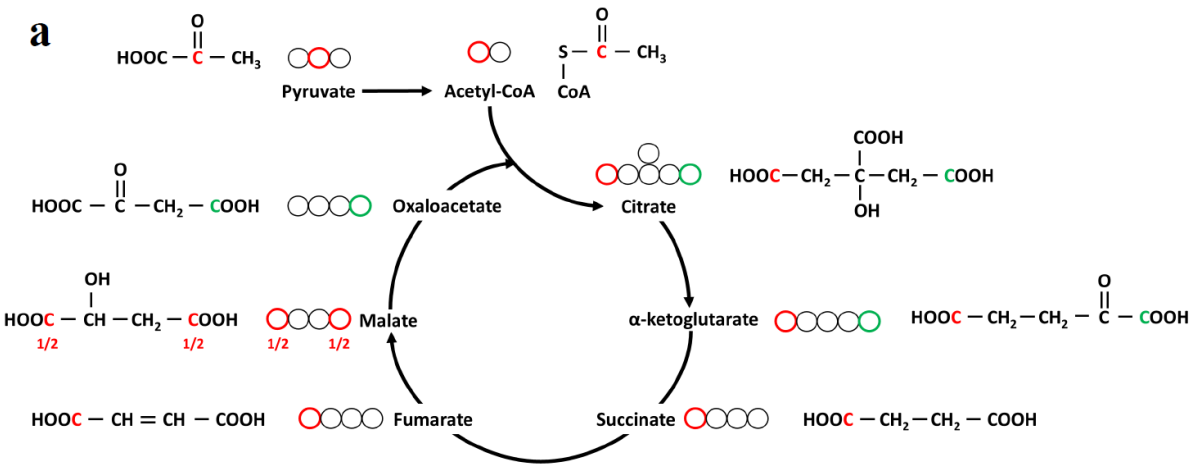

Figure 3.1 a. Chemical structures of TCA cycle metabolites and carbon transition maps highlighting the positional information through reactions. Circles represent carbon atoms with the same position as referenced to the actual chemical structures of the metabolites. Carbon atoms highlighted in red and green indicate how AcCoA is combined with oxaloacetate through citrate synthase (CS) to make citrate. Note that only the green-labeled carbon is lost through α-

ketoglutarate dehydrogenase, due to the fact that aconitase removes and then adds back the water molecule only on the pro-R arm of citrate.

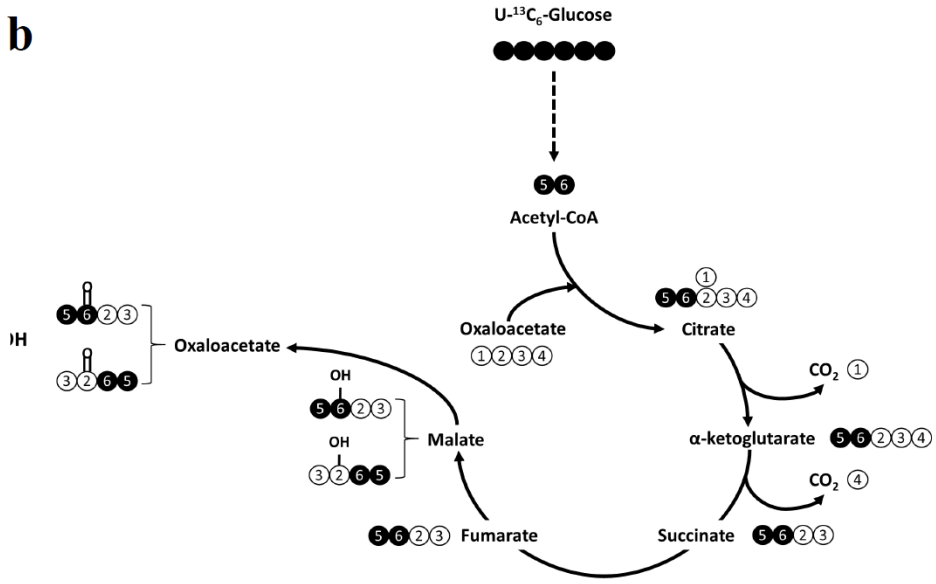

Figure 3.1 b. Labeling results of TCA cycle intermediates after the first round of cycling. The first round generates 1,2- and 3,4-$^{13}C_2$-oxaloacetate.

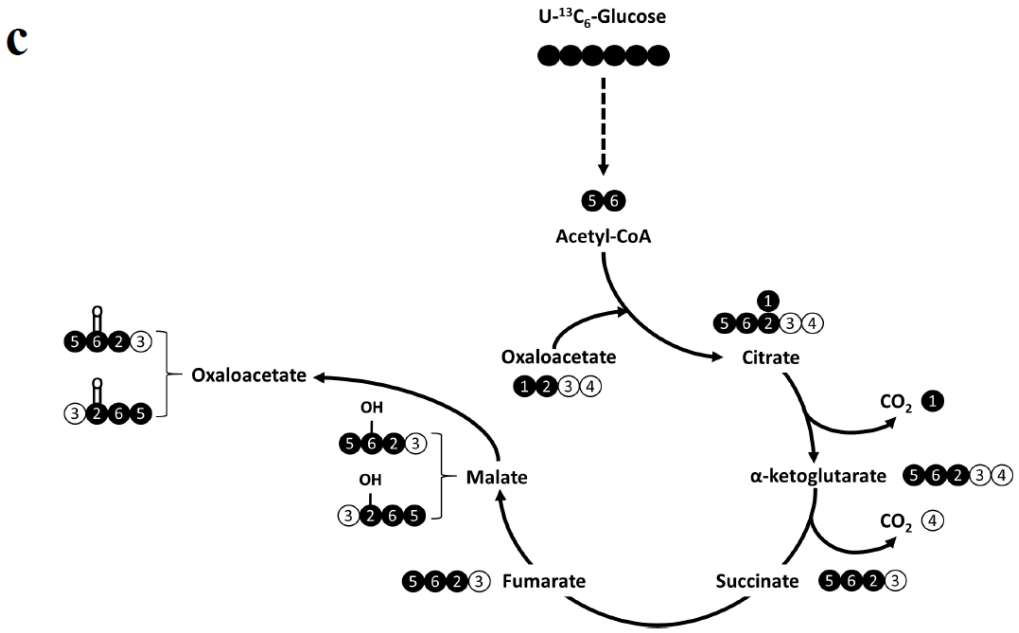

Figure 3.1 c. Labeling results of TCA cycle intermediates after the second round of cycling by 1,2-$^{13}C_2$-oxaloacetate. This second round generates 1,2,3- and 2,3,4-$^{13}C_3$-oxaloacetate.

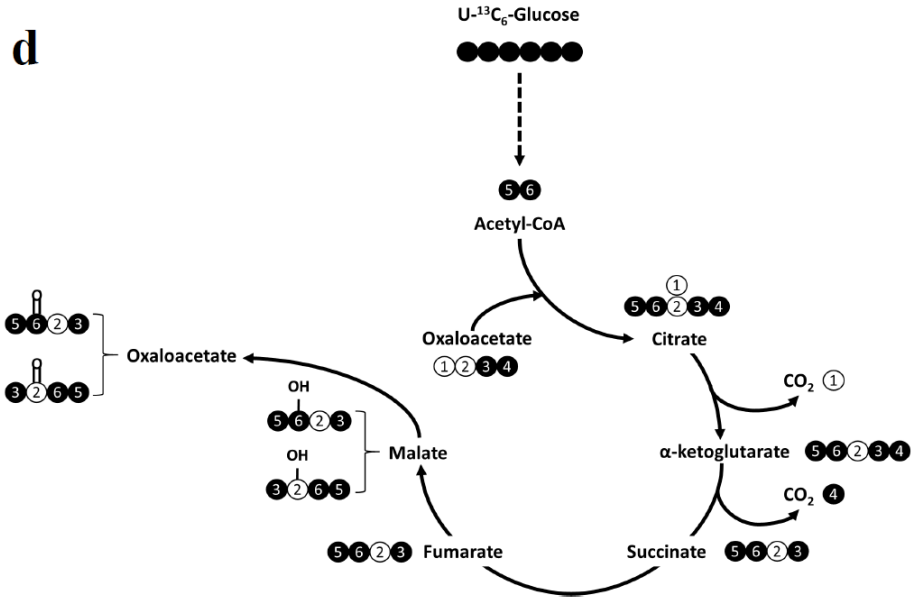

Figure 3.1 d. Labeling results of TCA cycle intermediates after the second round of cycling by 3,4-$^{13}C_2$-oxaloacetate. This second round generates 1,2,4- and 1,3,4-$^{13}C_3$-oxaloacetate.

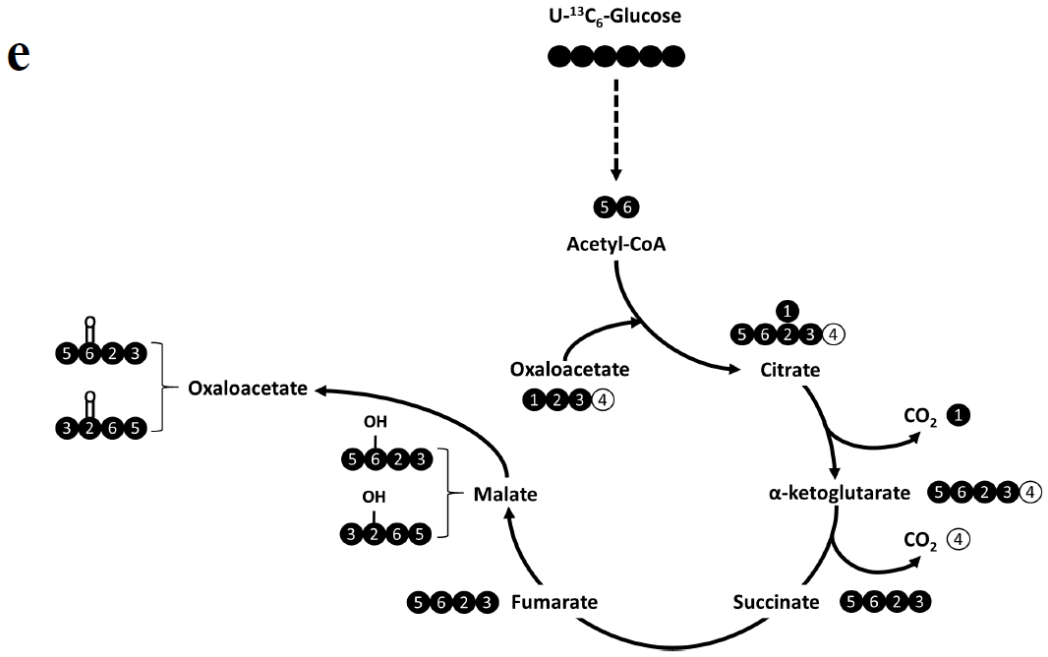

Figure 3.1 e. Labeling results of TCA cycle intermediates after the third round of cycling by 1,2,3-$^{13}C_3$-oxaloacetate. This third round generates fully labeled U-$^{13}C_4$-oxaloacetate.

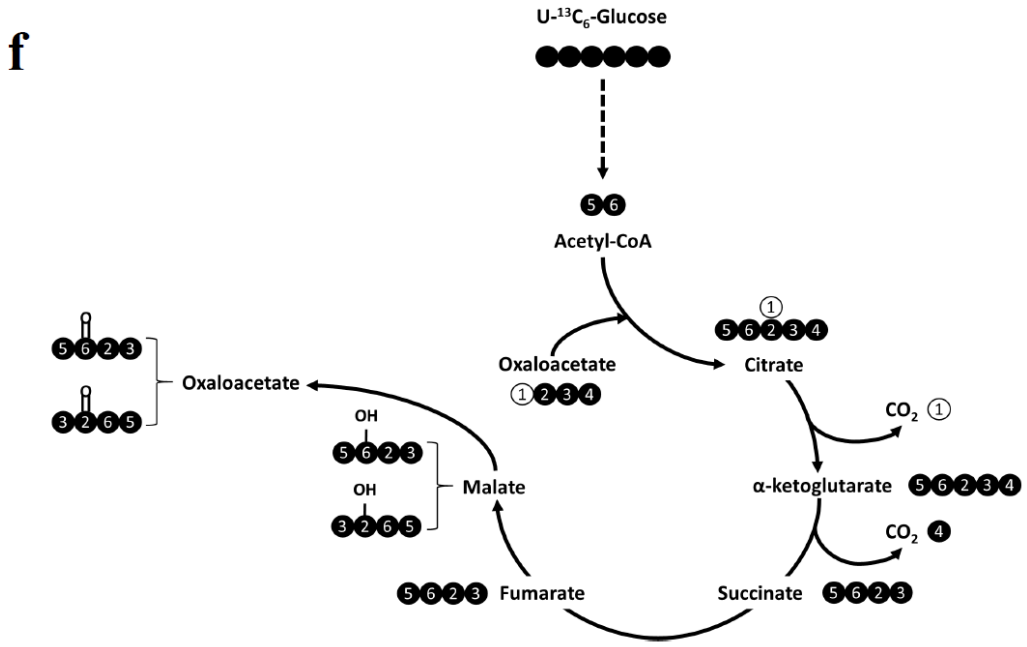

Figure 3.1 f. Labeling results of TCA cycle intermediates after the third round of cycling by 2,3,4-$^{13}C_3$-oxaloacetate. This third round generates fully labeled U-$^{13}C_4$-oxaloacetate.

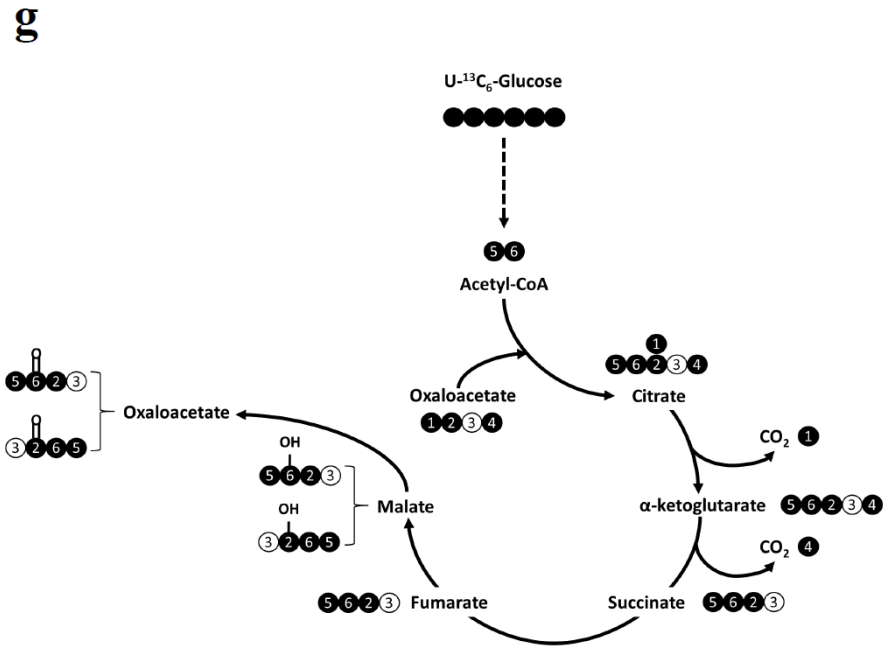

Figure 3.1 g. Labeling results of TCA cycle intermediates after the third round of cycling by 1,2,4-$^{13}C_3$-oxaloacetate. This third round generates 1,2,3- and 2,3,4-$^{13}C_3$-oxaloacetate.

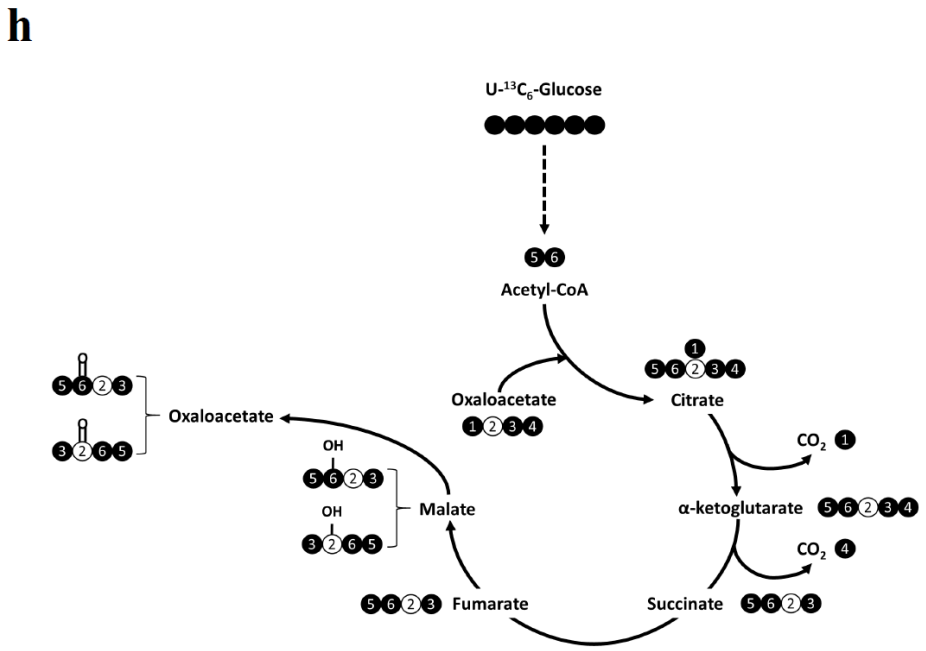

Figure 3.1 h. Labeling results of TCA cycle intermediates after the third round of cycling by 1,3,4-$^{13}C_3$-oxaloacetate. This third round generates 1,2,4- and 1,3,4-$^{13}C_3$-oxaloacetate.

Carbon number is ordered consistent with the atomic sequence as shown in **a**, and is associated with the same carbon throughout the diagram for the purpose of tracing, rather than following IUPAC naming rules. Oxaloacetate: 1, carboxyl; 2, carbonyl; 3, methylene bridge; 4, carboxyl. AcCoA: 5, carbonyl; 6, methyl. Scrambling of labeling results is shown for malate and oxaloacetate, but not for fumarate and succinate due to molecular symmetry. Hydroxyl and carbonyl groups are drawn in malate and oxaloacetate, respectively. Filled and empty circles refer to ^{13}C- and ^{12}C-labeled carbon atoms, respectively. Solid and dashed arrows refer to single- or multi-step reactions, respectively.

Table 3.1. Labeling patterns of oxaloacetate by U-$^{13}C_6$-glucose at each round of the TCA cycle with PDH as the only contributing reaction.

Each round is defined by the citrate synthase (CS) reaction as the boundary. Results are obtained based on the assumption that each round consumes all available isotopomers generated from the previous round, and the resulting products are the only available species beginning the next cycle. The darkness of gray color suggests the abundance of the associated isotopomer. $n \geq 3$.

Isotopomer	Round 1	Round 2	Round 3	Round 4	Round 5	Round 6	Round n
M+0	100%	0	0	0	0	0	0
M+1	0	0	0	0	0	0	0
M+2	0	100%	0	0	0	0	0
M+3	0	0	100%	50%	25%	12.5%	$(0.5)^{(n-3)}\times100\%$
M+4	0	0	0	50%	75%	87.5%	$1-(0.5)^{(n-3)}\times100\%$

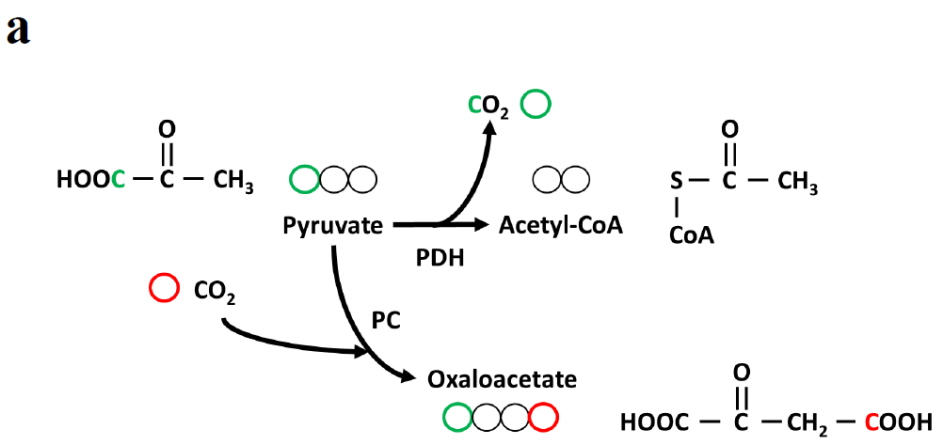

Figure 3.2 a. Chemical structures and carbon transition maps highlighting the positional information through the PC reaction. Circles represent carbon atoms with the same position as referenced to the actual chemical structures of the metabolites. Carbon atoms highlighted in red indicate how CO_2 is combined with pyruvate through the PC reaction to make oxaloacetate. Carbon atoms highlighted in green indicate how the carboxyl group in pyruvate is cleaved through the PDH reaction to make AcCoA.

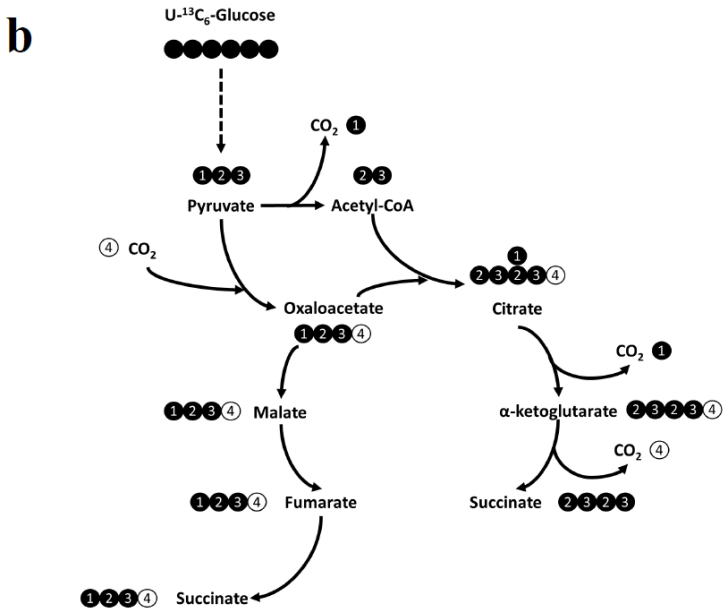

Figure 3.2 b. Labeling results of TCA cycle intermediates within the first round of cycling with both PDH and PC reactions, assuming the PC flux cannot reverse the entire TCA cycle but dominates the labeling patterns along the reversible reactions within the cycle.

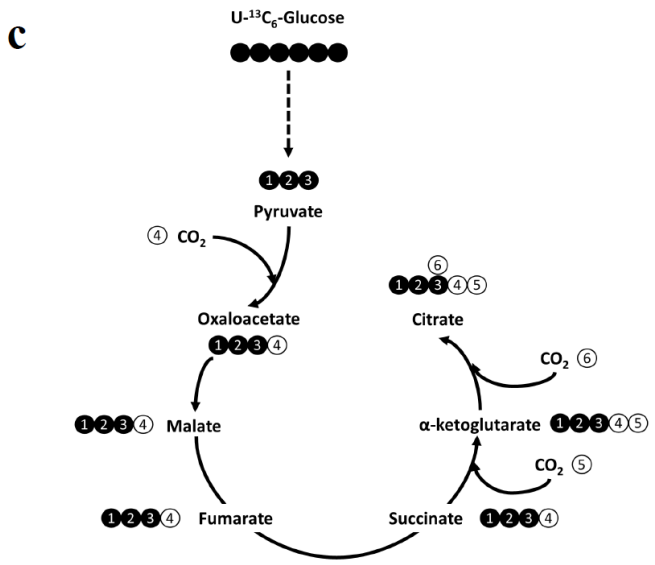

Figure 3.2 c. Labeling results of TCA cycle intermediates within the first round of cycling with both PDH and PC reactions, assuming the PC flux totally reverses and dominates the entire TCA cycle.

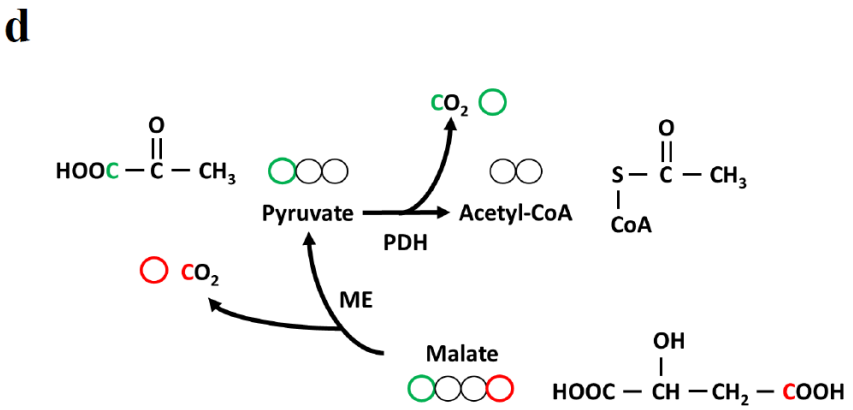

Figure 3.2 d. Chemical structures and carbon transition maps highlighting the positional information through the ME reaction. Circles represent carbon atoms with the same position as referenced to the actual chemical structures of the metabolites. Carbon atoms highlighted in red indicate how the carboxyl group in malate is cleaved through the ME reaction to make pyruvate. Carbon atoms highlighted in green indicate how the carboxyl group in pyruvate is cleaved through the PDH reaction to make AcCoA.

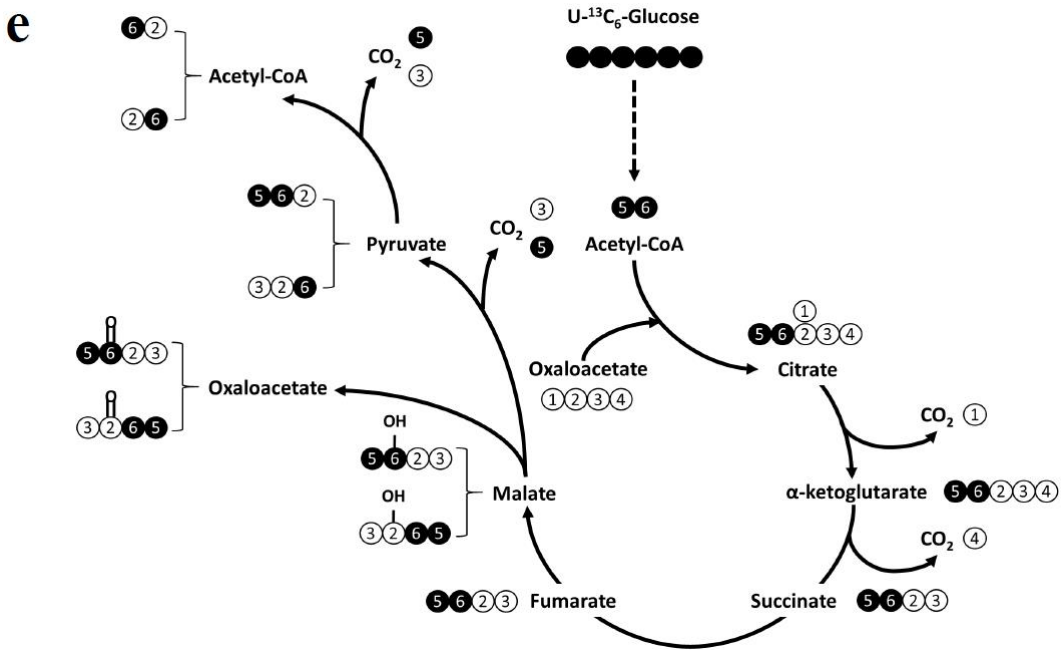

Figure 3.2 e. Labeling results of TCA cycle intermediates within the first round of cycling with both PDH and ME reactions.

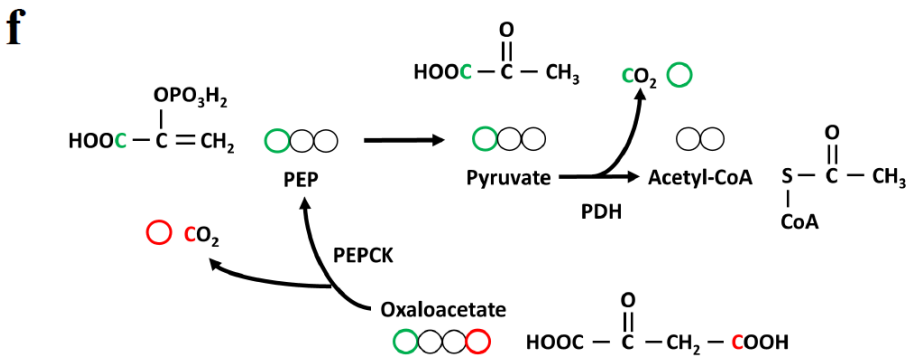

Figure 3.2 f. Chemical structures and carbon transition maps highlighting the positional information through the PEPCK reaction. Circles represent carbon atoms with the same position as referenced to the actual chemical structures of the metabolites. Carbon atoms highlighted in red indicate how the carboxyl group in oxaloacetate is cleaved through PEPCK reaction to make PEP. Carbon atoms highlighted in green indicate how the carboxyl group in pyruvate is cleaved through the PDH reaction to make AcCoA.

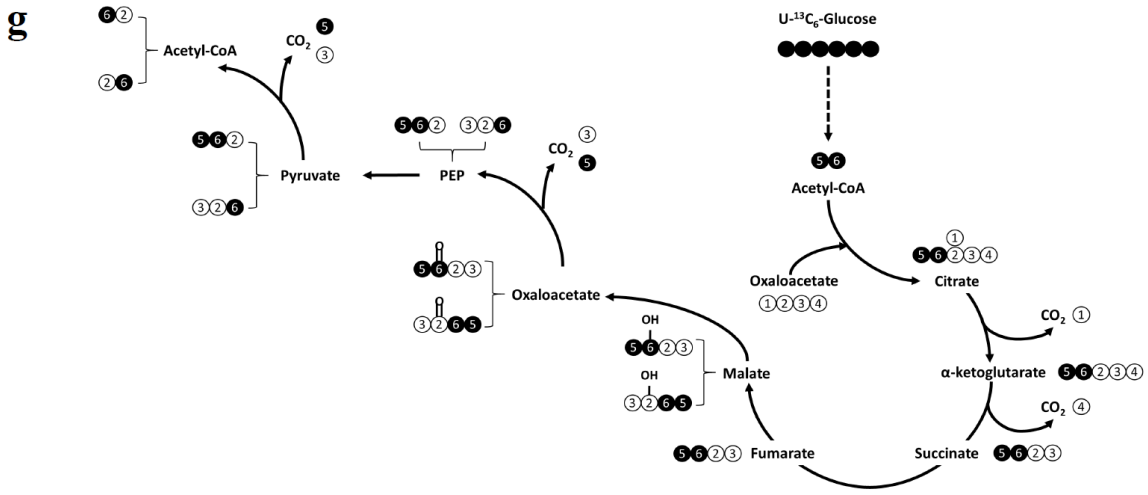

Figure 3.2 g. Labeling results of TCA cycle intermediates within the first round of cycling with both PDH and PEPCK reactions.

Carbon number is ordered consistent with the atomic sequence as shown in **a, d** and **f**, and is associated with the same carbon throughout the diagram for the purpose of tracing, rather than following IUPAC naming rules. Pyruvate: 1, carboxyl; 2, carbonyl; 3, methyl. Oxaloacetate: 1, carboxyl; 2, carbonyl; 3, methylene bridge; 4, carboxyl. AcCoA: 5, carbonyl; 6, methyl. Carbon scrambling effects in oxaloacetate and malate are not shown, but are included in Figure 3. Filled and empty circles refer to ^{13}C- and ^{12}C-labeled carbon atoms, respectively. Solid and dashed arrows refer to single- or multi-step reactions, respectively.

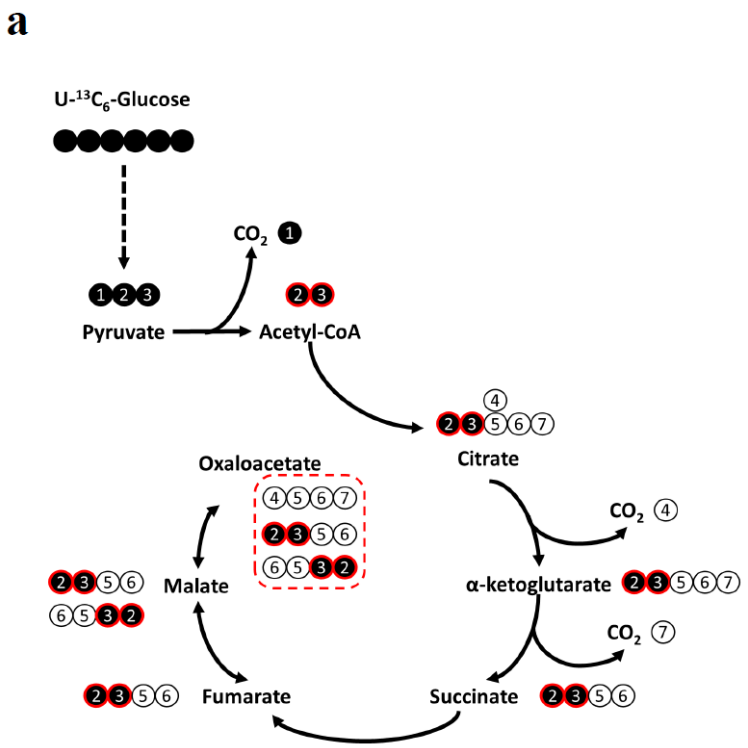

Figure 3.3 a. Labeling patterns of TCA cycle intermediates after the first round of PDH cycling.

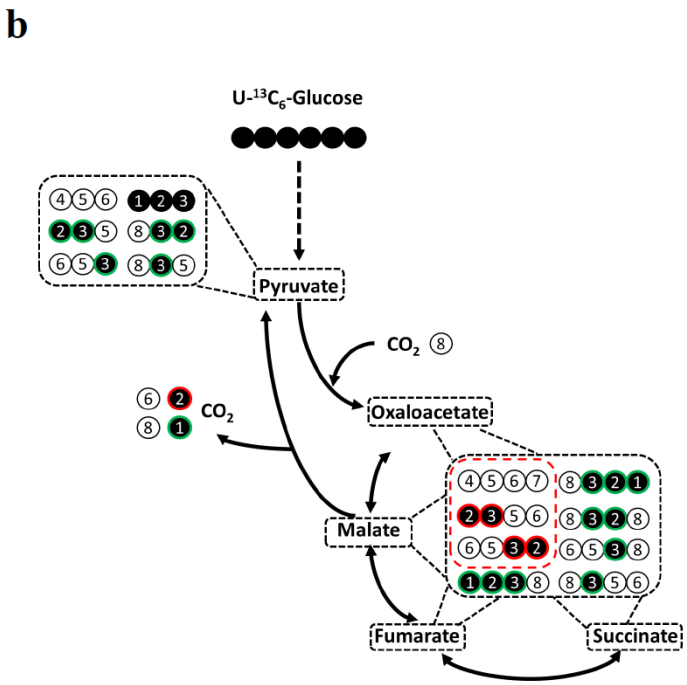

Figure 3.3 b. Alterations of labeling patterns by PC, ME/PEPCK and the reversible scrambling reactions among oxaloacetate, malate, fumarate and succinate during the first round of cycling.

The isotopomers in the red box are from the first round of PDH cycling. For example, isotopomer 8-3-2-8 (M+2 malate/oxaloacetate) is formed by the following series of reactions: tracer-derived 1-2-3 (M+3 pyruvate) is converted by PC to 1-2-3-8 (M+3 malate/oxaloacetate); isotopomer 1-2-3-8 (M+3 malate/oxaloacetate) is inverted to 8-3-2-1 (M+3 malate/oxaloacetate) by reversible scrambling reactions and molecular symmetry; isotopomer 8-3-2-1 (M+3 malate/oxaloacetate) is converted by ME/PEPCK to 8-3-2 (M+2 pyruvate); isotopomer 8-3-2 (M+2 pyruvate) is converted by PC to 8-3-2-8 (M+2 malate/oxaloacetate).

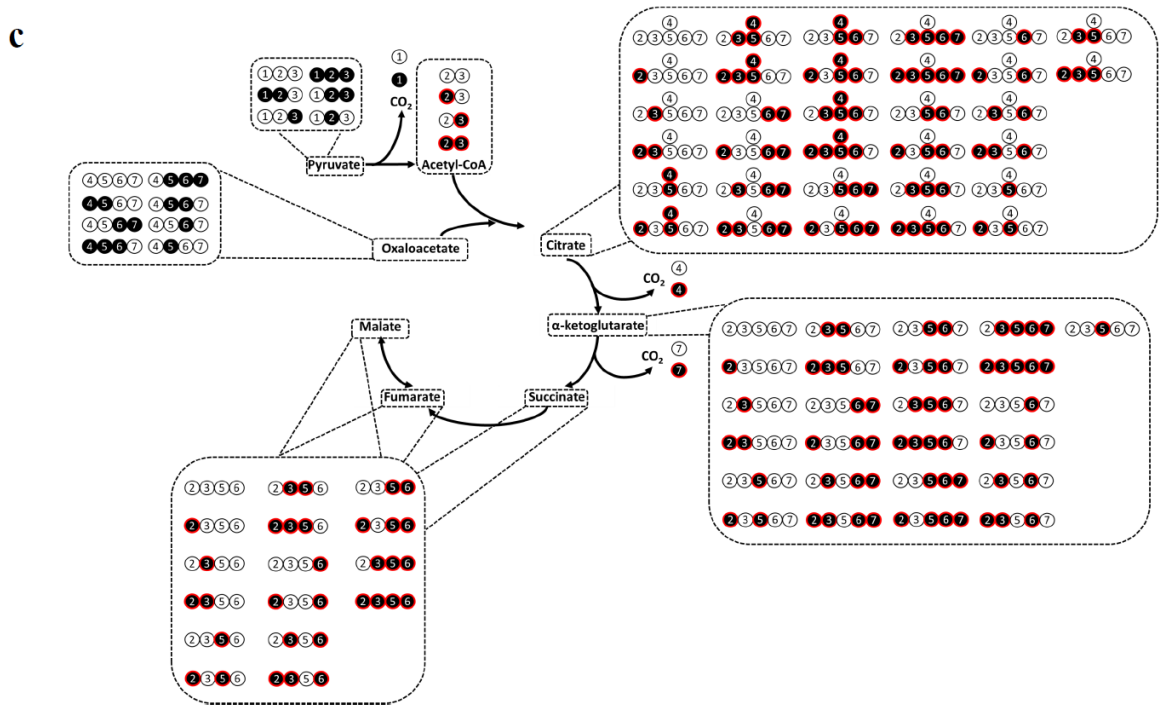

Figure 3.3 c. Labeling patterns of TCA cycle intermediates after the second round of PDH cycling, based on available isotopomers of oxaloacetate and pyruvate from the previous round.

Carbon number is ordered consistent with the atomic sequence as shown in Figure 1a, and is associated with the same carbon throughout the diagram for the purpose of tracing, rather than following IUPAC naming rules. **a**, Pyruvate: 1, carboxyl; 2, carbonyl; 3, methyl. Oxaloacetate: 4, carboxyl; 5, carbonyl; 6, methylene bridge; 7, carboxyl. Filled and empty circles refer to ^{13}C- and ^{12}C-labeled carbon atoms, respectively. ^{13}C-carbon atoms highlighted in red track PDH-derived isotopomers. ^{13}C-carbon atoms highlighted in green track the isotopomers derived from PC, ME/PEPCK and the reversible scrambling reactions. ^{13}C-carbon atoms without highlighted colors indicate initial set of isotopomers to begin a cycle. Note that the unlabeled isotopomer is

always available and is included prior to the initial set. Solid and dashed arrows refer to single- or multi-step reactions, respectively.

3.4 Glutamine-driven TCA cycle probed by U-$^{13}C_5$-, 1-^{13}C- and 5-^{13}C-glutamine

Although glucose is usually the most highly consumed carbon substrate, the vital role of glutamine anaplerosis has also been reported in literature[19,27–29]. Glutamate can be produced from glutamine through glutaminase and is then further deaminated or transaminated to yield α-ketoglutarate. At this point, there are two types of metabolism following different directions of the TCA cycle. The oxidative metabolism of α-ketoglutarate generates succinate and turns the TCA cycle in the canonical way (Figure 3.4a), producing nicotinamide adenine dinucleotide (NADH) and flavin adenine dinucleotide ($FADH_2$). Alternatively, through the reversal of the IDH reaction, α-ketoglutarate can be reductively carboxylated to make citrate, which can be used to fuel *de novo* lipogenesis in cytosol[19].

To distinguish these two types of metabolism, U-$^{13}C_5$-glutamine can be used to generate distinct labeling patterns of TCA cycle intermediates. Similar to the analysis of U-$^{13}C_6$-glucose, turns of the TCA cycle are artificially broken into rounds, each separated at the step of OGDC (Figure 4b-f). The oxidative route yields M+4 labeled TCA cycle metabolites except for M+5 α-ketoglutarate after the first round (Figure 3.4b), with PDH being the only additional contributing reaction. In contrast, the reductive metabolism of glutamine retains all ^{13}C atoms from U-$^{13}C_5$-glutamine, yielding M+5 citrate and M+3 oxaloacetate, malate and fumarate (Figure 3.4c). If the contribution from glutamine anaplerosis is large relative to that of the PDH reaction, these labeling patterns (Figure 3.4) will dominate those from PDH (Table 3.2; Figure 3.5-6).

Therefore, the ratio of percentages of M+5 to M+4 citrate, or that of M+3 to M+4 oxaloacetate, malate and fumarate indicate the relative magnitudes of reductive to oxidative metabolism of glutamine.

However, following the same type of cyclic analysis as for U-$^{13}C_6$-glucose, M+2 and M+3 succinate, fumarate, malate and oxaloacetate can also be generated in the presence of PC and ME/PEPCK reactions (Figure 3.4d). Furthermore, all isotopomeric forms of oxaloacetate and AcCoA are produced by the end of the third round, which suggests that all isotopomers of TCA cycle intermediates are available after the fourth round of cycling (Figure 3.4f). Since these additional anaplerotic reactions are able to generate more isotopomeric forms of pyruvate, the resulting citrate molecules exhibit labeling states of M+2 through M+6 even after the first round (Figure 3.4d). Those divergent labeling results (Figure 3.4d-f) could undermine the validity of the aforementioned MID analysis since both the reductive and oxidative routes can generate M+5 citrate as well as M+3 oxaloacetate, malate and fumarate within one round of TCA cycling (Figure 3.4d).

As an alternative for U-$^{13}C_5$-glutamine, the use of 1-(carboxyl)-^{13}C-glutamine can improve the ability to compare the relative magnitudes of those two types of glutamine metabolism. If the α-ketoglutarate molecule derived from 1-(carboxyl)-^{13}C-glutamine is committed to the oxidative TCA cycle, the ^{13}C-carboxyl group adjacent to the carbonyl group is lost in the form of CO_2 though OGDC, and the entire TCA cycle is unlabeled (Figure 3.7a). Importantly, the scrambling reactions such as ME and PC/PEPCK reactions do not alter the labeling patterns since none of the TCA cycle intermediates besides α-ketoglutarate contains ^{13}C atoms. The reductive pathway, however, combines an unlabeled carbon from CO_2 with M+1 α-ketoglutarate and produces M+1 citrate, which is then converted to M+1 oxaloacetate, malate

and fumarate (Figure 3.7b). Therefore, the emergence of M+1 TCA cycle intermediates from 1-(carboxyl)-^{13}C-glutamine strongly indicates the presence of reductive metabolism of glutamine through the IDH reaction, whereas the labeling percentage of M+0 isotopomers indicates the strength of the oxidative TCA cycle.

Similar to 1-(carboxyl)-^{13}C-glutamine, the tracer 5-(amine)-^{13}C-glutamine also generates differential labeling patterns of TCA cycle intermediates along the two types of glutamine metabolism. Following the oxidative pathway, the M+1 labeling pattern from the tracer is retained through the TCA cycle, resulting in M+1 isotopomers for all TCA cycle metabolites (Figure 3.7c). Even with ME and PC/PEPCK reactions, the labeling patterns are unaffected since these anaplerotic reactions cannot generate additional isotopomers based on the M+1 isotopomers of malate and oxaloacetate (Figure 3.7d). Moreover, the M+1 α-ketoglutarate generated after the first round of the TCA cycle harbors the ^{13}C atom at the carboxyl group adjacent to the carbonyl group, so the second round of the cycle is ready to deplete any remaining ^{13}C atoms through the step of OGDC. Therefore, M+1 is the only labeling state for all TCA cycle intermediates through oxidative metabolism of 5-(amine)-^{13}C-glutamine. In contrast, when the reductive route is present, the M+1 labeling state is retained only in α-ketoglutarate and citrate, as the ATP-citrate lyase (ACLY) reaction splits M+1 citrate into M+1 AcCoA and unlabeled oxaloacetate, which produces unlabeled malate and fumarate (Figure 3.7e). Therefore, the emergence of M+1 oxaloacetate, malate and fumarate from 5-(amine)-^{13}C-glutamine suggests the existence of oxidative TCA cycling, whereas the labeling percentage of M+0 isotopomers indicates the strength of the reductive pathway. In addition, the oxidative pathway generates citrate isotopomers that contain no ^{13}C atoms on its pro-S arm (Figure 3.7d), so the resulting AcCoA through ACLY is unlabeled. Through *de novo* lipogenesis, no ^{13}C-labeled fatty

acids can be produced. However, the reductive metabolism of 5-(amine)-^{13}C-glutamine yields M+1 citrate harboring ^{13}C-carboxyl group on the pro-S arm, resulting in the generation of M+1 AcCoA which further labels fatty acids by ^{13}C atoms (Figure 3.7e). Thus, the emergence of ^{13}C-labeled fatty acids from 5-(amine)-^{13}C-glutamine indicates the presence of reductive metabolism of glutamine, whereas the percentage of unlabeled fatty acids indicates the strength of the oxidative TCA cycle.

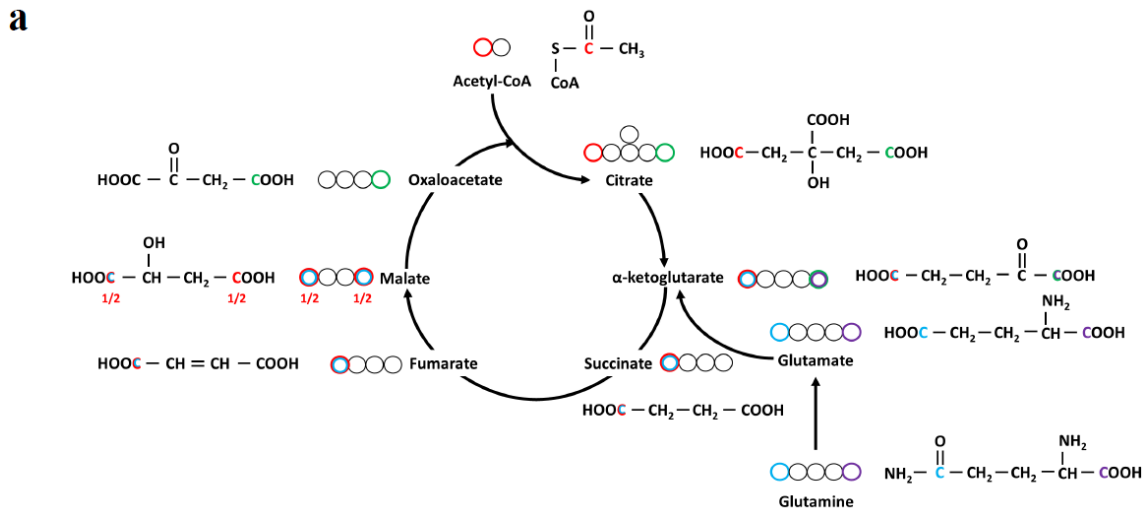

Figure 3.4 a. Labeling patterns of TCA cycle intermediates by U-$^{13}C_5$-glutamine through glutamine anaplerosis.

Chemical structures of TCA cycle metabolites and carbon transition maps highlighting the positional information through glutamine anaplerosis. Circles represent carbon atoms with the same position as referenced to the actual chemical structures of the metabolites. Carbon atoms highlighted in red and green indicate how AcCoA is combined with oxaloacetate through CS to make citrate. Carbon atoms highlighted in blue track the retention of amine-carbon through the TCA cycle. Carbon atoms highlighted in purple track the loss of carboxyl-carbon through α-ketoglutarate dehydrogenase (OGDC).

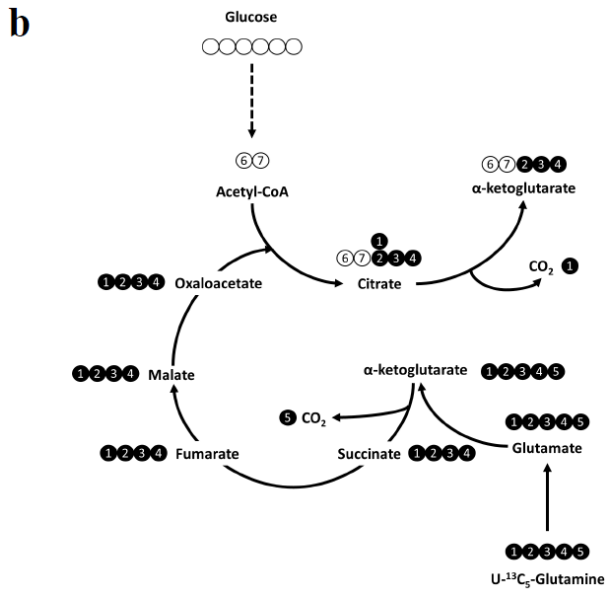

Figure 3.4 b. Labeling patterns of TCA cycle intermediates within the first round of oxidative cycling in the presence of both PDH and glutamine anaplerosis.

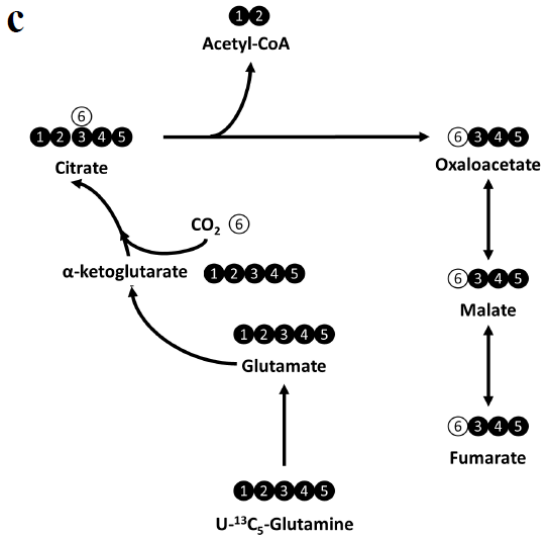

Figure 3.4 c. Labeling patterns of TCA cycle intermediates through reductive glutamine metabolism.

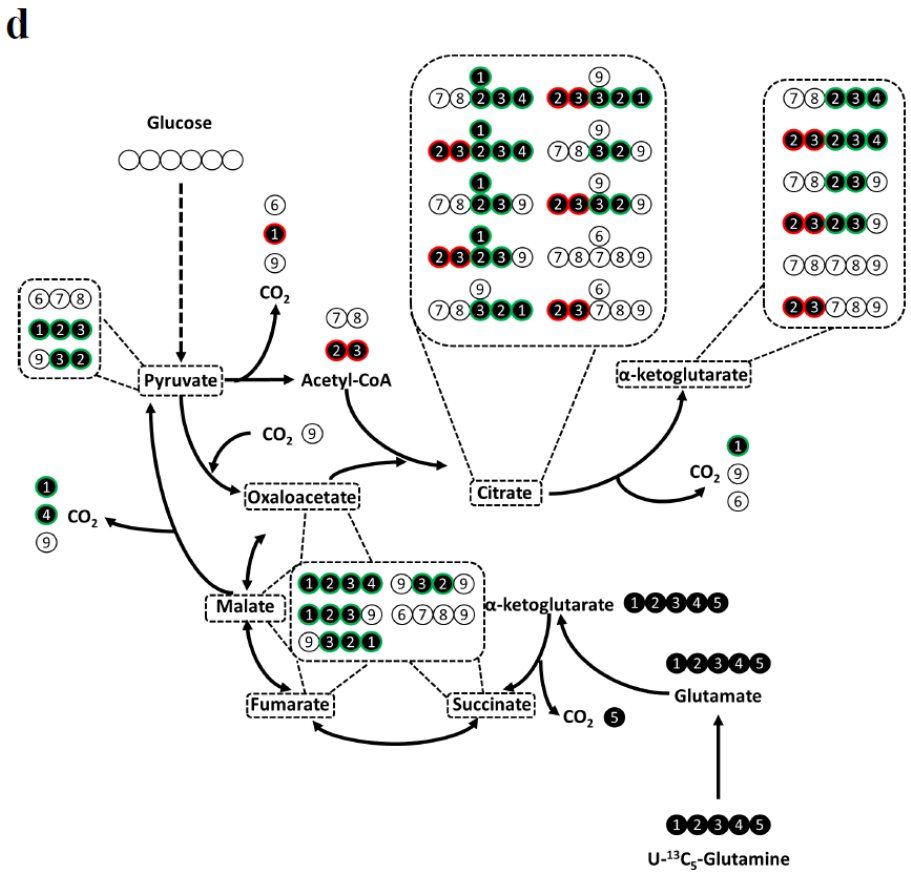

Figure 3.4 d. Alterations of labeling patterns by PC, ME/PEPCK and the reversible scrambling reactions among oxaloacetate, malate, fumarate and succinate during the first round of cycling.

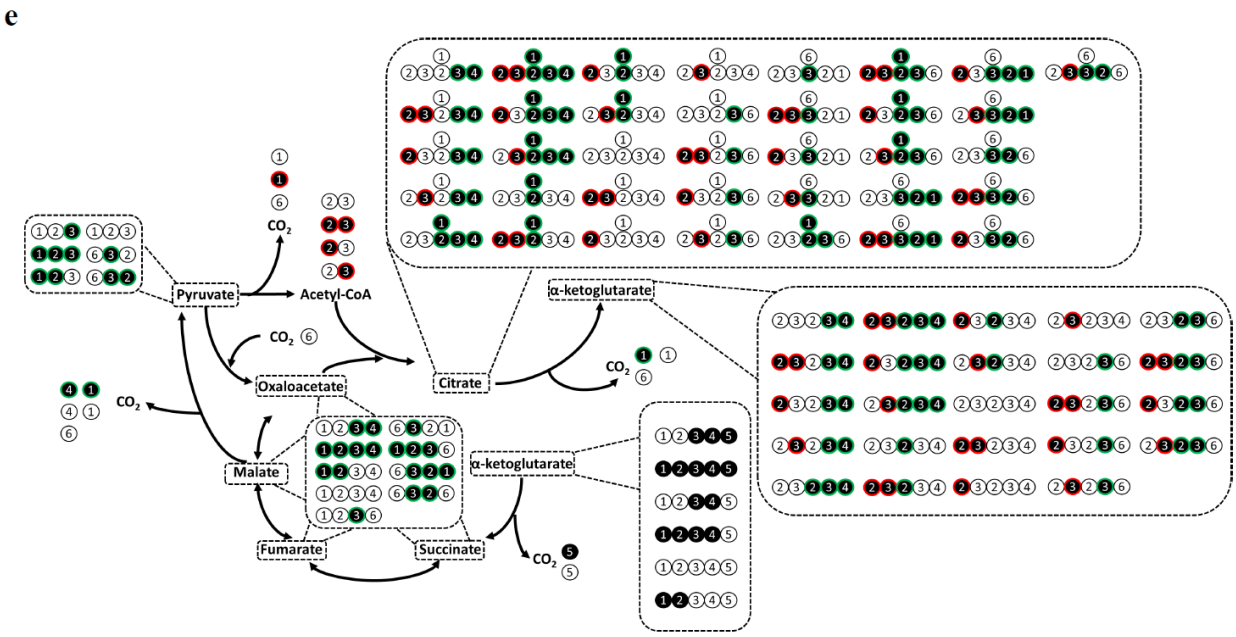

Figure 3.4 e. Labeling patterns of TCA cycle intermediates after the second round of oxidative cycling, based on available isotopomers of α-ketoglutarate from the previous round.

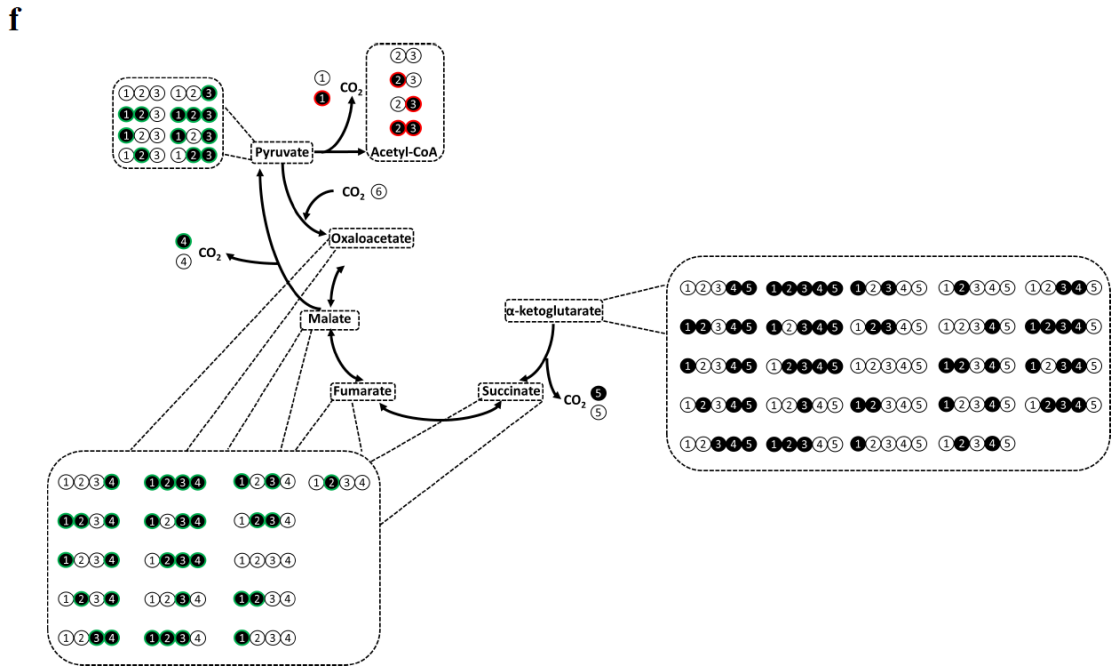

Figure 3.4 f. Labeling patterns of TCA cycle intermediates after the third round of oxidative cycling, based on available isotopomers of α-ketoglutarate from the previous round. Note that all

isotopomeric forms of oxaloacetate and AcCoA have been generated through the progression of α-ketoglutarate in the presence of PC and ME/PEPCK reactions.

Carbon number is ordered consistent with the atomic sequence as shown in **a**, and is associated with the same carbon throughout the diagram for the purpose of tracing, rather than following IUPAC naming rules. Glutamine: 1, amine; 5, carboxyl. Filled and empty circles refer to ^{13}C- and ^{12}C-labeled carbon atoms, respectively. ^{13}C-carbon atoms highlighted in red track PDH-derived isotopomers. ^{13}C-carbon atoms highlighted in green track the isotopomers derived from PC, ME/PEPCK and the reversible scrambling reactions. ^{13}C-carbon atoms without highlighted colors indicate initial set of isotopomers to begin a cycle. Note that the unlabeled isotopomer is always available and is included prior to the initial set. Solid and dashed arrows refer to single- or multi-step reactions, respectively. Turns of the TCA cycle are artificially broken into rounds, each separated at the step of α-ketoglutarate dehydrogenase (OGDC).

Table 3.2. Labeling patterns of oxaloacetate at each round by U-$^{13}C_5$-glutamine dominated by PDH that supplies unlabeled AcCoA.

Each round is defined by the citrate synthase (CS) reaction as the boundary. Results are obtained based on the assumption that each round consumes all available isotopomers generated from the previous round, and the resulting products are the only available species beginning the next cycle. The darkness of gray color suggests the abundance of the associated isotopomer. n≥3.

Isotopomer	Round 1	Round 2	Round 3	Round 4	Round 5	Round 6	Round n
M+4	100%	0	0	0	0	0	0
M+3	0	0	0	0	0	0	0
M+2	0	100%	0	0	0	0	0
M+1	0	0	100%	50%	25%	12.5%	$(0.5)^{(n-3)}\times100\%$
M+0	0	0	0	50%	75%	87.5%	$1-(0.5)^{(n-3)}\times100\%$

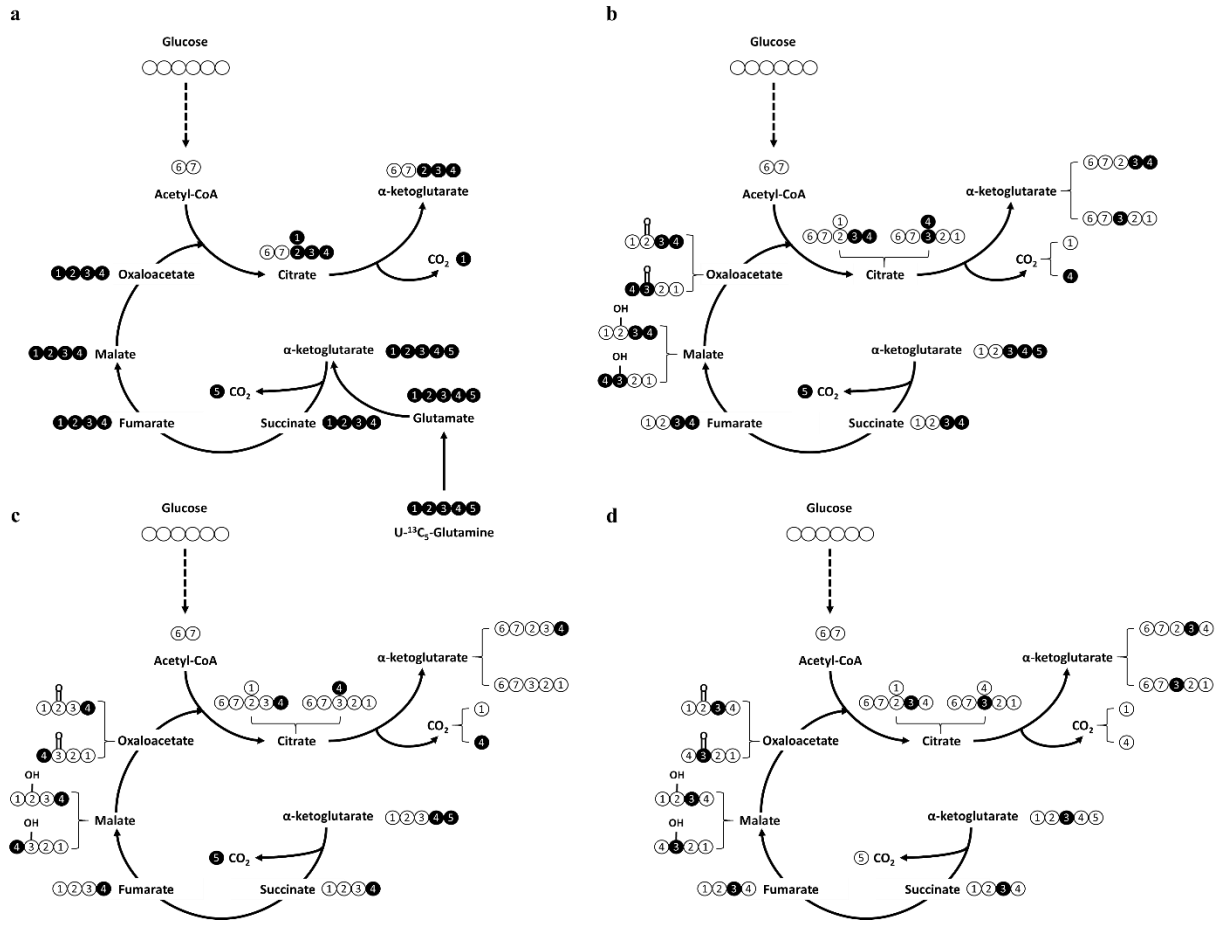

Figure 3.5. Labeling patterns of TCA cycle intermediates by U-$^{13}C_5$-glutamine dominated by pyruvate dehydrogenase (PDH) that supplies unlabeled acetyl-CoA (AcCoA).

a, Labeling results after the first round of cycling. The first round generates 3,4,5-$^{13}C_3$-α-ketoglutarate.

b, Labeling results after the second round of cycling by 3,4,5-$^{13}C_3$-α-ketoglutarate. This second round generates 4,5-$^{13}C_2$-and 3-^{13}C-α-ketoglutarate.

c, Labeling results after the third round of cycling by 4,5-$^{13}C_2$-α-ketoglutarate. This third round generates 5-^{13}C-and unlabeled α-ketoglutarate.

d, Labeling results after the third round of cycling by 3-^{13}C-α-ketoglutarate. This third round generates 4-^{13}C-and 3-^{13}C-α-ketoglutarate.

Carbon number is ordered consistent with the atomic sequence as shown in Figure 4a, and is associated with the same carbon throughout the diagram for the purpose of tracing, rather than following IUPAC naming rules. α-ketoglutarate: 1, carboxyl; 2, methylene bridge; 3, methylene bridge; 4, carbonyl; 5, carboxyl. AcCoA: 6, carbonyl; 7, methyl. Scrambling of labeling results is shown for malate and oxaloacetate, but not for fumarate and succinate due to molecular symmetry. Hydroxyl and carbonyl groups are drawn in malate and oxaloacetate, respectively. Filled and empty circles refer to ^{13}C- and ^{12}C-labeled carbon atoms, respectively. Solid and dashed arrows refer to single- or multi-step reactions, respectively.

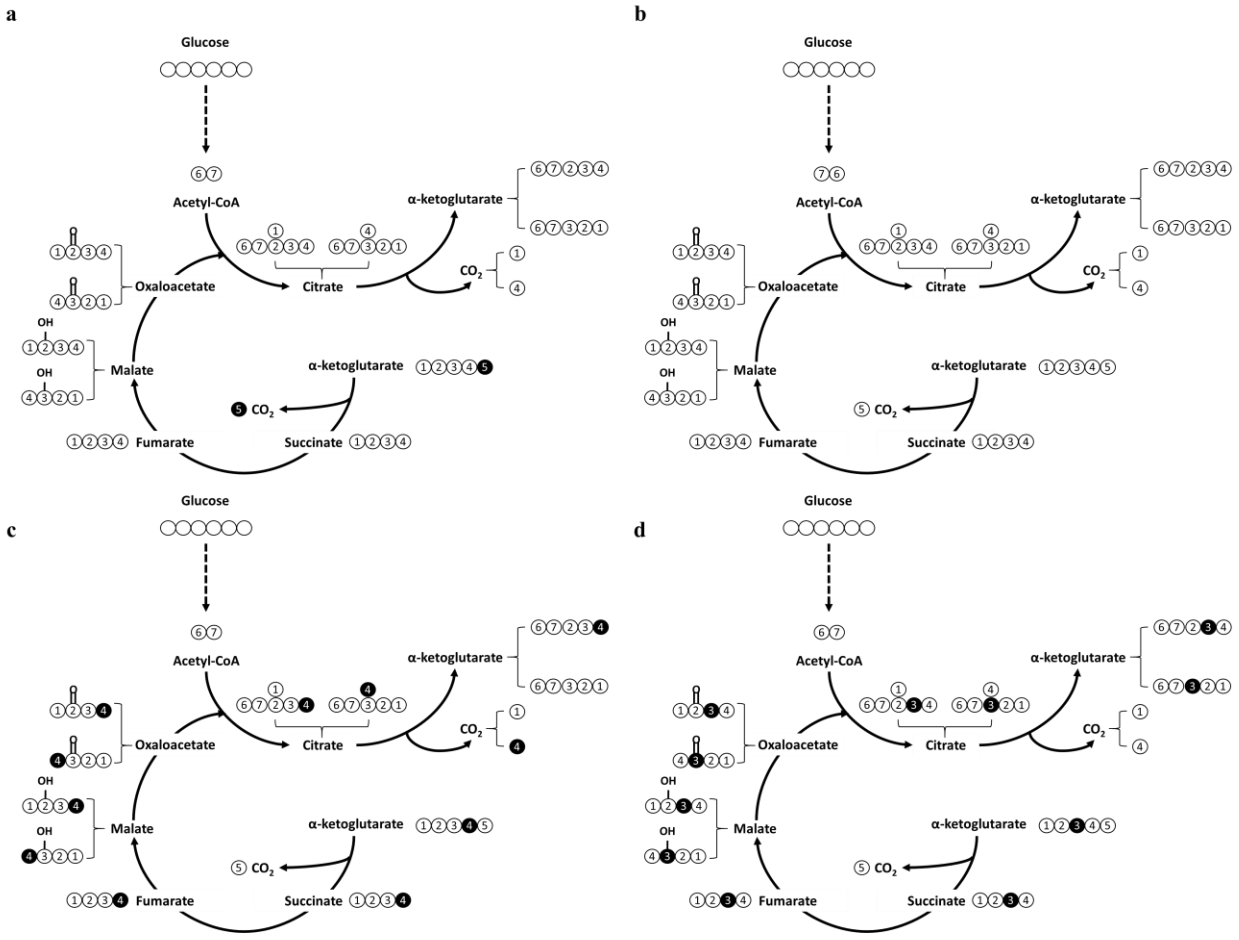

Figure 3.6. Additional labeling patterns of TCA cycle intermediates by U-$^{13}C_5$-glutamine dominated by pyruvate dehydrogenase (PDH) that supplies unlabeled acetyl-CoA (AcCoA).

a, Labeling results after the fourth round of cycling by 5-^{13}C-α-ketoglutarate. This fourth round generates unlabeled α-ketoglutarate.

b, Labeling results after the fourth round of cycling by unlabeled-α-ketoglutarate. This fourth round generates unlabeled α-ketoglutarate.

c, Labeling results after the fourth round of cycling by 4-^{13}C-α-ketoglutarate. This fourth round generates 5-^{13}C-and unlabeled α-ketoglutarate.

d, Labeling results after the fourth round of cycling by 5-^{13}C-α-ketoglutarate. This fourth round generates 4-^{13}C-and 3-^{13}C-α-ketoglutarate.

Carbon number is ordered consistent with the atomic sequence as shown in Figure 4a, and is associated with the same carbon throughout the diagram for the purpose of tracing, rather than following IUPAC naming rules. α-ketoglutarate: 1, carboxyl; 2, methylene bridge; 3, methylene bridge; 4, carbonyl; 5, carboxyl. AcCoA: 6, carbonyl; 7, methyl. Scrambling of labeling results is shown for malate and oxaloacetate, but not for fumarate and succinate due to molecular symmetry. Hydroxyl and carbonyl groups are drawn in malate and oxaloacetate, respectively. Filled and empty circles refer to ^{13}C- and ^{12}C-labeled carbon atoms, respectively. Solid and dashed arrows refer to single- or multi-step reactions, respectively.

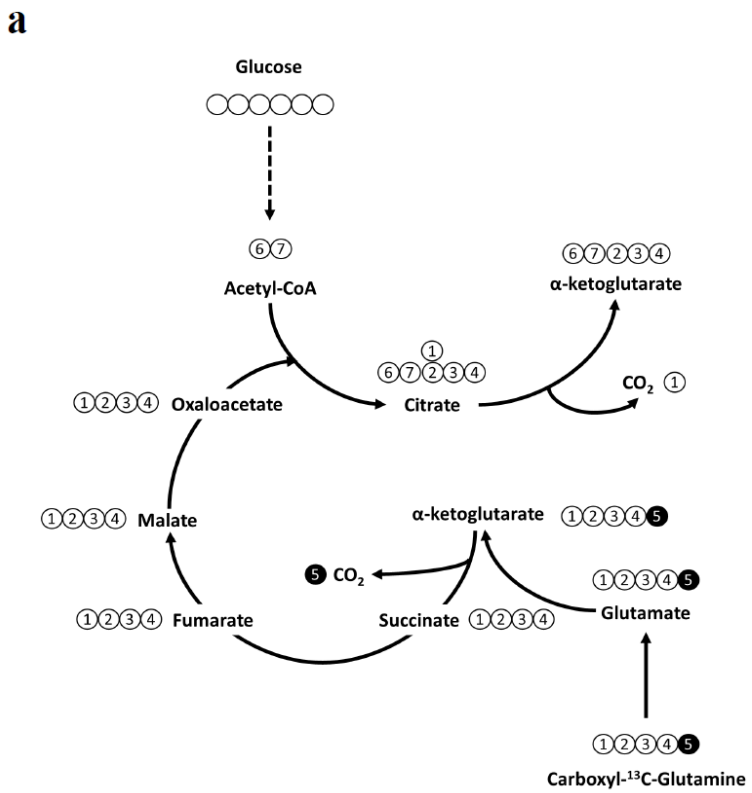

Figure 3.7 a. Labeling patterns of TCA cycle intermediates by 1-(carboxyl)-^{13}C- and 5-(amine)-^{13}C-glutamine through glutamine anaplerosis.

Labeling results of TCA cycle intermediates by 1-(carboxyl)-^{13}C-glutamine within the first round of oxidative cycling in the presence of both PDH and glutamine anaplerosis.

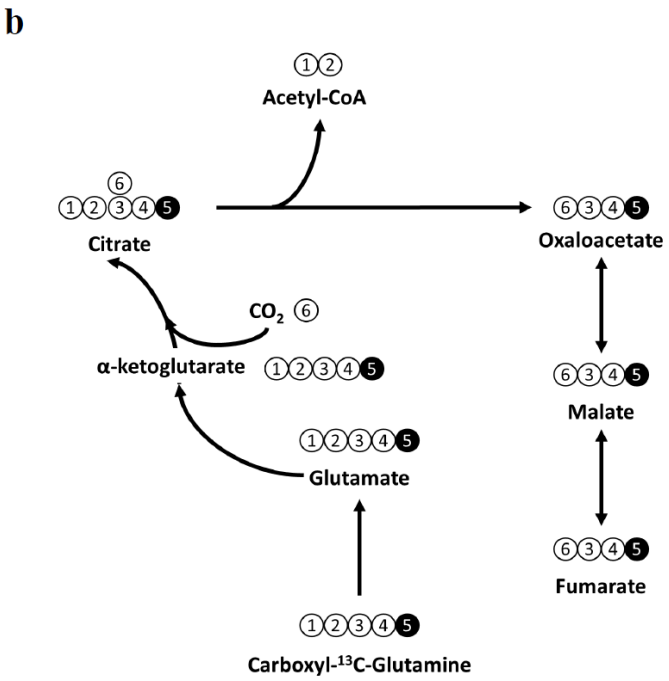

Figure 3.7 b. Labeling results of TCA cycle intermediates by 1-(carboxyl)-^{13}C-glutamine through reductive glutamine metabolism.

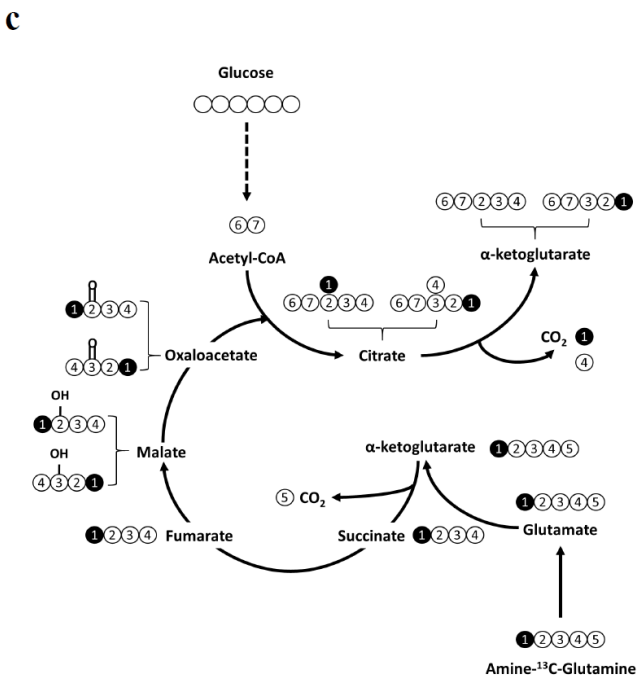

Figure 3.7 c. Labeling results of TCA cycle intermediates by 5-(amine)-^{13}C-glutamine within the first round of oxidative cycling in the presence of both PDH and glutamine anaplerosis.

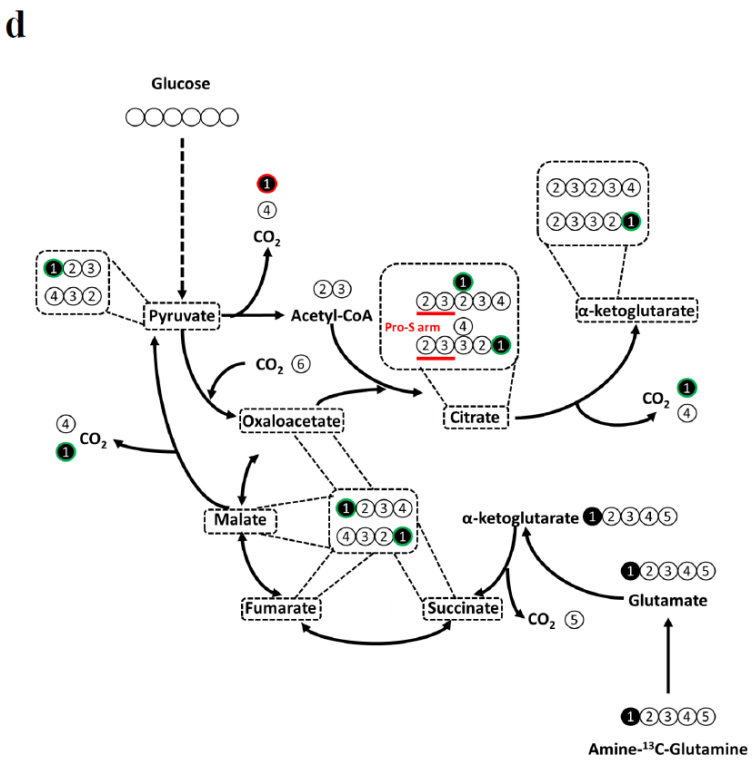

Figure 3.7 d. The presence of PC and ME/PEPCK reactions does not change the labeling patterns of TCA cycle intermediates by 5-(amine)-^{13}C-glutamine**.** ^{13}C-carbon atoms highlighted in red track PDH-derived isotopomers. ^{13}C-carbon atoms highlighted in green track the isotopomers derived from PC, ME/PEPCK and the reversible scrambling reactions. ^{13}C-carbon atoms without highlighted colors indicate initial set of isotopomers to begin a cycle. Note that the unlabeled isotopomer is always available and is included prior to the initial set.

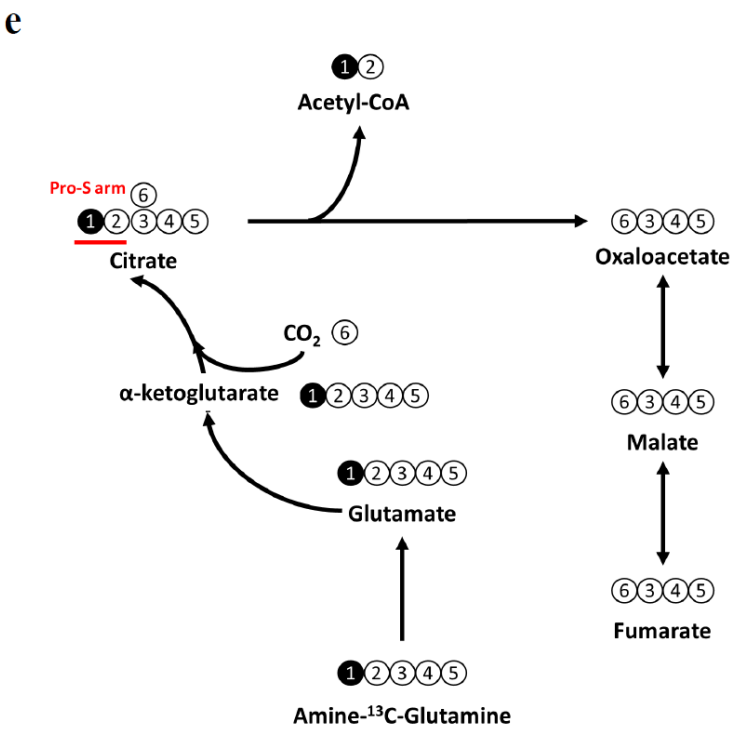

Figure 3.7 e. Labeling results of TCA cycle intermediates by 5-(amine)-^{13}C-glutamine through reductive glutamine metabolism.

Carbon number is ordered consistent with the atomic sequence as shown in Figure 4a, and is associated with the same carbon throughout the diagram for the purpose of tracing, rather than following IUPAC naming rules. Glutamine: 1, amine; 5, carboxyl. Note that 1-(carboxyl)-^{13}C-glutamine has carbon-5 labeled as ^{13}C, and that 5-(amine)-^{13}C-glutamine has carbon-1 labeled as ^{13}C in this diagram, so that the ordering of carbons for TCA cycle intermediates is the same as that shown in other figures. Filled and empty circles refer to ^{13}C- and ^{12}C-labeled carbon atoms, respectively. Solid and dashed arrows refer to single- or multi-step reactions, respectively. Turns of the TCA cycle are artificially broken into rounds, each separated at the step of α-ketoglutarate dehydrogenase (OGDC).

3.5 Acetate-driven TCA cycle probed by 1,2-$^{13}C_2$-acetate and 1-^{13}C-/1,6-$^{13}C_2$-glucose

In addition to glucose and glutamine anaplerosis, acetate also plays an important role in brain metabolism. Particularly in astrocytes, acetate can be directly utilized to produce AcCoA and thus contributes to the TCA cycle[30]. Dynamic experiments are usually performed to focus on the labeling patterns of the first round of the TCA cycle[15]. When fully labeled AcCoA derived from 1,2-$^{13}C_2$-acetate enters the TCA cycle, M+2 metabolites are produced along the PDH reaction after the first round (Figure 3.8a). However, 1-^{13}C-glucose or 1,6-$^{13}C_2$-glucose only generates M+1 pyruvate and AcCoA, resulting in M+1 metabolites throughout the TCA cycle (Figure 3.8b). The ME and PC/PEPCK reactions do not change the M+1 labeling pattern during the first round of TCA cycling (Figure 3.8c). Through simultaneous labeling of 1-^{13}C-glucose/1,6-$^{13}C_2$-glucose and 1,2-$^{13}C_2$-acetate, it has been discovered that acetate and glucose are responsible for anaplerosis in glial astrocytes and neurons, respectively[15]. It is worth noting that more labeling rounds of 1-^{13}C-glucose/1,6-$^{13}C_2$-glucose in the TCA cycle can generate other forms of isotopomers (Figure 3.8d-f). Through TCA cycling analysis, all isotopomeric forms of oxaloacetate and AcCoA have been produced at the end of the third round, which means that the fourth round is able to yield all isotopomers for each TCA cycle intermediate (Figure 3.8f).

a

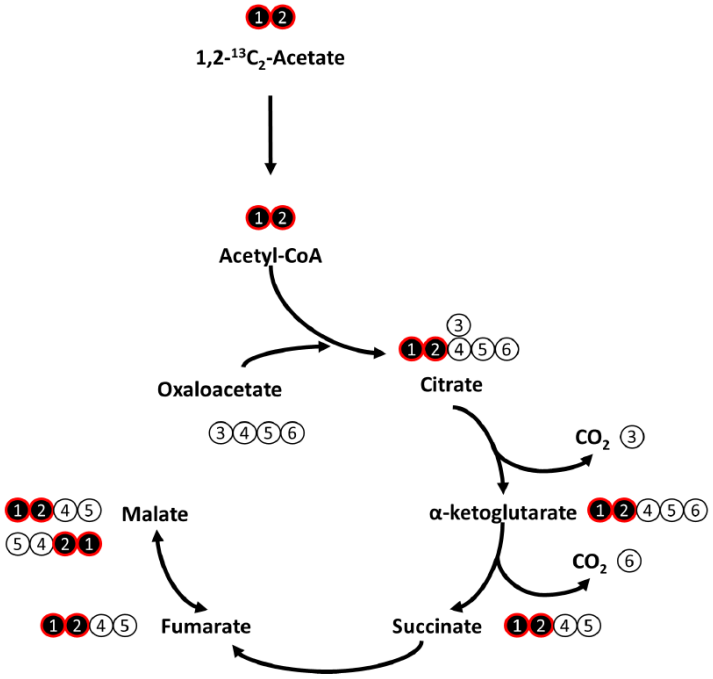

Figure 3.8 a. Labeling patterns of TCA cycle intermediates by 1,2-$^{13}C_2$-acetate and 1-^{13}C-/1,6-$^{13}C_2$-glucose. Labeling results of TCA cycle intermediates by 1,2-$^{13}C_2$-acetate within the first round of PDH cycling. AcCoA: 1, carbonyl; 2, methyl. Oxaloacetate: 3, carboxyl; 4, carbonyl; 5, methylene bridge; 6, carboxyl.

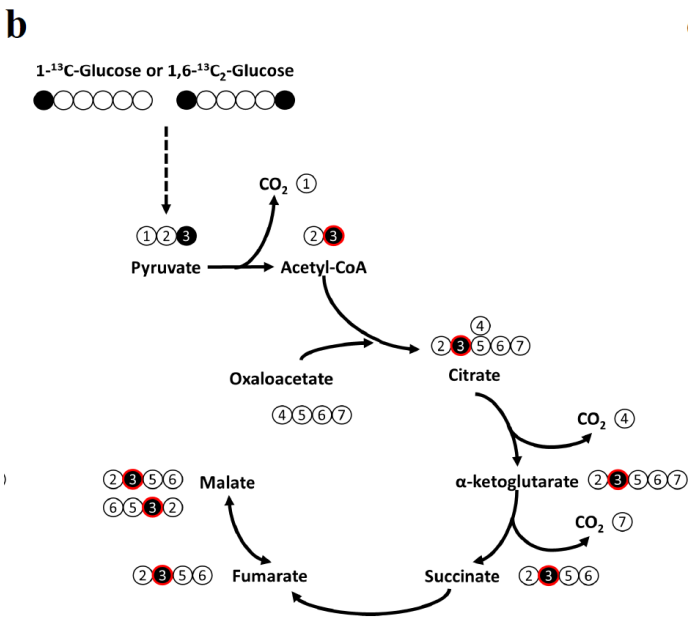

Figure 3.8 b. Labeling results of TCA cycle intermediates by 1-^{13}C-/1,6-$^{13}C_2$-glucose within the first round of PDH cycling. Pyruvate: 1, carboxyl; 2, carbonyl; 3, methyl. Oxaloacetate: 4, carboxyl; 5, carbonyl; 6, methylene bridge; 7, carboxyl.

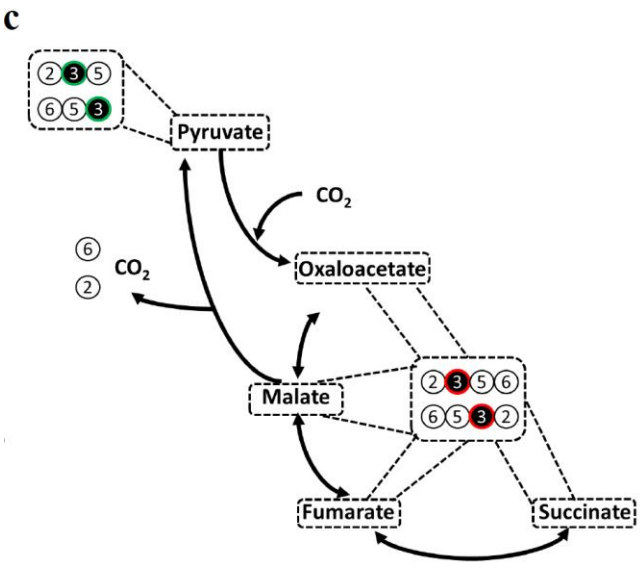

Figure 3.8 c. Alterations of labeling patterns by PC, ME/PEPCK and the reversible scrambling reactions among oxaloacetate, malate, fumarate and succinate during the first round of cycling.

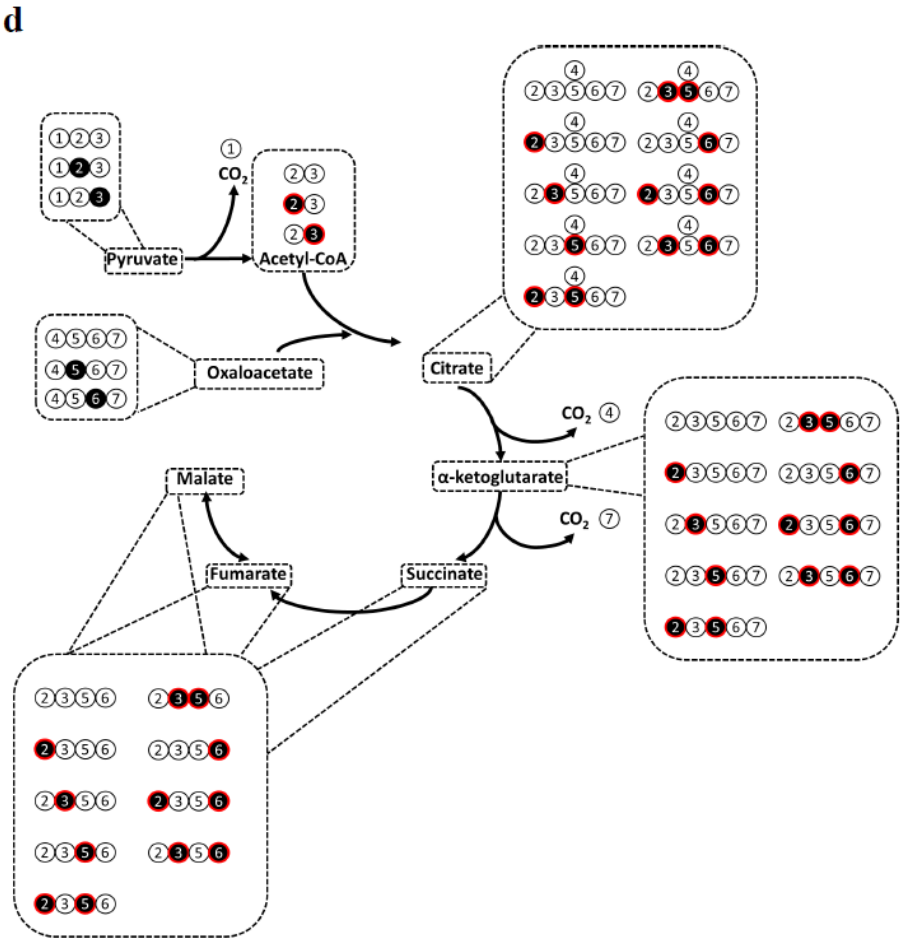

Figure 3.8 d. Labeling results of TCA cycle intermediates after the second round of PDH cycling, based on available isotopomers of oxaloacetate and pyruvate from the previous round.

e

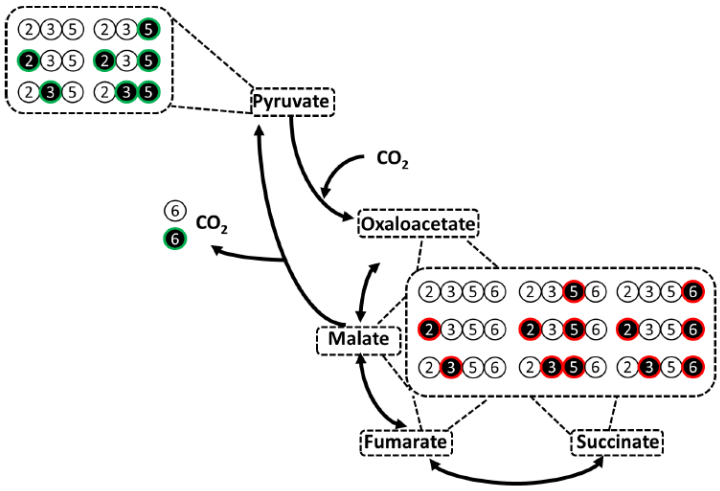

Figure 3.8 e. Alterations of labeling patterns by PC, ME/PEPCK and the reversible scrambling reactions among oxaloacetate, malate, fumarate and succinate during the second round of cycling.

f

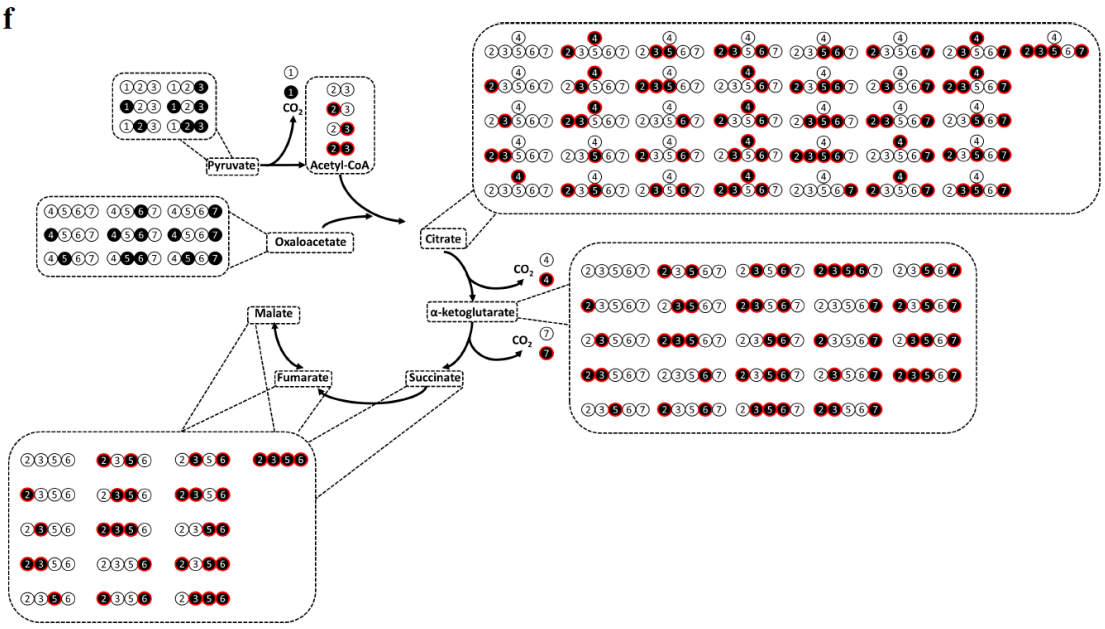

Figure 3.8 f. Labeling results of TCA cycle intermediates after the third round of PDH cycling, based on available isotopomers of oxaloacetate and pyruvate from the previous round.

Carbon number is ordered consistent with the atomic sequence as shown in Figure 1a, and is associated with the same carbon throughout the diagram for the purpose of tracing, rather than following IUPAC naming rules. ^{13}C-carbon atoms highlighted in red track PDH-derived isotopomers. ^{13}C-carbon atoms highlighted in green track the isotopomers derived from PC, ME/PEPCK and the reversible scrambling reactions. ^{13}C-carbon atoms without highlighted colors indicate initial set of isotopomers to begin a cycle. Note that the unlabeled isotopomer is always available and is included prior to the initial set. Solid and dashed arrows refer to single- or multi-step reactions, respectively.

3.6 Pentose phosphate pathway (PPP) probed by 1,2-$^{13}C_2$-, 2-^{13}C- and 3-^{13}C-glucose

In addition to the TCA cycle, PPP is another crucial component of the central carbon metabolism, responsible for promoting nucleotide biosynthesis, redox defense and reductive anabolism[31–33]. The bifurcation of the oxidative pentose phosphate pathway (oxPPP) and glycolysis is located at the point of glucose-6-phosphate (G6P). Through reactions by glucose-6-phosphate dehydrogenase (G6PD), 6-phosphogluconolactonase and 6-phosphogluconate dehydrogenase (6PGD), one molecule of carbon dioxide (CO_2) is produced per molecule of G6P, yielding ribulose-5-phosphate (Ru5P). Ru5P is then isomerized to ribose-5-phosphate (R5P) and xylulose-5-phosphate (Xu5P), which then react with each other to produce sedoheptulose-7-phosphate (S7P) and glyceraldehyde-3-phosphate (GAP) through the transketolase (TKT) enzyme. The transaldolase (TAL) enzyme further produces erythrose-4-phosphate (E4P) and fructose-6-phosphate (F6P) from S7P and GAP. In addition, the transketolase enzyme also catalyzes the transformation of Xu5P and E4P into F6P and GAP, which can then be diverted back to the glycolytic pathway. These series of PPP reactions and a simplified version of glycolysis are depicted in Figure 3.9a. Isotopic tracers 1,2-$^{13}C_2$-glucose, 2-^{13}C-glucose and 3-^{13}C-glucose are capable of investigating the relative magnitudes along glycolysis and the oxPPP[17,18]. The resulting labeling patterns from these tracers can be clearly explained by simultaneously following the metabolic routes of three molecules of glucose.

Taking 1,2-$^{13}C_2$-glucose as an example, the carbon skeleton remains intact along the PPP until the formation of 6-phosphogluconate (6PG). The oxidative PPP step then takes place and generates three molecules of M+1 Ru5P with only one ^{13}C atom remaining for each molecule at the distal end away from the phosphate group. Next, through ribulose-5-phosphate epimerase and

ribulose-5-phosphate isomerase, two molecules of M+1 Xu5P and one molecule of M+1 R5P are generated from three molecules of M+1 Ru5P, maintaining the atomic position of ^{13}C atoms. M+1 R5P then reacts with one of the M+1 Xu5P molecules through TKT, which produces a molecule of M+0 GAP and a molecule of M+2 S7P. Next, the M+2 S7P acquires one of the ^{13}C atoms from its original carbon backbone inherited from M+1 R5P and the other ^{13}C atom from the transfer of a C_2 unit from M+1 Xu5P. The M+0 GAP and M+2 S7P further undergo a carbon scrambling reaction catalyzed by TAL, and yield a molecule of M+0 E4P and a molecule of M+2 F6P. The net reaction outcome from M+1 R5P and M+1 Xu5P is M+0 E4P, which retains four unlabeled carbons from M+1 R5P, and M+2 F6P, which combines all carbon atoms from the M+1 Xu5P with the ^{13}C atom from M+1 R5P. M+2 F6P can be then diverted back to glycolysis and cleaved to yield an equimolar mixture of M+2 and M+0 pyruvate. The M+0 E4P then reacts with the M+1 Xu5P initially derived from one of the three molecules of 1,2-$^{13}C_2$-glucose to form M+0 GAP and M+1 F6P. The glycolytic pathway subsequently produces M+0 pyruvate from GAP and M+1 F6P, as well as M+1 pyruvate from the latter (Figure 3.9b). In contrast, when 1,2-$^{13}C_2$-glucose is metabolized exclusively along glycolysis (Figure 3.9c), only M+2 and M+0 pyruvate isotopomers can be produced (Figure 3.9d). Therefore, the ratio of M+1 to M+2 pyruvate serves as an indicator of the relative magnitudes along the oxPPP and glycolysis.

Alternatively, 2-^{13}C-glucose and 3-^{13}C-glucose are also employed to perform similar analyses. When 2-^{13}C-glucose and 3-^{13}C-glucose are oxidized though the PPP, M+2 F6P is generated and cleaved, yielding M+2 pyruvate (Figure 3.9e-f). The glycolytic pathway, however, only generates M+1 and M+0 pyruvate (Figure 3.9g-h). Thus, the ratio of M+2 to M+1 pyruvate can be used to compare oxPPP against glycolysis.

a

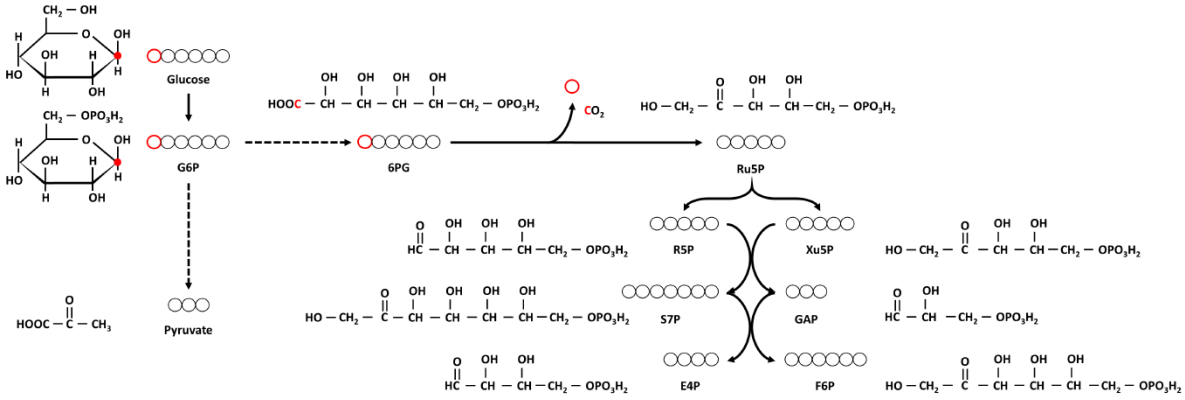

Figure 3.9 a. The pentose phosphate pathway (PPP) and glycolysis probed by 1,2-$^{13}C_2$-, 2-^{13}C- and 3-^{13}C-glucose.

Chemical structures and carbon transition maps highlighting the positional information through the PPP. Circles represent carbon atoms with the same position as referenced to the actual chemical structures of the metabolites. Carbon atoms highlighted in red indicate how the carboxyl group in 6PG is cleaved in the oxidative step to make Ru5P.

b

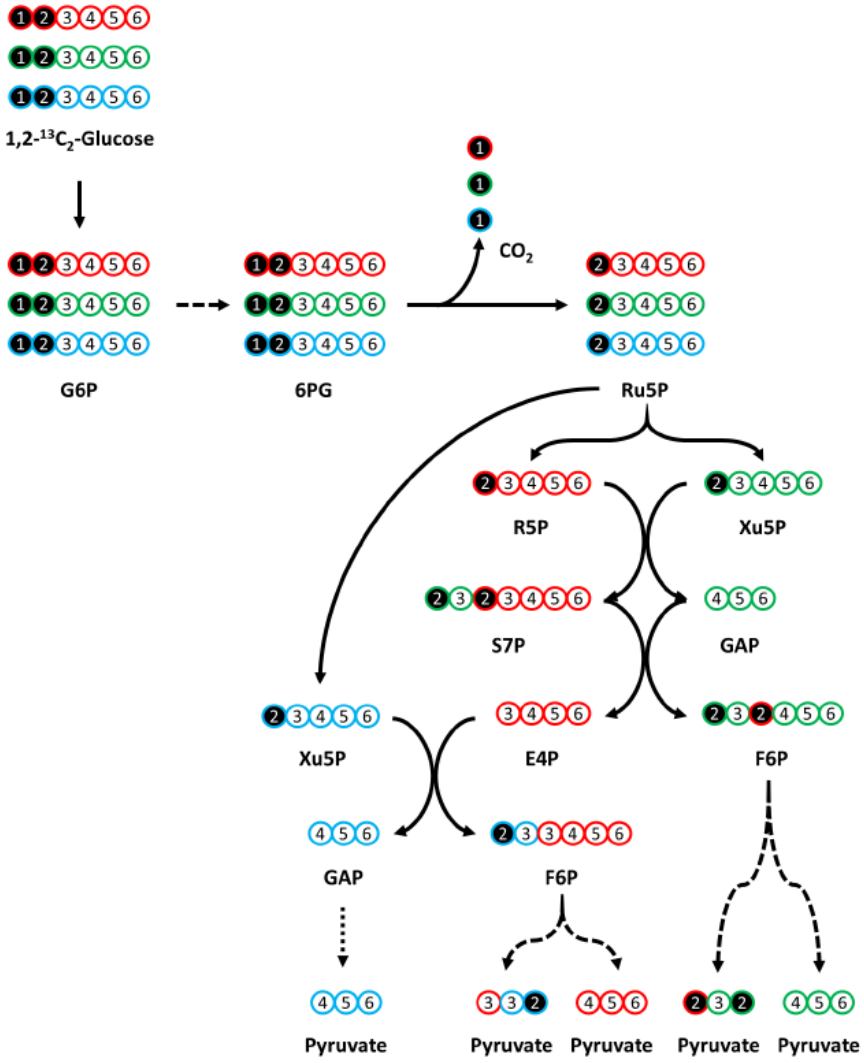

Figure 3.9 b. Labeling patterns of PPP intermediates by 1,2-$^{13}C_2$-glucose, assuming no backward cycling of ^{13}C-labeled F6P. Carbon atoms are highlighted in red, green and blue to show their origins from three different glucose molecules.

c

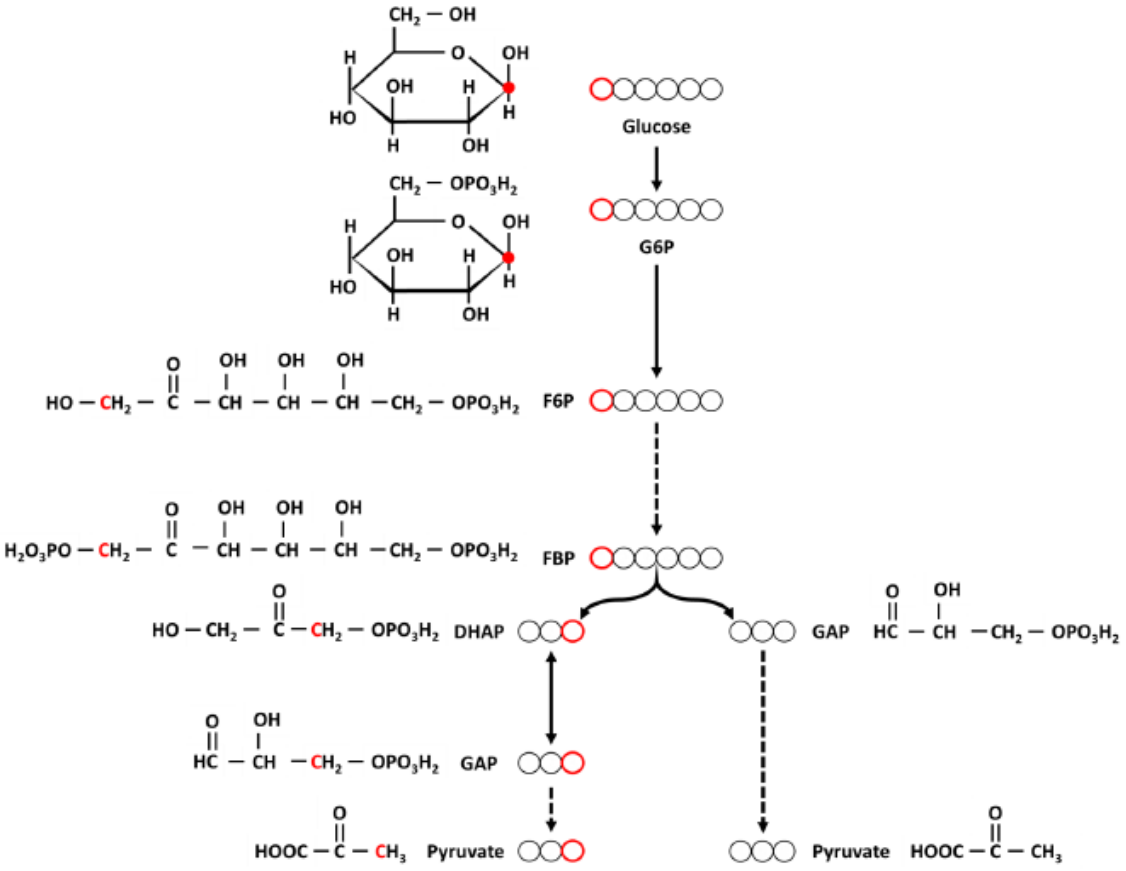

Figure 3.9 c. Chemical structures and carbon transition maps highlighting the positional information through glycolysis. Circles represent carbon atoms with the same position as referenced to the actual chemical structures of the metabolites. Carbon atoms highlighted in red track the splitting of hexoses to trioses.

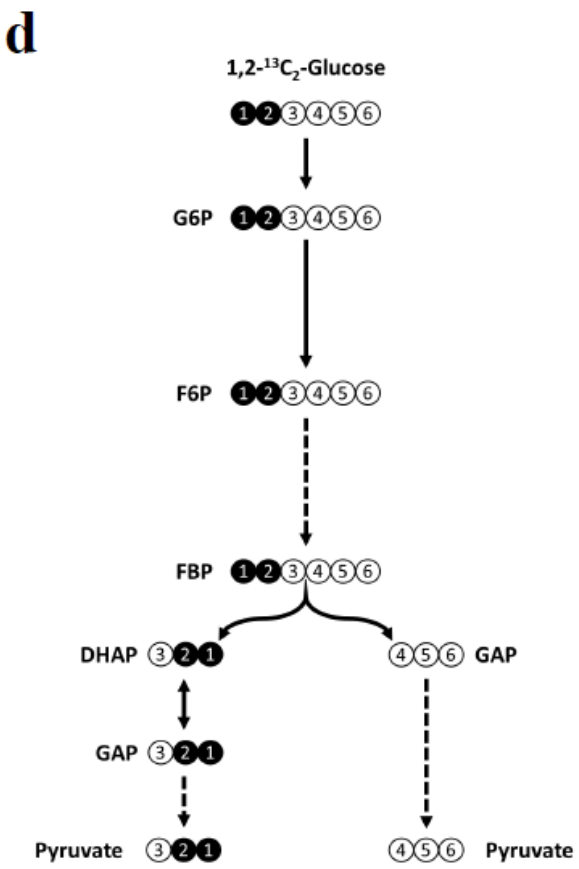

Figure 3.9 d. Labeling patterns of glycolytic intermediates by 1,2-$^{13}C_2$-glucose.

e

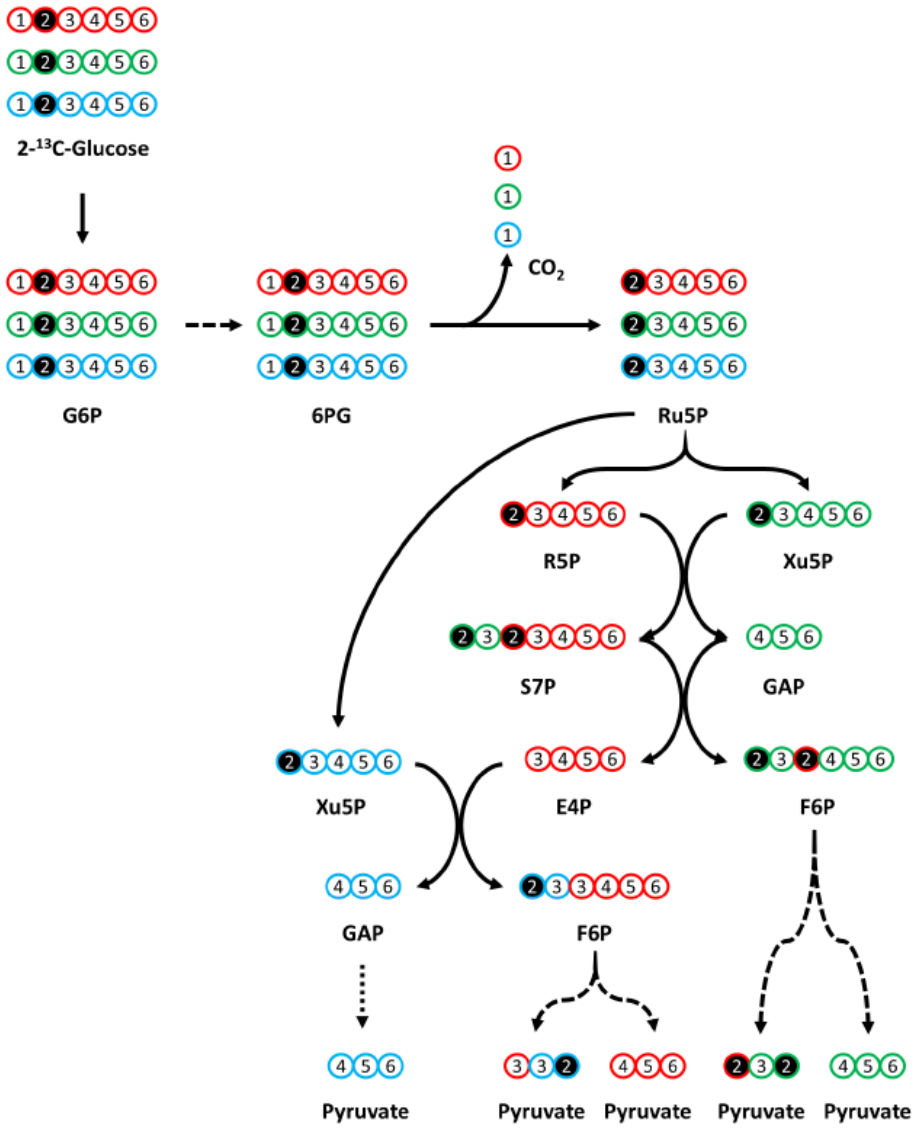

Figure 3.9 e. Labeling patterns of PPP intermediates by 2-^{13}C-glucose, assuming no backward cycling of ^{13}C-labeled F6P. Carbon atoms are highlighted in red, green and blue to show their origins from three different glucose molecules.

f

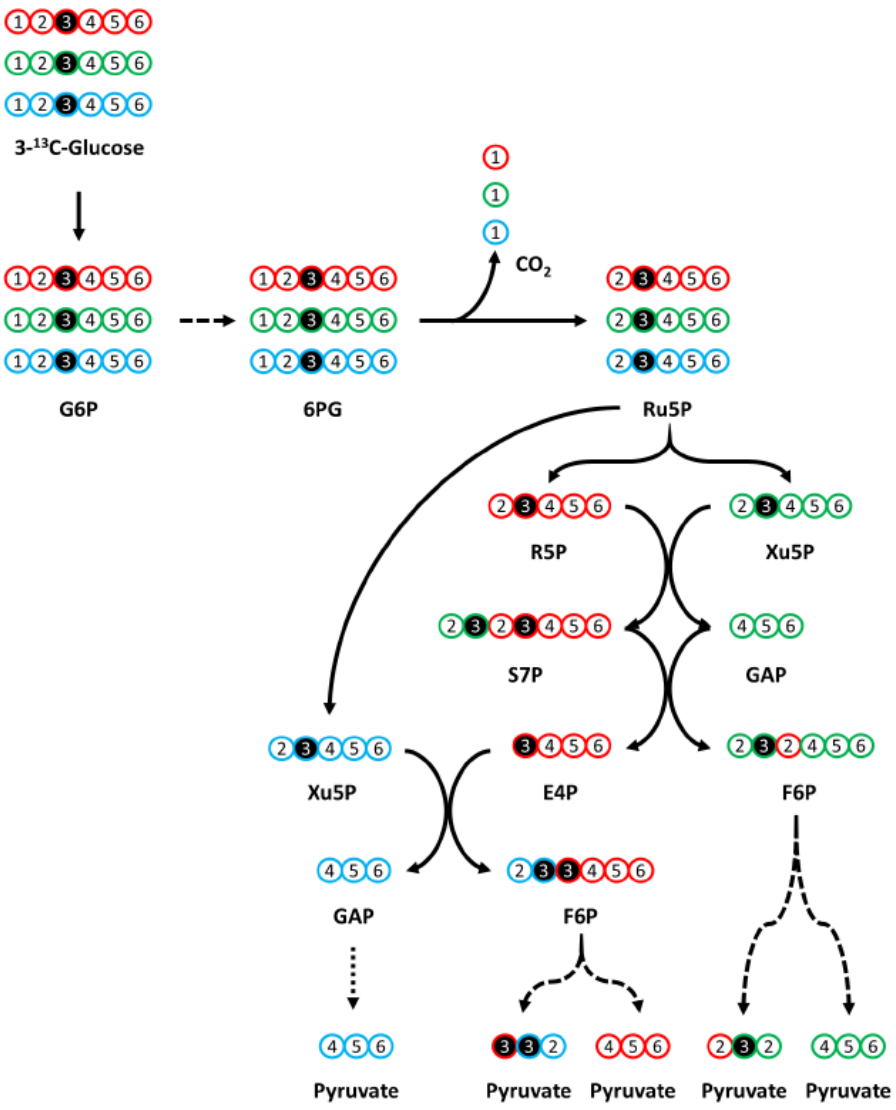

Figure 3.9 f. Labeling patterns of PPP intermediates by 3-^{13}C-glucose, assuming no backward cycling of ^{13}C-labeled F6P. Carbon atoms are highlighted in red, green and blue to show their origins from three different glucose molecules.

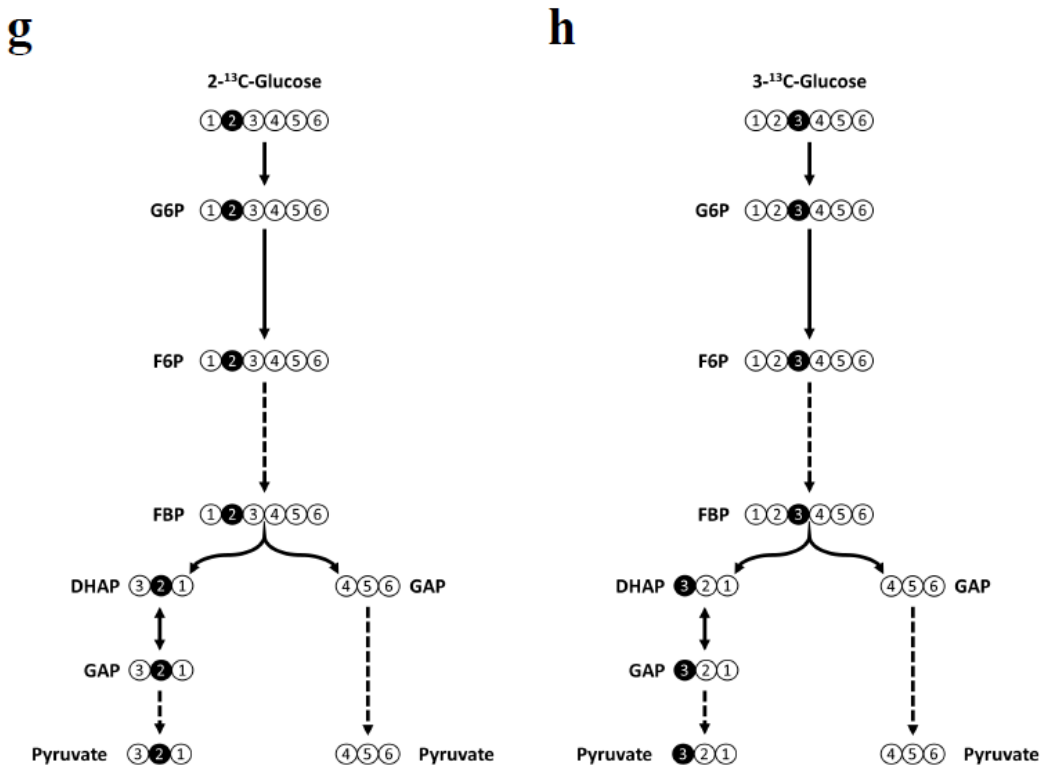

Figure 3.9 g-h. Labeling patterns of glycolytic intermediates by 2-^{13}C-glucose (g) and 3-^{13}C-glucose (h). Carbon number is ordered consistent with the atomic sequence as shown in **a** and **c**, and is associated with the same carbon throughout the diagram for the purpose of tracing, rather than following IUPAC naming rules. Filled and empty circles refer to ^{13}C- and ^{12}C-labeled carbon atoms, respectively. Solid and dashed arrows refer to single- or multi-step reactions, respectively.

3.7 ^{2}H-isotopic tracers

Compared to the use of ^{13}C-tracers for studying the central carbon metabolism, deuterium (^{2}H) isotopic tracers have been widely used for assessing activities of NAD(P)H production pathways as well as fatty acid and amino acid synthesis in mammalian cells[24,34–38]. Pyridine nucleotides such as NADH and NADPH serve as electron carriers by transferring electrons in the form of hydride ions (H^-). Deuterium isotopic tracers have been applied in tacking the flow of electrons involved in redox reactions such as NAD(P)-dependent dehydrogenase pathways (Figure 3.10a)[39,40].

^{2}H-glucose tracers have been used to determine metabolic activities involved in the generation of NADPH along the oxPPP[24]. For instance, 1-^{2}H-glucose tracer can monitor the extent of NADPH generation via the G6PD reaction (Figure 3.10b)[35]. As G6P is converted to 6PG, the ^{2}H atom in 1-^{2}H-glucose is transferred to $NADP^+$, yielding $NADP^2H$. The ^{2}H-labeled NADPH can be subsequently measured using LC/MS[35]. In addition, 3-^{2}H-glucose tracer is used to probe the activity of 6PGD, the third step in the oxPPP that generates both NADPH and CO_2 (Figure 3.10b)[34]. The kinetic isotope effect of these ^{2}H glucose tracers is minimal, and the labeling of deuterium in NADPH has been shown to be fast with a half-time ($t_{1/2}$) of approximately 5 minutes, making it feasible to observe changes in pathway activities within a short time frame[34,35]. As a result, these tracers are useful in assessing the contribution of the oxPPP for the production of NADPH in mammalian cells. Moreover, significant labeling strength has been observed in central carbon metabolites by 4-^{2}H-glucose such as lactate, malate and glycerol-3-phosphate (Glyc-3P), through reactions that require NADH as a cofactor (Figure 3.10c)[34]. Thus, 4-^{2}H-glucose is used as a tracer for probing NADH-related metabolism.

Along with ^{2}H-glucose tracers, 3,3-$^{2}H_2$-serine, 2,3,3-$^{2}H_3$-serine and 2,2-$^{2}H_2$-glycine have been employed to investigate the metabolism through serine hydroxymethyltransferase (SHMT) and methylenetetrahydrofolate dehydrogenase (MTHFD) (Figure 3.10d)[34]. ^{2}H atoms in these tracers can be transferred to either cytosolic or mitochondrial NAD(P)H, characterizing the directionality of serine/glycine metabolism in two compartments with a 2-hydroxyglutarate reporter system[34]. In addition, 2,2,3,3-$^{2}H_4$-dimethyl succinate has recently been designed for investigating ME-dependent NADPH production in adipocytes (Figure 3.10e)[36]. As fatty acid synthesis requires an ample supply of reducing equivalents such as NADPH, the labeling patterns of fatty acids such as palmitate can also be examined using 2,2,3,3-$^{2}H_4$-dimethyl succinate.

Additionally, deuterium oxide ($^{2}H_2O$) has been utilized for examinations of *de novo* fatty acid and amino acid syntheses (Figure 3.10f). Lee at al. measured the extent of deuterium incorporated into the synthesis of fatty acids in nervous and liver tissues by feeding rats with $^{2}H_2O$, and found $t_{1/2}$ of newly synthesized lipids from nervous tissues to be 5 to 28 days, which turned out to be slower than that of liver ($t_{1/2}$ < 4 days)[41]. Recently, Zhang et al. demonstrated that hydrogen transfer between $^{2}H_2O$ and NADPH was mediated via flavin enzymes and provided evidence that NADPH accounts for almost 50% of redox-active hydrogen[38]. In addition, they formulated an equation to predict fatty acid labeling patterns consistent with data obtained from $^{2}H_2O$ tracing experiments. In regards to the measurements of amino acid synthesis *in vivo*, Busch et al. used $^{2}H_2O$ and examined MIDs of newly synthesized amino acids such as alanine and leucine, the hydrogens of which were labeled by ^{2}H transferred from $^{2}H_2O$.

a

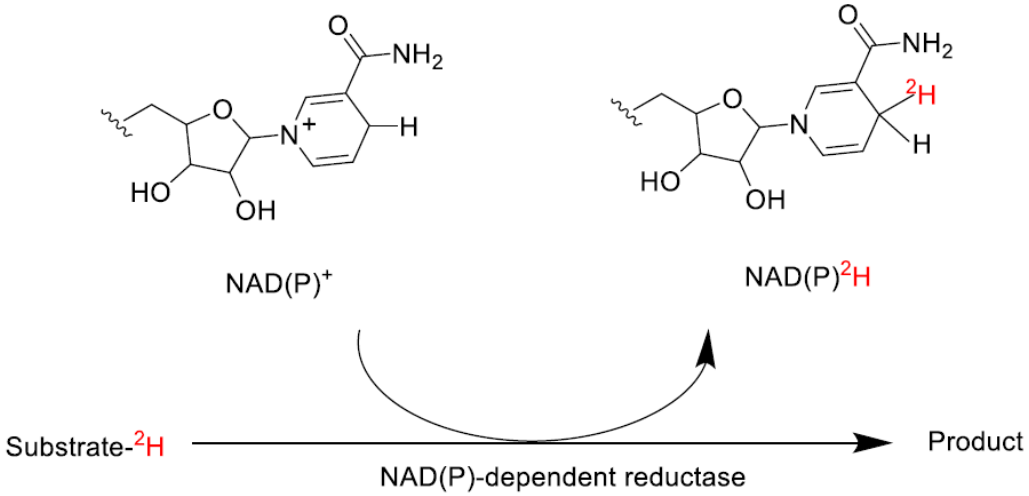

Figure 3.10 a. Deuterium isotopic tracers for assessing pathway activities of NAD(P)H generation as well as fatty acid and amino acid synthesis.

Deuterium, the labeled hydride ion, is transferred to NAD(P) via NAD(P)-dependent reductases, yielding deuterium-labeled NAD(P)H. Redox reactions occur in the fourth position of the nicotinamide group, where the hydride ion acts as a nucleophile. The oxidized form of NADPH serves as a hydride acceptor while the reduced form serves as a donor. The adenine nucleotide phosphate group is not shown.

b

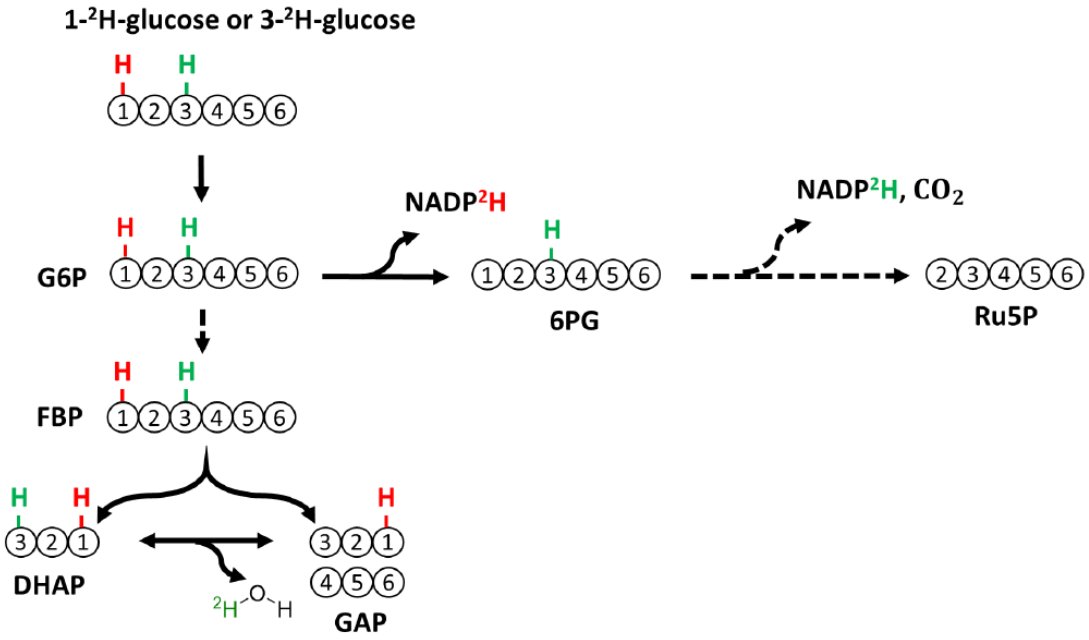

Figure 3.10 b. 1-^{2}H-glucose and 3-^{2}H-glucose are used to label NADPH in the oxPPP and the upper part of glycolysis**.** Hydrogen in red indicates deuterium placed at the first carbon of glucose. Hydrogen in green represents deuterium positioned at the third carbon of glucose. Deuterium positioned at the third carbon in DHAP is lost at the triose phosphate isomerase (TPI) reaction step. Carbon number is ordered consistent with the atomic sequence as shown in Figure 7a and 7c, and is associated with the same carbon throughout the diagram for the purpose of tracing, rather than following IUPAC naming rules.

c

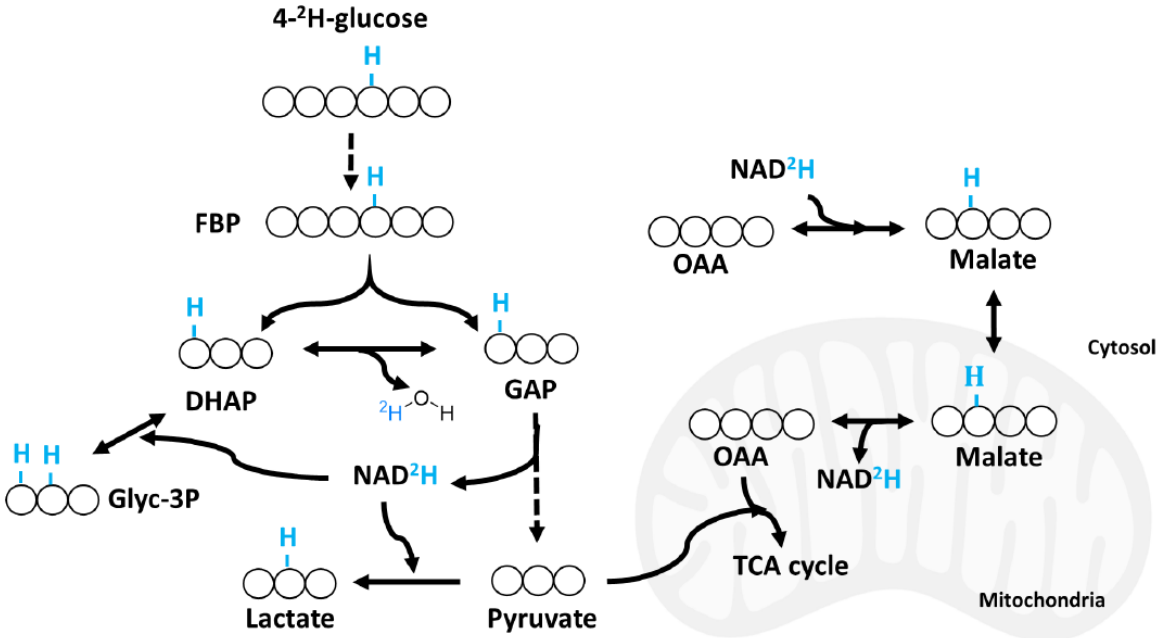

Figure 3.10 c. 4-^{2}H-glucose is used to label NADH. Deuterium-labeled NADH, generated by GAPDH, is incorporated into glycolytic and TCA metabolites such as lactate, malate and Glyc-3P via NAD-dependent reductases such as LDH and MDH.

d

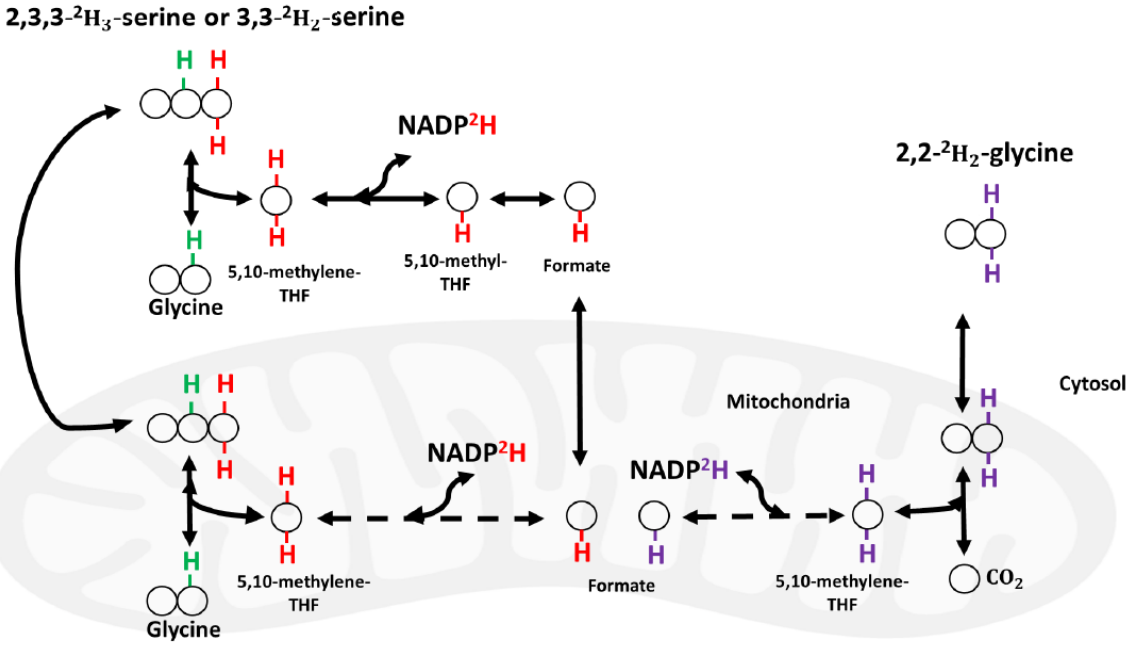

Figure 3.10 d. 2,3,3-$^{2}H_3$-serine, 3-3-$^{2}H_2$-serine and 2-2-$^{2}H_2$–glycine are used to label NADPH in cytosol and mitochondria. 2,3,3-$^{2}H_3$-serine is converted to M+1 deuterium-labeled glycine along with M+2 deuterium-labeled 5,10-methyl-THF via SHMT. The one carbon unit subsequently undergoes a series of reactions to formate, in which deuterium is transferred to NADPH via MTFHD. 2-2-$^{2}H_2$-glycine is cleaved to carbon dioxide and M+2 deuterium-labeled 5,10-methyl-THF, the deuterium of which is transferred to NADPH via MTFHD.

e

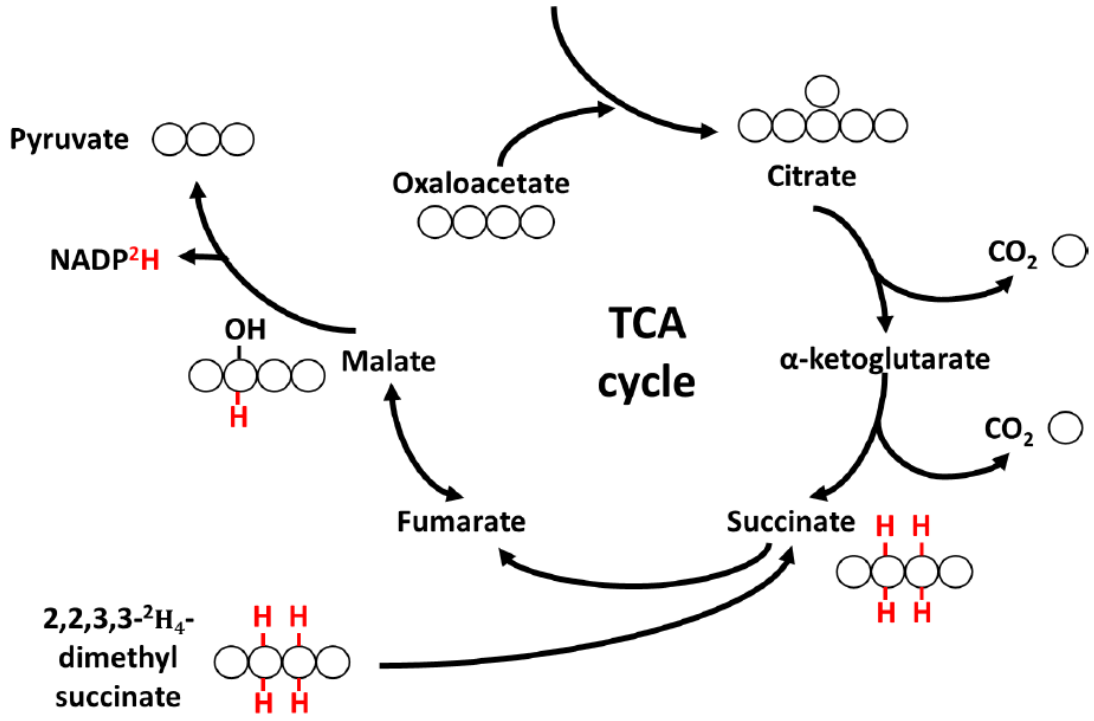

Figure 3.10 e. 2,2,3,3-$^{2}H_4$-dimethyl succinate is incorporated into the TCA cycle, allowing hydride transfer of the second carbon of malate to NADPH via the ME reaction. Since succinate is symmetrical, any deuterium in 2,2,3,3-$^{2}H_4$-dimethyl succinate can label NADPH.

f

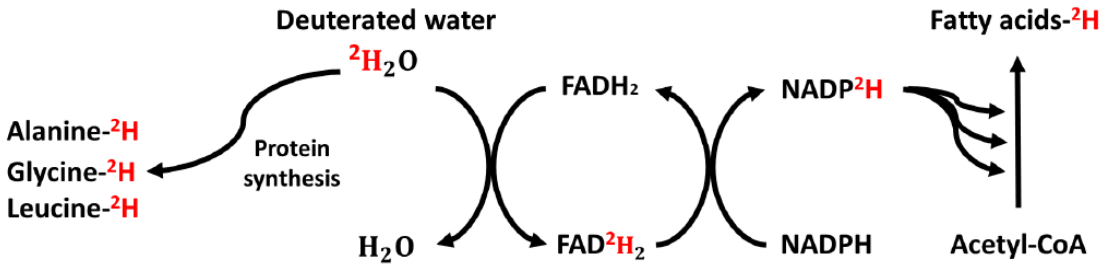

Figure 3.10 f. Deuterium oxide (^2H_2O) is used to examine relative pathway magnitudes of *de novo* fatty acid and amino acid syntheses. ^2H from deuterium oxide is transferred to NADPH through hydride shuttling of $FADH_2$. Deuterium-labeled NADPH is then incorporated into fatty acid synthesis pathways. Similarly, deuterium is incorporated into newly synthesized amino acids such as alanine, glycine and leucine by ^2H_2O.

3.8 ^{13}C-metabolic flux analysis (^{13}C-MFA)

Although the use of a single isotopic tracer can provide sufficient information to investigate some parts of metabolism, it is sometimes of interest to fully resolve the entire metabolic network by consolidating data from multiple tracers, which requires the estimation of metabolic fluxes. Usually metabolic fluxes are dynamic, posing challenges to accurate and reliable quantification[42]. However, under metabolic and isotopic steady states, metabolic fluxes are constant over time, making it possible to perform ^{13}C-MFA.

To illustrate the capability of ^{13}C-MFA to quantitatively resolve intricate metabolic networks, we performed analyses on a metabolic model centered upon the TCA cycle with major anaplerotic reactions (Figure 3.11a), using our in-house MATLAB-based software Metran[43]. Both U-$^{13}C_6$-glucose and unlabeled glutamine are included as carbon substrates, and the uptake rates of those two species as well as the excretion rates of lactate and glutamate are set to be constant. We then created three cases where the MIDs of TCA cycle intermediates are different, while maintaining the same extracellular fluxes (Figure 3.11b). ^{13}C-MFA was then employed to estimate metabolic fluxes based on the model (Figure 3.11c).

Due to the presence of a large variety of isotopomers in each TCA cycle metabolite, it is difficult to deduce flux distribution patterns by analyzing MIDs alone. In addition, the cyclic TCA metabolism is further entangled with multiple contributing reactions such as PDH, PC and ME reactions. Moreover, ^{13}C enrichment strength is diluted by glutamine anaplerotic flux, which enters at the point of α-ketoglutarate in the TCA cycle. However, this demonstration will show how ^{13}C-MFA is capable of analyzing complex labeling data and acquiring systematic understanding of metabolic patterns.

Case I represents a metabolic scheme in which the fluxes along PDH, PC, ME and MDH reactions are comparable. In addition, *de novo* lipogenesis as indicated by the ACLY flux is negligible compared to lower TCA cycling, which consists of reactions catalyzed by α-ketoglutarate dehydrogenase (OGDC), succinyl-CoA synthetase (SCS), succinate dehydrogenase (SDH) and fumarase (FH). Case II exhibits similar metabolic patterns as Case I, except that the PC reaction is essentially inactive and the ME reaction is attenuated. In addition, the PDH and MDH reactions are enhanced. Case III is an example of a drastically reprogrammed metabolic network, in which the directionality of two TCA cycle reactions is reversed – MDH and IDH are operating along the reductive direction, consuming NAD(P)H instead of producing it. Concomitantly, *de novo* lipogenesis is significantly enhanced compared to Case I and II, whereas lower TCA cycling is considerably reduced. These metabolic insights are readily deducible by examining the ^{13}C-MFA results.

In contrast to ^{13}C-MFA, only a subset of metabolic conclusions may be drawn correctly by scrutinizing the MID results. For example, based on the metabolic network model (Figure 3.11a), *de novo* lipogenesis is the major route that depletes carbon sources from the TCA cycle. The labeling strength of TCA cycle metabolites in each case is calculated (Figure 3.11d), and it suggests that Case III exhibits the least ^{13}C-enriched pools of TCA cycle intermediates. The similar conclusion can be drawn by examining the MIDs from Case III (Figure 3.11b), and noting that the ^{13}C-fractional enrichment of heavy isotopomers such as M+4 and M+5 is greatly attenuated compared to that in Case I and II. Without performing ^{13}C-MFA, we can conclude that *de novo* lipogenesis should be enhanced in Case III. However, analyses based on MID results alone can sometimes lead to ambiguous or even completely incorrect conclusions. For example, increased PC flux can result in elevated abundances of M+3 labeled succinate,

fumarate and malate (Figure 3.2b). It is then tempting to claim that the PC flux is augmented in Case II because of increased M+3 fractions. However, increased M+3 abundances for those metabolites do not need to result from an upregulated PC reaction, as our previous analysis has shown that an enhanced PDH reaction can also enrich M+3 isotopomers in the lower TCA cycle (Figure 3.1c-d). In fact, the PC reaction is attenuated in Case II (Figure 3.11c), suggesting that MID analysis is incapable of investigating the PC reaction conclusively. Therefore, ^{13}C-MFA is highly recommended to be applied to studying such complex networks so that the metabolism can be fully understood without inconclusive or incorrect interpretations.

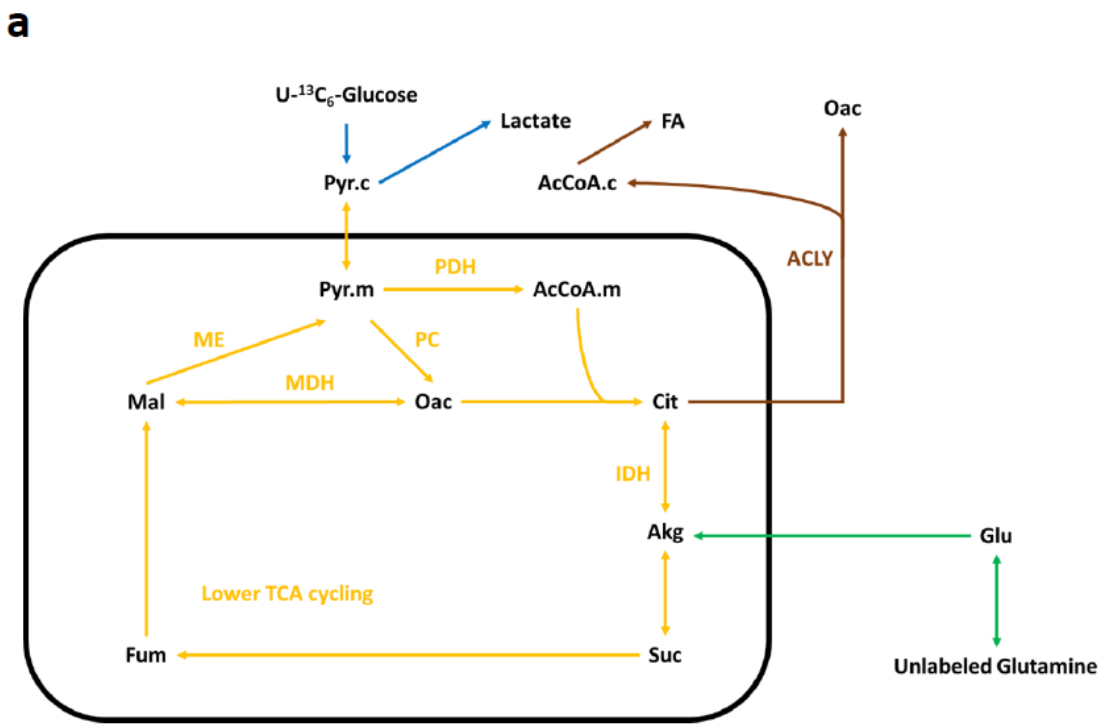

Figure 3.11 a. Demonstration of ^{13}C-metabolic flux analysis (^{13}C-MFA) for resolving complex metabolic patterns in the TCA cycle with multiple anaplerotic reactions.

The metabolic model used in the ^{13}C-MFA demonstration. Metabolic pathways are color coded to indicate different parts of metabolism: blue, glycolysis; orange, the tricarboxylic acid (TCA) cycle; green, glutamine anaplerosis; brown, *de novo* lipogenesis. Single- and double-headed arrows refer to unidirectional and bidirectional reactions, respectively. The rounded rectangle refers to the boundary of a mitochondrion. Abbreviations: Pyr.c, cytosolic pyruvate; Pyr.m, mitochondrial pyruvate; AcCoA.c, cytosolic acetyl-CoA; AcCoA.m, mitochondrial acetyl-CoA; FA, fatty acids; Mal, malate; Oac, oxaloacetate; Cit, citrate; Akg, α-ketoglutarate; Glu, glutamate; Fum, fumarate; Suc, succinate.

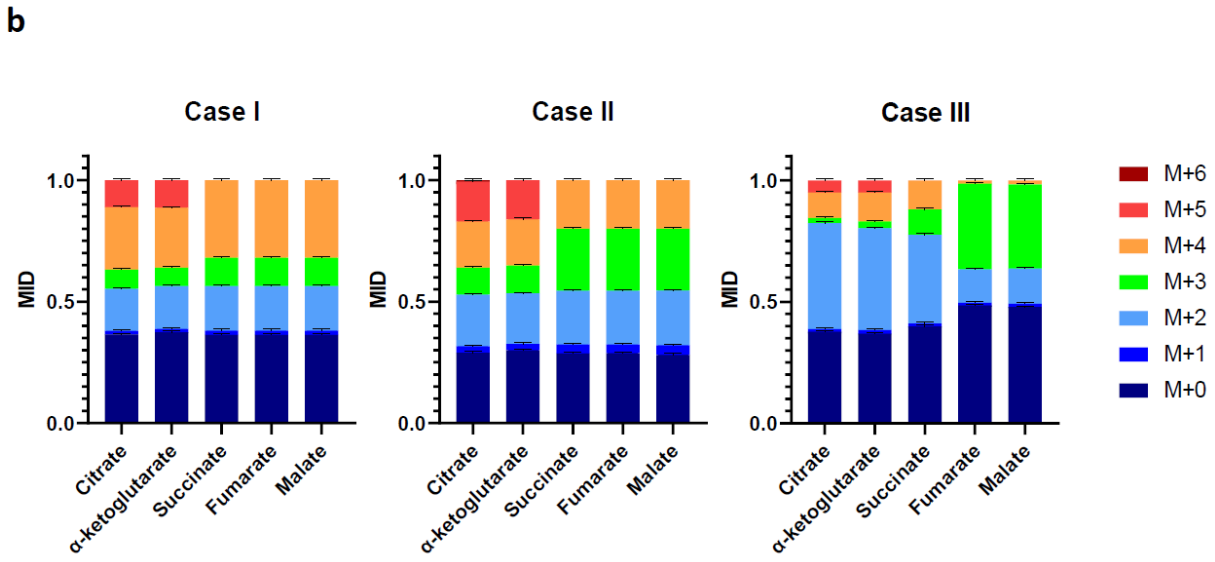

Figure 3.11 b. Mass isotopomer distributions (MIDs) of TCA cycle intermediates in three different cases.

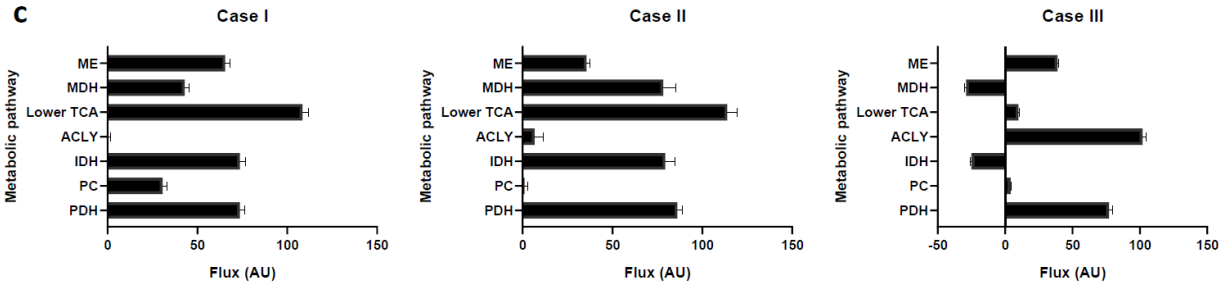

Figure 3.11 c. Metabolic fluxes of major TCA cycle and anaplerotic reactions in three different cases. Note that the following extracellular fluxes are fixed to constant across cases: glucose consumption rate, 100 AU; lactate excretion rate, 160 AU; glutamine consumption rate, 40 AU; glutamate excretion rate, 5 AU. Abbreviations: ME, malic enzyme reaction; MDH, malate dehydrogenase reaction; ACLY, ATP-citrate lyase reaction; IDH, isocitrate dehydrogenase reaction; PC, pyruvate carboxylase reaction; PDH, pyruvate dehydrogenase reaction; AU, arbitrary unit.

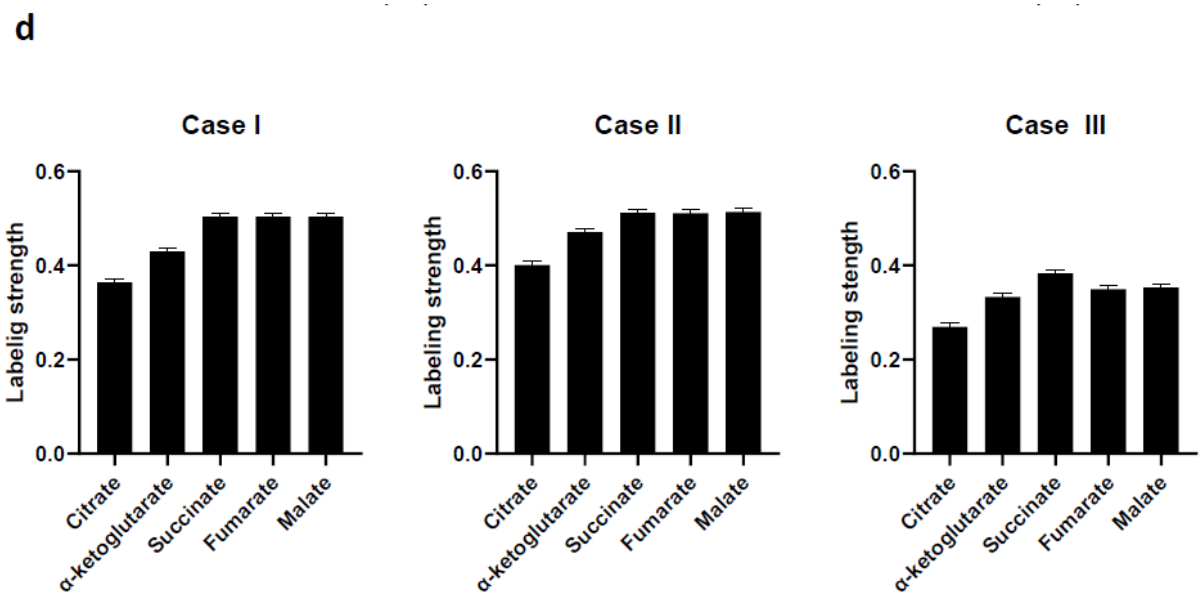

Figure 3.11 d. Labeling strength of TCA cycle intermediates in three different cases. Labeling strength is calculated based on the following equation: Labeling strength $= \sum_{i=0}^{n}(i \times m_i) / (n \times \sum_{i=0}^{n} m_i)$, where n is the number of carbon atoms in a metabolite, m_i the abundance of a mass isotopomer and i the labeling state (M+i) of a mass isotopomer.

Error bars, 0.005 for MIDs error (**b**), 95% confidence intervals (**c**) and propagated errors (**d**).

3.9 Discussion and conclusion

In this paper, we have reviewed common ^{13}C- and ^{2}H-isotopic tracers employed to investigate mammalian cell metabolism. Through detailed analysis of labeling profiles within central carbon metabolism, we demonstrate the capability of isotopic tracers to distinguish different substrate utilization patterns and determine relative magnitudes of competing pathways. Although similar information has been shown in the literature, it usually covers only a subset of tracers. Moreover, although the TCA cycle and PPP are crucial components of central carbon metabolism, the isotope enrichment profiles of TCA cycle and PPP intermediates are often explained in simplified scenarios. For example, only one round of cycling or one anaplerotic reaction is considered for the TCA cycle, and the labeling patterns within the non-oxidative PPP are often neglected. Here, we provide a comprehensive review of all major tracers used in investigating mammalian cell metabolism. The labeling profiles of those tracers are explained and analyzed with significant molecular details. We also believe our proposed roadmap for interpreting TCA cycle labeling patterns – artificial breakdowns of cycles and stepwise progressions of isotope transfers – offers a reliable and systematic approach to understand complex labeling results within a cyclic metabolic network. Additionally, the method of following the fates of multiple tracer molecules into the PPP is generally applicable to the analysis of pathways involving a series of scrambling reactions.

By explaining how tracers are used, we hope to support the notion that isotopic tracing techniques are powerful tools for investigating metabolic networks. Applications of selected ^{13}C- and ^{2}H-isotopic tracers are shown in Table 3.3-4. In short, ^{13}C-tracers are primarily used to study the central carbon metabolism including glycolysis, PPP and the TCA cycle. Metabolic fates of cofactors such as NAD(P)H and compartmentalized reactions are investigated by ^{2}H-tracers.

Moreover, a mixture of tracers can be designed and employed to precisely probe a specific pathway. For instance, labeling patterns from 1,2-$^{13}C_2$-glucose alone are not sufficient for estimating transketolase-like protein 1 (TKTL1) activity[44]. To address the issue, several equimolar mixtures of glucose tracers have been used to study TKTL1 and its interaction with the PPP[44,45].

In addition to dissecting biochemical reaction networks, isotopic tracers are also widely used for other applications. For example, the activity of competing metabolic enzymes can be compared through labeling experiments, since pathway activities are governed by the associated enzymes. Furthermore, isotopic tracing techniques are also implemented to examine enzymatic regulations on metabolic fluxes. If alterations of enzymatic activity result in no change of metabolic fluxes, the pathway controlled by the enzyme is considered to be a rigid node and thus heavily regulated. On the contrary, if metabolic fluxes can be manipulated with ease, a flexible node exists and suggests weak enzymatic regulation. One can therefore plot metabolic fluxes against enzyme activity to quantitatively assess corresponding regulatory behavior.

The last tracer application mentioned above relies on fluxes determined by MFA, a systems approach that integrates and analyzes metabolomics data. Through a case study where a single metabolic model is assigned with three different sets of MIDs, we demonstrate how ^{13}C-MFA fully resolves the distinct metabolic patterns that turn out to be challenging to interpret through analyses based solely on MIDs. It is worth noting that optimal selection of tracers is critical in MFA. Experimental and computational work has validated that 1,2-$^{13}C_2$-glucose, U-$^{13}C_5$-glutamine and U-$^{13}C_6$-glucose are some of the best tracers to investigate central carbon metabolism[46]. A genetic algorithm[47] and elementary metabolite units decomposition[48] have been used to propose novel tracers and tracer combinations to probe specific metabolic pathways.

Additionally, a new scoring system was recently applied to determine the optimal tracers for parallel labeling experiments[25]. Continued research in this area will improve the ability of ^{13}C-MFA to accurately and reliably resolve metabolic networks.

In addition to quantitatively estimating metabolic fluxes, ^{13}C-MFA can also be employed to discover new pathways. For instance, if one cannot fit isotopic labeling and extracellular flux data into a metabolic model, there is a chance that the proposed reaction network is incorrect. It is then recommended that the model should be modified by either supplementing or removing metabolic pathways. In many cases, additional metabolic pathways are likely to promote successful convergence. ^{13}C-MFA therefore indicates a possible existence of new pathways that have not been accounted for in the model. If the flux magnitudes of the new pathways are significant compared to those of existing ones, it further argues the importance of the newly included pathways in constituting the overall metabolic network. Conversely, successful convergence of a ^{13}C-MFA attempt indicates a representative depiction of a metabolic network, validating the notion that a complex metabolic system can be simplified and modeled accordingly without significant loss of information. We believe that the applications of ^{13}C-MFA and other similar approaches such as flux balance analysis (FBA)[49] and metabolic control analysis (MCA)[50] can considerably enhance the power of isotopic tracing techniques, facilitating a better understanding toward complex yet important metabolic behavior in mammalian cells.

Table 3.3. Applications of selected ^{13}C-isotopic tracers.

Tracers	Pathways	Descriptions	References
U-$^{13}C_6$-glucose	TCA cycle	^{13}C is introduced to the TCA cycle via various routes such as PDH, PC, ME and PEPCK reactions, yielding complex labeling results	24–26
1,2-$^{13}C_2$-glucose	oxPPP	Differential labeling patterns in lactate and pyruvate are generated along glycolysis and the oxPPP	17,51
2-^{13}C-glucose			
3-^{13}C-glucose			
U-$^{13}C_5$-glutamine	Glutamine metabolism	Oxidative TCA cycle and reductive metabolism of glutamine result in different labeling patterns in TCA cycle intermediates	19
1-^{13}C-glutamine			
5-^{13}C-glutamine			
1-^{13}C-glucose	Acetate anaplerosis	Need specific tracking of first round labeling results to examine M+1 labeled TCA cycle intermediates	15
1,6-$^{13}C_2$-glucose			
1,2-$^{13}C_2$-acetate		Produce M+2 labeled TCA cycle intermediates within the first round	
4,5,6-$^{13}C_3$-glucose	Non-oxidative PPP	Differential labeling patterns in F6(B)P are generated along glycolysis and the non-oxidative PPP	32,44
3-^{13}C-glucose	Pyruvate carboxylase reaction	^{13}C is retained in the TCA cycle through pyruvate carboxylase but lost through pyruvate dehydrogenase (Figure S3)	52,53

Table 3.4. Applications of selected ^{2}H-isotopic tracers.

Tracers	Metabolite targets	Pathways	Descriptions	References
1-^{2}H-glucose	NADPH	G6PD/ oxPPP	^{2}H is transferred to $NADP^{+}$, yielding $NADP^{2}H$. NADPH labeling fraction can be assessed for measurement of oxPPP activity	34,54
3-^{2}H-glucose				
4-^{2}H-glucose	NADH	MDH, LDH	^{2}H is transferred to NAD^{+} during glycolysis and ^{2}H-labeled NADH subsequently transfers ^{2}H to central carbon metabolites such as lactate and malate	
3,3-$^{2}H_2$-serine	NADPH	SHMT, MTHFD/Folate metabolism	The directionality of folate metabolism for the production of NADPH is determined by tracers with 2-hydroxyglutarate measurement, which is heterologously expressed as a reporter system	
2,3,3-$^{2}H_3$-serine				
2,2-$^{2}H_2$-glycine				
2,2,3,3-$^{2}H_4$-dimethyl succinate	NADPH, lipids	Malic enzyme-dependent NADPH production and lipogenesis pathway	Malic enzyme-dependent NADPH production was traced in differentiating adipocytes	36
$^{2}H_2O$	NADPH	Solvent-NADPH interaction	^{2}H transfer between NADPH and water is mediated by flavin enzymes as direct H-D exchange and is intrinsically limited in C-H bonds of NADPH	38
	lipids	Lipogenesis pathway	Mass isotopomer analysis for $^{2}H_2O$ incorporated in fatty acids allows the measurement of fatty acid and cholesterol synthesis	38,41,55
	Amino acids (alanine, glycine and leucine)	Amino acid synthesis	Mass isotopomer analysis for $^{2}H_2O$ utilized in alanine, glycine and leucine in various tissues measures turnover rates of respective amino acid synthesis	56

3.10 Nomenclature

5,10-methyl-THF: 5,10-methylenetetrahydrofolate

6PG: 6-phosphogluconate

6PGD: 6-phosphogluconate dehydrogenase

AcCoA: acetyl-CoA

ACLY: ATP-citrate lyase

CO_2: carbon dioxide

CS: citrate synthase

DHAP: dihydroxyacetone phosphate

E4P: erythrose-4-phosphate

F6P: fructose-6-phosphate

$FADH_2$: flavin adenine dinucleotide

FBA: flux balance analysis

FBP: fructose 1,6-bisphosphate

FH: fumarase

G6P: glucose-6-phosphate

G6PD: glucose-6-phosphate dehydrogenase

GAP: 3-phosphoglyceraldehyde

GAPDH: glyceraldehyde 3-phosphate dehydrogenase

Glyc-3P: glycerol 3-phosphate

IDH: isocitrate dehydrogenase

LDH: lactate dehydrogenase

MCA: metabolic control analysis

MDH: malate dehydrogenase

ME: malic enzyme

MFA: metabolic flux analysis

MID: mass isotopomer distribution

MTFHD: methylenetetrahydrofolate dehydrogenase

NADH: nicotinamide adenine dinucleotide

NADPH: nicotinamide adenine dinucleotide phosphate

OGDC: α-ketoglutarate dehydrogenase

oxPPP: oxidative pentose phosphate

PC: pyruvate carboxylase

PDH: pyruvate dehydrogenase

PEPCK: phosphoenolpyruvate carboxykinase

PPP: pentose phosphate pathway

Pyr: pyruvate

R5P: ribose-5-phosphate

Ru5P: ribulose-5-phosphate

S7P: sedoheptulose-7-phosphate

SHMT: serine hydroxymethyltransferase

SCS: succinyl-CoA synthetase

SDH: succinate dehydrogenase

TAL: transaldolase

TCA: tricarboxylic acid

TKT: transketolase

TKTL1: transketolase-like protein 1

TPI: triose phosphate isomerase

Xu5P: xylulose-5-phosphate

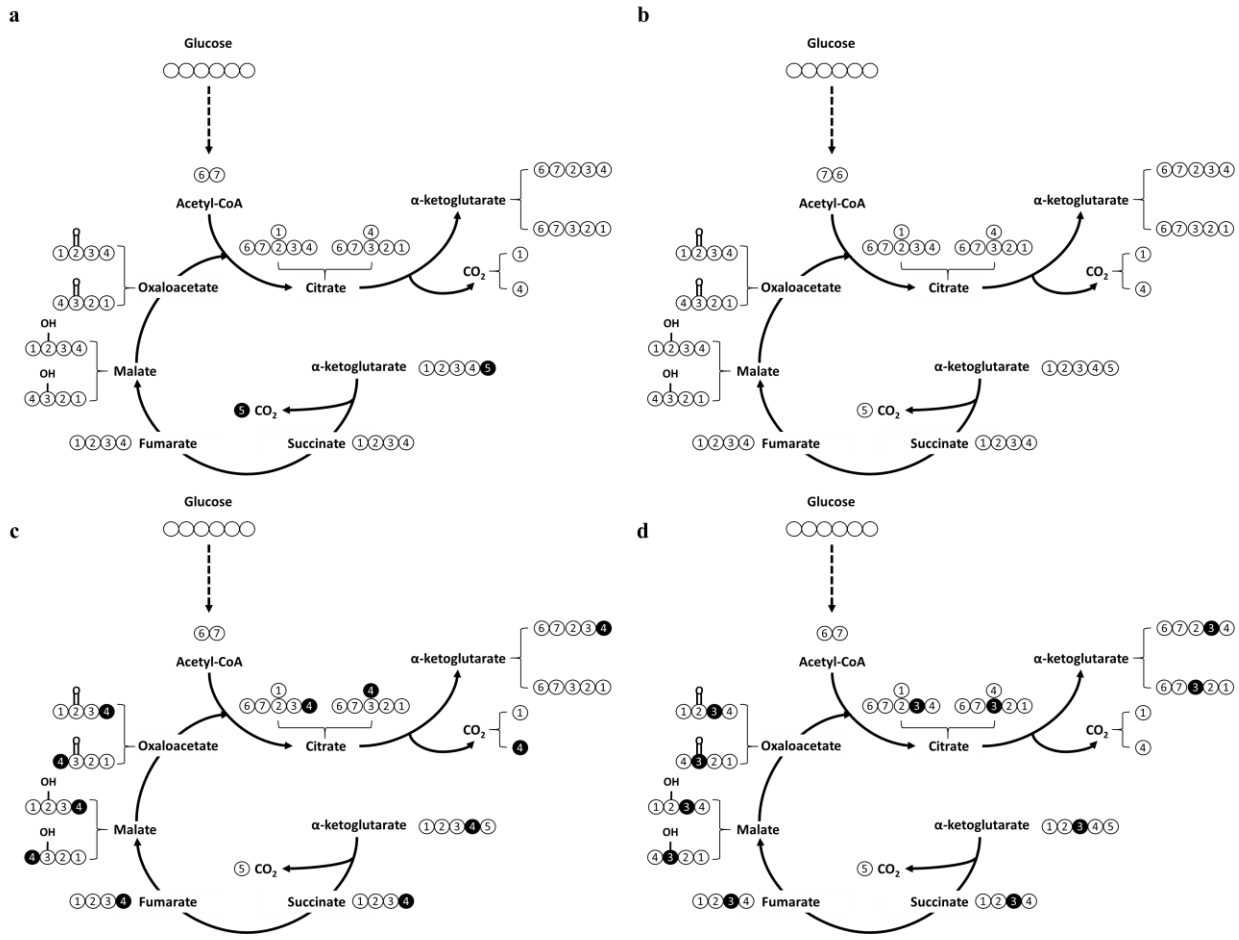

Figure 3.12. Labeling patterns of TCA cycle intermediates by U-$^{13}C_5$-glutamine dominated by pyruvate dehydrogenase (PDH) that supplies unlabeled acetyl-CoA (AcCoA).

a, Labeling results after the fourth round of cycling by 5-^{13}C-α-ketoglutarate. This fourth round generates unlabeled α-ketoglutarate.

b, Labeling results after the fourth round of cycling by unlabeled-α-ketoglutarate. This fourth round generates unlabeled α-ketoglutarate.

c, Labeling results after the fourth round of cycling by 4-^{13}C-α-ketoglutarate. This fourth round generates 5-^{13}C-and unlabeled α-ketoglutarate.

d, Labeling results after the fourth round of cycling by 5-^{13}C-α-ketoglutarate. This fourth round generates 4-^{13}C-and 3-^{13}C-α-ketoglutarate.

Carbon number is ordered consistent with the atomic sequence as shown in Figure 4a, and is associated with the same carbon throughout the diagram for the purpose of tracing, rather than following IUPAC naming rules. α-ketoglutarate: 1, carboxyl; 2, methylene bridge; 3, methylene bridge; 4, carbonyl; 5, carboxyl. AcCoA: 6, carbonyl; 7, methyl. Scrambling of labeling results is shown for malate and oxaloacetate, but not for fumarate and succinate due to molecular symmetry. Hydroxyl and carbonyl groups are drawn in malate and oxaloacetate, respectively. Filled and empty circles refer to ^{13}C- and ^{12}C-labeled carbon atoms, respectively. Solid and dashed arrows refer to single- or multi-step reactions, respectively.

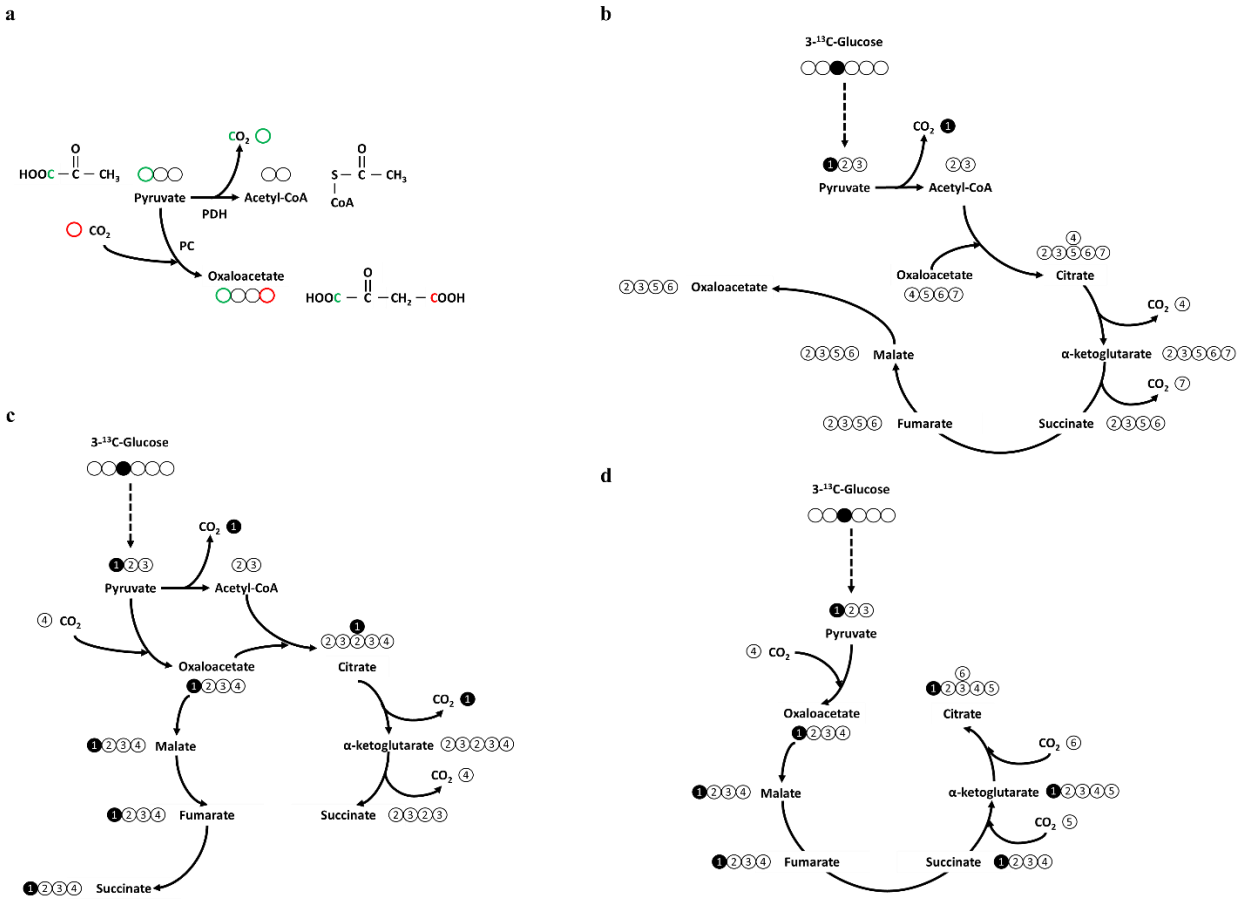

Figure 3.13. First round labeling patterns of TCA cycle intermediates by 3-^{13}C-glucose**.**

a, Chemical structures and carbon transition maps highlighting the positional information through the PC reaction. Circles represent carbon atoms with the same position as referenced to the actual chemical structures of the metabolites. Carbon atoms highlighted in red indicate how CO_2 is combined with pyruvate through the PC reaction to make oxaloacetate. Carbon atoms highlighted in green indicate how the carboxyl group in pyruvate is cleaved through the PDH reaction to make AcCoA.

b, The ^{13}C atom is lost when the tracer-derived 1-^{13}C-pyruvate is metabolized through the PDH reaction.

c, The ^{13}C atom is retained when the tracer-derived 1-^{13}C-pyruvate is metabolized through the PC reaction. The pattern assumes that PC flux cannot reverse the entire TCA cycle but dominates the labeling patterns along the reversible reactions within the cycle.

d, The ^{13}C atom is retained when the tracer-derived 1-^{13}C-pyruvate is metabolized through the PC reaction. The pattern assumes that PC flux totally reverses and dominates the entire TCA cycle.

Carbon number is ordered consistent with the atomic sequence as shown in Figure a, and is associated with the same carbon throughout the diagram for the purpose of tracing, rather than following IUPAC naming rules. Pyruvate: 1, carboxyl; 2, carbonyl; 3, methyl. Oxaloacetate: 4, carboxyl; 5, carbonyl; 6, methylene bridge; 7, carboxyl. Scrambling of labeling results is not shown. Filled and empty circles refer to ^{13}C- and ^{12}C-labeled carbon atoms, respectively.

Table 3.5. Biochemical reactions and carbon atom transitions used in ^{13}C-MFA.

Single- and double-headed arrows refer to unidirectional and bidirectional reactions, respectively. Abbreviations are the same as noted in the main text of the paper. Letters in the bracket indicate the position of carbon atoms. The subscript .x refers to extracellular localization, .c cytosolic localization, .m mitochondrial localization, .mnt measurement.

<u>Extracellular fluxes and biomass production</u>	
Glc.x (abcdef) -> Pyr.c (cba) + Pyr.c (def)	Glucose import and pyruvate generation
Lac (abc) → Lac.x (abc)	Lactate export
Gln.x (abcde) → Gln (abcde)	Glutamine import
Glu (abcde) → Glu.x (abcde)	Glutamate export
<u>Scaling fluxes</u>	
Pyr.mnt (abc) → Pyr.fix (abc)	Pyruvate scaling flux
<u>Lactate production</u>	
Pyr.c (abc) ↔ Lac (abc)	Lactate dehydrogenase
<u>TCA cycle and anaplerotic fluxes</u>	
Pyr.m (abc) + CO2 (d) → Oac (abcd)	Pyruvate carboxylase
Mal (abcd) ↔ Pyr.m (abc) + CO2 (d)	Malic enzyme
Glu (abcde) ↔ Akg (abcde)	Glutamate trans/deaminases
Gln (abcde) ↔ Glu (abcde)	Glutaminase
Pyr.m (abc) → AcCoA.m (bc) + CO2 (a)	Pyruvate dehydrogenase
AcCoA.m (ab) + Oac (cdef) → Cit (fedbac)	Citrate synthase
Cit (abcdef) ↔ Akg (abcde) + CO2 (f)	Aconitase and isocitrate dehydrogenase
Akg (abcde) → Suc (bcde) + CO2 (a)	α-ketoglutarate dehydrogenase and succinyl-CoA synthetase
Suc (abcd) ↔ Fum (abcd)	Succinate dehydrogenase

Fum (abcd) ↔ Mal (abcd)	Fumarase
Mal (abcd) ↔ Oac (abcd)	Malate dehydrogenase
Oac (abcd) ↔ Asp (abcd)	Transaminases

Fatty acid synthesis

Cit (abcdef) → AcCoA.c (ed) + Oac (fcba)	ATP-citrate lyase
AcCoA.c (ab) → FA (ab)	Fatty acid synthase

Dilution and mixing fluxes

0 Pyr.c (abc) → Pyr.mnt (abc)	Pyruvate compartmentalization (from cytosol)
0 Pyr.m (abc) → Pyr.mnt (abc)	Pyruvate compartmentalization (from mitochondria)

Compartmentalized reactions

Pyr.c (abc) ↔ Pyr.m (abc)

Pyruvate compartmentalization (between cytosol and mitochondrion)

Table 3.6. ^{13}C-MFA results for Case I. Unit of fluxes and 95% confidence intervals is arbitrary (AU).

Pathway	Directionality	Flux	95% confidence interval	
			Lower bound	Upper bound
Glc.x → Pyr.c + Pyr.c	net	99.86	97.9	101.3
Lac → Lac.x	net	160.9	158.1	163.9
Gln.x→ Gln	net	39.82	39.05	40.59
Glu → Glu.x	net	5.003	4.905	5.1
Pyr.mnt → Pyr.fix	net	1	1	1
Pyr.c ↔ Lac	net	160.9	158.1	163.9
	exch	2.248	0	Inf
Pyr.m + CO2 → Oac	net	3.07E+01	28.15	32.76
Mal ↔ Pyr.m + CO2	net	65.51	62.72	68
	exch	1E-07	0	1.192
Glu ↔ Akg	net	34.82	34.06	35.59
	exch	4.12E+02	2.45E+01	Inf
Gln ↔ Glu	net	39.82	39.05	40.59
	exch	0.2744	0	Inf
Pyr.m → AcCoA.m + CO2	net	73.68	68.74	76.31
AcCoA.m + Oac → Cit	net	73.68	68.74	76.31
Cit ↔ Akg + CO2	net	73.68	68.7	76.33
	exch	5965000	3138	Inf
Akg → Suc + CO2	net	108.5	103.4	111.7
Suc ↔ Fum	net	108.5	103.4	111.7
	exch	3724000	0	Inf
Fum ↔ Mal	net	108.5	103.4	111.7
	exch	3.83E+03	0	Inf
Mal ↔ Oac	net	42.98	39.72	44.76
	exch	-0.00027	0	2.85
Oac ↔ Asp	net	0	0	0
	exch	0.3623	0	Inf
Cit → AcCoA.c + Oac	net	1E-07	0	1.7
AcCoA.c → FA	net	1E-07	0	1.7
0 Pyr.c → Pyr.mnt	net	0.192	0	1
0 Pyr.m → Pyr.mnt	net	0.808	0	1
Pyr.c ↔ Pyr.m	net	38.87	33.96	41.02
	exch	10000000	5154	Inf

Table 3.7. ^{13}C-MFA results for Case II. Unit of fluxes and 95% confidence intervals is arbitrary (AU).

Pathway	Directionality	Flux	95% confidence interval	
			Lower bound	Upper bound
Glc.x → Pyr.c + Pyr.c	net	103.5	102.1	104.9
Lac → Lac.x	net	155.5	152.9	158.1
Gln.x→ Gln	net	39.58	38.81	40.35
Glu → Glu.x	net	5.007	4.909	5.104
Pyr.mnt → Pyr.fix	net	1	1	1
Pyr.c ↔ Lac	net	155.5	152.9	158.1
	exch	75.21	0	Inf
Pyr.m + CO2 → Oac	net	1.04E+00	0	2.809
Mal ↔ Pyr.m + CO2	net	35.62	33.91	37.43
	exch	9.534	6.853	12.43
Glu ↔ Akg	net	34.57	33.8	35.35
	exch	1.00E-07	0.00E+00	3.658
Gln ↔ Glu	net	39.58	38.81	40.35
	exch	3.036	0	Inf
Pyr.m → AcCoA.m + CO2	net	86.1	83.53	88.67
AcCoA.m + Oac → Cit	net	86.1	83.53	88.67
Cit ↔ Akg + CO2	net	79.36	75.19	85.3
	exch	1699	978.8	3560
Akg → Suc + CO2	net	113.9	109.6	120.3
Suc ↔ Fum	net	113.9	109.6	120.3
	exch	10000000	474.5	Inf
Fum ↔ Mal	net	113.9	109.6	120.3
	exch	1.53E+04	457.3	Inf
Mal ↔ Oac	net	78.32	72.81	85.51
	exch	1E-07	0	29.57
Oac ↔ Asp	net	0	0	0
	exch	0.4047	0	Inf
Cit → AcCoA.c + Oac	net	6.74	1.227	10.97
AcCoA.c → FA	net	6.74	1.227	10.97
0 Pyr.c → Pyr.mnt	net	0.8418	0	1
0 Pyr.m → Pyr.mnt	net	0.1582	0	1
Pyr.c ↔ Pyr.m	net	51.53	49.39	53.71
	exch	212.4	160.7	300.2

Table 3.8. ^{13}C-MFA results for Case III. Unit of fluxes and 95% confidence intervals is arbitrary (AU).

Pathway	Directionality	Flux	95% confidence interval	
			Lower bound	Upper bound
Glc.x → Pyr.c + Pyr.c	net	100.7	99.36	102.1
Lac → Lac.x	net	159.2	156.7	161.8
Gln.x→ Gln	net	39.92	39.23	40.68
Glu → Glu.x	net	5.001	4.903	5.098
Pyr.mnt → Pyr.fix	net	1	1	1
Pyr.c ↔ Lac	net	159.2	156.7	161.8
	exch	1.801	0	Inf
Pyr.m + CO2 → Oac	net	4.03E+00	2.765	5.177
Mal ↔ Pyr.m + CO2	net	38.95	37.44	40.44
	exch	35.76	33.92	37.54
Glu ↔ Akg	net	34.92	34.22	35.68
	exch	9.90E-08	0.00E+00	18.05
Gln ↔ Glu	net	39.92	39.23	40.68
	exch	0.1188	0	Inf
Pyr.m → AcCoA.m + CO2	net	77.14	74.49	80.57
AcCoA.m + Oac → Cit	net	77.14	74.49	80.57
Cit ↔ Akg + CO2	net	-24.96	-26.41	-23.69
	exch	10000000	2773	Inf
Akg → Suc + CO2	net	9.956	8.657	11.13
Suc ↔ Fum	net	9.956	8.657	11.13
	exch	3.271	2.772	3.787
Fum ↔ Mal	net	9.956	8.657	11.13
	exch	5.50E+06	650.5	Inf
Mal ↔ Oac	net	-28.99	-31.22	-26.93
	exch	32.21	27.89	36.63
Oac ↔ Asp	net	0	0	0
	exch	0.8227	0	Inf
Cit → AcCoA.c + Oac	net	102.1	98.57	105.8
AcCoA.c → FA	net	102.1	98.57	105.8
0 Pyr.c → Pyr.mnt	net	0.3502	0	1
0 Pyr.m → Pyr.mnt	net	0.6498	0	1
Pyr.c ↔ Pyr.m	net	42.22	40.06	45.53
	exch	10000000	1484	Inf

3.11 References

(1) Hsu, P. P.; Sabatini, D. M. Cancer Cell Metabolism: Warburg and Beyond. *Cell* **2008**, *134* (5), 703–707.

(2) Pavlova, N. N.; Thompson, C. B. The Emerging Hallmarks of Cancer Metabolism. *Cell Metab.* **2016**, *23* (1), 27–47.

(3) Vander Heiden, M. G. Targeting Cancer Metabolism: A Therapeutic Window Opens. *Nat. Rev. Drug Discov.* **2011**, *10* (9), 671–684.

(4) Boden, G. Effects of Free Fatty Acids (FFA) on Glucose Metabolism: Significance for Insulin Resistance and Type 2 Diabetes. *Exp. Clin. Endocrinol. Diabetes* **2003**, *111* (3), 121–124.

(5) Krycer, J. R.; Yugi, K.; Hirayama, A.; Fazakerley, D. J.; Quek, L. E.; Scalzo, R.; Ohno, S.; Hodson, M. P.; Ikeda, S.; Shoji, F.; Suzuki, K.; Domanova, W.; Parker, B. L.; Nelson, M. E.; Humphrey, S. J.; Turner, N.; Hoehn, K. L.; Cooney, G. J.; Soga, T.; et al. Dynamic Metabolomics Reveals That Insulin Primes the Adipocyte for Glucose Metabolism. *Cell Rep.* **2017**, *21* (12), 3536–3547.

(6) Muoio, D. M.; Newgard, C. B. Mechanisms of Disease: Molecular and Metabolic Mechanisms of Insulin Resistance and β-Cell Failure in Type 2 Diabetes. *Nat. Rev. Mol. Cell Biol.* **2008**, *9* (3), 193–205.

(7) Shyh-Chang, N.; Daley, G. Q.; Cantley, L. C. Stem Cell Metabolism in Tissue Development and Aging. *Development* **2013**, *140* (12), 2535–2547.

(8) Zhang, J.; Ratanasirintrawoot, S.; Chandrasekaran, S.; Wu, Z.; Ficarro, S. B.; Yu, C.;

Ross, C. A.; Cacchiarelli, D.; Xia, Q.; Seligson, M.; Shinoda, G.; Xie, W.; Cahan, P.; Wang, L.; Ng, S. C.; Tintara, S.; Trapnell, C.; Onder, T.; Loh, Y. H.; et al. LIN28 Regulates Stem Cell Metabolism and Conversion to Primed Pluripotency. *Cell Stem Cell* **2016**, *19* (1), 66–80.

(9) Folmes, C. D. L.; Dzeja, P. P.; Nelson, T. J.; Terzic, A. Metabolic Plasticity in Stem Cell Homeostasis and Differentiation. *Cell Stem Cell* **2012**, *11* (5), 596–606.

(10) O'Neill, L. A. J.; Kishton, R. J.; Rathmell, J. A Guide to Immunometabolism for Immunologists. *Nat. Rev. Immunol.* **2016**, *16* (9), 553–565.

(11) Mathis, D.; Shoelson, S. E. Immunometabolism: An Emerging Frontier. *Nat. Rev. Immunol.* **2011**, *11* (2), 81.

(12) Vodnala, S. K.; Eil, R.; Kishton, R. J.; Sukumar, M.; Yamamoto, T. N.; Ha, N. H.; Lee, P. H.; Shin, M. H.; Patel, S. J.; Yu, Z.; Palmer, D. C.; Kruhlak, M. J.; Liu, X.; Locasale, J. W.; Huang, J.; Roychoudhuri, R.; Finkel, T.; Klebanoff, C. A.; Restifo, N. P. T Cell Stemness and Dysfunction in Tumors Are Triggered by a Common Mechanism. *Science* **2019**, *363* (6434).

(13) Adeva-Andany, M.; López-Ojén, M.; Funcasta-Calderón, R.; Ameneiros-Rodríguez, E.; Donapetry-García, C.; Vila-Altesor, M.; Rodríguez-Seijas, J. Comprehensive Review on Lactate Metabolism in Human Health. *Mitochondrion* **2014**, *17*, 76–100.

(14) Atkinson, C.; Frankenfeld, C. L.; Lampe, J. W. Gut Bacterial Metabolism of the Soy Isoflavone Daidzein: Exploring the Relevance to Human Health. *Exp. Biol. Med.* **2005**, *230* (3), 155–170.

(15) Deelchand, D. K.; Nelson, C.; Shestov, A. A.; Uğurbil, K.; Henry, P. G. Simultaneous Measurement of Neuronal and Glial Metabolism in Rat Brain in Vivo Using Co-Infusion of [1,6-13C2]Glucose and [1,2-13C2]Acetate. *J. Magn. Reson.* **2009**, *196* (2), 157–163.

(16) De Feyter, H. M.; Mason, G. F.; Shulman, G. I.; Rothman, D. L.; Petersen, K. F. Increased Brain Lactate Concentrations without Increased Lactate Oxidation during Hypoglycemia in Type 1 Diabetic Individuals. *Diabetes* **2013**, *62* (9), 3075–3080.

(17) Brekke, E. M. F.; Walls, A. B.; Schousboe, A.; Waagepetersen, H. S.; Sonnewald, U. Quantitative Importance of the Pentose Phosphate Pathway Determined by Incorporation of 13 C from 2-13 C-and 3-13 Cglucose into TCA Cycle Intermediates and Neurotransmitter Amino Acids in Functionally Intact Neurons. *J. Cereb. Blood Flow Metab.* **2012**, *32* (9), 1788–1799.

(18) Dong, W.; Keibler, M. A.; Stephanopoulos, G. Review of Metabolic Pathways Activated in Cancer Cells as Determined through Isotopic Labeling and Network Analysis. *Metab. Eng.* **2017**, *43*, 113–124.

(19) Metallo, C. M.; Gameiro, P. A.; Bell, E. L.; Mattaini, K. R.; Yang, J.; Hiller, K.; Jewell, C. M.; Johnson, Z. R.; Irvine, D. J.; Guarente, L.; Kelleher, J. K.; Vander Heiden, M. G.; Iliopoulos, O.; Stephanopoulos, G. Reductive Glutamine Metabolism by IDH1 Mediates Lipogenesis under Hypoxia. *Nature* **2012**, *481* (7381), 380–384.

(20) Srivastava, S.; Chan, C. Application of Metabolic Flux Analysis to Identify the Mechanisms of Free Fatty Acid Toxicity to Human Hepatoma Cell Line. *Biotechnol Bioeng.* **2008**, *99* (2), 399–410.

(21) Antoniewicz, M. R. A Guide to 13C Metabolic Flux Analysis for the Cancer Biologist.

Exp. Mol. Med. **2018**, *50* (4), 19.

(22) Long, C. P.; Antoniewicz, M. R. High-Resolution 13C Metabolic Flux Analysis. *Nat. Protoc.* **2019**, *14* (10), 2856–2877.

(23) Buescher, J. M.; Antoniewicz, M. R.; Boros, L. G.; Burgess, S. C.; Brunengraber, H.; Clish, C. B.; DeBerardinis, R. J.; Feron, O.; Frezza, C.; Ghesquiere, B.; Gottlieb, E.; Hiller, K.; Jones, R. G.; Kamphorst, J. J.; Kibbey, R. G.; Kimmelman, A. C.; Locasale, J. W.; Lunt, S. Y.; Maddocks, O. D. K.; et al. A Roadmap for Interpreting 13C Metabolite Labeling Patterns from Cells. *Curr. Opin. Biotechnol.* **2015**, *34*, 189–201.

(24) Jang, C.; Chen, L.; Rabinowitz, J. D. Leading Edge Primer Metabolomics and Isotope Tracing. *Cell* **2018**, *173*, 822–837.

(25) Crown, S. B.; Long, C. P.; Antoniewicz, M. R. Optimal Tracers for Parallel Labeling Experiments and 13 C Metabolic Flux Analysis: A New Precision and Synergy Scoring System. *Metab. Eng.* **2016**, *38*, 10–18.

(26) Green, C. R.; Wallace, M.; Divakaruni, A. S.; Phillips, S. A.; Murphy, A. N.; Ciaraldi, T. P.; Metallo, C. M. Branched-Chain Amino Acid Catabolism Fuels Adipocyte Differentiation and Lipogenesis. *Nat. Chem. Biol.* **2016**, *12* (1), 15–21.

(27) Mullen, A. R.; Wheaton, W. W.; Jin, E. S.; Chen, P. H.; Sullivan, L. B.; Cheng, T.; Yang, Y.; Linehan, W. M.; Chandel, N. S.; Deberardinis, R. J. Reductive Carboxylation Supports Growth in Tumour Cells with Defective Mitochondria. *Nature* **2012**, *481* (7381), 385–388.

(28) Gameiro, P. A.; Yang, J.; Metelo, A. M.; Pérez-Carro, R.; Baker, R.; Wang, Z.; Arreola,

A.; Rathmell, W. K.; Olumi, A.; López-Larrubia, P.; Stephanopoulos, G.; Iliopoulos, O. In Vivo HIF-Mediated Reductive Carboxylation Is Regulated by Citrate Levels and Sensitizes VHL-Deficient Cells to Glutamine Deprivation. *Cell Metab.* **2013**, *17* (3), 372–385.

(29) Fendt, S. M.; Bell, E. L.; Keibler, M. A.; Davidson, S. M.; Wirth, G. J.; Fiske, B.; Mayers, J. R.; Schwab, M.; Bellinger, G.; Csibi, A.; Patnaik, A.; Blouin, M. J.; Cantley, L. C.; Guarente, L.; Blenis, J.; Pollak, M. N.; Olumi, A. F.; Vander Heiden, M. G.; Stephanopoulos, G. Metformin Decreases Glucose Oxidation and Increases the Dependency of Prostate Cancer Cells on Reductive Glutamine Metabolism. *Cancer Res.* **2013**, *73* (14), 4429–4438.

(30) Cruz, N. F.; Lasater, A.; Zielke, H. R.; Dienel, G. A. Activation of Astrocytes in Brain of Conscious Rats during Acoustic Stimulation: Acetate Utilization in Working Brain. *J. Neurochem.* **2005**, *92* (4), 934–947.

(31) Patra, K. C.; Hay, N. The Pentose Phosphate Pathway and Cancer. *Trends Biochem. Sci.* **2014**, *39* (8), 347–354.

(32) Ahn, W. S.; Dong, W.; Zhang, Z.; Cantor, J. R.; Sabatini, D. M.; Iliopoulos, O.; Stephanopoulos, G. Glyceraldehyde 3-Phosphate Dehydrogenase Modulates Nonoxidative Pentose Phosphate Pathway to Provide Anabolic Precursors in Hypoxic Tumor Cells. *AIChE J.* **2018**, *64* (12), 4289–4296.

(33) Stincone, A.; Prigione, A.; Cramer, T.; Wamelink, M. M. C.; Campbell, K.; Cheung, E.; Olin-Sandoval, V.; Grüning, N. M.; Krüger, A.; Tauqeer Alam, M.; Keller, M. A.; Breitenbach, M.; Brindle, K. M.; Rabinowitz, J. D.; Ralser, M. The Return of Metabolism:

Biochemistry and Physiology of the Pentose Phosphate Pathway. *Biol. Rev.* **2015**, *90* (3), 927–963.

(34) Lewis, C. A.; Parker, S. J.; Fiske, B. P.; McCloskey, D.; Gui, D. Y.; Green, C. R.; Vokes, N. I.; Feist, A. M.; Vander Heiden, M. G.; Metallo, C. M. Tracing Compartmentalized NADPH Metabolism in the Cytosol and Mitochondria of Mammalian Cells. *Mol. Cell* **2014**, *55* (2), 253–263.

(35) Fan, J.; Ye, J.; Kamphorst, J. J.; Shlomi, T.; Thompson, C. B.; Rabinowitz, J. D. Quantitative Flux Analysis Reveals Folate-Dependent NADPH Production. *Nature* **2014**, *10* (7504), 298–302.

(36) Liu, L.; Shah, S.; Fan, J.; Park, J. O.; Wellen, K. E.; Rabinowitz, J. D. Malic Enzyme Tracers Reveal Hypoxia-Induced Switch in Adipocyte NADPH Pathway Usage. *Nat. Chem. Biol.* **2016**, *12* (5), 345–352.

(37) Grassian, A. R.; Parker, S. J.; Davidson, S. M.; Divakaruni, A. S.; Green, C. R.; Zhang, X.; Slocum, K. L.; Pu, M.; Lin, F.; Vickers, C.; Joud-Caldwell, C.; Chung, F.; Yin, H.; Handly, E. D.; Straub, C.; Growney, J. D.; Vander Heiden, M. G.; Murphy, A. N.; Pagliarini, R.; et al. IDH1 Mutations Alter Citric Acid Cycle Metabolism and Increase Dependence on Oxidative Mitochondrial Metabolism. *Cancer Res.* **2014**, *74* (12), 3317–3331.

(38) Zhang, Z.; Chen, L.; Liu, L.; Su, X.; Rabinowitz, J. D. Chemical Basis for Deuterium Labeling of Fat and NADPH. *J. Am. Chem. Soc.* **2017**, *139* (41), 14368–14371.

(39) Katz, J.; Rognstad, R. Futile Cycling in Glucose Metabolism. *Trends Biochem. Sci.* **1978**, *3* (3), 171–174.

(40) Hermes, J. D.; Roeske, C. A.; O'Leary, M. H.; Cleland, W. W. Use of Multiple Isotope Effects To Determine Enzyme Mechanisms and Intrinsic Isotope Effects. Malic Enzyme and Glucose-6-Phosphate Dehydrogenase. *Biochemistry* **1982**, *21* (20), 5106–5114.

(41) Lee, W. N.; Bassilian, S.; Ajie, H. O.; Schoeller, D. A.; Edmond, J.; Bergner, E. A.; Byerley, L. O. In Vivo Measurement of Fatty Acids and Cholesterol Synthesis Using D2O and Mass Isotopomer Analysis. *Am. J. Physiol. Metab.* **1994**, *266* (5), E699–E708.

(42) Leighty, R. W.; Antoniewicz, M. R. Dynamic Metabolic Flux Analysis (DMFA): A Framework for Determining Fluxes at Metabolic Non-Steady State. *Metab. Eng.* **2011**, *13* (6), 745–755.

(43) Antoniewicz, M. R.; Kelleher, J. K.; Stephanopoulos, G. Elementary Metabolite Units (EMU): A Novel Framework for Modeling Isotopic Distributions. *Metab. Eng.* **2007**, *9* (1), 68–86.

(44) Ahn, W. S.; Crown, S. B.; Antoniewicz, M. R. Evidence for Transketolase-like TKTL1 Flux in CHO Cells Based on Parallel Labeling Experiments and 13C-Metabolic Flux Analysis. *Metab. Eng.* **2016**, *37*, 72–78.

(45) Diaz-Moralli, S.; Aguilar, E.; Marin, S.; Coy, J. F.; Dewerchin, M.; Antoniewicz, M. R.; Meca-Cortés, O.; Notebaert, L.; Ghesquière, B.; Eelen, G.; Thomson, T. M.; Carmeliet, P.; Cascante, M. A Key Role for Transketolase-like 1 in Tumor Metabolic Reprogramming. *Oncotarget* **2016**, *7* (32).

(46) Metallo, C. M.; Walther, J. L.; Stephanopoulos, G. Evaluation of 13C Isotopic Tracers for Metabolic Flux Analysis in Mammalian Cells. *J. Biotechnol.* **2009**, *144* (3), 167–174.

(47) Walther, J. L.; Metallo, C. M.; Zhang, J.; Stephanopoulos, G. Optimization of 13C Isotopic Tracers for Metabolic Flux Analysis in Mammalian Cells. *Metab. Eng.* **2012**, *14* (2), 162–171.

(48) Crown, S. B.; Ahn, W. S.; Antoniewicz, M. R. Rational Design of 13C-Labeling Experiments for Metabolic Flux Analysis in Mammalian Cells. *BMC Syst. Biol.* **2012**, *6* (43).

(49) Heirendt, L.; Arreckx, S.; Pfau, T.; Mendoza, S. N.; Richelle, A.; Heinken, A.; Haraldsdóttir, H. S.; Wachowiak, J.; Keating, S. M.; Vlasov, V.; Magnusdóttir, S.; Ng, C. Y.; Preciat, G.; Žagare, A.; Chan, S. H. J.; Aurich, M. K.; Clancy, C. M.; Modamio, J.; Sauls, J. T.; et al. Creation and Analysis of Biochemical Constraint-Based Models Using the COBRA Toolbox v.3.0. *Nat. Protoc.* **2019**, *14* (3), 639–702.

(50) Moreno-Sánchez, R.; Saavedra, E.; Rodríguez-Enríquez, S.; Gallardo-Pérez, J. C.; Quezada, H.; Westerhoff, H. V. Metabolic Control Analysis Indicates a Change of Strategy in the Treatment of Cancer. *Mitochondrion* **2010**, *10* (6), 626–639.

(51) Carpenter, K. L. H.; Jalloh, I.; Gallagher, C. N.; Grice, P.; Howe, D. J.; Mason, A.; Timofeev, I.; Helmy, A.; Murphy, M. P.; Menon, D. K.; Kirkpatrick, P. J.; Carpenter, T. A.; Sutherland, G. R.; Pickard, J. D.; Hutchinson, P. J. 13C-Labelled Microdialysis Studies of Cerebral Metabolism in TBI Patients. *Eur. J. Pharm. Sci.* **2014**, *57* (100), 87–97.

(52) Jang, C.; Chen, L.; Rabinowitz, J. D. Metabolomics and Isotope Tracing. *Cell* **2018**, *173* (4), 822–837.

(53) Keibler, M. A.; Fendt, S. M.; Stephanopoulos, G. Expanding the Concepts and Tools of

Metabolic Engineering to Elucidate Cancer Metabolism. *Biotechnol. Prog.* **2012**, *28* (6), 1409–1418.

(54) Fan, J.; Ye, J.; Kamphorst, J. J.; Shlomi, T.; Thompson, C. B.; Rabinowitz, J. D. Quantitative Flux Analysis Reveals Folate-Dependent NADPH Production. *Nature* **2014**, *10* (7504), 298–302.

(55) Wadke, M.; Brunengraber, H.; Lowenstein, J. M.; Dolhun, J. J.; Arsenault, G. P. Fatty Acid Synthesis by the Liver Perfused with Deuterated and Tritiated Water. *Biochemistry* **1973**, *12* (14), 2619–2624.

(56) Busch, R.; Kim, Y. K.; Neese, R. A.; Schade-Serin, V.; Collins, M.; Awada, M.; Gardner, J. L.; Beysen, C.; Marino, M. E.; Misell, L. M.; Hellerstein, M. K. Measurement of Protein Turnover Rates by Heavy Water Labeling of Nonessential Amino Acids. *Biochim. Biophys. Acta - Gen. Subj.* **2006**, *1760* (5), 730–744.

Oncogenic metabolic rewiring independent of proliferative control in human mammary epithelial cells

Chapter 4

Oncogenic metabolic rewiring independent of proliferative control in human mammary epithelial cells

Adapted from

Dong, W., Keibler, M. A., Moon, S. J., Cho, P., Liu, N., Berrios, C. J., Kelleher, J. K., Sikes, H. D., Iliopoulos, O., Coloff, J. L., Vander Heiden, M. G., & Stephanopoulos, G. Oncogenic metabolic rewiring independent of proliferative control in human mammary epithelial cells. Pending Submission.

Conceptualization, W.D., M.A.K. and G.S.; Methodology, W.D., M.A.K. and G.S.; Software, W.D., M.A.K. and N.L.; Validation, W.D., P.C. and J.L.C.; Formal analysis, W.D., M.A.K., S.J.M. and N.L.; Investigation, W.D. M.A.K. and S.J.M.; Resources, W.D., P.C., J.L.C., C.B. and G.S.; Writing – Original Draft, W.D. M.A.K. and P.C.; Writing – Review and Editing, W.D., M.A.K., S.J.M., P.C., J.L.C., N.L., J.K.K., M.G.V.H., O.I., H.D.S. and G.S., Supervision, J.K.K., M.G.V.H., O.I., H.D.S. and G.S.; Project Administration, G.S.; Funding Acquisition, G.S.

4.1 Abstract

The use of stable isotopic tracers and bioreaction network analysis has unveiled a number of metabolic pathways differentially activated in cancer cells. These rewired metabolic pathways provide opportunities for drug targeting. To support efforts to design effective therapies, we sought to distinguish metabolic behavior in cancer versus normal cells growing at the same rate, and obtain a systematic understanding of cancer metabolism. To this end, we performed ^{13}C-isotopic labeling and metabolic flux analysis (MFA) in human mammary epithelial cells (HMECs) that have been genetically modified to exhibit different levels of tumorigenicity. We discovered a distinct substrate utilization pattern in the tricarboxylic acid (TCA) cycle and *de novo* lipogenesis. Specifically, we found that glucose was catabolized in the TCA cycle up to the formation of citrate, which was then used primarily for lipogenesis. The majority of the TCA cycle flux, however, was maintained by glutamine anaplerosis. ^{13}C-MFA further revealed that some metabolic reactions were more activated in more tumorigenic HMECs. By introducing a new quantity termed metabolic flux intensity, defined as pathway flux divided by the specific growth rate, we identified three most enhanced reactions – oxidative pentose phosphate pathway (oxPPP), malate dehydrogenase (MDH) and isocitrate dehydrogenase (IDH) in the most tumorigenic HMEC. Targeting of these three pathways with small molecule inhibitors selectively reduced growth in the cancerous HMEC line. In addition, our study provides direct evidence that metabolism may be dually controlled by proliferation and oncogenotypes.

4.2 Introduction

Changes in metabolism is one of the hallmarks of cancer[1], and our knowledge of such changes has now extended beyond the Warburg effect[2–7], which refers to the paradoxical phenomenon that cancer cells preferentially metabolize glucose to lactate regardless of oxygen availability[8]. During the past decades, various scientific and medical discoveries have been made, which uncovered numerous metabolic shifts in cancer cells and elucidated the underlying mechanisms responsible for these rewired cellular energetics. Yet, a fundamental question still remains unanswered: whether there is a difference in the metabolism of cancerous, fast growing cells and normal proliferative cells. The answer to this question not only addresses the long-lasting speculations on the similarity between these two types of metabolism, but also reevaluates the therapeutic potential of targeting metabolism to treat cancer.

Although the difference between cancer and normal proliferative metabolism has not been directly assessed, it was hypothesized that these two types of metabolism could be treated indistinguishably[1,9,1023,24]. Consistent with this hypothesis, certain metabolic rewiring phenomena have been observed in both cancer and normal growing cells[11–20]. Examples include the Warburg effect[1,11–15,21,22], selective expression of pyruvate kinase isoform 2[16–18] and reductive carboxylation of glutamine[19,20]. However, other work contradicted this notion and suggested that cancer metabolism might be different than normal proliferative metabolism. Differential metabolic behavior has been reported for glutamine[23], serine, glycine [24,25]and proline metabolism[26]. In addition to the conflicting evidence, a key confounding factor was not accounted for, which limited our ability to unambiguously assess the potential difference between these two types of metabolism: the growth rates in cancer and normal cells were not

well-controlled. As a result, the observed metabolic shifts in cancer cells may be conferred by both oncogenotyes and reprogrammed cellular growth.

In order to answer this question unambiguously, we developed a panel of HMECs derived from the same genetic background but exhibiting different levels of tumorigenicity based on genetically engineered genotypes. We applied ^{13}C-MFA and introduced a new quantity referred to as metabolic flux intensity (MFI). MFI analysis revealed that proliferation was not the only factor governing metabolic behavior. In fact, several metabolic pathways were relied upon more heavily in cancer cells. Drug targeting of these pathways was more toxic for the most tumorigenic HMEC compared to the normal growing counterpart. In addition, our ^{13}C-isotope tracing and network analysis also uncovered a distinct substrate utilization pattern. A truncated TCA cycle was observed throughout the panel of HMECs. Through this truncated cycle, glutamine and glucose were utilized mainly for anaplerosis and *de novo* lipogenesis, respectively. Our results provide direct evidence that cancer and normal proliferative metabolism is different.

4.3 Construction of HMECs with differing levels of tumorigenicity

To compare cancer and proliferative metabolism, we developed a panel of HMECs exhibiting different levels of tumorigenicity. The resulting HMECs share the same parental cell genetic background: an immortalized, yet non-cancerous, HMEC 184A1 (ATCC), the growth of which is dependent on the amount of epidermal growth factor (EGF) present in media. We increased the level of tumorigenicity in the original HMEC 184A1 by overexpressing defined oncogenes and dominant negative mutant forms of tumor suppressors.

Based on the characteristic properties of cancer cells[27], we considered three key properties relevant to our specific *in vitro* system for modulating tumorigenicity: growth factor independence, apoptotic evasion and limitless replicative potential. We then generated several genetically modified HMECs exhibiting different levels of tumorigenicity (Figure 4.1a-d). The constitutively active mutant form of EGF receptor (EGFR L858R) and the oncogenic K-ras (KRas) were stably integrated into HMECs to confer growth-factor independent proliferation[28], and the resulting modified cell lines are referred to as HMEC-EGFR and HMEC-KRas, respectively. To promote apoptotic evasion[29], we introduced a dominant negative mutant form of p53 (p53DD) to HMEC-KRas and generated HMEC-p53DD-KRas. Moreover, we developed another cell line harboring Simian Virus 40 Early Region (SV40ER), which also attenuates apoptosis due to the inhibitory role of SV40 large T antigen (LT) on p53. We refer to the resulting cell line developed from HMEC-KRas as HMEC-SV40ER-KRas. The successful expression of these genetic elements was validated by Western blot (Figure 4.1a-d). In addition, we also obtained an HMEC line carrying Simian Virus 40 large T antigen (SV40-LT), oncogenic H-ras (HRas) and human telomerase reverse transcriptase (hTERT)[30]. In this cell line, HRas and SV40-LT are able to induce growth factor-independent proliferation and evasion of apoptosis[31], respectively. The introduction of hTERT further enhances cellular replicative potential, so the resulting cell line HMEC-hTERT-LT-HRas possesses three characteristic properties of cancer[1] relevant to our *in vitro* system. Therefore, it is expected to be the most tumorigenic cell line among other HMEC variants (Figure 4.1e).

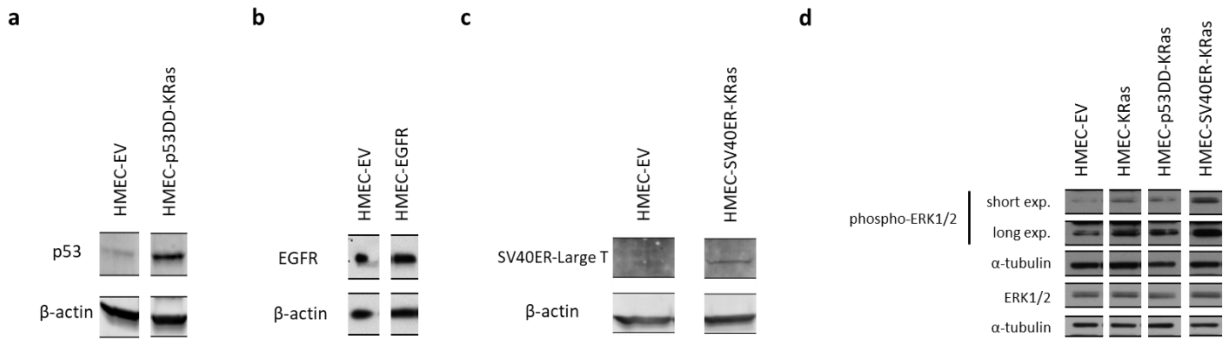

Figure 4.1 a-d. Western blotting validations for the overexpression of oncogenes and dominant negative mutant forms of tumor suppressors in HMECs developed in this study.

a, Successful integration of p53DD in HMEC-p53DD-KRas was validated by the p53 antibody (BD 554293) with β-actin (Sigma A1978) as the loading control.

b, Elevated expression of EGFR in HMEC-EGFR was validated by the EGFR antibody (Thermo MS-400-P1) with β-actin (Sigma Fisher A1978) as the loading control.

c, Successful integration of SV40ER in HMEC-SV40ER-KRas was validated by the SV40ER-Larte T antibody (SC 147) with β-actin (Sigma A1978) as the loading control.

d, Elevated expression of Ras in HMEC-KRas, HMEC-p53DD-KRas and HMEC-SV40ER-KRas were validated by the enhanced phosphorylation states of the downstream target ERK1/2 probed by the phospho-ERK1/2 antibody (Cell Signaling 4370), with the total amount of ERK1/2 probed by the ERK1/2 antibody (Cell Signaling 9102) and α-tubulin (Cell Signaling 3873) as the loading control. Exp. Exposure.

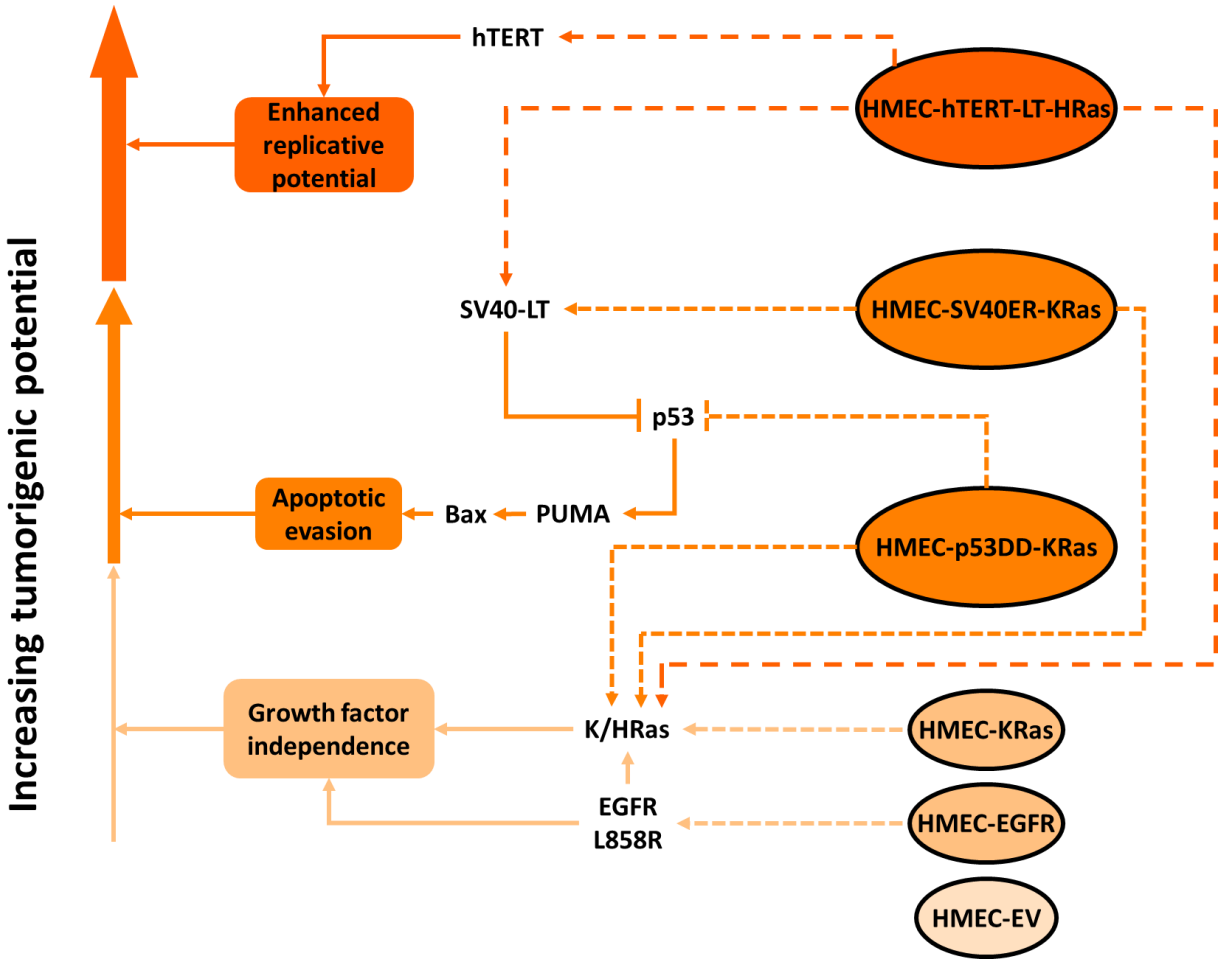

Figure 4.1 e. Overexpression of defined oncogenes and dominant negative mutant forms of tumor suppressors in HMECs increased tumorigenicity. Ovals indicate HEMC lines. Rounded rectangles indicate cancer-associated characteristics of cancer achieved during cell line development. Pointed and blunt-end arrows within the signaling pathway denote activation and inhibition, respectively. Darker orange color indicates higher levels of tumorigenicity.

Before characterizing the metabolic behavior of these cell lines, we first performed proliferation assays. Parental and empty vector-expressing HMECs exhibited exponential growth and were sensitive to EGF (Figure 4.1f). Based on exponential cell growth, we calculated specific growth rates at different EGF concentrations. EV cells proliferated faster at higher EGF

concentrations, and the maximum specific growth rate was achieved at 5 ng/mL EGF (Figure 4.1g). We next performed proliferation assays in the oncogenic and tumorigenic HMECs with 5 ng/mL or no EGF (+/- EGF). Upon the integration of EGFR, cells began to acquire a small extent of growth factor independence, which means that they were able to actively proliferate in the absence of EGF. The uncontrolled proliferation was further enhanced in HMECs carrying KRas, p53DD-KRas, SV40ER-KRas and hTERT-LT-HRas. Accordingly, the panel of HMECs was ranked by increasing growth factor independence in Figure 4.1h. In addition, HMECs in this order also exhibited increasing oncogene multiplicity (including downregulation of tumor suppressor genes), with EV carrying no oncogene, EGFR and KRas harboring one, p53DD-KRas and SV40ER-KRas carrying two, and hTERT-LT-HRas possessing three oncogenic elements. Furthermore, previous work[30] has validated that HMEC-hTERT-LT-HRas is capable of undergoing anchorage-independent growth and forming tumors in immunodeficient mice, demonstrating the greatest level of tumorigenicity among all HMECs (Figure 4.1h). All in all, this work allowed us to construct and assemble a panel of cells exhibiting varying levels of tumorigenicity. These HMECs with the same genetic background and defined oncogenic modifications enabled us to investigate whether cancer metabolism differs from normal proliferative metabolism in a well-controlled manner.

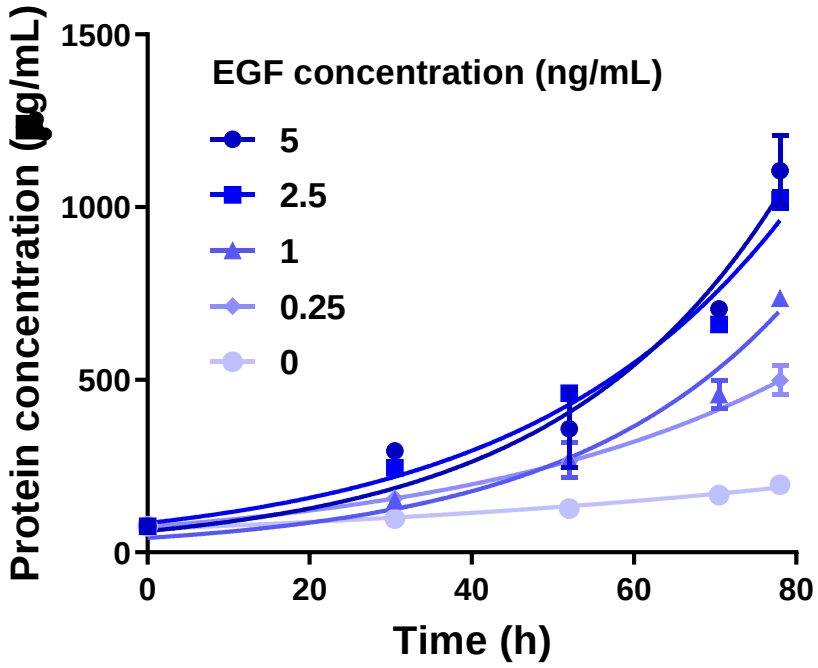

Figure 4.1 f. Proliferation of the normal HMECs in response to different EGF concentrations.

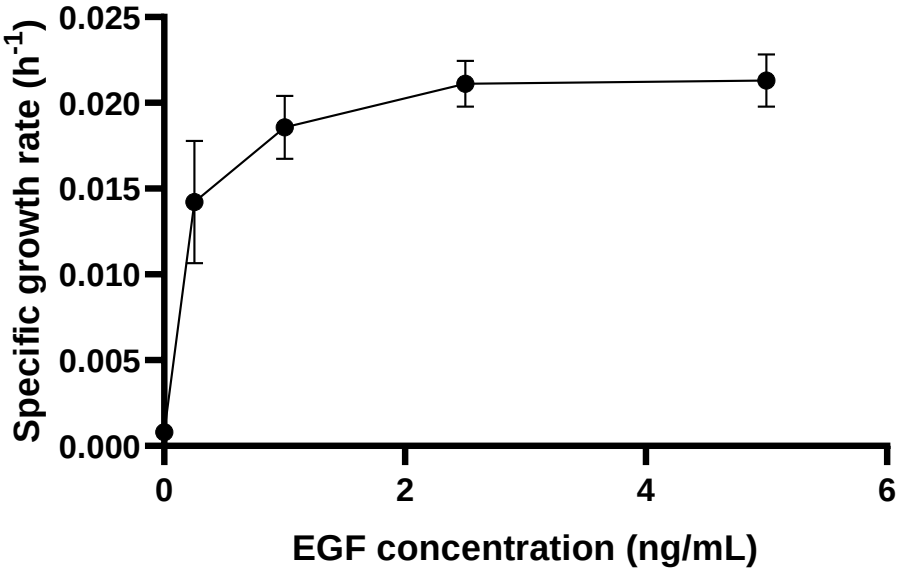

Figure 4.1 g. Specific growth rate of the normal HMECs as a function of EGF concentration.

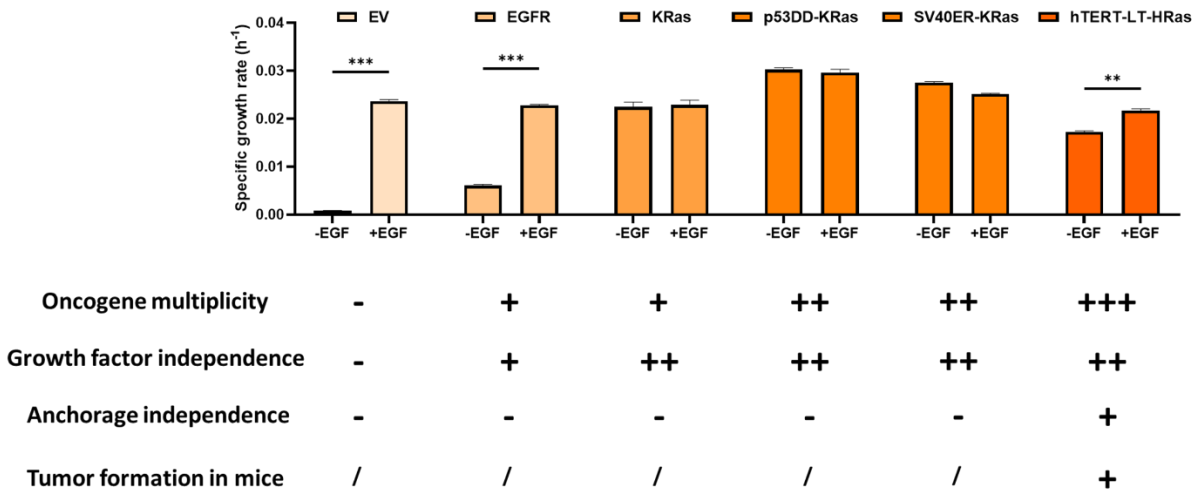

Figure 4.1 h. Growth factor independence observed in genetically modified HMECs with increasing levels of tumorigenicity, which was further corroborated by several other criteria. Error bars, s.e.m (n=3). **P<0.005. ***P<0.001.

4.4 Quantification of extracellular fluxes suggests dual control of metabolism by proliferation and oncogenotypes

We selected the extracellular fluxes of glucose, lactate, glutamine and glutamate as metrics of the metabolism of HMECs exhibiting different levels of tumorigenicity [32]. The extracellular fluxes followed a similar trend as the proliferation rate: the difference between +/- EGF conditions was smaller in cell lines with higher levels of tumorigenicity (Figure 4.2a). We further calculated lactate yield on glucose and glutamate yield on glutamine by dividing the respective extracellular fluxes and accounting for the stoichiometry of converting glucose to lactate and glutamine to glutamate (Figure 4.2b). Interestingly, although the glutamate yield from glutamine exhibited a similar pattern as the extracellular fluxes, the lactate yield from glucose was not significantly different at varying oncogenotype or in the presence or absence of EGF (Figure 4.2b). The only

exception was the -EGF HMEC-EV condition, which showed a relatively small lactate yield. The invariant yield of lactate suggests the strong presence of the Warburg effect while cells are actively proliferating[1,21,22].

Since the pattern of differential extracellular fluxes between +/- EGF conditions (Figure 4.2a) parallels that of growth (Figure 4.1h), we sought to investigate whether growth rate regulates extracellular fluxes. To this end, we plotted extracellular fluxes against specific growth rates. All major extracellular fluxes (Figure 4.2c) and glutamate yield (Figure 4.2d) were higher at elevated growth, except for lactate yield, which stayed constant again presumably because of the Warburg effect (Figure 4.2d). Remarkably, the extracellular fluxes from both +/- EGF conditions tend to collapse onto a single regression line, which suggests the presence of direct control of extracellular fluxes by proliferation (Figure 4.2c). However, although the entire data set can be described by regression lines to some extent, a closer examination of the data points with comparable specific growth rates (0.02-0.025 h^{-1}) suggests that extracellular fluxes are not solely determined by proliferation (Figure 4.2c). In fact, we constructed separate plots for HMECs grown at the +EGF condition (Figure 4.2e). The apparent proliferative control of extracellular fluxes, as indicated by the R^2 values, was reduced when considering only the +EGF condition (Figure 4.2e) compared to those in both +/-EGF conditions (Figure 4.2c and 4.2g-h). Collectively, these data suggest that metabolism, at least manifested by extracellular fluxes, may be dually controlled by proliferation and specific oncogenotypes. In addition, proliferative control of metabolism was reduced in +EGF HMECs that shared similar growth rates.

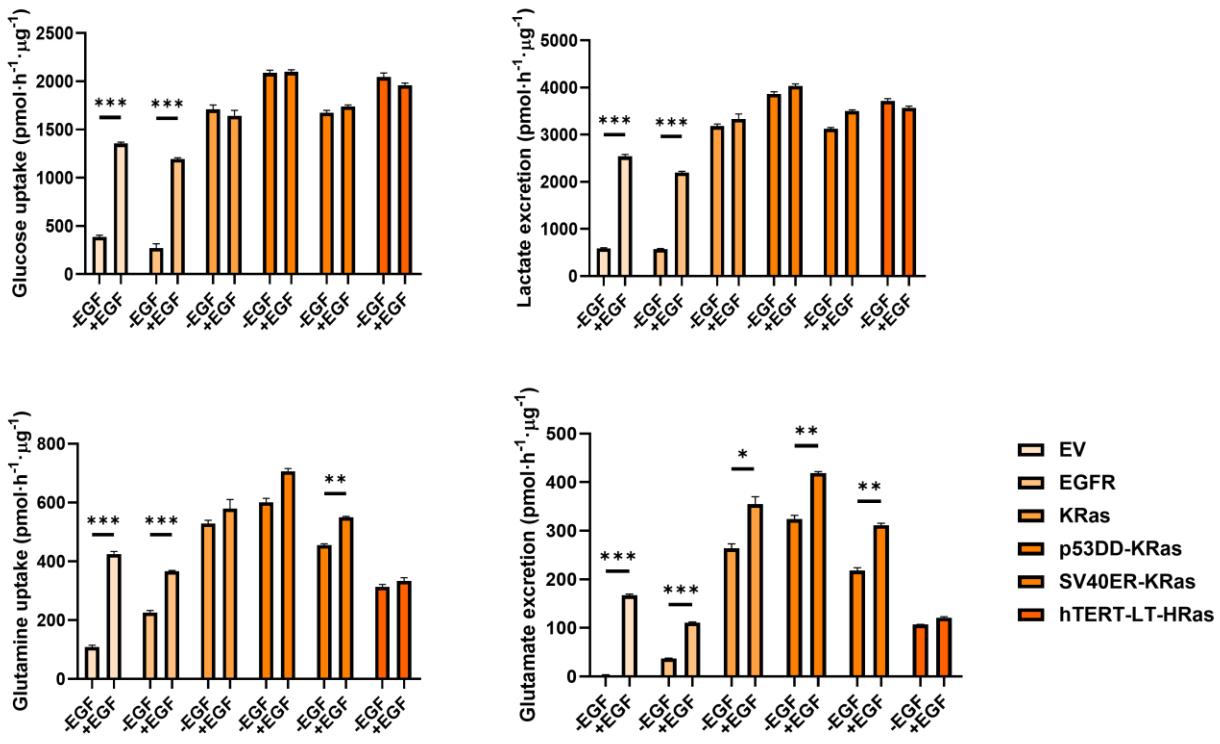

Figure 4.2 a. Extracellular fluxes of glucose, lactate, glutamine and glutamate for HMECs at +/- EGF conditions. Darker orange color indicates higher levels of tumorigenicity. Error bars, s.e.m (n=3). *P<0.05. **P<0.005. ***P<0.001.

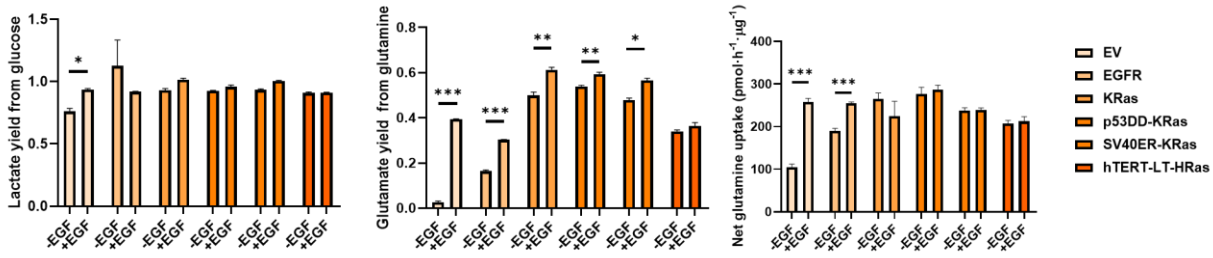

Figure 4.2 b. Lactate yields from glucose, glutamate yields from glutamine and net glutamine uptake rates for HMECs at +/- EGF conditions. Darker orange color indicates higher level of tumorigenicity. Error bars, s.e.m (n=3). *P<0.05. **P<0.005. ***P<0.001.

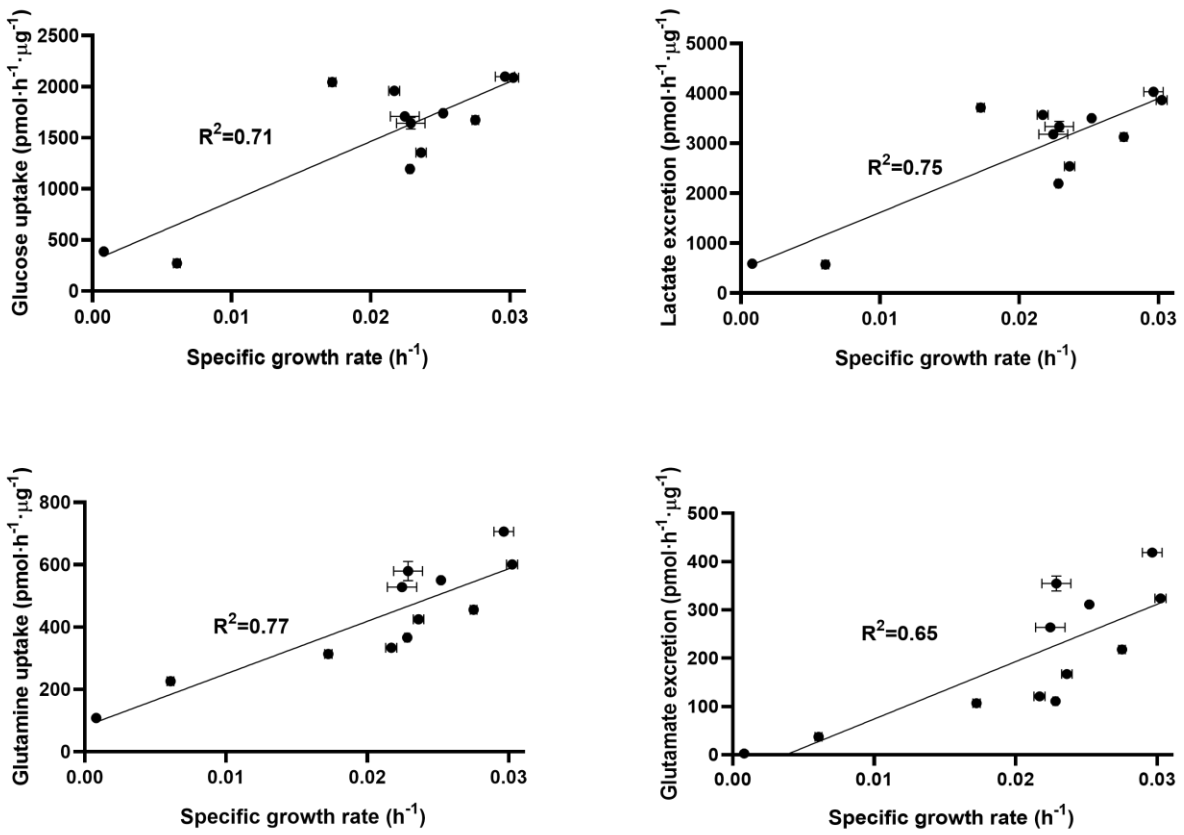

Figure 4.2 c. Extracellular fluxes of +/- EGF HMECs plotted against specific growth rates. Error bars, s.e.m (n=3). *P<0.05. **P<0.005. ***P<0.001.

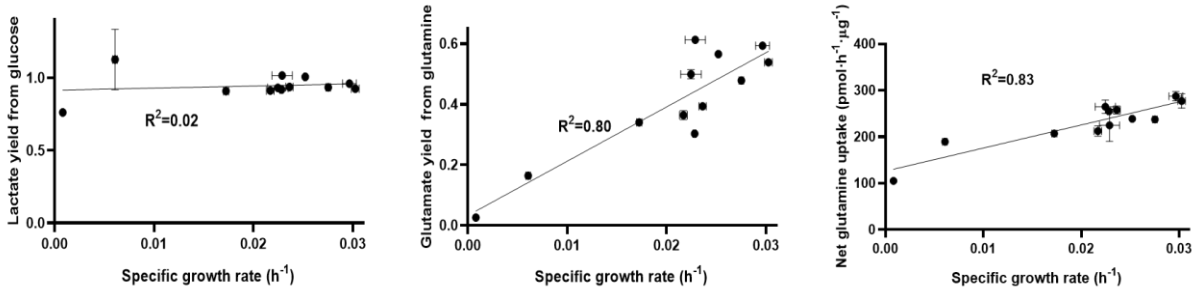

Figure 4.2 d. Lactate yields from glucose, glutamate yields from glutamine and net glutamine uptake rates against specific growth rates for both +/- EGF conditions. Error bars, s.e.m (n=3). *P<0.05. **P<0.005. ***P<0.001.

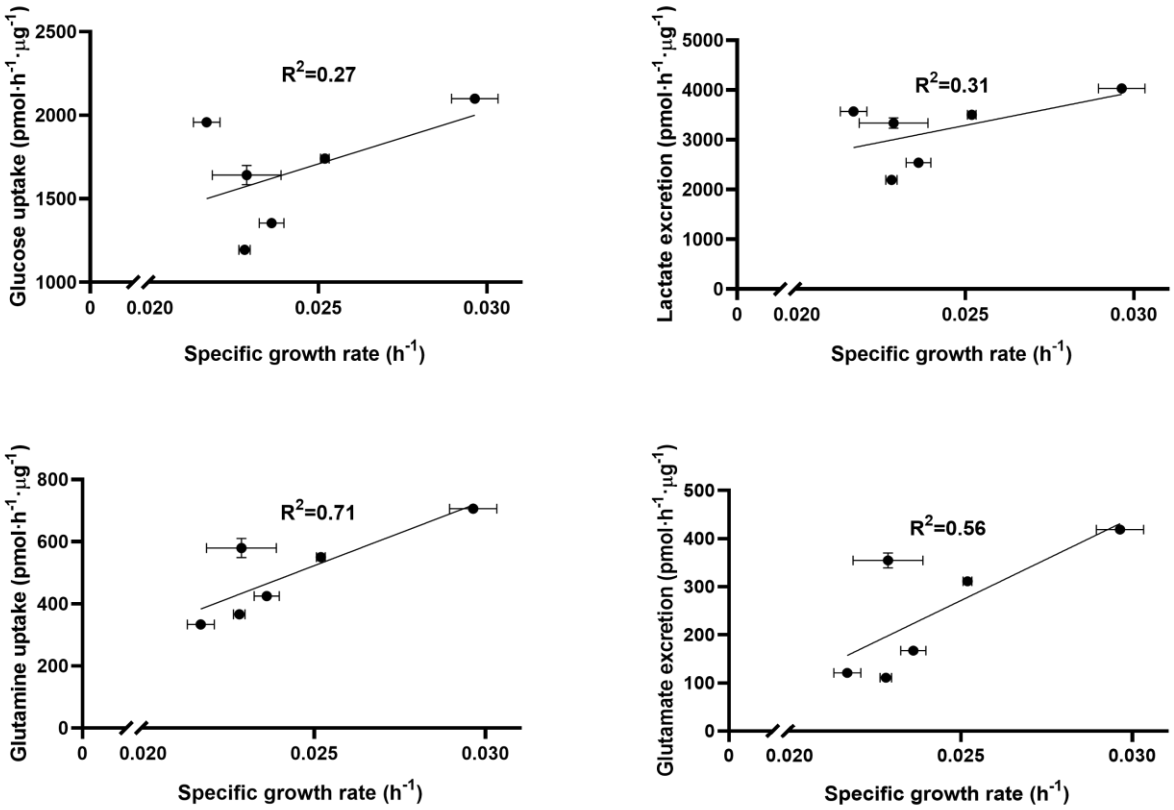

Figure 4.2 e. Extracellular fluxes of only the +EGF HMECs plotted against specific growth rates. Error bars, s.e.m (n=3). *P<0.05. **P<0.005. ***P<0.001.

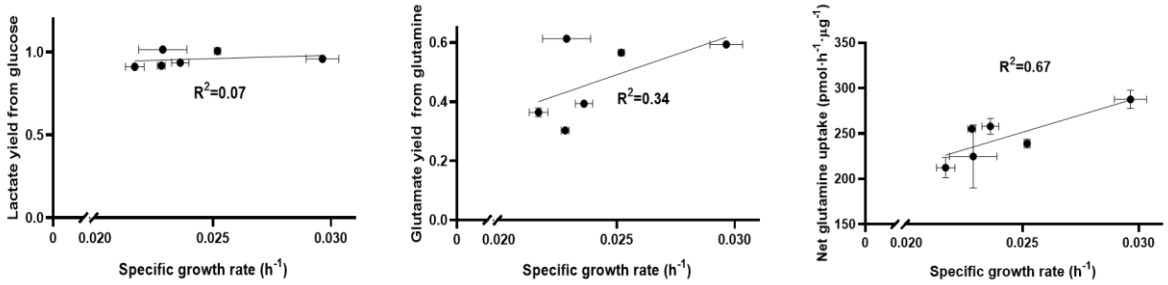

Figure 4.2 f. Lactate yields from glucose, glutamate yields from glutamine and net glutamine uptake rates against specific growth rates for only the +EGF condition. Error bars, s.e.m (n=3). *P<0.05. **P<0.005. ***P<0.001.

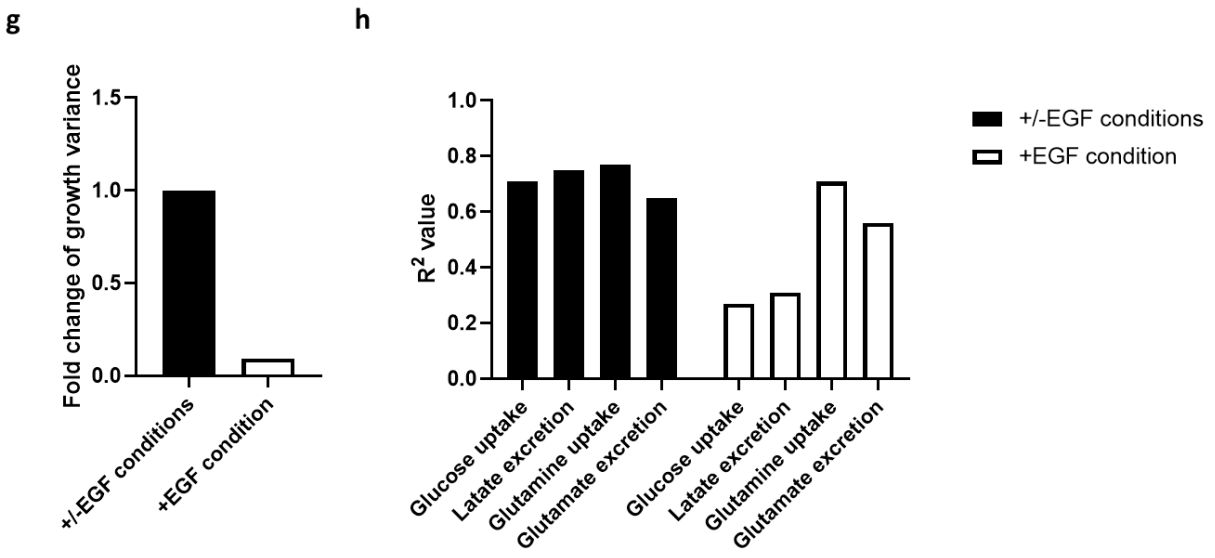

Figure 4.2 g-h. Reduced level of control on metabolism by proliferation for HMECs grown at the +EGF condition.

g, Compared to HMECs growth at both +/-EGF conditions, the +EGF subgroup exhibited similar growth rates.

h, Compared to HMECs growth at both +/-EGF conditions, the proliferative control of metabolism, as measured by the R^2 values, was decreased in the +EGF subgroup.

4.5 ^{13}C-isotopic labeling reveals distinct substrate utilization patterns in the TCA cycle and *de novo* lipogenesis

To determine further metabolic changes, we performed ^{13}C-isotopic labeling experiments by culturing HMECs in media separately containing three different tracers: uniformly ^{13}C-labeled glucose (U-$^{13}C_6$-glucose); 1,2-^{13}C-labeled glucose (1,2-$^{13}C_2$-glucose); and uniformly ^{13}C-labeled glutamine (U-$^{13}C_5$-glutamine). Previous studies have shown that these three tracers give the best resolution of fluxes for glycolysis, PPP and the TCA cycle[33]. Measurement of isotope enrichment of TCA cycle intermediates and amino acids revealed a distinct substrate utilization

pattern in all HMECs used in our study. The canonical view of anaplerosis predicts strong enrichment of all TCA cycle intermediates by U-$^{13}C_6$-glucose. However, we observed a low level of enrichment for all U-$^{13}C_6$-glucose-derived metabolites of the TCA cycle. In fact, the majority of TCA cycle metabolites were weakly labeled by U-$^{13}C_6$-glucose, except for citrate, which was mainly labeled by two ^{13}C atoms (M+2). This labeling pattern indicated that the ^{13}C influx from glucose stopped at the point of citrate (Figure 4.3a). This conclusion was further corroborated by 1,2-$^{13}C_2$-glucose labeling, which generated similar profiles compared to those from U-$^{13}C_6$-glucose, consistent with the notion that M+2 citrate was the only metabolite moderately labeled by glucose tracers (Figure 4.3b).

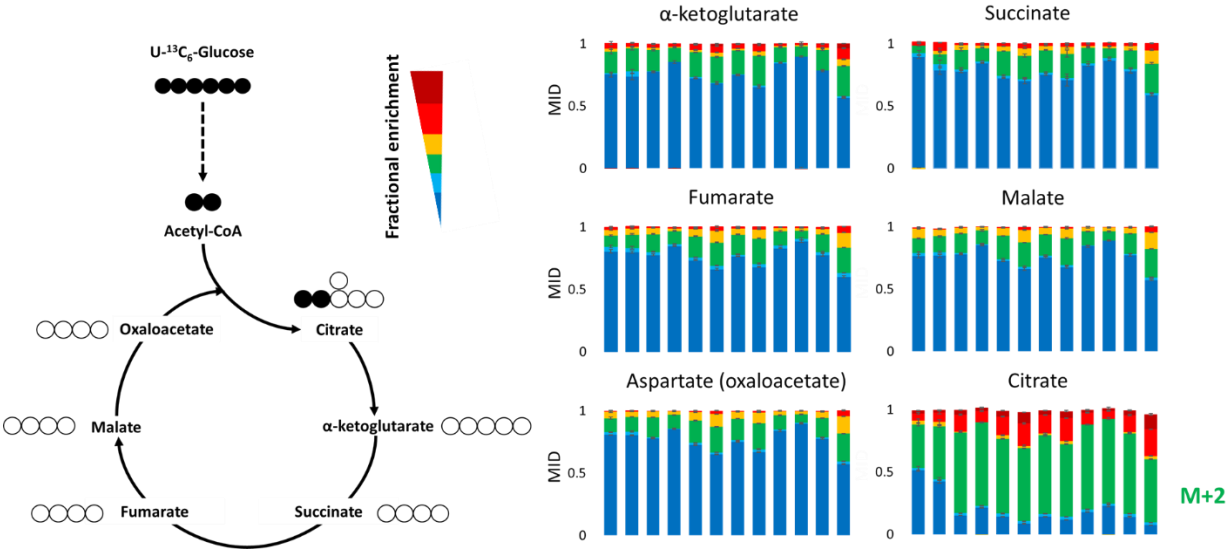

Figure 4.3 a. U-$^{13}C_6$-glucose labeling pattern suggests weak incorporations of glucose-derived carbons into the TCA cycle except for citrate, the majority of which stays at M+2. Error bars, s.e.m (n=3).

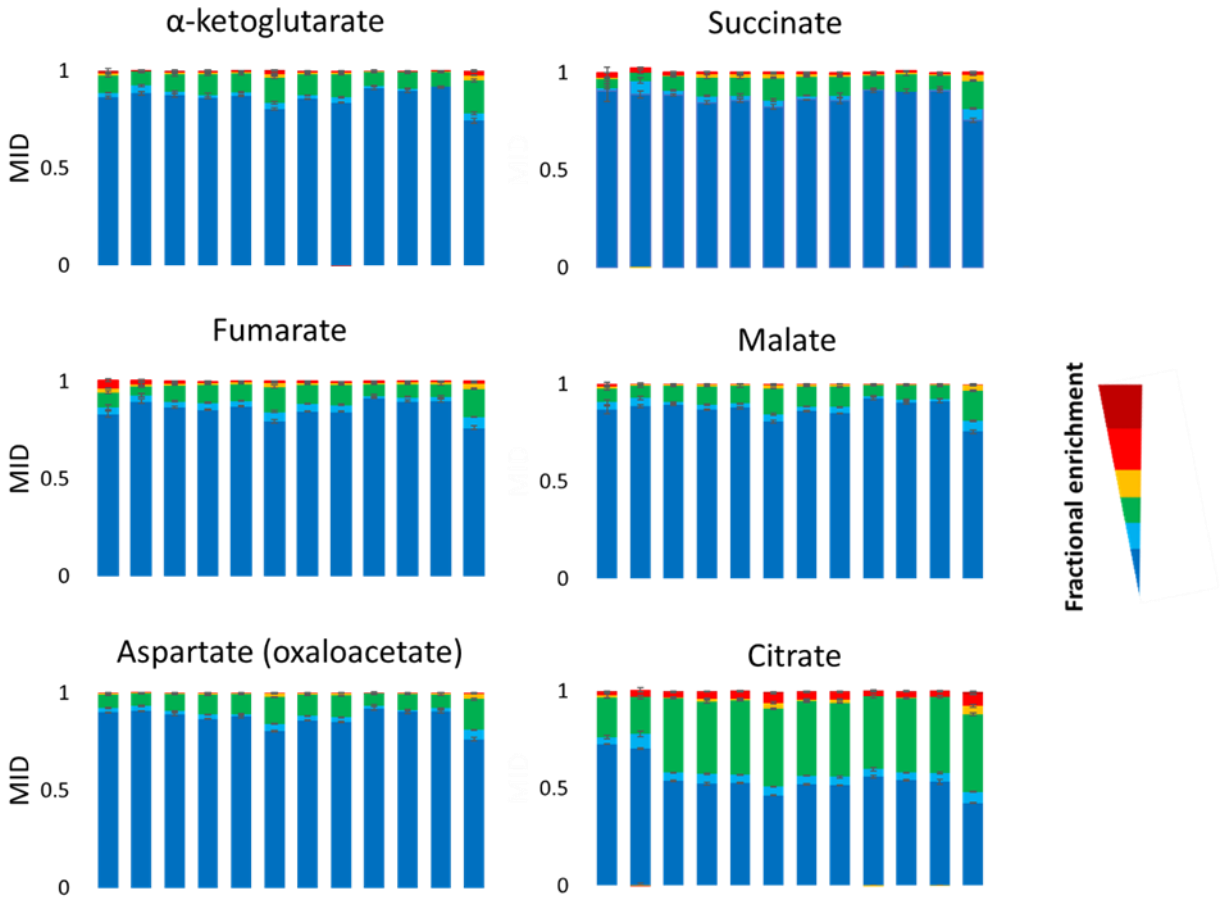

Figure 4.3 b. Labeling profiles of TCA cycling intermediates by 1,2-$^{13}C_2$-glucose confirmed that glucose is not the primary anaplerotic substrate, and that citrate is the only TCA cycle metabolite moderately labeled by glucose tracers. Error bars, s.e.m (n=3).

Columns along the axis of abscissas in each bar graph indicate ^{13}C-isotopic labeling data from the following cell line and EGF conditions in the order from left to right: EV -EGF, EGFR -EGF, KRas -EGF, SV40ER-KRas -EGF, p53DD-KRas -EGF, hTERT-LT-HRas -EGF; EV +EGF, EGFR +EGF, KRas +EGF, SV40ER-KRas +EGF, p53DD-KRas +EGF, hTERT-LT-HRas +EGF.

Intrigued by this stark distribution pattern of glucose-derived carbon, we further labeled cells with U-$^{13}C_5$-glutamine, hypothesizing that glutamine may be the primary carbon substrate fueling the TCA cycle. The crucial role of glutamine anaplerosis has been reported in various studies. In several types of cancer cells grown under hypoxia, glutamine provides carbon sources for *de novo* lipogenesis through the reversal of isocitrate dehydrogenase (IDH)[34–36]. In contrast to reductive metabolism, in our HMECs, glutamine was primarily incorporated into the oxidative TCA cycle. Mass isotopomer distribution (MID) data showed that TCA intermediates were labeled much more strongly by U-$^{13}C_5$-glutamine than U-$^{13}C_6$-glucose. Across all cell lines, TCA cycle metabolites were approximately 50% enriched to the highest isotopomer states (M+4/5) when cultures were labeled by U-$^{13}C_5$-glutamine. Moreover, M+4 abundance was much greater than that of M+5 for citrate, indicating that the primary route of glutamine anaplerosis was oxidative cycling rather than reductive carboxylation[37]. This data suggests that glutamine, but not glucose, is the primary carbon source that fuels the oxidative TCA cycle (Figure 4.3c).

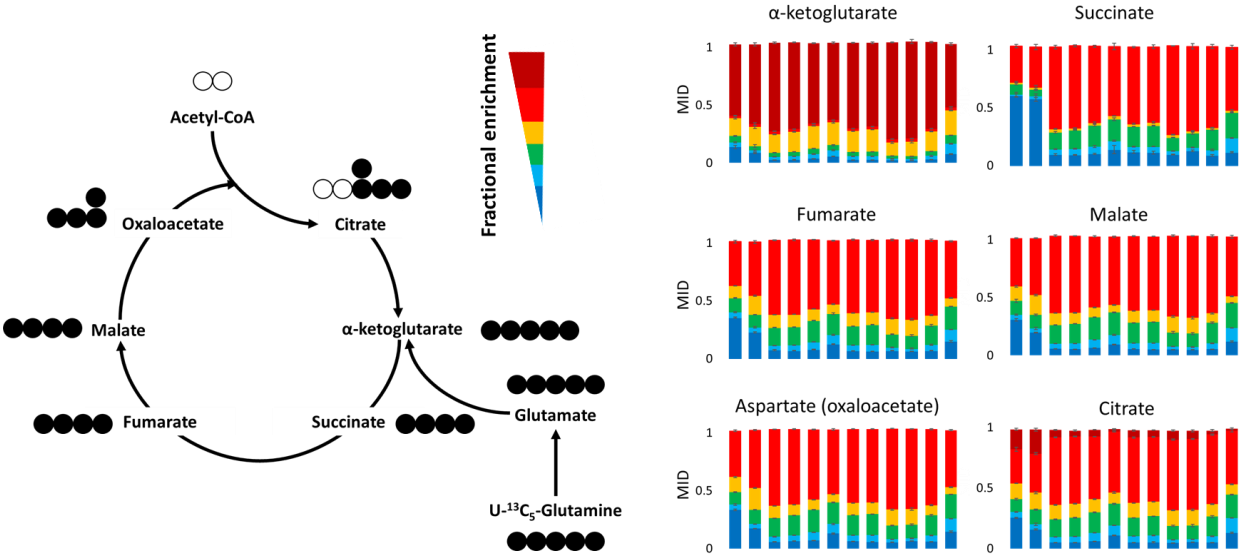

Figure 4.3 c. U-$^{13}C_5$-glutamine labeling pattern suggests much stronger incorporations of glutamine-derived carbons into the TCA cycle. Error bars, s.e.m (n=3).

In addition to glutamine anaplerosis, we also investigated the metabolic fate of glucose-derived carbons. Aside from citrate, TCA cycle metabolites were minimally labeled by U-$^{13}C_6$-glucose (Figure 3a). This labeling pattern suggests that glucose-derived fluxes are diverted away from the TCA cycle at the point of citrate. Because citrate initiates *de novo* lipogenesis, we analyzed the nonpolar metabolites from cells cultured in ^{13}C-labeled substrates to identify the metabolic fate of citrate. The MIDs of palmitate and stearate suggest that glucose, rather than glutamine, was the main contributor to *de novo* fatty acid synthesis (Figure 4.3d-e). To further quantify the fractional contributions of glucose and glutamine to acetyl-CoA, a two-carbon unit recruited for *de novo* lipogenesis, we performed isotopomer spectral analysis (ISA)[38]. ISA confirmed the lipogenic role of glucose relative to glutamine (Figure 4.3f-g). The labeling and ISA results suggested that glucose-derived carbons were mostly utilized for *de novo* lipogenesis. Taken together, our ^{13}C-isotopic labeling results identified a distinct substrate utilization pattern regarding the TCA cycle and *de novo* lipogenesis in HMECs. In all cell lines that we studied, the TCA cycle functions in a truncated fashion: glutamine supplies the majority of the carbon substrates for TCA cycle intermediates, while lipogenesis is maintained primarily by glucose rather than glutamine (Figure 3h).

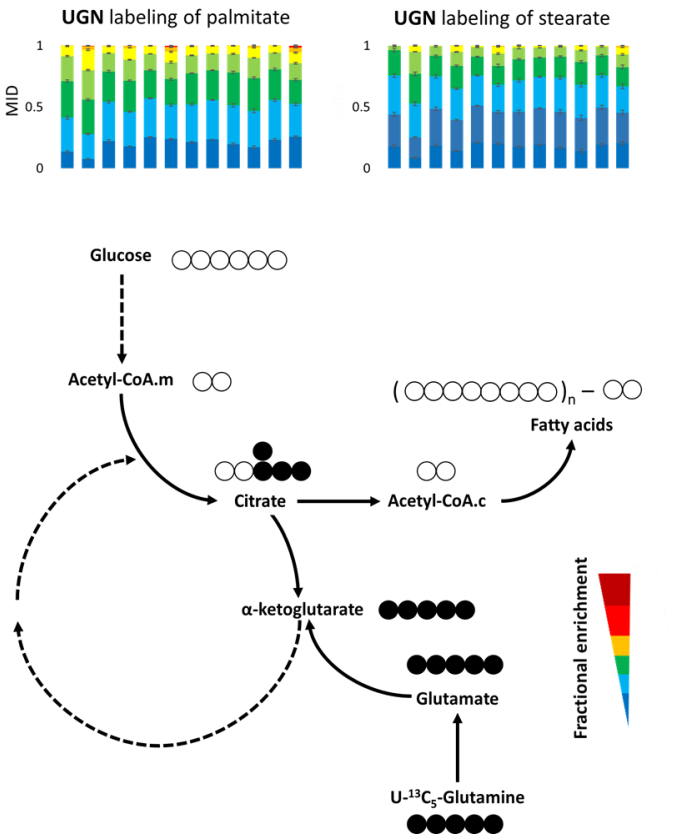

Figure 4.3 d. U-$^{13}C_5$-glutamine labeling pattern suggests weak incorporations of glutamine-derived carbons into *de novo* fatty acid synthesis. Error bars, s.e.m (n=3).

Columns along the axis of abscissas in each bar graph represent ^{13}C-isotopic labeling data in the following order: EV -EGF, EGFR -EGF, KRas -EGF, p53DD-KRas -EGF, SV40ER-KRas -EGF, hTERT-LT-HRas -EGF; EV +EGF, EGFR +EGF, KRas +EGF, p53DD-KRas +EGF, SV40ER-KRas +EGF, hTERT-LT-HRas +EGF. Open and filled circles in the schematics indicate ^{12}C an ^{13}C atoms within the metabolites, respectively. Abbreviations: UGN: U-$^{13}C_5$-glutamine.

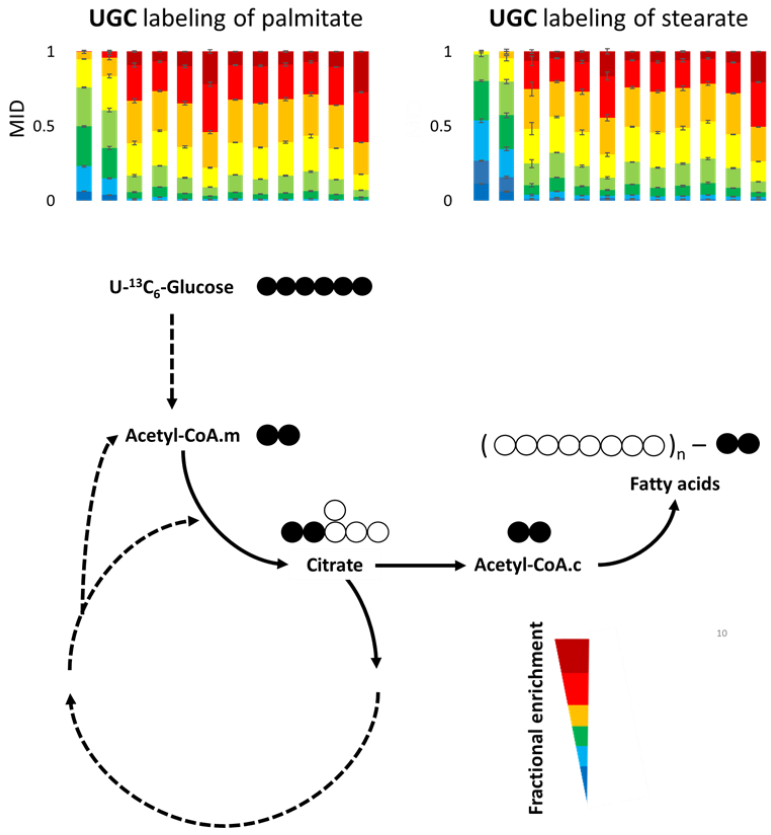

Figure 4.3 e. U-$^{13}C_6$-glucose labeling pattern suggests stronger incorporations of glucose-derived carbons into *de novo* fatty acid synthesis. Error bars, s.e.m (n=3).

Columns along the axis of abscissas in each bar graph represent ^{13}C-isotopic labeling data in the following order: EV -EGF, EGFR -EGF, KRas -EGF, p53DD-KRas -EGF, SV40ER-KRas -EGF, hTERT-LT-HRas -EGF; EV +EGF, EGFR +EGF, KRas +EGF, p53DD-KRas +EGF, SV40ER-KRas +EGF, hTERT-LT-HRas +EGF. Open and filled circles in the schematics indicate ^{12}C an ^{13}C atoms within the metabolites, respectively. Acetyl-CoA.c and acetyl-CoA.m refer to cytosolic and mitochondrial acetyl-CoA, respectively. Abbreviations: UGC, U-$^{13}C_6$-glucose.

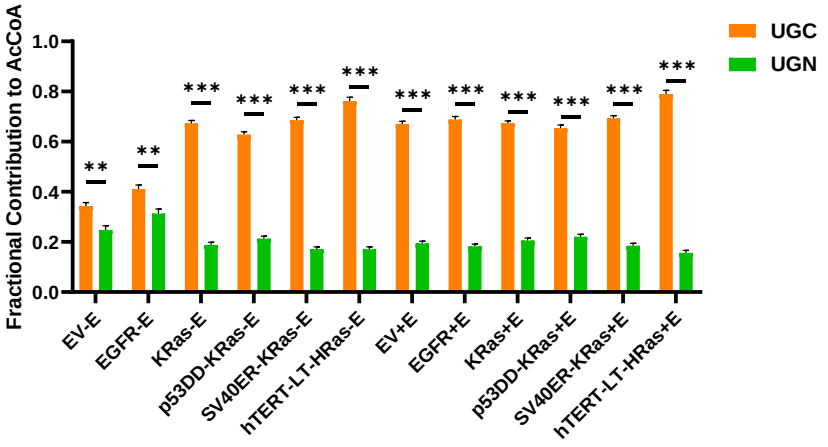

Figure 4.3 f. Isotopomer spectral analysis (ISA) confirmed that glucose dominated lipogenesis over glutamine. Error bars, s.e.m (n=3). Abbreviations: UGC, U-$^{13}C_6$-glucose; UGN: U-$^{13}C_5$-glutamine.

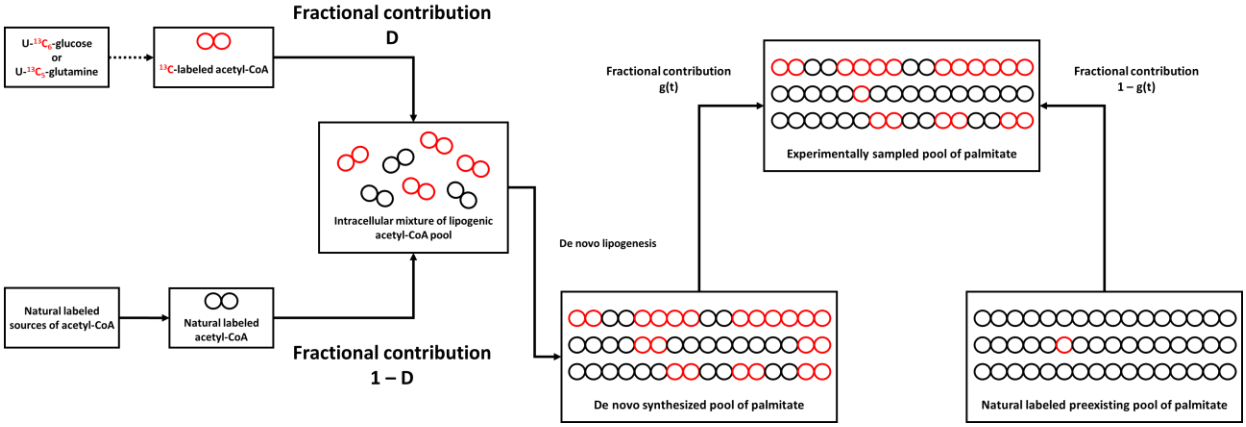

Figure 4.3 g. Schematic overview of isotopomer spectral analysis (ISA).

^{13}C-labeled acetyl-CoA from U-$^{13}C_6$-glucose or U-$^{13}C_6$-glutamine forms an intracellular mixture of lipogenic precursors with the naturally unlabeled acetyl-CoA. The fractional contribution, D, measures the enrichment of ^{13}C in this well mixed pool. Acetyl-CoA from this pool is utilized to make palmitate via *de novo* lipogenesis. The resulting *de novo* synthesized palmitate pool is enriched with ^{13}C compared with the one formed by natural labeled preexisting palmitate. The experimentally sampled pool is contributed by these two palmitate mixtures weighted by corresponding fractions g(t) and 1-g(t). Note that these fractions are time-dependent. ISA

estimated both D and g(t) through nonlinear regression. D values for U-$^{13}C_6$-glucose or U-$^{13}C_6$-glutamine are plotted in Figure 4.3f. This figure is adapted from (Kelleher & Nickol, 2015)[38] and (Metallo et al., 2012)[34].

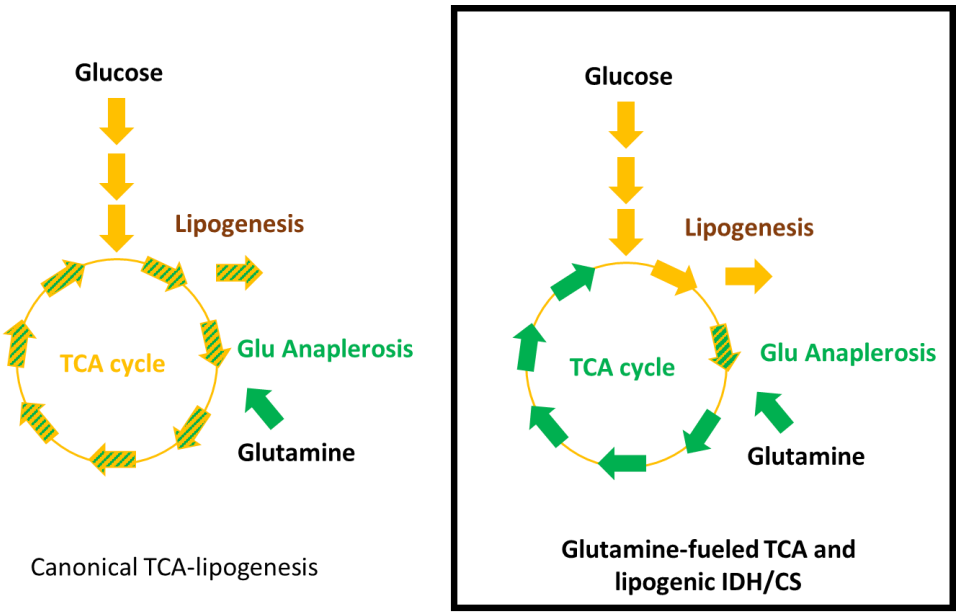

Figure 4.3 h. ^{13}C-isotopic labeling analysis revealed a distinct substrate utilization pattern within the TCA cycle and *de novo* lipogenesis in contrast to the canonical view. Abbreviations: Glu, glutamate.

4.6 Quantification of intracellular metabolism via ^{13}C-metabolic flux analysis (^{13}C-MFA) corroborates proliferative control of metabolism

In order to quantitatively investigate intracellular metabolism in HMECs, we performed ^{13}C-metabolic flux analysis (^{13}C-MFA). Briefly, ^{13}C-MFA estimates metabolic fluxes by fitting them such as to most closely reproduce the measured metabolite isotopic enrichment patterns[39] (Figure 4.4a). The metabolic network model constructed for our ^{13}C-MFA consists of major biochemical reactions within central carbon metabolism (Figure 4.4b and Table 4.1). ^{13}C-MFA was performed under pseudo-steady state hypothesis, which was difficult to achieve in slowly growing cells. Accordingly, we report converged ^{13}C-MFA flux results for all +EGF HMECs and those -EGF HMECs that still actively proliferated (KRas, p53DD-KRas, SV40ER-KRas and hTERT-LT-HRas).

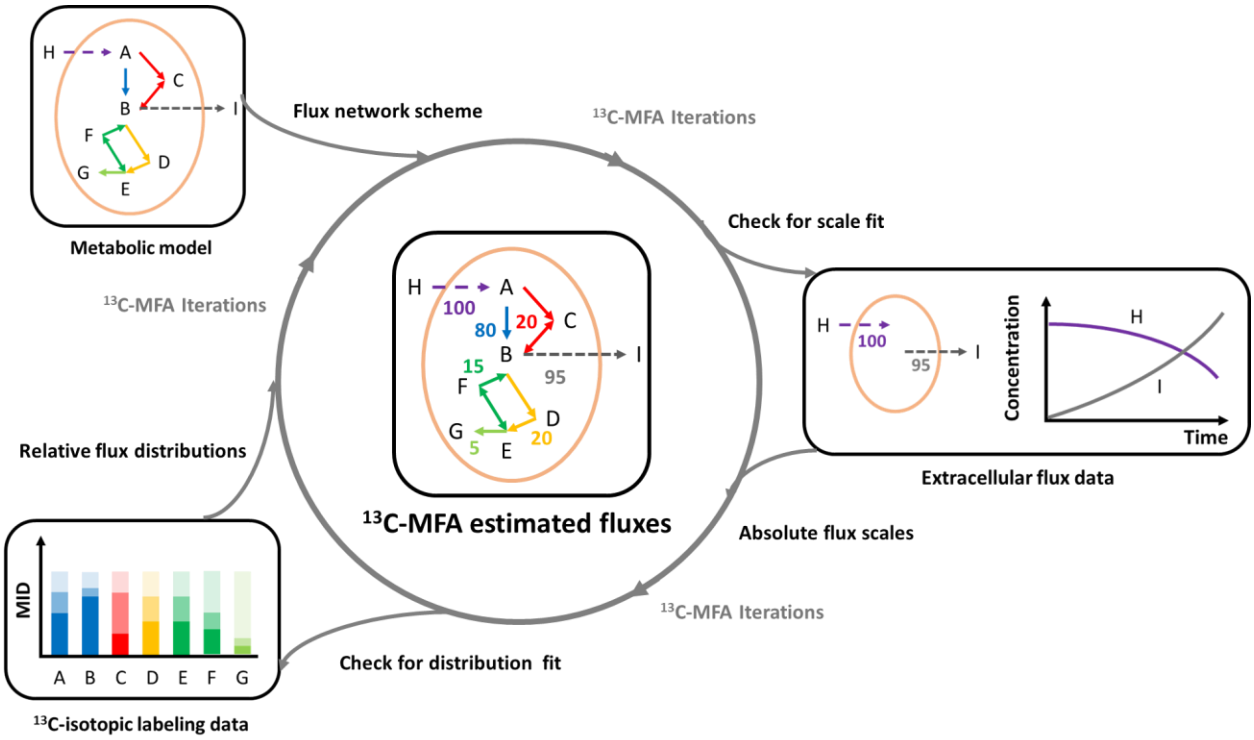

Figure 4.4 a. Essential components and steps for ^{13}C-metabolic flux analysis (^{13}C-MFA). Based on a detailed metabolic network model, ^{13}C-MFA determines absolute flux scales from extracellular flux data. To resolve intracellular flux distributions, ^{13}C-MFA utilizes ^{13}C-isotopic labeling data. The numerical algorithm works through iterations, during which ^{13}C-MFA frequently checks the fit of experimentally determined extracellular fluxes and ^{13}C-isotopic labeling data by values simulated by hypothesized flux distributions. The converged results are shown at the center of the schematic.

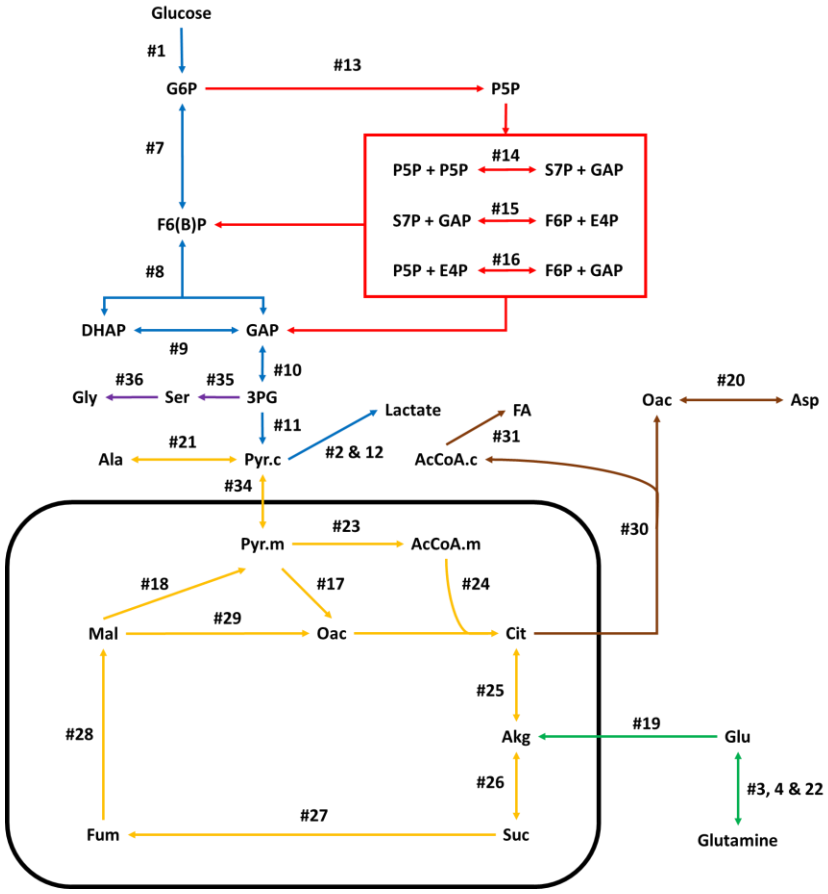

Figure 4.4 b. Metabolic pathways are color coded to indicate different parts of the metabolism: blue, glycolysis; red, pentose phosphate pathway (PPP); purple, serine-glycine metabolism; orange, the tricarboxylic acid (TCA) cycle; green, glutamine anaplerosis; brown, *de novo* lipogenesis. Single- and double-headed arrows refer to unidirectional and bidirectional reactions, respectively. The rounded rectangle refers to the boundary of a mitochondrion. Reactions are numbered and the carbon atom transitions are depicted in detail in Table S1.

Abbreviations: G6P, glucose-6-phosphate; S7P, sedoheptulose-7-phosphate; E4P, erythrose-4-phosphate; F6P, fructose-6-phosphate; FBP, fructose-1,6-bisphosphate; DHAP, dihydroxyacetone phosphate; GAP, glyceraldehyde-3-phosphate; 3PG, 3-phosphoglycerate; Ser, serine; Gly, glycine; Pyr.c, cytosolic pyruvate; Pyr.m, mitochondrial pyruvate; Ala, alanine; AcCoA.c, cytosolic acetyl-CoA; AcCoA.m, mitochondrial acetyl-CoA; FA, fatty acids; Mal, malate; Oac, oxaloacetate; Cit, citrate; Akg, α-ketoglutarate; Glu, glutamate; Fum, fumarate; Suc, succinate; Asp, aspartate. P5P refers to ribose-5-phosphate and ribulose-5-phosphate, indistinguishably.

We first compared flux distributions along glycolysis and the oxidative pentose phosphate pathway (oxPPP). For example, culturing cells with 1,2-$^{13}C_2$-glucose allows estimation of relative fluxes between glycolysis and oxPPP. In brief, the glycolytic pathway retains both ^{13}C atoms from 1,2-$^{13}C_2$-glucose and therefore generates M+2 labeled lactate as the main product. The oxidative branch of the PPP, on the other hand, involves a decarboxylation reaction which results in a loss of a ^{13}C atom in the form of carbon dioxide, yielding M+1 labeled lactate[37,40,41]. Relative magnitude of glycolysis and oxPPP can therefore be deduced by comparing the MIDs of M+2 against M+1 lactate. This ratio can be compared with the same ratio calculated from the MFA-estimated fluxes using different isotopic labels. In accordance with the ^{13}C-labeling pattern indicating a significantly lower fraction of M+1 (0.03) as opposed to M+2 lactate (0.45), ^{13}C-MFA results also suggested a minor diversion of fluxes into oxPPP (50 pmol·h^{-1}·μg^{-1}) from glycolysis (2813 pmol·h^{-1}·μg^{-1}). Consistent results were also obtained from other HMEC lines. Moreover, we cultured HMECs with U-$^{13}C_5$-glutamine and U-$^{13}C_6$-glucose, and calculated fractional enrichments of major TCA intermediates. The labeling results suggested that the TCA cycle was maintained primarily by glutamine. Consistently, MFA also indicated stronger anaplerotic flux by glutamine than that by glucose (Figure 4.4c).

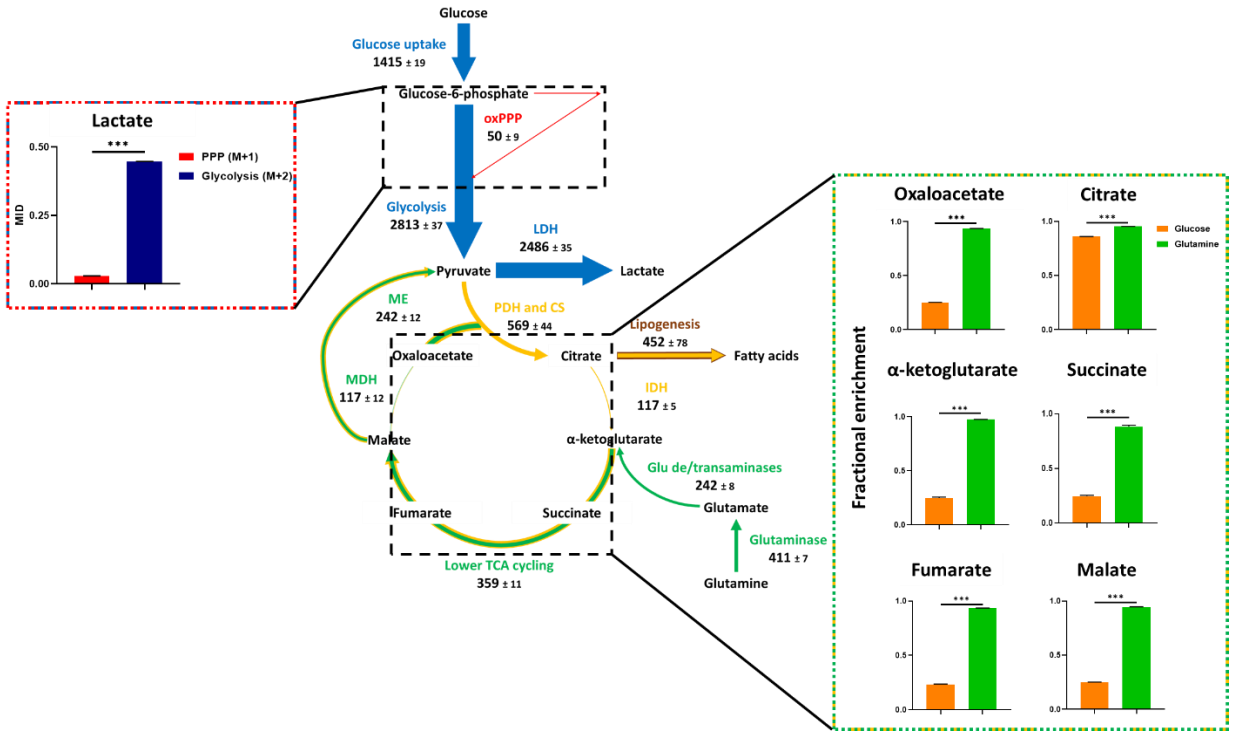

Figure 4.4 c. ^{13}C-MFA generated consistent results with the labeling data regarding the partition of fluxes between glycolysis and oxPPP and the anaplerotic contributions from glucose and glutamine. Flux results of +EGF HMEC-EV are shown here as an example. Unit of metabolic fluxes, pmol·h^{-1}·μg^{-1}. Uncertainties are shown as 95% confidence intervals.

Error bars, s.e.m. (n=3). ***P<0.001.

Abbreviations: oxPPP, oxidative pentose phosphate pathway; LDH, lactate dehydrogenase; ME: malic enzyme; MDH, malate dehydrogenase; PDH, pyruvate dehydrogenase; CS, citrate synthase; IDH, isocitrate dehydrogenase; TCA cycle, tricarboxylic acid cycle; Glu, glutamate.

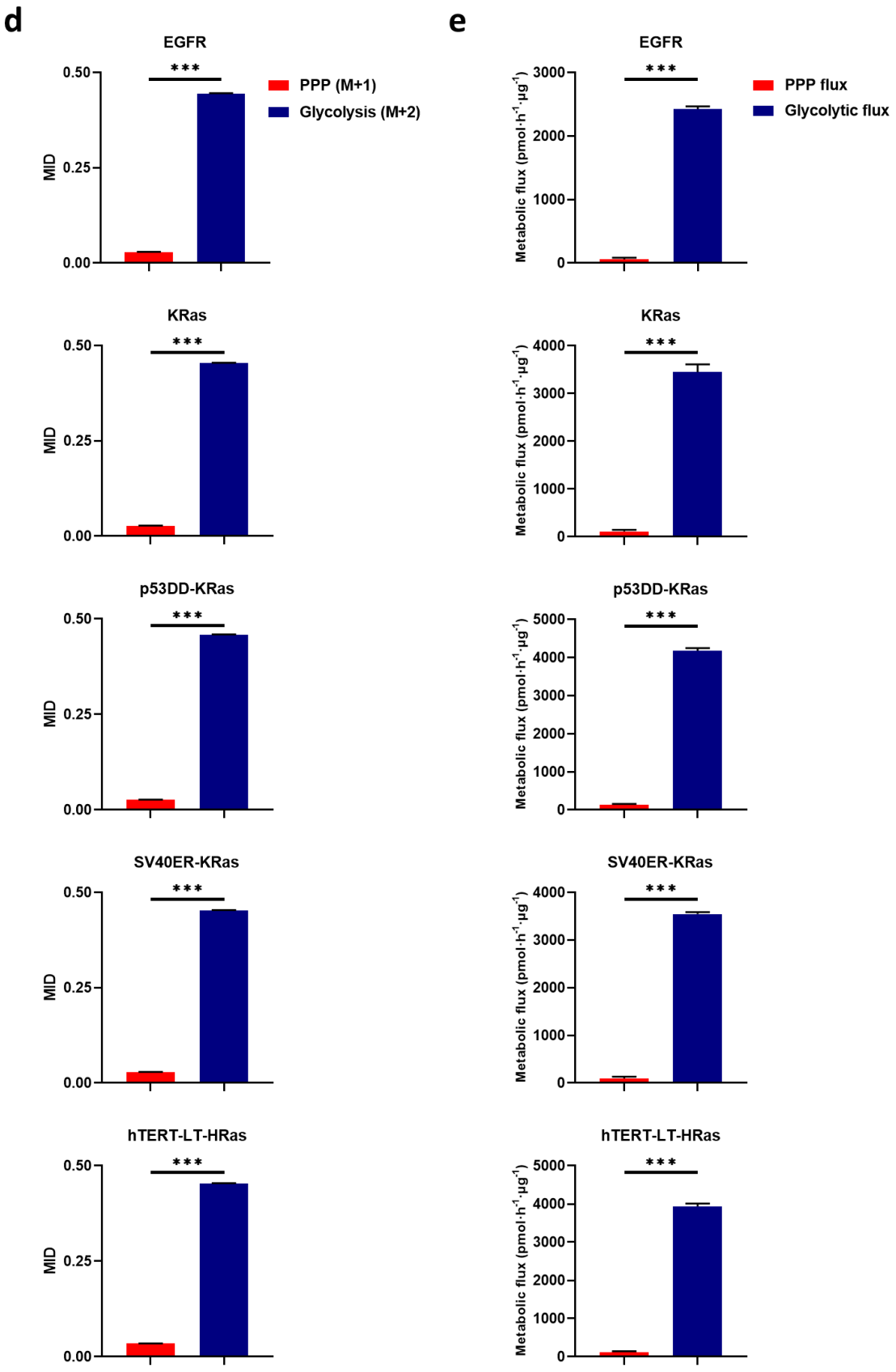
d
e
EGFR
KRas
p53DD-KRas
SV40ER-KRas
hTERT-LT-HRas
***
PPP (M+1)
Glycolysis (M+2)
PPP flux
Glycolytic flux
MID
Metabolic flux (pmol·h-1·µg-1)
0.00
0.25
0.50
0
1000
2000
3000
4000
5000

Figure 4.4 d-e. ^{13}C-isotopic labeling analysis and ^{13}C-MFA yield consistent results regarding the relative pathway magnitude between glycolysis and PPP.

d, ^{13}C-isotopic labeling analysis suggests that the strength of PPP as measured by the MID of M+1 lactate (m/z 262) is significantly smaller than that of glycolysis as measured by the MID of M+2 lactate (m/z 263), in HMEC-EGFR, HMEC-KRas, HMEC-p53DD-KRas and HMEC-hTERT-LT-HRas. Error bars, s.e.m (n=3). ***P<0.001.

e, Consistent with ^{13}C-isotopic labeling analysis, ^{13}C-MFA also indicates that the absolute metabolic flux of PPP is significantly smaller than that of glycolysis, in HMEC-EGFR, HMEC-KRas, HMEC-p53DD-KRas and HMEC-hTERT-LT-HRas. Error bars, 95% confidence intervals. ***P<0.001.

It has been hypothesized that metabolic behavior in cancer and normal proliferative cells can be regarded similarly[1,9,10,42]. To test this notion and investigate how proliferation affects metabolism, we plotted major intracellular fluxes against specific growth rates in all HMECs with converged results. The regression trend lines suggest that glycolysis and lactate excretion increased as cells grew faster, consistent with the Warburg Effect (Figure 4.4f). As expected, the malic enzyme (ME) reaction was also enhanced, potentially regenerating NADPH for cellular redox needs[43–45] (Figure 4.4f). Moreover, glutamine anaplerosis was enhanced when cells grew faster. This metabolic pattern further pinpoints the vital role of glutamine metabolism in maintaining the TCA cycle (Figure 4.3h). Additionally, ^{13}C-MFA results suggested that PDH, rather than pyruvate carboxylase (PC), catalyzed the primary route of pyruvate entry into the TCA cycle (Figure 4.4g), consistent with what has been reported in other cell lines[2]. Importantly, although the overall trend lines suggested that metabolic fluxes were controlled by growth rate at some level, we also noticed non-negligible deviations of certain fluxes from the regression lines

(Figure 5). Such deviations indicated that growth was not the only factor determining fluxes. In other words, metabolism is affected by both proliferation and oncogenotypes.

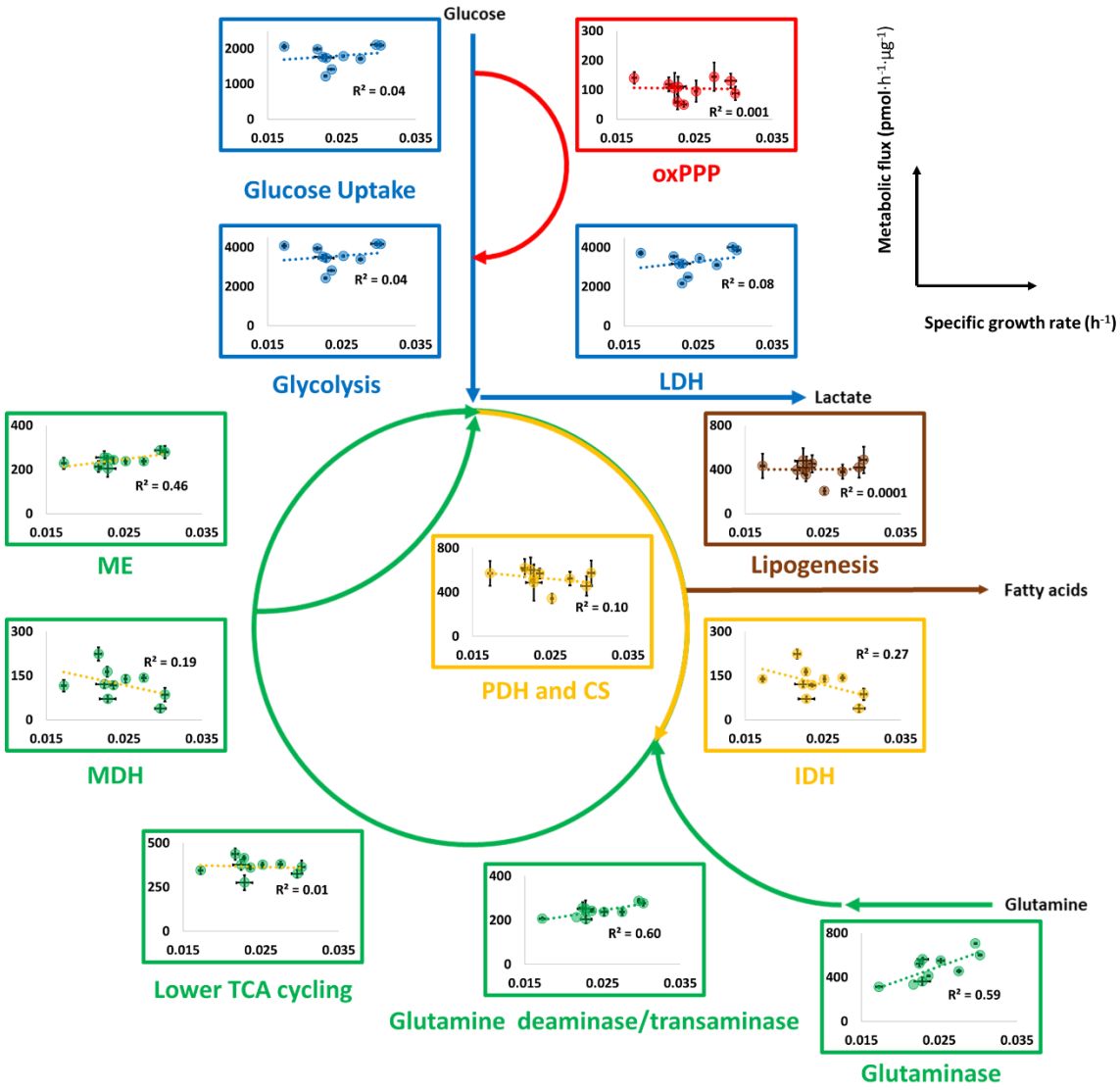

Figure 4.4 f. ^{13}C-MFA suggested that both intracellular and extracellular metabolism may be dually controlled by proliferation and oncogenotypes.

Error bars, 95% confidence intervals. Abbreviations: oxPPP, oxidative pentose phosphate pathway; LDH, lactate dehydrogenase; ME: malic enzyme; MDH, malate dehydrogenase; PDH, pyruvate dehydrogenase; CS, citrate synthase; IDH, isocitrate dehydrogenase; TCA cycle, tricarboxylic acid cycle; Glu, glutamate.

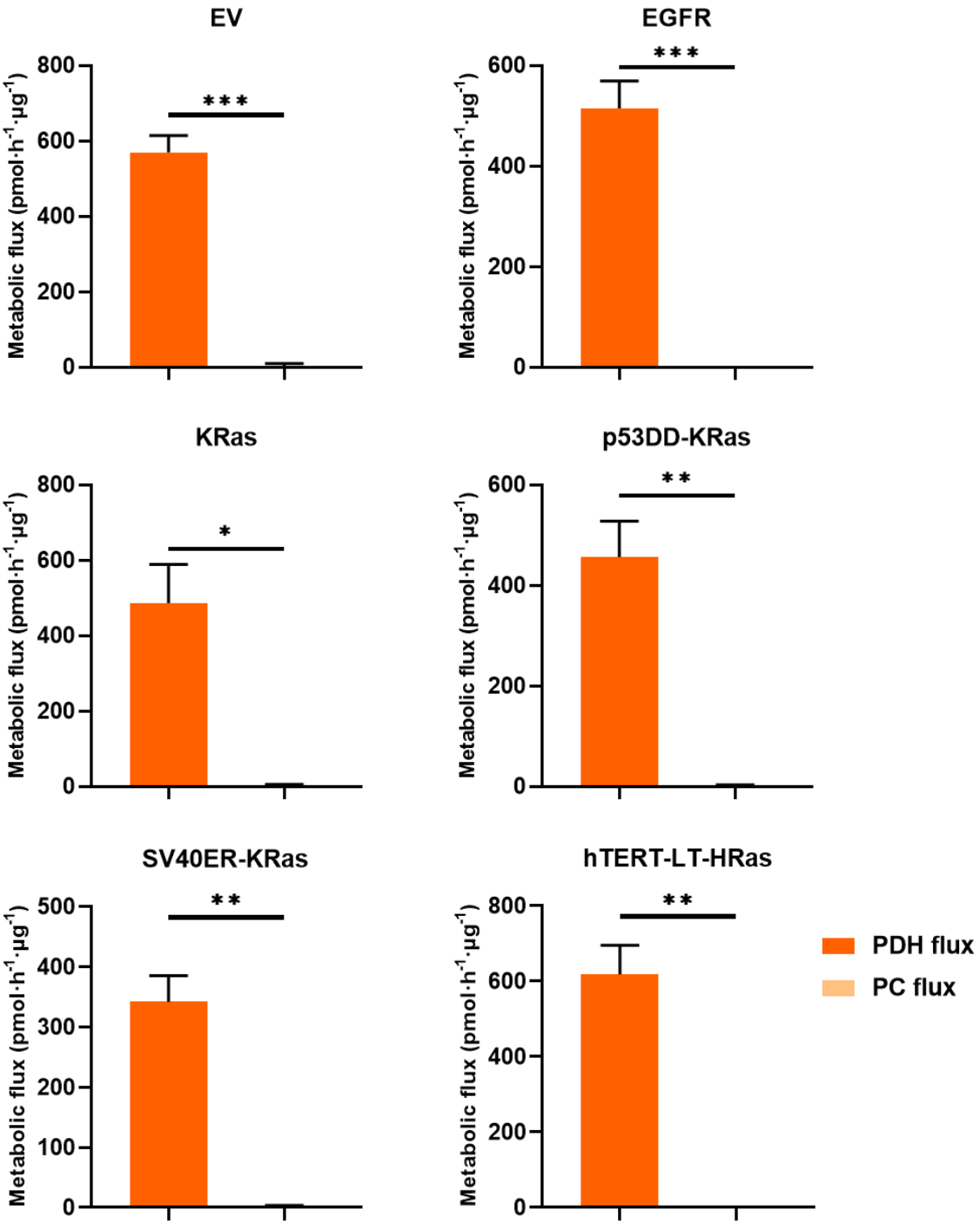

Figure 4.4 g. ^{13}C-MFA suggests that the pyruvate dehydrogenase (PDH) pathway is the main route of acetyl-CoA anaplerosis rather than the pyruvate carboxylase (PC) pathway.

Error bars, 95% confidence intervals. *P<0.05. **P<0.005. ***P<0.001.

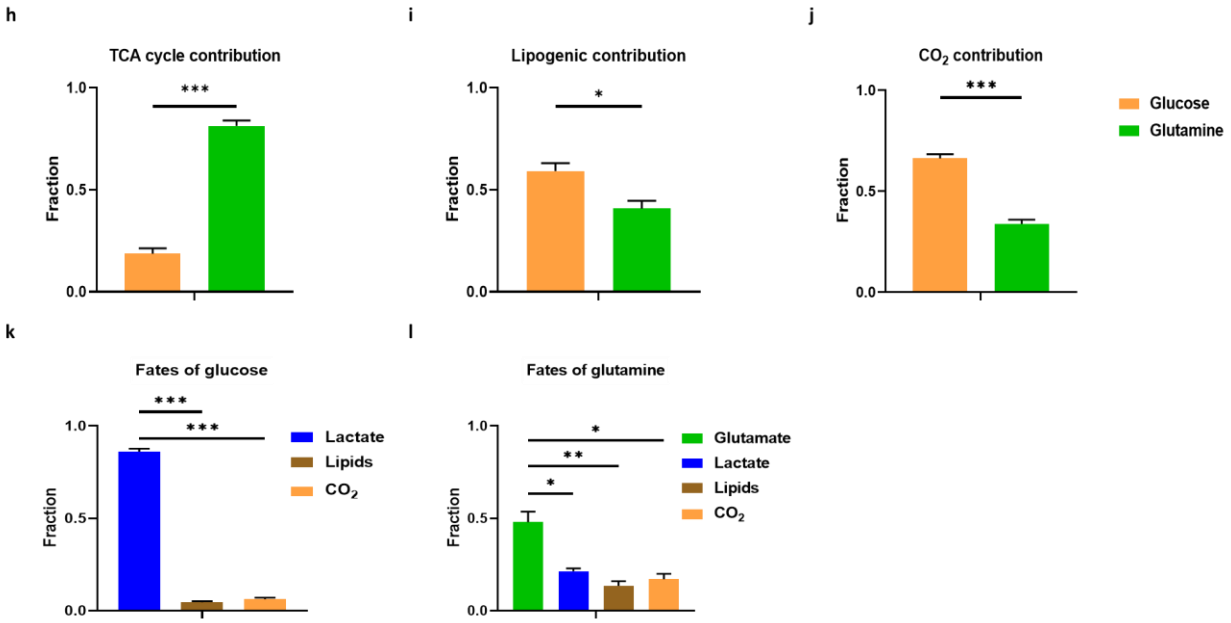

Figure 4.4 h-l. Contributions of glucose and glutamine to the TCA cycle, lipogenesis and CO_2 as well as fates of glucose and glutamine to major metabolic products calculated from averaged ^{13}C-MFA results from +EGF HMECs.

h, TCA contribution from glucose and glutamine.

i, Lipogenic contribution from glucose and glutamine.

j, CO_2 contribution from glucose and glutamine.

k, Fates of glucose to lactate, lipids and CO_2.

l, Fates of glutamine to glutamate, lactate, lipids and CO_2.

Error bars, 95% confidence intervals. *P<0.05. **P<0.005. ***P<0.001.

4.7 Normalizing fluxes against growth by introducing metabolic flux intensity (MFI)

Our ^{13}C-MFA results (Figure 4.4f) and the extracellular fluxes (Figure 4.2) suggest that metabolism may be dually controlled by both proliferation and oncogenotypes. Indeed, there may be two modes of action through which metabolism is regulated: an indirect route through which oncogene-altered proliferation affects metabolism and a direct oncogenic effect independent of proliferative control (Figure 4.5a).

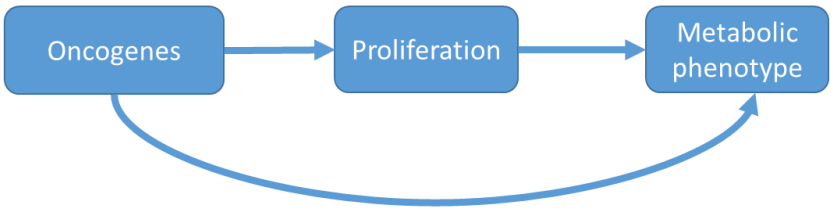

Q: How to decouple those two modes of action?
A: Divide metabolic flux by specific growth rate.

We defined a new quantity – **Metabolic flux intensity (MFI)**

$$\text{Metabolic flux intensity(MFI)} = \frac{\text{Metabolic Flux}}{\text{Specific growth rate}} [=] \frac{\text{pmol}\cdot\text{hour}^{-1}\,\mu\text{g of cell mass}^{-1}}{\text{hour}^{-1}} [=] \frac{\text{pmol}}{\mu\text{g of cell mass}}$$

Figure 4.5 a. Two modes through which oncogenotypes and proliferation affect metabolism, as well as the rationale and mathematical definition of the new quantity – metabolic flux intensity (MFI).

The two modes of control were uncoupled by dividing metabolic fluxes by the specific growth rate (Figure 4.5a). We term the resulting quantity as Metabolic Flux Intensity (MFI).

When the MFI of a pathway increases under some conditions, this suggests that cells require a higher flux along the pathway to sustain the same level of growth, whereas lower MFI suggests that the corresponding metabolic pathway plays a less essential role in sustaining cellular growth. Therefore, the MFI of a pathway is an indicator of how strongly cells rely on the pathway to proliferate. By defining this new quantity, we can potentially assess the direct impact of oncogenotypes on metabolism independent of proliferation.

We thus calculated MFIs for all major metabolic pathways and constructed the plots of MFIs against specific growth rates (Figure 4.5b). To isolate the impact of oncogenotype alone, we chose to focus on the +EGF HMECs. In addition, MFIs were averaged for HMECs with intermediate levels of tumorigenicity (EGFR, KRas, p53DD-KRas and SV40ER-KRas) to underscore the overall trend with increasing levels of tumorigenicity. We noticed that MFIs of certain metabolic pathways were increased in more tumorigenic lines, while other pathways remained unchanged (Figure 6). (Figure 4.5b). Interestingly, the glycolytic pathway and the lactate dehydrogenase (LDH) reaction exhibited enhanced MFIs, suggesting that the Warburg effect extends beyond the simple notion of proliferative upregulation of aerobic glycolysis (Figure 4.5b). Instead, cells with higher levels of tumorigenicity may need even greater glycolytic and LDH fluxes per growth rate to maintain proliferation. Furthermore, pathways with the greatest MFIs were oxPPP, malate dehydrogenase (MDH) and isocitrate dehydrogenase (IDH). Based on the definition of MFI, these may be the most critical reactions for sustaining growth in HMEC-hTERT-LT-HRas relative to the control cell line (Figure 4.5 b).

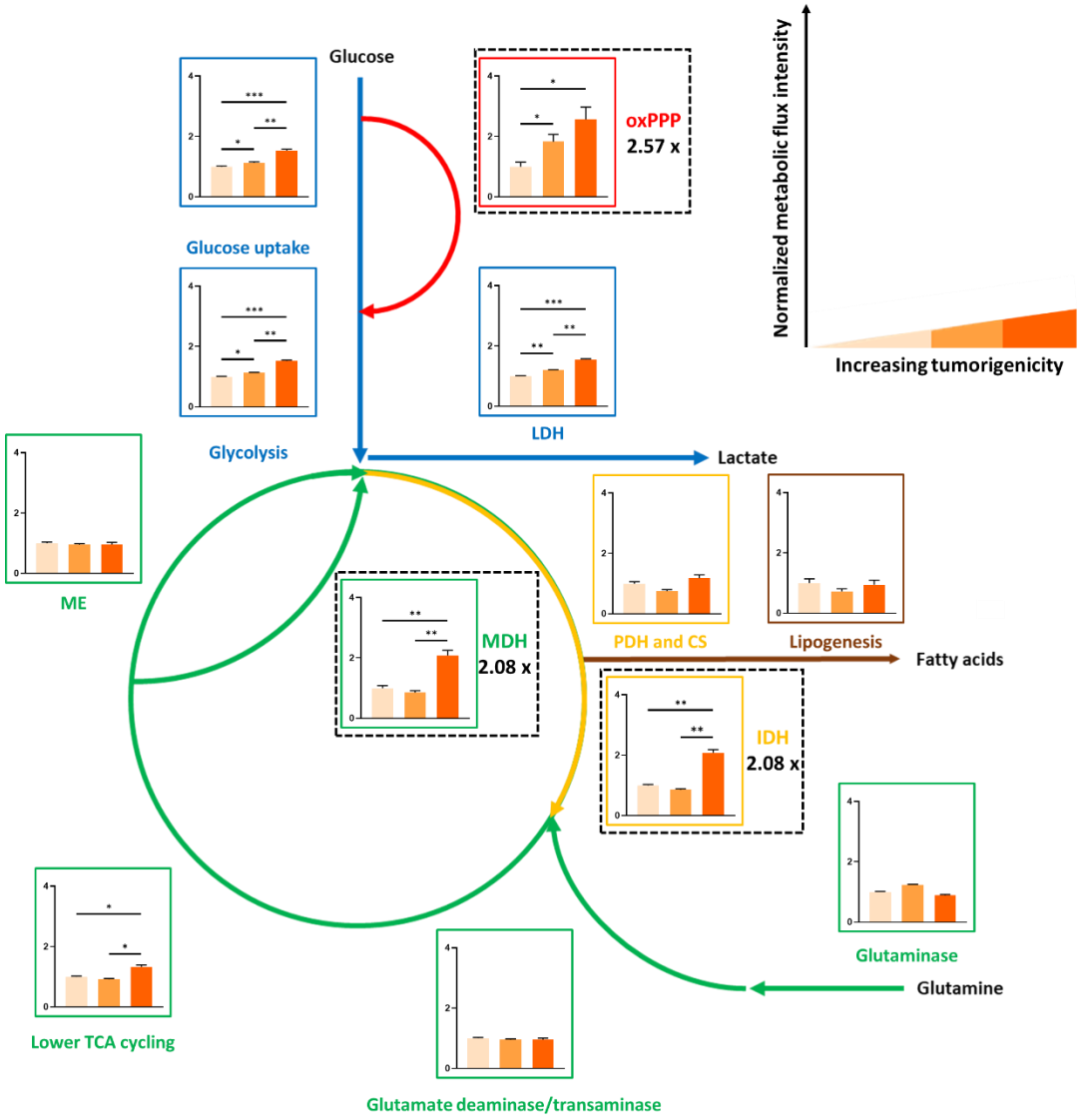

Figure 4.5 b. Quantitative ^{13}C-MFI analysis validated that oncogenotypes directly impact metabolism independent of proliferative control.

Normalized MFI results for all +EGF HMECs. Darker orange color indicates higher levels of tumorigenicity.

Error bars, 95% confidence intervals. *P<0.05. **P<0.005. ***P<0.001. Abbreviations: oxPPP, oxidative pentose phosphate pathway; MDH, malate dehydrogenase; IDH, isocitrate dehydrogenase; LDH, lactate dehydrogenase; ME: malic enzyme; PDH, pyruvate dehydrogenase; CS, citrate synthase; TCA cycle, tricarboxylic acid cycle.

4.8 Assessing the therapeutic potential of targeting oxPPP, MDH and IDH

Our MFI analysis identified oxPPP, MDH and IDH as the most enhanced reactions in HMECs harboring hTERT-LT-HRas. Interestingly, these three pathways are essential sources regenerating NADH and NADPH. OxPPP is one of the primary routes of NADPH synthesis, which can also be replenished by ME (Figure 4.6a). However, ME exhibited statistically invariant MFIs across cell lines, whereas the reliance on oxPPP was higher in more tumorigenic HMECs (Figure 4.5b). Additionally, MDH and IDH play an important role in maintaining the integrity of the TCA cycle, which functions as a central hub for supplying ATP, NADH and amino-anabolic precursors (Figure 4.6b). Therefore, inhibition of oxPPP, MDH and IDH may be selectively toxic in cancerous HMECs.

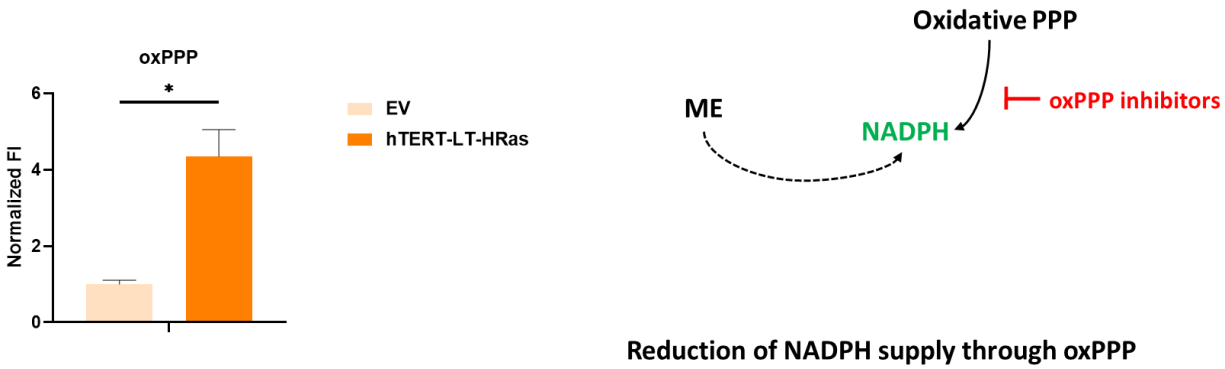

Figure 4.6 a. ^{13}C-MFI analysis identified oxPPP as the most enhanced reaction in HMEC-hTERT-LT-HRas. Targeting oxPPP is expected to impair NADPH regeneration.

Error bars, 95% confidence intervals. *P<0.05.

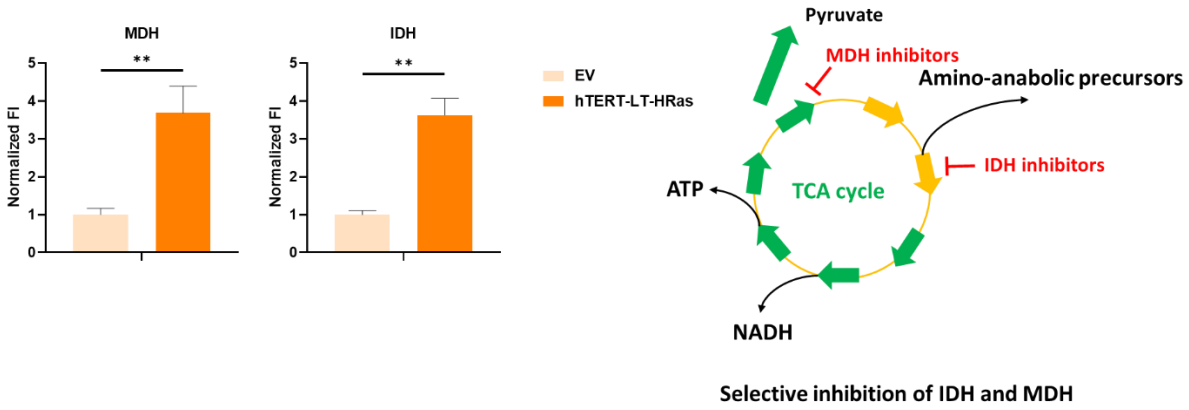

Figure 4.6 b. ^{13}C-MFI analysis identified MDH and IDH as one of the most enhanced reactions in HMEC-hTERT-LT-HRas. Targeting MDH and IDH is expected to impair NADH regeneration and the TCA cycle.

Error bars, 95% confidence intervals. **P<0.005.

To test these two strategies, we performed drug inhibition experiments for the most tumorigenic HMEC-hTERT-LT-HRas against the control line HMEC-EV. We used 6-aminonicotinamide (6AN), LW6 and GSK864 to inhibit oxPPP[46], MDH[47] and IDH[48], respectively. The fold changes of cell count for drug-treated compared to DMSO-treated cells at different drug concentrations are shown in Figure 4.6c. We found that these inhibitors were selectively more toxic in the most tumorigenic HMEC. Specifically, 0.5 μM 6AN, 100 μM LW6 or 10 μM GSK864 significantly reduced the proliferation of HMEC-hTERT-LT-HRas compared to the control cell line. It is worth noting that drug targeting of the metabolic pathways exhibiting statistically invariant MFIs might not be able to achieve selective toxicity (Figure 4.6d). Therefore, pathways with the greatest MFIs in the tumorigenic line may serve as better drug targets. These experiments underscore the therapeutic potentials of targeting oxPPP, MDH and IDH for selectively killing cancerous HMECs.

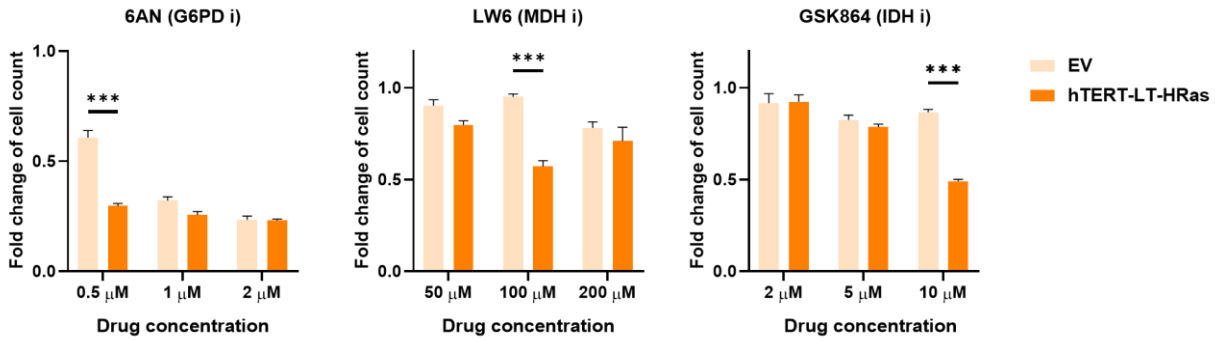

Figure 4.6 c. Drug targeting results for oxPPP, MDH and IDH.

Error bars, s.e.m. ***P<0.001.

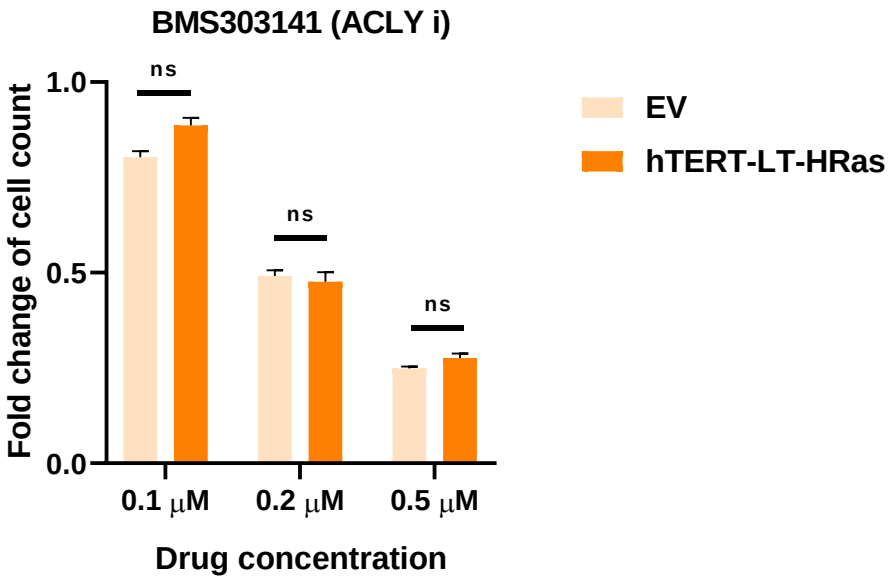

Figure 4.6 d. Drug targeting of ATP-citrate lyase (ACLY), which showed invariant MFI across tumorigenicity, yielded no selective toxicity.

4.9 Discussion and conclusions

We have demonstrated the use of ^{13}C-isotopic labeling and MFA to quantitatively resolve the metabolic fluxes of HMECs with different levels of tumorigenicity. We found a distinct substrate utilization pattern involving a truncated TCA cycle and glucose-supported lipogenesis. Moreover, we introduced the concept of MFI to unveil proliferation-independent oncogenic metabolic rewiring that helped identify pathways like oxPPP, MDH and IDH as new drug targets with improved selective toxicity. Our data and analysis provide direct evidence that the metabolisms of cancer and normal proliferative cells differ and this can be the basis for identifying targets for selective cancer treatment.

Our work further underscores the metabolic significance of glutamine anaplerosis. The fact that glutamine is metabolized as one of the major respiratory substrates in cancer cells has been previously reported[49–51]. More recently, the important role of glutamine in supporting *de novo* lipogenesis has been elucidated[20,34,36]. In contrast to these works, here we revealed another type of glutamine metabolism: a truncated TCA cycle for glutamine oxidation with glucose mainly supporting the lipogenic pathway. It is worth mentioning that a truncated TCA cycle has been reported in previous investigations. For example, glutamine can be utilized to fuel the TCA cycle in cancer cell lines harboring heterozygous IDH-1 mutations under hypoxia or mitochondrial inhibition[52]. Moreover, cell lines exhibiting a truncated TCA cycle exhibited reduced proliferation due to their inability to perform a fully functional reductive glutamine metabolism along IDH[52]. In contrast, our results show that the presence of a truncated TCA cycle does not undermine cellular growth in HMECs (Figure 4.1 f-h). In line with our results, the truncated TCA cycle and glucose-supported lipogenesis have also been reported in glioblastomas, and such rewired metabolism does not impair cancer cell proliferation either[2].

Importantly, our work shows that the truncated TCA cycle is present in all HMECs being studied, indicating that this metabolic pattern is not unique to cancer cells. Furthermore, we employed ^{13}C-MFA to fully resolve all major metabolic pathways and quantified fluxes within the truncated TCA cycle and *de novo* lipogenesis. This quantitative depiction provides opportunities to further investigate this metabolic pattern in depth. For example, the mechanism by which this metabolic phenomenon occurs is still unclear at this point and remains to be elucidated by future work. These rewired energetics may expose potential metabolic vulnerabilities that can be exploited for therapeutic intervention to treat cancer. This idea is in line with the therapeutic efforts to target both glucose and glutamine metabolism for enhanced overall effectiveness of chemotherapy[53–55].

Our quantitative flux results enabled us to address the question of whether cancer and normal proliferative metabolisms are different. One of the hallmarks of cancer – the Warburg effect – has been proposed to be shared by both cancer and proliferating cells[1,21,22]. However, there has been no study directly investigating whether and how cancer metabolism is different from proliferative metabolism beyond the Warburg effect. In fact, it would be difficult to eliminate confounding factors such as different cell types and genetic backgrounds if common existing cancer cell lines were used in such studies. These concerns prompted us to develop a new panel of HMECs that shared the same original genetic background by modifying defined genetic elements. More importantly, we believe that the main challenge to study the difference between cancer and normal proliferative metabolism is to decouple the growth-independent impact by oncogenotypes from that by altered growth phenotypes[56].

To decouple these two modes through which cancer metabolism is manifested, we introduced a new quantity called metabolic flux intensity (MFI) obtained by dividing metabolic

fluxes by the specific growth rate. In this way, the effect of growth on metabolism is normalized when one compares MFIs across different cell lines. MFI essentially serves as an indicator gauging the importance of a certain metabolic pathway in sustaining cellular growth. MFIs are different across our HMEC variants, which suggests that proliferation is not the only factor governing metabolic behavior.

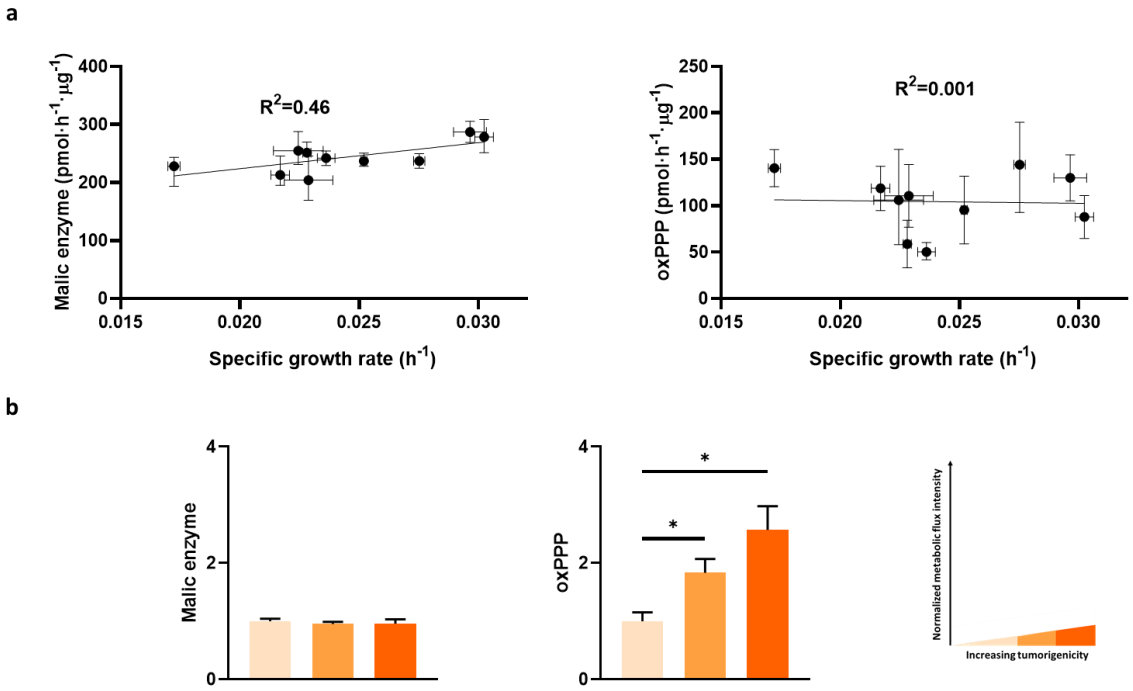

Figure 4.7 a-b. Demonstration of the connection between metabolic fluxes and flux intensities.

a, Metabolic fluxes of the malic enzyme (left) and the oxPPP (right) reactions. The R^2 value, which measures the proliferative control of metabolism, is higher for the malic enzyme than the oxPPP.

b, Consistent with the metabolic flux results, the flux intensities of the malic enzymes stayed constant across different levels of tumorigenicity, suggesting strong proliferative control. In contrast, the flux intensities of the oxPPP are significantly different, indicating proliferation-independent control on metabolism.

*P<0.05.

MFI analysis helps in selecting targets for treating cancer. Based on the definition of MFI, metabolic pathways with higher MFIs are relied upon by the cell more heavily than those with lower MFIs for supplying metabolites and energy for growth. Therefore, pathways with higher MFIs can be therapeutically more relevant in exerting selective toxicity on cancer cells. MFI analysis emphasizes the notion of selective toxicity because it compares flux changes independent of proliferative control of metabolism. Therefore, MFI may be more suitable for identifying potential drug targets.

Since oxPPP, MDH and IDH are responsible for producing NADPH and NADH, cofactor regeneration may be one of the key constraints limiting cancer cell growth. In line with this idea, inhibition of these reactions rendered a more drastic reduction of proliferation in the most tumorigenic HMEC line. Previous studies also reported similar promising results[57–60]. We believe that MFI analysis can be helpful in identifying potential drug targets in other types of cancer.

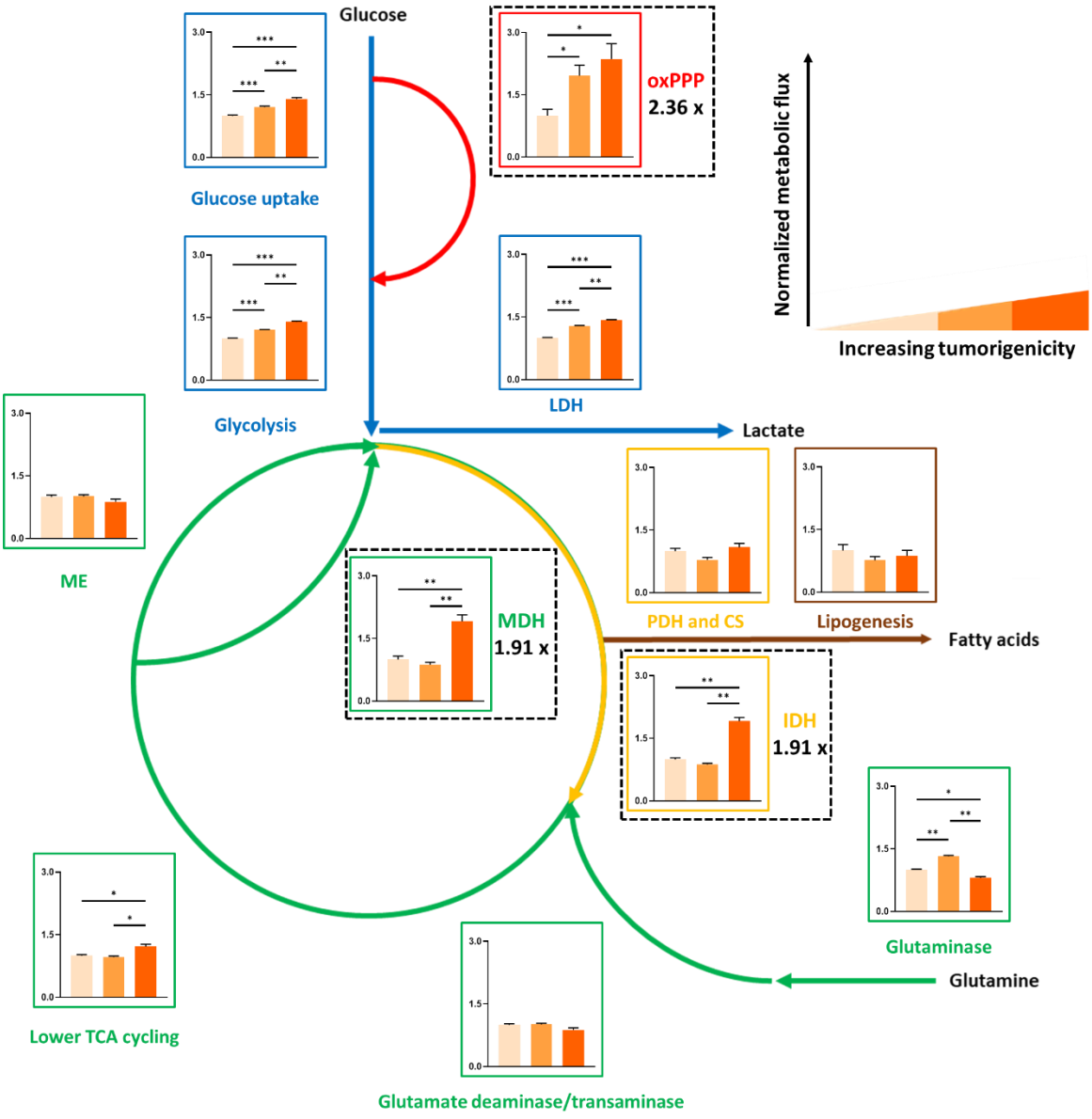

Figure 4.7 c. Normalized MFA results for all HMECs at +EGF condition. Darker orange color indicates higher levels of tumorigenicity.

Error bars, 95% confidence intervals. **P<0.005.

Normalized MFI results for all +EGF HMECs. Darker orange color indicates higher levels of tumorigenicity. Error bars, 95% confidence intervals. *P<0.05. **P<0.005. ***P<0.001. Abbreviations: oxPPP, oxidative pentose phosphate pathway; MDH, malate dehydrogenase; IDH, isocitrate dehydrogenase; LDH, lactate dehydrogenase; ME: malic enzyme; PDH, pyruvate dehydrogenase; CS, citrate synthase; TCA cycle, tricarboxylic acid cycle.

4.10 Experimental procedures

Cell culture conditions

All cell lines were obtained from ATCC, tested for mycoplasma and cultured at 37 ºC and 5% CO_2. The MCDB 170 medium was used for regular subculture on 10-cm tissue-culture treated polystyrene dishes (Corning). The complete formulation of the MCDB 170 medium includes a mammary epithelial basal medium (MEBM) (Lonza) supplemented with 5 µg/mL insulin, 0.5 µg/ml hydrocortisone, 5 µg/mL transferrin, 0.07 mg/mL bovine pituitary extract (BPE) (Hammond), 10 uL isoproterenol and 5 ng/mL EGF (Peprotech). Trypsin-EDTA (0.25%) (Thermo Fisher) was used as the dissociation reagent to passage cells upon 70-80% confluence for up to 4 passages. Fresh media (15 mL per plate) was replaced every 2-3 days. Cells were plated and tested on 6-well plates (Corning) for the experiments determining growth rates and extracellular fluxes. Dulbecco's Modified Eagle's Medium (DMEM) (without glucose, glutamine and sodium pyruvate, Corning) was used as the basal medium (2.5 mL per well) supplemented with other MCDB 170 components, 10 mM glucose, 4 mM glutamine, 0.1 mM ethanolamine, 0.1 mM phosphoethanolamine and 10 mM HEPEs. All components were obtained from Sigma unless otherwise noted.

Transfection/infection and drug selection for HMECs

HMEC 184A1 was used as the parental cell line to develop all HMEC variants, except for HMEC-hTERT-LT-HRas, which was kindly provided by W. Hahn (Dana-Farber Cancer Institute). An empty vector, K-ras G12V, EGFR L858R, p53DD and SV40ER (Addgene) were stably integrated into HMEC 184A1 through γ-retroviral infections under the CMV promoter.

HEK 293 T cells at 40-60% confluence were transfected with 5.25 µg pBABE-puro EV, pBABE-puro K-ras G12V, pBABE-puro EGFR L858R, pBABE-neo p53DD or pBABE-neo SV40ER, 4.725 µg gag/pol vector, 0.525 µg VSV-G and 31.5 µL XtremeGENE HP DNA Transfection Reagent (Roche). All components were premixed and equilibrated for 15 min at 25 ºC before being transferred in a dropwise manner into HEK 293 T cells grown in a 10-cm dish with 10 mL DMEM and 10 vol % fetal bovine serum (FBS) (Sigma SAFC). Media containing γ-retroviruses was harvested after 36-48 h incubation at 37 ºC and 5% CO_2 and was passed through 0.45 µm filters (Pall). The retentate (~10 mL) containing γ-retroviruses was then mixed with 8 µg/mL Polybrene (Millipore) and added into HMECs at 20-30% confluence grown in a 10-cm dish. After 24-36 hours, the spent media with retroviruses was aspirated and the plate was washed by 10 mL PBS (Corning) for three times.

HMEC-EV, HMEC-EGFR and HMEC-KRas with successful integrations of retroviral vectors were selected with 0.5 µg/mL puromycin. HMEC-p53DD-KRas and HMEC-SV40ER-KRas were selected with 0.5 µg/mL puromycin and subsequently with 400 µg/mL G418. The concentrations of these drugs were verified to be able to kill all mock-infected HMECs. To avoid bias due to position effect, the final population of each cell line was composed of at least 25 independent clones. HMEC lines after drug selection were then cryopreserved by mixing 1.5-3×10^6 cells with 1mL freezing media containing 75 vol % MEBM, 15 vol % FBS and 10 vol % glycerol (Sigma).

Western blots

Cells were lysed in RIPA buffer (Thermo) containing protease and phosphatase inhibitor cocktails (Bimake B14001 and B15001-B). Protein concentration was quantified by BCA assay (Thermo Fisher). Equal amounts of protein were run on 4-20% Tris-Glycine gels (Invitrogen) and transferred to PVDF membranes. Membranes were blocked with 5% bovine serum albumin and probed with the following primary antibodies: β-actin (Sigma, Cat. No. A1978), EGFR (Thermo Fisher, Cat. No. MS-400-P1), ERK1/2 (Cell Signaling, Cat. No. 9102) phospho-ERK1/2 (Cell Signaling, Cat. No. 4370), p53 (BD Biosciences, Cat. No. 554293), SV40 T Ag (Santa Cruz, Cat. No. SC-147), α-Tubulin (Cell Signaling, Cat. No. 3873). Blots were imaged using Luminata Western HRP substrate (EMD Millipore).

Determinations of specific growth rates and extracellular fluxes

Protein concentrations for cells within 6-well plates were quantified by BCA assay (Thermo Pierce). Specific growth rates (μ) were determined by the following equation:

$$\mu = \frac{1}{t} ln \left(\frac{X_t}{X_0}\right)$$

where X_t and X_0 are the protein concentrations at time 0 and time t, respectively. The initial cell seeding densities were 80×10^3 and 35×10^3 per well for -EGF and +EGF conditions, respectively. MCDB 170 medium was used during seeding (D-3), and DMEM with MCDB 170 components at +/-EGF conditions was used after 24 hours during media change (D-2), preceded by a two-time wash with PBS. Spent media was collected and new media was replaced after another 48 hours following a one-time wash with 2mL/well PBS (D0). Another 48 hours later, the spent

media was harvested, and the cells (D2) were first washed once by 2 mL/well PBS. Then 500 µL/well of cold RIPA buffer (Thermo) was pipetted into each well, and the 6-well plates were shaken briefly and placed at 4 ºC for overnight incubation. Cell lysates were then harvested, vortexed and centrifuged for the retrieval of supernatant. Protein concentration within each well was then measured in 96-well plates through colorimetric detection and quantification according to the standard protocol of BCA assay.

Concentrations of extracellular glucose, lactate, glutamine and glutamate in spent media were then measured by Yellow Spring Instruments (YSI) 2950. Based on the equation governing extracellular fluxes during the exponential growth phase, the extracellular fluxes for glucose, lactate and glutamate were determined according to the following equation [32]:

$$v = \frac{C_t - C_0}{e^{\mu t} - 1} \frac{\mu}{X_0}$$

where v is the extracellular flux of a metabolite, C_t the concentration of that metabolite at time t, C_0 the concentration of that metabolite at time 0, µ the specific growth rate and X_0 the initial protein content at time 0.

Due to the fact that glutamine is unstable and undergoes spontaneous degradation in normal cell culture condition, the extracellular fluxes for glutamine were determined based on the following equation with an additional term of decay constant k [32]:

$$v = \frac{C_t e^{kt} - C_0}{e^{(\mu+k)t} - 1} \frac{\mu + k}{X_0}$$

where the first-order decay constant k was determined based on the following equation:

$$k = \frac{1}{t} ln\left(\frac{C_{0,d}}{C_{t,d}}\right)$$

where $C_{t,d}$ and $C_{0,d}$ are the glutamine concentrations in media without cells at time t and time 0, respectively.

^{13}C-isotopic labeling experiments and intracellular metabolite extraction

^{13}C-isotopic tracers (U-$^{13}C_6$-glucose, 1,2-$^{13}C_2$-glucose and U-$^{13}C_5$-glutamine, Cambridge Isotope Laboratory) were administered at the same concentrations as the unlabeled counterparts (10 mM for the glucose tracers and 4 mM for the glutamine tracer). The tracers were used one at a time at full enrichment. For example, 10 mM of U-$^{13}C_6$-glucose was used with 4 mM unlabeled glutamine in the U-$^{13}C_6$-glucose tracing experiment. The media formulation is exactly the same as that used in the growth and extracellular flux experiments. The experimental procedures are the same as that for the growth and extracellular flux experiments until D2. Instead of harvesting at D2, we prolonged the ^{13}C-istopic labeling duration to 72 hours (D3) after the second media change (D0) to allow for more sufficient time to reach metabolic and isotopic steady states.

To harvest metabolites with minimal metabolic perturbations, we immediately placed the 6-well plates on ice once the plates were out of the incubator. Spent media was then quickly aspirated, and each well was washed once by cold (0-4 ºC) saline, followed by addition of 500 µL freezing cold (-20 ºC) methanol. Next, 300 µL cold (0-4 ºC) milliQ water containing 2 µg norvaline (Sigma) as an internal standard was pipetted to each well. Cells were then quickly scrapped off from the wells by pipette tips in the presence of the liquid mixture, and the mixture was transferred to microcentrifuge tubes. These steps were performed one at a time for each well. Metabolite extraction was then performed by adding 600 µL freezing cold (-20 ºC) chloroform to each microcentrifuge tube and then quickly vortexing the mixture at 4 ºC for 10

min, followed by a centrifugation at 21000×g for 10 min. After these steps, the mixture was separated into two phases with the top and bottom layers containing polar and nonpolar metabolites, respectively. The two layers were then retrieved and placed into separate microcentrifuge tubes, dried by air and then stored at -80 ºC for less than 1-2 weeks before being derivatized and loaded onto GC/MS.

Metabolite derivatization and GC/MS analysis

Polar metabolites were derivatized by incubating dried samples in each microcentrifuge tube with 15 µL methoxyamine in pyridine (MOX) (Thermo) at 40 ºC for 1.5 hours, followed by another incubation with 20 µL N-(tert-butyldimethylsilyl)-N-methyl-trifluoroacetamide with 1% tert-Butyldimethylchlorosilane (TBDMS) (Sigma) at 60 ºC for 1 hour. The derivatized mixture was then briefly vortexed, centrifuged and transferred into polypropylene GC/MS vials (Agilent). Nonpolar metabolites were treated by incubating dried samples in each microcentrifuge tube with 500 µL methanol with 2 vol % sulfuric acid at 60 ºC for 3 hours. Next, 600 µL hexane and 175 µL saturated sodium chloride solution were added, and the mixture was vortexed at room temperature for 30 min and subsequently centrifuged at 21000×g for 1 min. The resulting mixture was separated into two phases, and the top phase containing nonpolar metabolites was retrieved into a separate microcentrifuge tube, dried by air, reconstituted by 30-50 µL hexane and transferred into amber glass GC/MS vials with glass inserts (Agilent).

Agilent 6890N GC and 5975B Inert XL MS were used for polar metabolite analysis. The column for the 6890N GC is Agilent J&W DB-35ms (35%-phenyl-methylpolysiloxane, mid-polarity) and the electron ionization mode with 70 eV was used for the 5975B MS.

Chromatography grade helium (Airgas) at 1mL/min flow rate was used as the carrier gas. The inlet temperature for the 6890N GC was set to 270 ºC, and the oven temperature was first maintained at 100 ºC, and ramped to 300 ºC at a speed of 2.5 ºC/min. Samples of either 1 or 2 µL were injected into the instrument with either split or splitless mode based on sample abundances. The scan mode with a detection range of 150-625 m/z was used for all measurements. Mass isotopomer distributions (MIDs) have been corrected for natural abundance.

Agilent 7890B GC and 5977B MS were used for nonpolar metabolite analysis. The column for the 7890B GC is Agilent J&W HP-5ms (5%-phenyl-methylpolysiloxane, nonpolar) and the electron ionization mode with 70 eV was used for the 5977B MS. Ultra high purity grade helium (Airgas) at 3 mL/min was used as the carrier gas. The inlet temperature for the 7890B GC was set to 280 ºC, and the oven temperature was first maintained at 165 ºC and then ramped to 226 °C at a speed of 2 ºC/min. Samples of 1 µL were injected into the instrument with the splitless mode. The scan mode with a detection range of 200-400 m/z was used for all measurements. MIDs have been corrected for natural abundance.

^{13}C-metabolic flux analysis (^{13}C-MFA)

An elementary metabolite unit (EMU)-based software Metran coded within MATLAB (MathWorks) was used to perform ^{13}C-MFA[39,61]. Experimentally determined extracellular fluxes of glucose, lactate, glutamine and glutamate, as well as the ^{13}C-labeling data were used in conjunction with a metabolic reaction model (Figure S3) to generate ^{13}C-MFA results. The 95% confidence intervals for metabolic fluxes were obtained by performing parameter continuation on converged flux results [62].

Inhibition of oxPPP, MDH and IDH

HMEC-hTERT-LT-HRas and HMEC-EV were seeded at 35×10^3 per well with 5ng/mL EGF in 6-well plates. The small molecule drugs 6-aminonicotinamide (6AN), LW6 and GSK864 at different concentrations were administered in the usual MEBM-based MCDB 170 medium. DMSO was used to prepare the initial concentrated drug solutions. Cell counts were measured by Cellometer (Nexcelom) 48 hours after seeding.

Definition of quantities

Fractional enrichments from ^{13}C-isotopic tracers were calculated using MID data corrected for natural abundance based on the following equation:

$$\text{Fractional enrichment} = \sum_{i=0}^{n}(i \times m_i) \,/(n \times \sum_{i=0}^{n} m_i)$$

where n is the number of carbon atoms in a metabolite, m_i the abundance of a mass isotopomer and i the labeling state (M+i) of a mass isotopomer.

Metabolic flux intensities (MFIs) were defined and calculated based on the following equation:

$$\text{MFI} = \frac{v}{\mu}$$

where v and μ refer to metabolic flux (pmol·h^{-1}·μg^{-1}) and specific growth rate (h^{-1}), respectively. The unit of MFI is therefore pmol·μg^{-1}.

Table 4.1. Biochemical reactions and carbon atom transitions used in ^{13}C-MFA.

Single- and double-headed arrows refer to unidirectional and bidirectional reactions, respectively. Abbreviations are the same as in Figure S3. Reactions are numbered consistent as shown in Figure S3. Letters in the bracket indicate the position of carbon atoms. The subscript .x refers to extracellular localization, .c cytosolic localization, .m mitochondrial localization, .mnt measurement.

<u>Extracellular fluxes and biomass production</u>		
#1	Glc.x (abcdef) → G6P (abcdef)	Glucose import and hexokinase
#2	Lac (abc) → Lac.x (abc)	Lactate export
#3	Gln.x (abcde) → Gln (abcde)	Glutamine import
#4	Glu (abcde) → Glu.x (abcde)	Glutamate export
#5	0.18 Asp + 0.23 Glu + 0.15 Ala + 0.16 Gln + 0.17 Ser + 0.11 Gly → Biomass	Biomass production
<u>Scaling fluxes</u>		
#6	Pyr.mnt (abc) → Pyr.fix (abc)	Pyruvate scaling flux
<u>Glycolysis</u>		
#7	G6P (abcdef) ↔ F6P (abcdef)	Phosphoglucose isomerase
#8	F6P (abcdef) → DHAP (cba) + GAP (def)	Aldolase
#9	DHAP (abc) ↔ GAP (abc)	Triose phosphate isomerase
#10	GAP (abc) ↔ 3PG (abc)	Glyceraldehyde-3-phosphate dehydrogenase and phosphoglycerate kinase
#11	3PG (abc) → Pyr.c (abc)	Phosphoglycerate mutase, enolase and pyruvate kinase
#12	Pyr.c (abc) ↔ Lac (abc)	Lactate dehydrogenase

Table 4.1 (continued). Biochemical reactions and carbon atom transitions used in ^{13}C-MFA.

Pentose phosphate pathway (PPP)		
#13	G6P (abcdef) → P5P (bcdef) + CO2 (a)	6-phosphogluconate dehydrogenase
#14	P5P (abcde) + P5P (fghij) ↔ S7P (abfghij) + GAP (cde)	Transaldolase
#15	S7P (abcdefg) + GAP (hij) ↔ F6P (abchij) + E4P (defg)	Transaldolase
#16	P5P (abcde) + E4P (fghi) ↔ F6P (abfghi) + GAP (cde)	Transaldolase
Anaplerotic and amino acids metabolism		
#17	Pyr.m (abc) + CO2 (d) → Oac (abcd)	Pyruvate carboxylase
#18	Mal (abcd) ↔ Pyr.m (abc) + CO2 (d)	Malic enzyme
#19	Glu (abcde) ↔ Akg (abcde)	Glutamate trans/deaminases
#20	Oac (abcd) + Glu (efghi) ↔ Asp (abcd) + Akg (efghi)	Asp-Glu transaminase
#21	Pyr.c (abc) + Glu (defgh) ↔ Ala (abc) + Akg (defgh)	Ala-Glu transaminase
#22	Gln (abcde) ↔ Glu (abcde)	Glutaminase
TCA cycle		
#23	Pyr.m (abc) → AcCoA.m (bc) + CO2 (a)	Pyruvate dehydrogenase
#24	AcCoA.m (ab) + Oac (cdef) → Cit (fedbac)	Citrate synthase
#25	Cit (abcdef) ↔ Akg (abcde) + CO2 (f)	Aconitase and isocitrate dehydrogenase
#26	Akg (abcde) → Suc (bcde) + CO2 (a)	α-ketoglutarate dehydrogenase and succinyl-CoA synthetase
#27	Suc (abcd) ↔ Fum (abcd)	Succinate dehydrogenase
#28	Fum (abcd) ↔ Mal (abcd)	Fumarase
#29	Mal (abcd) ↔ Oac (abcd)	Malate dehydrogenase
Fatty acid synthesis		
#30	Cit (abcdef) → AcCoA.c (ed) + Oac (fcba)	ATP-citrate lyase
#31	AcCoA.c (ab) → FA (ab)	Fatty acid synthase

Table 4.1 (continued). Biochemical reactions and carbon atom transitions used in ^{13}C-MFA.

Dilution and mixing fluxes		
#32	0 Pyr.c (abc) → Pyr.mnt (abc)	Pyruvate compartmentalization (from cytosol)
#33	0 Pyr.m (abc) → Pyr.mnt (abc)	Pyruvate compartmentalization (from mitochondria)
Compartmentalized reactions		
#34	Pyr.c (abc) ↔ Pyr.m (abc)	Pyruvate compartmentalization (between cytosol and mitochondrion)
#35	3PG (abc) + Glu (defgh) → Ser (abc) + Akg (defgh)	Phosphoglycerate dehydrogenase, phosphoserine aminotransferase and phosphoserine phosphatase
#36	Ser (abc) → Gly (ab) + MEETHF (c)	Serine hydroxymethyltransferase

4.11 References

(1) Hanahan, D.; Weinberg, R. A. Hallmarks of Cancer: The next Generation. *Cell*. 2011, pp 646–674.

(2) DeBerardinis, R. J.; Mancuso, A.; Daikhin, E.; Nissim, I.; Yudkoff, M.; Wehrli, S.; Thompson, C. B. Beyond Aerobic Glycolysis: Transformed Cells Can Engage in Glutamine Metabolism That Exceeds the Requirement for Protein and Nucleotide Synthesis. *Proc. Natl. Acad. Sci. U. S. A.* **2007**, *104* (49), 19345–19350.

(3) Hsu, P. P.; Sabatini, D. M. Cancer Cell Metabolism: Warburg and Beyond. *Cell* **2008**, *134* (5), 703–707.

(4) Liberti, M. V.; Locasale, J. W. The Warburg Effect: How Does It Benefit Cancer Cells? *Trends Biochem. Sci.* **2016**, *41* (3), 211–218.

(5) Bensinger, S. J.; Christofk, H. R. New Aspects of the Warburg Effect in Cancer Cell Biology. *Seminars in Cell and Developmental Biology*. 2012.

(6) Koppenol, W. H.; Bounds, P. L.; Dang, C. V. Otto Warburg's Contributions to Current Concepts of Cancer Metabolism. *Nature Reviews Cancer*. 2011.

(7) Tran, T. Q.; Hanse, E. A.; Habowski, A. N.; Li, H.; Ishak Gabra, M. B.; Yang, Y.; Lowman, X. H.; Ooi, A. M.; Liao, S. Y.; Edwards, R. A.; Waterman, M. L.; Kong, M. α-Ketoglutarate Attenuates Wnt Signaling and Drives Differentiation in Colorectal Cancer. *Nat. Cancer* **2020**.

(8) Warburg, O. On the Origin of Cancer Cells. *Science (80-.).* **1956**.

(9) Ward, P. S.; Thompson, C. B. Metabolic Reprogramming: A Cancer Hallmark Even

Warburg Did Not Anticipate. *Cancer Cell*. 2012.

(10) Schulze, A.; Harris, A. L. How Cancer Metabolism Is Tuned for Proliferation and Vulnerable to Disruption. *Nature* **2012**, *491* (7424), 364–373.

(11) Ananieva, E. Targeting Amino Acid Metabolism in Cancer Growth and Anti-Tumor Immune Response. *World J. Biol. Chem.* **2015**.

(12) Chen, Z.; Liu, M.; Li, L.; Chen, L. Involvement of the Warburg Effect in Non-Tumor Diseases Processes. *J. Cell. Physiol.* **2017**.

(13) Vacanti, N. M.; Metallo, C. M. Exploring Metabolic Pathways That Contribute to the Stem Cell Phenotype. *Biochimica et Biophysica Acta - General Subjects*. 2013.

(14) Folmes, C. D. L.; Dzeja, P. P.; Nelson, T. J.; Terzic, A. Metabolic Plasticity in Stem Cell Homeostasis and Differentiation. *Cell Stem Cell* **2012**, *11* (5), 596–606.

(15) Agathocleous, M.; Harris, W. A. Metabolism in Physiological Cell Proliferation and Differentiation. *Trends in Cell Biology*. 2013.

(16) Vander Heiden, M. G.; Lunt, S. Y.; Dayton, T. L.; Fiske, B. P.; Israelsen, W. J.; Mattaini, K. R.; Vokes, N. I.; Stephanopoulos, G.; Cantley, L. C.; Metallo, C. M.; Locasale, J. W. Metabolic Pathway Alterations That Support Cell Proliferation. *Cold Spring Harb. Symp. Quant. Biol.* **2011**, *76*, 325–334.

(17) Christofk, H. R.; Vander Heiden, M. G.; Harris, M. H.; Ramanathan, A.; Gerszten, R. E.; Wei, R.; Fleming, M. D.; Schreiber, S. L.; Cantley, L. C. The M2 Splice Isoform of Pyruvate Kinase Is Important for Cancer Metabolism and Tumour Growth. *Nature* **2008**, *452* (7184), 230–233.

(18) Kim, B.; Li, J.; Jang, C.; Arany, Z. Glutamine Fuels Proliferation but Not Migration of Endothelial Cells. *EMBO J.* **2017**.

(19) Metallo, C. M.; Gameiro, P. A.; Bell, E. L.; Mattaini, K. R.; Yang, J.; Hiller, K.; Jewell, C. M.; Johnson, Z. R.; Irvine, D. J.; Guarente, L.; Kelleher, J. K.; Heiden, M. G. Vander; Iliopoulos, O.; Stephanopoulos, G. Reductive Glutamine Metabolism by IDH1 Mediates Lipogenesis under Hypoxia. TL - 481. *Nature* **2011**, *481 VN*- (7381), 380–384.

(20) Mullen, A. R.; Wheaton, W. W.; Jin, E. S.; Chen, P.-H.; Sullivan, L. B.; Cheng, T.; Yang, Y.; Linehan, W. M.; Chandel, N. S.; DeBerardinis, R. J. Reductive Carboxylation Supports Growth in Tumour Cells with Defective Mitochondria. *Nature* **2012**, *481* (7381), 385–388.

(21) Vander Heiden, M. G.; Cantley, L. C.; Thompson, C. B.; Mammalian, P.; Exhibit, C.; Metabolism, A. Understanding the Warburg Effect : Cell Proliferation. *Science (80-.).* **2009**, *324* (5), 1029–1034.

(22) Vander Heiden, M. G.; DeBerardinis, R. J. Understanding the Intersections between Metabolism and Cancer Biology. *Cell*. 2017.

(23) Méndez-lucas, A.; Lin, W.; Driscoll, P. C.; Legrave, N.; Novellasdemunt, L.; Xie, C.; Charles, M.; Wilson, Z.; Jones, N. P.; Rayport, S.; Rodríguez-justo, M.; Li, V.; Macrae, J. I.; Hay, N.; Chen, X.; Yuneva, M. Identifying Strategies to Target the Metabolic Flexibility of Tumours. *Nat. Metab.* **2020**, *2* (April), 335–350.

(24) Beroukhim, R.; Mermel, C. H.; Porter, D.; Wei, G.; Raychaudhuri, S.; Donovan, J.; Barretina, J.; Boehm, J. S.; Dobson, J.; Urashima, M.; McHenry, K. T.; Pinchback, R. M.; Ligon, A. H.; Cho, Y. J.; Haery, L.; Greulich, H.; Reich, M.; Winckler, W.; Lawrence, M.

S.; et al. The Landscape of Somatic Copy-Number Alteration across Human Cancers. *Nature* **2010**.

(25) Locasale, J. W.; Grassian, A. R.; Melman, T.; Lyssiotis, C. A.; Mattaini, K. R.; Bass, A. J.; Heffron, G.; Metallo, C. M.; Muranen, T.; Sharfi, H.; Sasaki, A. T.; Anastasiou, D.; Mullarky, E.; Vokes, N. I.; Sasaki, M.; Beroukhim, R.; Stephanopoulos, G.; Ligon, A. H.; Meyerson, M.; et al. Phosphoglycerate Dehydrogenase Diverts Glycolytic Flux and Contributes to Oncogenesis. *Nat. Genet.* **2011**, *43* (9), 869–874.

(26) Olivares, O.; Mayers, J. R.; Gouirand, V.; Torrence, M. E.; Gicquel, T.; Borge, L.; Lac, S.; Roques, J.; Lavaut, M. N.; Berthezène, P.; Rubis, M.; Secq, V.; Garcia, S.; Moutardier, V.; Lombardo, D.; Iovanna, J. L.; Tomasini, R.; Guillaumond, F.; Vander Heiden, M. G.; et al. Collagen-Derived Proline Promotes Pancreatic Ductal Adenocarcinoma Cell Survival under Nutrient Limited Conditions. *Nat. Commun.* **2017**.

(27) Hanahan, D.; Weinberg, R. A. The Hallmarks of Cancer. *Cell*. 2000.

(28) Schlaeth, M.; Berger, S.; Derer, S.; Klausz, K.; Lohse, S.; Dechant, M.; Lazar, G. A.; Schneider-Merck, T.; Peipp, M.; Valerius, T. Fc-Engineered EGF-R Antibodies Mediate Improved Antibody-Dependent Cellular Cytotoxicity (ADCC) against KRAS-Mutated Tumor Cells. *Cancer Sci.* **2010**.

(29) Polyak, K.; Xia, Y.; Zweier, J. L.; Kinzler, K. W.; Vogelstein, B. A Model for P53-Induced Apoptosis. *Nature* **1997**.

(30) Elenbaas, B.; Spirio, L.; Koerner, F.; Fleming, M. D.; Zimonjic, D. B.; Donaher, J. L.; Popescu, N. C.; Hahn, W. C.; Weinberg, R. A. Human Breast Cancer Cells Generated by Oncogenic Transformation of Primary Mammary Epithelial Cells. *Genes Dev.* **2001**.

(31) Shen, Y.; Shenk, T. E. Viruses and Apoptosis. *Curr. Opin. Genet. Dev.* **1998**, *5*, 105–111.

(32) Murphy, T. A.; Young, J. D. ETA: Robust Software for Determination of Cell Specific Rates from Extracellular Time Courses. *Biotechnol. Bioeng.* **2013**, *110* (6), 1748–1758.

(33) Metallo, C. M.; Walther, J. L.; Stephanopoulos, G. Evaluation of 13C Isotopic Tracers for Metabolic Flux Analysis in Mammalian Cells. *J. Biotechnol.* **2009**, *144* (3), 167–174.

(34) Metallo, C. M.; Gameiro, P. A.; Bell, E. L.; Mattaini, K. R.; Yang, J.; Hiller, K.; Jewell, C. M.; Johnson, Z. R.; Irvine, D. J.; Guarente, L.; Kelleher, J. K.; Vander Heiden, M. G.; Iliopoulos, O.; Stephanopoulos, G. Reductive Glutamine Metabolism by IDH1 Mediates Lipogenesis under Hypoxia. *Nature* **2012**, *481* (7381), 380–384.

(35) Yoo, H.; Antoniewicz, M. R.; Stephanopoulos, G.; Kelleher, J. K. Quantifying Reductive Carboxylation Flux of Glutamine to Lipid in a Brown Adipocyte Cell Line. *J. Biol. Chem.* **2008**, *283* (30), 20621–20627.

(36) Gameiro, P. A.; Yang, J.; Metelo, A. M.; Pérez-Carro, R.; Baker, R.; Wang, Z.; Arreola, A.; Rathmell, W. K.; Olumi, A.; López-Larrubia, P.; Stephanopoulos, G.; Iliopoulos, O. In Vivo HIF-Mediated Reductive Carboxylation Is Regulated by Citrate Levels and Sensitizes VHL-Deficient Cells to Glutamine Deprivation. *Cell Metab.* **2013**, *17* (3), 372–385.

(37) Dong, W.; Keibler, M. A.; Stephanopoulos, G. Review of Metabolic Pathways Activated in Cancer Cells as Determined through Isotopic Labeling and Network Analysis. *Metab. Eng.* **2017**, *43*, 113–124.

(38) Kelleher, J. K.; Nickol, G. B. Isotopomer Spectral Analysis: Utilizing Nonlinear Models

in Isotopic Flux Studies. In *Methods in Enzymology*; 2015.

(39) Antoniewicz, M. R.; Kelleher, J. K.; Stephanopoulos, G. Elementary Metabolite Units (EMU): A Novel Framework for Modeling Isotopic Distributions. *Metab. Eng.* **2007**, *9* (1), 68–86.

(40) Dong, W.; Moon, S. J.; Kelleher, J. K.; Stephanopoulos, G. Dissecting Mammalian Cell Metabolism through 13C- And 2H-Isotope Tracing: Interpretations at the Molecular and Systems Levels. *Ind. Eng. Chem. Res.* **2019**.

(41) Carpenter, K. L. H.; Jalloh, I.; Gallagher, C. N.; Grice, P.; Howe, D. J.; Mason, A.; Timofeev, I.; Helmy, A.; Murphy, M. P.; Menon, D. K.; Kirkpatrick, P. J.; Carpenter, T. A.; Sutherland, G. R.; Pickard, J. D.; Hutchinson, P. J. 13C-Labelled Microdialysis Studies of Cerebral Metabolism in TBI Patients. *Eur. J. Pharm. Sci.* **2014**, *57* (100), 87–97.

(42) Sun, W.; Liu, Y.; Glazer, C. A.; Shao, C.; Bhan, S.; Demokan, S.; Zhao, M.; Rudek, M. A.; Ha, P. K.; Califano, J. A. TKTL1 Is Activated by Promoter Hypomethylation and Contributes to Head and Neck Squamous Cell Carcinoma Carcinogenesis through Increased Aerobic Glycolysis and HIF1α Stabilization. *Clin. Cancer Res.* **2010**.

(43) Fan, J.; Ye, J.; Kamphorst, J. J.; Shlomi, T.; Thompson, C. B.; Rabinowitz, J. D. Quantitative Flux Analysis Reveals Folate-Dependent NADPH Production. *Nature* **2014**, *10* (7504), 298–302.

(44) Jiang, P.; Du, W.; Mancuso, A.; Wellen, K. E.; Yang, X. Reciprocal Regulation of P53 and Malic Enzymes Modulates Metabolism and Senescence. *Nature* **2013**.

(45) DeBerardinis, R. J.; Chandel, N. S. Fundamentals of Cancer Metabolism. *Sci. Adv.* **2016**.

(46) Tsouko, E.; Khan, A. S.; White, M. A.; Han, J. J.; Shi, Y.; Merchant, F. A.; Sharpe, M. A.; Xin, L.; Frigo, D. E. Regulation of the Pentose Phosphate Pathway by an Androgen Receptor-MTOR-Mediated Mechanism and Its Role in Prostate Cancer Cell Growth. *Oncogenesis* **2014**.

(47) Zhang, X.; Liu, P.; Shang, Y.; Kerndl, H.; Kumstel, S.; Gong, P.; Vollmar, B.; Zechner, D. Metformin and LW6 Impairs Pancreatic Cancer Cells and Reduces Nuclear Localization of YAP1. *J. Cancer* **2020**.

(48) Calvert, A. E.; Chalastanis, A.; Wu, Y.; Hurley, L. A.; Kouri, F. M.; Bi, Y.; Kachman, M.; May, J. L.; Bartom, E.; Hua, Y.; Mishra, R. K.; Schiltz, G. E.; Dubrovskyi, O.; Mazar, A. P.; Peter, M. E.; Zheng, H.; James, C. D.; Burant, C. F.; Chandel, N. S.; et al. Cancer-Associated IDH1 Promotes Growth and Resistance to Targeted Therapies in the Absence of Mutation. *Cell Rep.* **2017**.

(49) Moreadith, R. W.; Lehninger, A. L. Purification, Kinetic Behavior, and Regulation of NAD(P)+ Malic Enzyme of Tumor Mitochondria. *J. Biol. Chem.* **1984**.

(50) Parlo, R. A.; Coleman, P. S. Enhanced Rate of Citrate Export from Cholesterol-Rich Hepatoma Mitochondria. The Truncated Krebs Cycle and Other Metabolic Ramifications of Mitochondrial Membrane Cholesterol. *J. Biol. Chem.* **1984**.

(51) Piva, T. J.; McEvoy-Bowe, E. Oxidation of Glutamine in Hela Cells: Role and Control of Truncated TCA Cycles in Tumour Mitochondria. *J. Cell. Biochem.* **1998**.

(52) Grassian, A. R.; Parker, S. J.; Davidson, S. M.; Divakaruni, A. S.; Green, C. R.; Zhang,

X.; Slocum, K. L.; Pu, M.; Lin, F.; Vickers, C.; Joud-Caldwell, C.; Chung, F.; Yin, H.; Handly, E. D.; Straub, C.; Growney, J. D.; Vander Heiden, M. G.; Murphy, A. N.; Pagliarini, R.; et al. IDH1 Mutations Alter Citric Acid Cycle Metabolism and Increase Dependence on Oxidative Mitochondrial Metabolism. *Cancer Res.* **2014**, *74* (12), 3317–3331.

(53) Wise, D. R.; Thompson, C. B. Glutamine Addiction: A New Therapeutic Target in Cancer. *Trends in Biochemical Sciences*. 2010.

(54) Tennant, D. A.; Durán, R. V.; Gottlieb, E. Targeting Metabolic Transformation for Cancer Therapy. *Nature Reviews Cancer*. 2010.

(55) Jin, L.; Alesi, G. N.; Kang, S. Glutaminolysis as a Target for Cancer Therapy. *Oncogene*. 2016.

(56) Fritz, V.; Fajas, L. Metabolism and Proliferation Share Common Regulatory Pathways in Cancer Cells. *Oncogene*. 2010.

(57) Fujii, T.; Khawaja, M. R.; DiNardo, C. D.; Atkins, J. T.; Janku, F. Targeting Isocitrate Dehydrogenase (IDH) in Cancer. *Discov. Med.* **2016**.

(58) Levis, M. Targeting IDH: The next Big Thing in AML. *Blood* **2013**.

(59) Lee, K.; Ban, H. S.; Naik, R.; Hong, Y. S.; Son, S.; Kim, B. K.; Xia, Y.; Song, K. Bin; Lee, H. S.; Won, M. Identification of Malate Dehydrogenase 2 as a Target Protein of the HIF-1 Inhibitor LW6 Using Chemical Probes. *Angew. Chemie - Int. Ed.* **2013**.

(60) Ramos-Montoya, A.; Lee, W. N. P.; Bassilian, S.; Lim, S.; Trebukhina, R. V.; Kazhyna, M. V.; Ciudad, C. J.; Noé, V.; Centelles, J. J.; Cascante, M. Pentose Phosphate Cycle

Oxidative and Nonoxidative Balance: A New Vulnerable Target for Overcoming Drug Resistance in Cancer. *Int. J. Cancer* **2006**.

(61) Young, J. D.; Walther, J. L.; Antoniewicz, M. R.; Yoo, H.; Stephanopoulos, G. An Elementary Metabolite Unit (EMU) Based Method of Isotopically Nonstationary Flux Analysis. *Biotechnol. Bioeng.* **2008**.

(62) Antoniewicz, M. R.; Kelleher, J. K.; Stephanopoulos, G. Determination of Confidence Intervals of Metabolic Fluxes Estimated from Stable Isotope Measurements. *Metab. Eng.* **2006**.

Conclusions and suggestions for future work

Chapter 5

Conclusions and suggestions for future work

Adapted from

Dong, W.; Keibler, M. A.; Stephanopoulos, G. Review of Metabolic Pathways Activated in Cancer Cells as Determined through Isotopic Labeling and Network Analysis. Metab. Eng. 2017, 43, 113−124.

Dong, W., Moon, S. J., Kelleher, J. K., & Stephanopoulos, G. Dissecting mammalian cell metabolism through 13C- and 2H-isotope tracing: Interpretations at the molecular and systems levels. ACS Ind. Eng. Chem. Res., 2019, 59(6), 2593-2610.

Dong, W., Keibler, M. A., Moon, S. J., Cho, P., Liu, N., Berrios, C. J., Kelleher, J. K., Sikes, H. D., Iliopoulos, O., Coloff, J. L., Vander Heiden, M. G., & Stephanopoulos, G. Oncogenic metabolic rewiring independent of proliferative control in human mammary epithelial cells. Pending Submission.

5.1 Summary and concluding remarks

This thesis addressed a fundamental question of whether there is a difference in the metabolism of cancerous, fast growing cells and normal proliferative cells. We first reviewed metabolic pathways differentially activated in cancer cells, followed by detailed analysis of metabolic shifts in cancer cells using isotopic labeling and ^{13}C-metabolic flux analysis (^{13}C-MFA).

In **Chapter 2**, we introduced recent advances in cancer metabolism research. We briefly explained isotopic labeling analysis and MFA, which have been instrumental in identifying and investigating metabolic rewiring in cancer cells. Both classical and modern interpretations of the Warburg effect were reviewed. Metabolic alterations due to the M2 isoform of pyruvate kinase (PKM2) and glyceraldehyde-3-phosphate dehydrogenase (GAPDH) were also discussed. In addition, we summarized major discoveries for reductive metabolism of glutamine and explained the labeling patterns from relevant ^{13}C-labeled glucose and glutamine tracers. Moreover, we reviewed the metabolic consequences of isocitrate dehydrogenase (IDH) mutations and the metabolic functions of the oncometabolite 2-hydroxyglutarate. Next, we discussed rewired serine and glycine metabolism and its correlation with tumorigenesis. Additionally, acetate metabolism and alternative sources of acetyl-CoA were also reviewed. Lastly, we recapitulated key signaling pathways of several oncogenes, and summarized recent findings elucidating oncogene-specific metabolic rewiring.

In **Chapter 3**, we reviewed common ^{13}C- and ^{2}H-isotopic tracers applied in dissecting mammalian cell metabolism. Particularly, we emphasized on stepwise tracking in metabolic pathways involving cyclic and branching biochemical reactions. We first analyzed labeling patterns in the tricarboxylic acid (TCA) cycle from U-$^{13}C_6$-glucose without extra complications

due to anaplerosis. Labeling patterns for each cycle were predicted and generalized based on the simple depiction of the TCA cycle. Next, we included pyruvate carboxylase (PC), malic enzyme (ME) and phosphoenolpyruvate carboxykinase (PEPCK), and described the resulting alterations on labeling patterns. Then, the labeling patterns of TCA cycle intermediates by U-$^{13}C_5$-, 1-^{13}C- and 5-^{13}C-glutamine tracers were elucidated, first without PC, ME and PEPCK and then with these extra reactions. Generalized labeling patterns of TCA cycle metabolites were also reported. Furthermore, we analyzed the labeling patterns by 1,2-$^{13}C_2$-acetate and 1-^{13}C-/1,6-$^{13}C_2$-glucose with respect to acetate-driven TCA cycling. Stepwise molecular tracking of ^{13}C atoms provided a systematic approach to interpreting these labeling results. In addition, the labeling schemes of pentose phosphate pathway (PPP) intermediates were explained by simultaneously tracking multiple metabolites derived from 1,2-$^{13}C_2$-, 2-^{13}C- and 3-^{13}C-glucose. Moreover, the applications of various ^{2}H-tracers such as 1-^{2}H-glucose, 3,3-$^{2}H_2$-serine, 2,2-$^{2}H_2$-glycine, 2,3,3-$^{2}H_3$-serine, 4-^{2}H-glucose, 2,2,3,3-$^{2}H_4$-dimethyl succinate and $^{2}H_2O$ were also reviewed. We then concluded the discussion by a case study of ^{13}C-MFA, the use of which successfully resolved distinct metabolic behavior of three hypothetical scenarios. ^{13}C-MFA also generated several metabolic insights that would be otherwise difficult to interpret by conventional means.

In **Chapter 4**, we studied the metabolic difference between cancer and normal proliferative cells through ^{13}C-isotope tracing and MFA. We first generated a panel of human mammary epithelial cells (HMECs) exhibiting differing levels of tumorigenicity. Importantly, these HMECs share the same genetic origin. We then determined the extracellular fluxes of glucose, lactate, glutamine and glutamate. By plotting these fluxes against specific growth rates, we showed that metabolism, at least at the extracellular level, might be dually controlled by proliferation and oncogenotypes. To further study metabolism at the intracellular level, we

performed ^{13}C-isotopic labeling experiments using U-$^{13}C_6$-glucose, U-$^{13}C_5$-glutamine and 1,2-$^{13}C_2$-glucose. By calculating the fractional contributions of TCA intermediates from U-$^{13}C_6$-glucose and U-$^{13}C_5$-glutamine, we uncovered a distinct substrate utilization pattern (Figure 5.1). In short, the TCA cycle was truncated and maintained by glutamine anaplerosis. In addition, *de novo* lipogenesis was supported by glucose entry via pyruvate dehydrogenase (PDH) and citrate synthase (CS). Interestingly, this pattern was observed throughout the entire panel of cell lines, suggesting that this utilization pattern was not unique to cancer cells or a specific oncogenotype. Next, we combined extracellular fluxes and intracellular labeling results via ^{13}C-MFA, which completely resolved all major metabolic fluxes within cells. We then plotted these fluxes against specific growth rates and demonstrated that a majority of metabolic reactions might be simultaneously regulated by proliferation and oncogenotypes. To isolate the impact of the indirect route through which oncogenotypes affect metabolism via growth, we introduced the quantity called metabolic flux intensity (MFI). By dividing fluxes over specific growth rates, we calculated MFIs for all major pathways and showed that most biochemical reactions exhibited statistically different MFIs, further corroborating that growth is not the single determinant regulating metabolic behavior (Figure 5.2). In addition, we identified three most enhanced pathways in the most tumorigenic HMEC line: oxidative pentose phosphate pathway (oxPPP), malate dehydrogenase (MDH) and isocitrate dehydrogenase (IDH). Drug targeting of these three reactions were selectively more toxic for HMEC-hTERT-LT-HRas, demonstrating promising therapeutic potentials (Figure 5.3). Most importantly, our work provided direct evidence that cancer and normal proliferative metabolism may be different, supporting the continuous effort to target metabolism with minimized side effects on normal cells for more effective cancer therapies.

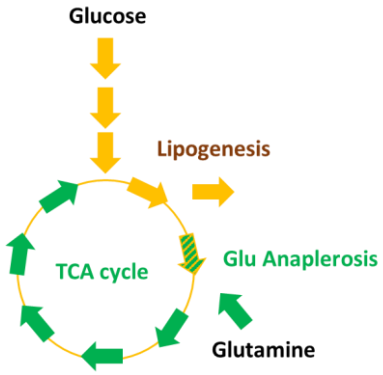

Figure 5.1. Truncated TCA cycle: glutamine-fueled TCA oxidation and glucose-supported lipogenesis.

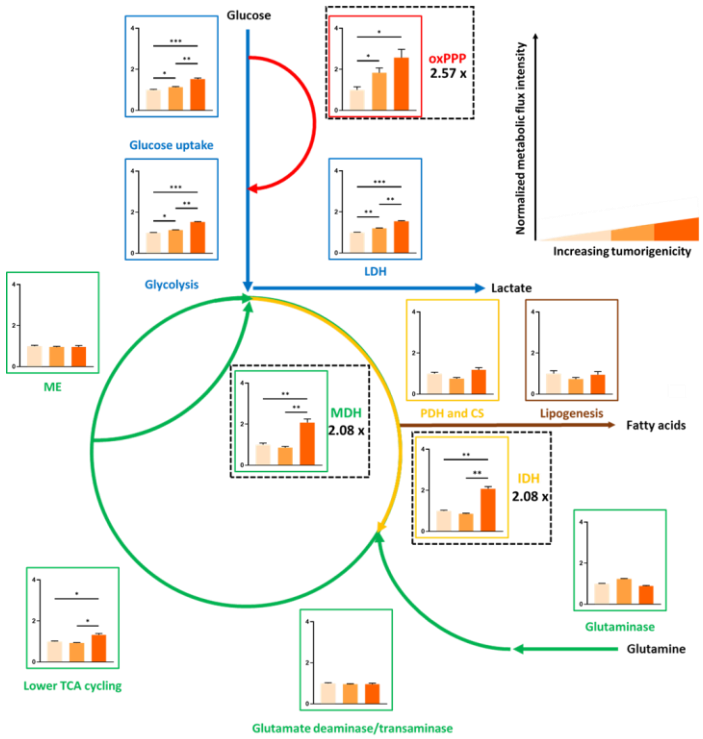

Figure 5.2. Metabolic flux intensity analysis suggested dual control of metabolism by proliferation and oncogenotypes.

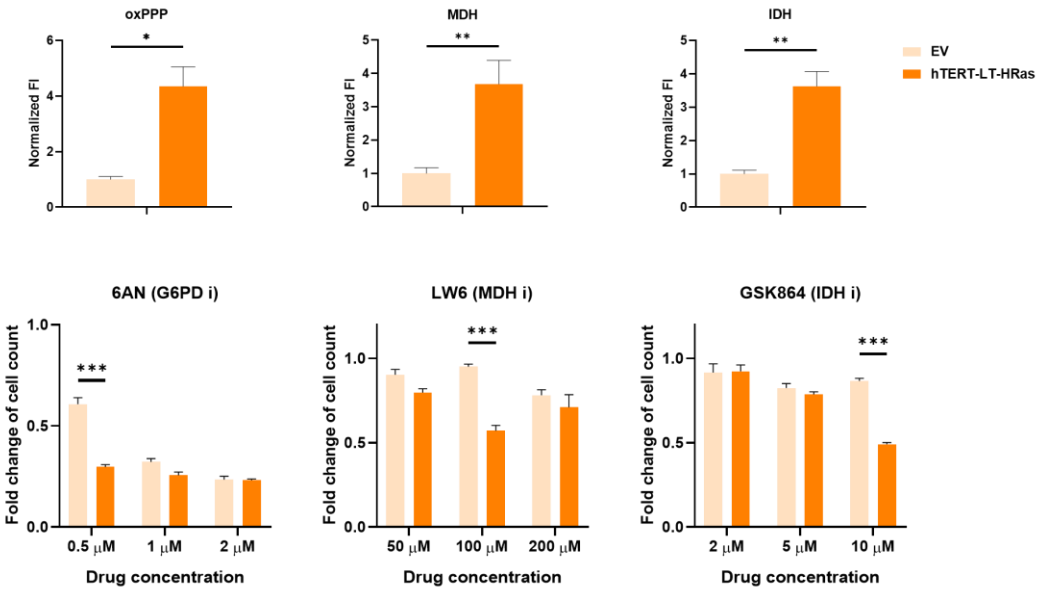

Figure 5.3. Metabolic flux intensity analysis (top) identified oxPPP, MDH and IDH to be the most enhanced pathways in the tumorigenic HMECs (hTERT-LT-HRas). Drug targeting of these pathways showed promising therapeutic potentials.

5.2 Future directions

In this thesis, we reviewed a plethora of metabolic rewiring phenomena and introduced state-of-the-art isotope tracing and flux analysis techniques to study cancer metabolism. More importantly, we applied these techniques and addressed a long-lasting question of whether metabolism of cancer cells is different than that of proliferating cells. Although steady progress has been made to better understand cancer metabolism, there still remains much to be discovered for cancer metabolism.

One area largely undeveloped in this field is subcellular characterization of metabolism. The major limitation is the challenge to separate compartment-specific metabolite pools. However, it is promising to witness that many techniques have been successfully developed to

enhance the spatial resolution for metabolic measurements. One example is the use of ^{2}H tracing in resolving mitochondrial and cytosolic compartments within intact cells[1]. Other alternatives include rapid isolation and harvesting of specific compartments. These methods demonstrate great potential to resolve subcellular metabolism[2,3]. Another emerging area is *in vivo* metabolic studies. Tumor microenvironment[4], heterogeneity in tumor tissues[5] and system-level fluxomics[6] are some excellent examples in line with this effort.

In addition to reviewing metabolic rewiring in cancer cells, we also introduced ^{13}C-isotope tracing techniques and their applications to various systems. The tracers reviewed in Chapter 2 do not offer a comprehensive list. In fact, we believe the use of other tracers carrying ^{13}C, ^{2}H, ^{18}O, ^{15}N will improve pathway-specific metabolic alterations[1,7–12]. In addition, radiolabeled tracers may provide enhanced resolution compared to stable isotopic tracers in some cases[13–15]. Moreover, several mixtures of tracers have been designed to better characterize certain metabolic pathways. For example, upregulated transketolase-like protein 1 (TKTL1) has been reported in certain types of cancer[16], but the use of 1,2-$^{13}C_2$-glucose alone was not able to generate sufficient information to assess this metabolic pathway. To address this issue, several equimolar mixtures of tracers such as 1-^{13}C-and 4,5,6-$^{13}C_3$-glucose, 2-^{13}C- and 4,5,6-$^{13}C_3$-glucose and 3-^{13}C- and 4,5,6-$^{13}C_3$-glucose have been developed[16]. These combinations of tracers were capable of resolving the interaction of TKTL1 and the pentose phosphate pathway (PPP)[16,17]. More combinations of tracers still remain to be discovered and better engineered to dissect intricate metabolic networks.

As an advanced approach to integrating isotopic labeling data, ^{13}C-MFA has been widely applicable in the field of metabolic engineering. Although its application has gained popularity in studying cancer metabolism over the past decades, there are still several challenges limiting its

use by the broader community: 1) the overall concept and methodology need to be better explained. Particularly, the notions of pseudo-steady state hypothesis, flux continuity and mass balances should be elucidated more frequently using non-technical languages and case studies; 2) Inclusion of graphical user interfaces (GUIs) are recommended for the pieces of software performing ^{13}C-MFA; 3) Efforts should be made to achieve pseudo-steady state in certain systems more easily. Although it is critical to address the first two challenges, we would like to share a few strategies to solve the last issue. In order to approach metabolic and isotopic steady states, it is highly recommended to select a cell culture system with high metabolic activity. Since steady states are achieved by turnovers of preexisting metabolic intermediates, higher metabolic fluxes drive this dynamic transition and thus shorten the time needed to reach a new metabolic state (whether after an acute physiological perturbation or replacement of unlabeled substrates by the labeled species). In addition, metabolic perturbations should be avoided during MFA sampling to prevent metabolic shifts. For example, metabolite collections should not coincide with genetic manipulations (siRNA knock-down, induced expressions of certain genes, etc.). Otherwise, metabolic states are unlikely to stay constant. Instead, these perturbations should be introduced prior to MFA sampling. Ideally, the optimal time points for perturbations and MFA should be determined experimentally.

Combining the knowledge of cancer metabolism and the toolbox to dissect complex bioreaction networks, we investigated whether cancer metabolism is different from proliferative metabolism in Chapter 4. Through isotopic labeling with glucose and glutamine tracers, we uncovered a distinct substrate utilization pattern and pinpointed the crucial role of glutamine anaplerosis in sustaining the TCA cycle[18–23]. Moreover, glucose was the primary substrate utilized for *de novo* lipid synthesis. In contrast to previous investigations, this pattern was not

unique to tumorigenic or oncogenic cell lines[24]. Neither did this pattern lead to any metabolic disadvantages[24,25]. However, the mechanism by which this metabolic pattern occurs still remains elusive. Our quantitative flux results may provide opportunity to further explore this area. Moreover, it is not clear whether these rewired energetics may potentiate metabolic vulnerabilities that can be exploited to develop additional therapeutic strategies. This idea is in line with the recent efforts to target multiple metabolic pathways for improved cancer therapies[26–28].

More importantly in Chapter 4, we introduced the concept of metabolic flux intensity (MFI). By dividing fluxes over specific growth rates, we proposed a quantitative metric to assess proliferation-independent control of metabolism. In addition, MFI analysis further identified the oxidative pentose phosphate pathway (oxPPP), malate dehydrogenase (MDH) and isocitrate dehydrogenase (IDH) as the most enhanced pathways in the most tumorigenic cell line. We believe that similar MFI analysis can also be applied to other research areas such as metabolic engineering. For example, one can calculate MFIs for major metabolic pathways in an engineered microorganism relative to the wild-type strain, and characterize potential metabolic shifts normalized by the impact of growth alterations. This insight enables researchers to focus on productivity enhancement independent of proliferation, as a boost in product titer may be explained by increased biomass accumulation. The idea to normalize fluxes by specific growth rates is also widely applicable to other diseases with metabolic implications where growth introduces confounding factors mediating the interplay between genotypes and metabolism.

5.3 References

(1) Lewis, C. A.; Parker, S. J.; Fiske, B. P.; McCloskey, D.; Gui, D. Y.; Green, C. R.; Vokes, N. I.; Feist, A. M.; Vander Heiden, M. G.; Metallo, C. M. Tracing Compartmentalized NADPH Metabolism in the Cytosol and Mitochondria of Mammalian Cells. *Mol. Cell* **2014**, *55* (2), 253–263.

(2) Chen, W. W.; Freinkman, E.; Wang, T.; Birsoy, K.; Sabatini, D. M. Absolute Quantification of Matrix Metabolites Reveals the Dynamics of Mitochondrial Metabolism. *Cell* **2016**, *166* (5), 1324-1337.e11.

(3) Abu-Remaileh, M.; Wyant, G. A.; Kim, C.; Laqtom, N. N.; Abbasi, M.; Chan, S. H.; Freinkman, E.; Sabatini, D. M. Lysosomal Metabolomics Reveals V-ATPase- and MTOR-Dependent Regulation of Amino Acid Efflux from Lysosomes. *Science (80-.).* **2017**.

(4) Davidson, S. M.; Papagiannakopoulos, T.; Olenchock, B. A.; Heyman, J. E.; Keibler, M. A.; Luengo, A.; Bauer, M. R.; Jha, A. K.; O'Brien, J. P.; Pierce, K. A.; Gui, D. Y.; Sullivan, L. B.; Wasylenko, T. M.; Subbaraj, L.; Chin, C. R.; Stephanopolous, G.; Mott, B. T.; Jacks, T.; Clish, C. B.; et al. Environment Impacts the Metabolic Dependencies of Ras-Driven Non-Small Cell Lung Cancer. *Cell Metab.* **2016**, *23* (3), 517–528.

(5) Hensley, C. T.; Faubert, B.; Yuan, Q.; Lev-Cohain, N.; Jin, E.; Kim, J.; Jiang, L.; Ko, B.; Skelton, R.; Loudat, L.; Wodzak, M.; Klimko, C.; McMillan, E.; Butt, Y.; Ni, M.; Oliver, D.; Torrealba, J.; Malloy, C. R.; Kernstine, K.; et al. Metabolic Heterogeneity in Human Lung Tumors. *Cell* **2016**, *164* (4), 681–694.

(6) Hui, S.; Ghergurovich, J. M.; Morscher, R. J.; Jang, C.; Teng, X.; Lu, W.; Esparza, L. A.;

Reya, T.; Zhan, L.; Yanxiang Guo, J.; White, E.; Rabinowitz, J. D. Glucose Feeds the TCA Cycle via Circulating Lactate. *Nature* **2017**.

(7) Fan, J.; Ye, J.; Kamphorst, J. J.; Shlomi, T.; Thompson, C. B.; Rabinowitz, J. D. Quantitative Flux Analysis Reveals Folate-Dependent NADPH Production. *Nature* **2014**, *10* (7504), 298–302.

(8) Liu, L.; Shah, S.; Fan, J.; Park, J. O.; Wellen, K. E.; Rabinowitz, J. D. Malic Enzyme Tracers Reveal Hypoxia-Induced Switch in Adipocyte NADPH Pathway Usage. *Nat. Chem. Biol.* **2016**, *12* (5), 345–352.

(9) Zhang, Z.; Chen, L.; Liu, L.; Su, X.; Rabinowitz, J. D. Chemical Basis for Deuterium Labeling of Fat and NADPH. *J. Am. Chem. Soc.* **2017**, *139* (41), 14368–14371.

(10) Wadke, M.; Brunengraber, H.; Lowenstein, J. M.; Dolhun, J. J.; Arsenault, G. P. Fatty Acid Synthesis by the Liver Perfused with Deuterated and Tritiated Water. *Biochemistry* **1973**, *12* (14), 2619–2624.

(11) Lee, W. N.; Bassilian, S.; Ajie, H. O.; Schoeller, D. A.; Edmond, J.; Bergner, E. A.; Byerley, L. O. In Vivo Measurement of Fatty Acids and Cholesterol Synthesis Using D2O and Mass Isotopomer Analysis. *Am. J. Physiol. Metab.* **1994**, *266* (5), E699–E708.

(12) Busch, R.; Kim, Y. K.; Neese, R. A.; Schade-Serin, V.; Collins, M.; Awada, M.; Gardner, J. L.; Beysen, C.; Marino, M. E.; Misell, L. M.; Hellerstein, M. K. Measurement of Protein Turnover Rates by Heavy Water Labeling of Nonessential Amino Acids. *Biochim. Biophys. Acta - Gen. Subj.* **2006**, *1760* (5), 730–744.

(13) Schuster, D. M.; Nanni, C.; Fanti, S. Evaluation of Prostate Cancer with Radiolabeled

Amino Acid Analogs. *J. Nucl. Med.* **2016**.

(14) Gambhir, S. S. Molecular Imaging of Cancer with Positron Emission Tomography. *Nature Reviews Cancer*. 2002.

(15) Yoshimoto, M.; Waki, A.; Obata, A.; Furukawa, T.; Yonekura, Y.; Fujibayashi, Y. Radiolabeled Choline as a Proliferation Marker: Comparison with Radiolabeled Acetate. *Nucl. Med. Biol.* **2004**.

(16) Ahn, W. S.; Crown, S. B.; Antoniewicz, M. R. Evidence for Transketolase-like TKTL1 Flux in CHO Cells Based on Parallel Labeling Experiments and 13C-Metabolic Flux Analysis. *Metab. Eng.* **2016**, *37*, 72–78.

(17) Diaz-Moralli, S.; Aguilar, E.; Marin, S.; Coy, J. F.; Dewerchin, M.; Antoniewicz, M. R.; Meca-Cortés, O.; Notebaert, L.; Ghesquière, B.; Eelen, G.; Thomson, T. M.; Carmeliet, P.; Cascante, M. A Key Role for Transketolase-like 1 in Tumor Metabolic Reprogramming. *Oncotarget* **2016**, *7* (32).

(18) Moreadith, R. W.; Lehninger, A. L. Purification, Kinetic Behavior, and Regulation of NAD(P)+ Malic Enzyme of Tumor Mitochondria. *J. Biol. Chem.* **1984**.

(19) Parlo, R. A.; Coleman, P. S. Enhanced Rate of Citrate Export from Cholesterol-Rich Hepatoma Mitochondria. The Truncated Krebs Cycle and Other Metabolic Ramifications of Mitochondrial Membrane Cholesterol. *J. Biol. Chem.* **1984**.

(20) Piva, T. J.; McEvoy-Bowe, E. Oxidation of Glutamine in Hela Cells: Role and Control of Truncated TCA Cycles in Tumour Mitochondria. *J. Cell. Biochem.* **1998**.

(21) Metallo, C. M.; Gameiro, P. A.; Bell, E. L.; Mattaini, K. R.; Yang, J.; Hiller, K.; Jewell,

C. M.; Johnson, Z. R.; Irvine, D. J.; Guarente, L.; Kelleher, J. K.; Vander Heiden, M. G.; Iliopoulos, O.; Stephanopoulos, G. Reductive Glutamine Metabolism by IDH1 Mediates Lipogenesis under Hypoxia. *Nature* **2012**, *481* (7381), 380–384.

(22) Gameiro, P. A.; Yang, J.; Metelo, A. M.; Pérez-Carro, R.; Baker, R.; Wang, Z.; Arreola, A.; Rathmell, W. K.; Olumi, A.; López-Larrubia, P.; Stephanopoulos, G.; Iliopoulos, O. In Vivo HIF-Mediated Reductive Carboxylation Is Regulated by Citrate Levels and Sensitizes VHL-Deficient Cells to Glutamine Deprivation. *Cell Metab.* **2013**, *17* (3), 372–385.

(23) Mullen, A. R.; Wheaton, W. W.; Jin, E. S.; Chen, P.-H.; Sullivan, L. B.; Cheng, T.; Yang, Y.; Linehan, W. M.; Chandel, N. S.; DeBerardinis, R. J. Reductive Carboxylation Supports Growth in Tumour Cells with Defective Mitochondria. *Nature* **2012**, *481* (7381), 385–388.

(24) Grassian, A. R.; Parker, S. J.; Davidson, S. M.; Divakaruni, A. S.; Green, C. R.; Zhang, X.; Slocum, K. L.; Pu, M.; Lin, F.; Vickers, C.; Joud-Caldwell, C.; Chung, F.; Yin, H.; Handly, E. D.; Straub, C.; Growney, J. D.; Vander Heiden, M. G.; Murphy, A. N.; Pagliarini, R.; et al. IDH1 Mutations Alter Citric Acid Cycle Metabolism and Increase Dependence on Oxidative Mitochondrial Metabolism. *Cancer Res.* **2014**, *74* (12), 3317–3331.

(25) DeBerardinis, R. J.; Mancuso, A.; Daikhin, E.; Nissim, I.; Yudkoff, M.; Wehrli, S.; Thompson, C. B. Beyond Aerobic Glycolysis: Transformed Cells Can Engage in Glutamine Metabolism That Exceeds the Requirement for Protein and Nucleotide Synthesis. *Proc. Natl. Acad. Sci. U. S. A.* **2007**, *104* (49), 19345–19350.

(26) Wise, D. R.; Thompson, C. B. Glutamine Addiction: A New Therapeutic Target in Cancer. *Trends in Biochemical Sciences*. 2010.

(27) Tennant, D. A.; Durán, R. V.; Gottlieb, E. Targeting Metabolic Transformation for Cancer Therapy. *Nature Reviews Cancer*. 2010.

(28) Jin, L.; Alesi, G. N.; Kang, S. Glutaminolysis as a Target for Cancer Therapy. *Oncogene*. 2016.